Raman Microspectroscopy and Fluorescence Lifetime Imaging Microscopy based Data-Driven Tissue Discrimination and Diagnostics

Dissertation
der Mathematisch-Naturwissenschaftlichen Fakultät
der Eberhard Karls Universität Tübingen
zur Erlangung des Grades eines
Doktors der Naturwissenschaften
(Dr. rer. nat.)

vorgelegt von

M. Sc. Lucas Becker

aus Ostfildern Ruit

Tübingen

2023

Gedruckt mit Genehmigung der Mathematisch-Naturwissenschaftlichen Fakultät der Eberhard Karls Universität Tübingen.

Tag der mündlichen Qualifikation: 12.07.2023
Dekan: Prof. Dr. Thilo Stehle
1. Berichterstatter/-in: Prof. Dr. Katja Schenke-Layland
2. Berichterstatter/-in: Prof. Dr.-Ing. Cristina Tarin

„Die Wissenschaft ist der Verstand der Welt, die Kunst ihre Seele.”

Maksim Gorki

Table of Contents

Abstract

The ultimate objective of any new interventional or surgical techniques is to achieve a balance of minimal invasiveness, optimal efficacy, and rapid treatment duration, all while minimizing the risk of complications. A pivotal component in the management of any disease is the distinction between the impacted target structures and the neighboring healthy tissue throughout all medical interventions, encompassing surgical procedures. Such differentiation is paramount in reducing harm to healthy tissue and augmenting the efficacy of the treatment. Within the current therapeutic procedures, innovations in the field of preoperative and postoperative diagnostics contribute to the improved differentiation of benign and malignant tissue structures. On the one hand, sophisticated imaging techniques support an improved surgical decision-making, while on the other hand, histopathological examination methods enable a precise classification of the tissue after surgery. In contrast, intraoperative tissue differentiation has been based on the time-consuming gold standard of frozen section diagnostics for many years. However, by incorporating the supplementary data provided by advanced imaging sensors during surgery, and integrating it with cutting-edge machine learning methodologies, it is feasible to augment the quality of information utilized for tissue differentiation, thereby increasing the precision of the overall process.

Another important task of modern medicine is the patient-specific treatment of cancer, as it has been found that different patients do not respond in the same way to drug treatment due to developed resistance mechanisms.

This thesis aimed to establish Raman microspectroscopy (RMS) as marker-independent, and non-destructive technique to monitor fibrotic and epigenetic modifications in malign and benign human tissue. Additionally, the potential of RMS and fluorescence lifetime imaging microscopy (FLIM) was evaluated to non-invasively monitor the drug efficacy on patient-derived organoids from cancer patients. Towards this aim, collagen type I (COL I) structures of formalin-fixed paraffin-embedded (FFPE) tissue sections of various fibrotic diseases were compared to respective control tissue sections. Incorporating Raman measurements into the experimental protocol, we conducted routine histological and immunofluorescence (IF) staining techniques to showcase the superior efficacy of RMS when paired with spectral deconvolution. This technique offers a time- and cost-efficient alternative to conventional procedures.

For the differentiation of pathological tissue, the identification of epigenetic modes of action is a promising and potentially successful approach. In alignment with IF imaging of the most abundant epigenetic modification of 5-methylcytosine (5mC), Raman spectra of cell nuclei were evaluated using multivariate data analysis. Compared to invasive staining methods, non-invasive RMS showed promising results for the differentiation of pathological tissue changes in cardiac fibrosis and endometriosis. In addition, RMS and FLIM have been used on several bladder and colon cancer organoids to evaluate their potential to monitor patient-specific responses to drug treatment. The results showed both that organoids are generally suitable as a screening platform for drug treatments and that Raman and FLIM have the potential to assess drug sensitivity.

This work highlights the potential of RMS for future applications in ex vivo tissue discrimination of fibrotic diseases and identification of epigenetic changes. In addition, this work demonstrates the proof of principle that RMS and FLIM are suitable for monitoring patient-specific responses to medications on organoid models.

Zusammenfassung

Das ultimative Ziel jeder neuen interventionellen oder chirurgischen Technik ist, ein Gleichgewicht zwischen minimaler Invasivität, optimaler Wirksamkeit und schneller Behandlungsdauer zu erreichen, während das Risiko von Komplikationen minimiert wird. Ein entscheidender Bestandteil bei der Behandlung jeder Krankheit ist die Unterscheidung zwischen den betroffenen Zielstrukturen und dem umliegenden gesunden Gewebe bei allen medizinischen Eingriffen, einschließlich chirurgischer Verfahren. Eine solche Unterscheidung ist von entscheidender Bedeutung, um Schäden am gesunden Gewebe zu minimieren und die Wirksamkeit der Behandlung zu maximieren. Innerhalb der aktuellen therapeutischen Verfahren tragen Innovationen im Bereich der präoperativen und postoperativen Diagnostik zur verbesserten Unterscheidung von benignen und malignen Gewebestrukturen bei. Einerseits unterstützen ausgefeilte Bildgebungstechniken eine verbesserte chirurgische Entscheidungsfindung, andererseits ermöglichen histopathologische Untersuchungsmethoden eine präzise Klassifizierung des Gewebes nach der Operation. Im Gegensatz dazu basiert die intraoperative Gewebeunterscheidung seit vielen Jahren auf dem zeitaufwändigen Goldstandard der gefrorenen Schnittdiagnostik. Durch die Einbeziehung der ergänzenden Daten, die während der Operation von fortschrittlichen Bildgebungssensoren geliefert werden, und durch die Integration mit modernen Machine-Learning-Methoden ist es jedoch möglich, die Qualität der für die Gewebeunterscheidung verwendeten Informationen zu verbessern und damit die Präzision des gesamten Prozesses zu erhöhen.

Eine weitere wichtige Aufgabe der modernen Medizin ist die patientenspezifische Behandlung von Krebs, da festgestellt wurde, dass verschiedene Patienten aufgrund entwickelter Resistenzmechanismen nicht in gleicher Weise auf die medikamentöse Behandlung ansprechen.

Diese Arbeit zielt darauf ab, die Raman-Mikrospektroskopie (RMS) als marker-unabhängige und zerstörungsfreie Technik zur Überwachung von fibrösen und epigenetischen Veränderungen in malignen und benignen menschlichen Geweben zu etablieren. Zusätzlich wurde das Potenzial von RMS und der Fluoreszenzlebensdauermikroskopie (FLIM) evaluiert, um die Wirksamkeit von Medikamenten an patientenabgeleiteten Organoiden von Krebspatienten nicht-invasiv zu überwachen. Zu diesem Zweck wurden Kollagen Typ I (COL I)-Strukturen von formalin-fixierten Paraffin-eingebetteten (FFPE) Gewebeschnitten verschiedener fibrotischer

Erkrankungen mit entsprechenden Kontrollgewebeschnitten verglichen. Durch die Integration von Raman-Messungen in das experimentelle Protokoll wurden Routine-Histologie- und Immunfluoreszenz (IF)-Färbemethoden durchgeführt, um die überlegene Wirksamkeit von RMS in Kombination mit spektraler Dekonvolution zu demonstrieren. Diese Technik bietet eine zeit- und kosteneffiziente Alternative zu konventionellen Verfahren.

Für die Differenzierung von pathologischem Gewebe ist die Identifizierung epigenetischer Wirkmechanismen ein vielversprechender und potenziell erfolgreicher Ansatz. In Anlehnung an die IF-Bildgebung der am häufigsten vorkommenden epigenetischen Modifikation 5-Methylcytosin (5mC) wurden Raman-Spektren von Zellkernen mittels multivariater Datenanalyse ausgewertet. Im Vergleich zu invasiven Färbemethoden zeigte die nicht-invasive RMS vielversprechende Ergebnisse für die Differenzierung von pathologischen Gewebeveränderungen bei Herzfibrose und Endometriose. Darüber hinaus wurden RMS und FLIM bei verschiedenen Organoiden von Blasen- und Darmkrebs eingesetzt, um deren Potenzial zur Überwachung der patientenspezifischen Reaktionen auf eine medikamentöse Behandlung zu bewerten. Die Ergebnisse zeigten sowohl, dass Organoide generell als Screening-Plattform für medikamentöse Behandlungen geeignet sind, als auch, dass Raman und FLIM das Potenzial haben, die Empfindlichkeit gegenüber Medikamenten zu bewerten.

Diese Arbeit unterstreicht das Potenzial von RMS für künftige Anwendungen bei der Ex-vivo-Gewebediskriminierung von fibrotischen Erkrankungen und der Identifizierung epigenetischer Veränderungen. Darüber hinaus beweist diese Arbeit, dass RMS und FLIM für die Überwachung patientenspezifischer Reaktionen auf Medikamente an organoiden Modellen geeignet sind.

Abbreviations

2D	Two-dimensional
3D	Three-dimensional
5mC	5-methyl cytosine
AI	Artificial intelligence
Acetyl-CoA	Acetyl-coenzyme A
a.u.	Arbitrary units
ATP	Adenosine triphosphate
BCO	Bladder cancer organoids
CARS	Coherent anti-Stokes Raman Spectroscopy
cis	Cisplatin
CCD	Charged-coupled device
COL I	Collagen type 1
COL III	Collagen type 3
COL IV	Collagen type 4
CpG	cytosine-phosphate-guanine
CRC	Colorectal cancer
DMSO	Dimethyl sulfoxide
DNA	Deoxyribonucleic acid
DNMT	DNA methyltransferase
EC_{50}	Effective concentration
ECM	Extracellular matrix
FAD	Flavin adenine dinucleotide
FFPE	Formalin-fixed paraffin-embedded
FLIM	Fluorescence lifetime imaging microscopy
Gly	Glycine
HSP	Heat shock protein
IF	Immunofluorescence
IHC	Immunohistochemical
LDA	Linear discriminant analysis
LDH	Lactate dehydrogenase
ML	Machine learning
MVA	Multivariate analysis

NADH	Nicotinamide adenine dinucleotide
NGS	Next generation sequencing
OCT	Optimal cutting temperature
PCA	Principal component analysis
PCR	Polymerase chain reaction
PMT	Photomultiplier tubes
PFA	Paraformaldehyde
PSR	Picrosirius red
rER	Rough endoplasmic reticulum
RMS	Raman microspectroscopy
ROS	Reactive oxygen species
SERS	Surface enhanced Raman spectroscopy
SHG	Second harmonic generation
αSMA	Alpha smooth muscle actin
SRS	Stimulated Raman spectroscopy
TCA	True component analysis
TCSPC	Time correlated single photon counting
TOPO	Topoisomerase
UCO	Urine derived organoids
UGT	Uridine diphosphate glucuronosyltransferase
vtx	Venetoclax
WHO	World health organization

List of Figures

List of Publications

Published Manuscripts

1. **Becker L.**, Fischer F., Fleck J., Harland N., Stenzl A., Aicher W.K., Schenke-Layland K., Marzi J., *Data-Driven Identification of Biomarkers for In Situ Monitoring of Drug Treatment*, Int. J. Mol. Sci. 2022, *23*(13), 6956; https://doi.org/10.3390/ijms23136956

2. **Becker L.**, Lu C., Montes-Mojarro I. A., Layland S. L., Khalil S., Nsair A., Duffy G. P., Fend, F., Marzi J., Schenke-Layland K., *Raman Microspectroscopy Identifies Fibrotic Tissues in Collagen-related Disorders Via Deconvoluted Collagen type I Spectra,* Acta Biomater., 2023, https:// dx.doi.org/10.2139/ssrn.4294703

3. **Becker L.**, Janssen N., Layland S L. Mürdter T. E., Nies A. N., Schenke-Layland K., Marzi J., *Raman Imaging and Fluorescence Lifetime Imaging Microscopy for Diagnosis of Cancer State and Metabolic Monitoring*, Cancers 2021, *13*(22), 5682; https://doi.org/10.3390/cancers13225682

4. **Becker L.**, Montes-Mojarro A., Layland S. L., Nsair A., Fend F., Marzi J., Schenke-Layland K., *Exploring the relationship between epigenetic DNA methylation and cardiac fibrosis through Raman microspectroscopy*, Am. J. Physiol. 2023, *325*(1), C332-C343; https://doi.org/10.1152/ajpcell.00209.2023

Submitted Manuscripts

5. **Becker L.,** Beyer T., Liebscher S., Carvajal-Berrio D., Bösmüller H., Krämer B., Rall K., Brucker S. Y., Schenke-Layland K., Weiss M., Marzi J., *Marker-independent imaging reveals a correlation of fibrotic and epigenetic alterations in endometriosis*

6. Marzi J., **Becker L.**, Schenke-Layland K., *Raman Imaging for Biomedical Applications*

Manuscripts in Preparation

7. **Becker L.**, Janssen N., Wallisch S., Mürdter T. E., Renner P., Dahlke M. H., Marzi J., Nies A. T., Schwab M., Schenke-Layland K., *Label-free Raman Microscopy-based Monitoring of Anti-cancer Drug Effects in Colorectal Cancer Organoids towards Patient-individualized Optimization of treatments*

Additional Publications

8. Holl M., **Becker L.**, Keller A., Feuerer N, Marzi J., Carvajal Berrio D. A., Jakubowski, P, Neis F., Pauluschke-Fröhlich J., Brucker S. Y., Schenke-Layland K., Krämer B., Weiss M.*, Laparoscopic Peritoneal Wash Cytology-Derived Primary Human Mesothelial Cells for In Vitro Cell Culture and Simulation of Human Peritoneum*, Biomedicines 2021, 9(2), 176; https://doi.org/10.3390/biomedicines9020176

9. Holl M., Rasch M., **Becker L**., Keller A., Schultze-Ronhoff, L, Ruoff, F, Templin M., Keller S., Neis F., Keßler F., Andress J., Bachmann C., Krämer B., Schenke-Layland K., Brucker S. Y., Marzi J., Weiss M., *Cell Type-Specific Anti-Adhesion Properties of Peritoneal Cell Treatment with Plasma-Activated Media (PAM)*, Biomedicines 2022 10(4): 927., 10.3390/biomedicines10040927

10. Zbinden A., Urbanczyk M., Layland S. L., **Becker L**., Marzi J., Bosch M., Loskill P., Duffy, G. P., Schenke-Layland K., *Collagen and endothelial cell co-culture improves β-cell functionality and rescues pancreatic ECM*, Tissue Engineering Part A, 2021 27:13-14, 977-991, https://doi.org/10.1089/ten.tea.2020.0250

Contributions

No.	Published	Number of authors	Position of the candidate in the list of authors	Scientific ideas by candidate (%)	Data generation by candidate (%)	Interpretation and analysis by candidate (%)	Paper writing by candidate (%)
1	Yes	9	1	40	50	50	40
2	Yes	10	1	40	40	40	35
3	Yes	5	1	Review	Review	Review	60
4	Yes	7	1	40	50	50	60
5	No	11	1	40	40	40	40
6	No	3	2	Book chapter	Book chapter	Book chapter	30
7	No	10	1	50	50	60	50

Chapter 1

Introduction

1 Introduction

1.1 Tissue Characterization

Tissue characterization is a field of study that encompasses the thorough examination and interpretation of the physical and chemical attributes of biological tissues. The characterization of tissues is essential in understanding their structure and function, as well as their response to various stimuli, such as disease or injury. Tissue characterization techniques can be used in a variety of applications, including medical diagnosis, drug discovery, and tissue engineering. In recent years, there has been a growing interest in developing non-invasive and quantitative techniques for tissue characterization, which has led to the development of advanced imaging modalities and spectroscopic methods. These methods have been shown to complement the gold standard histological techniques, which traditionally rely on invasive tissue biopsies and staining methods [1-6].

1.1.1 Histological Diagnostic

Histology is essential to many areas of medicine, applied sciences, and allied health professions as it relates microscopic structures of tissues and cells to their function [7]. In gold standard and daily-clinic procedures, human tissue samples procured from biopsies undergo formalin fixation and paraffin embedding (FFPE) prior to being sectioned. This intricate process is intended to optimize tissue preservation. Afterward, histological staining is performed, and the samples are scrutinized by proficient pathologists to discern any underlying illnesses or conditions. [8-11]. In addition to conventional and rapid hematoxylin-eosin (H&E) stains providing tissue overviews, immunohistochemical (IHC) and immunofluorescence (IF) stains are utilized to visualize essential cell proteins using monoclonal antibodies and fluorescence microscopy [12,13]. The image information is supplemented by cytogenetic and molecular biological methods (i.e., polymerase chain reaction (PCR), gene sequencing) enabling the detection of pathological changes in the genome and allowing or promising further extraordinary expansion of the diagnostic possibilities of pathology [14-16].

Although these techniques are efficacious, they possess certain limitations, such as elaborate staining procedures that consume time and chemical changes that occur due to the fixation process. As a result, the frozen section procedure was developed as an alternative. Rather than utilizing FFPE fixation, the tissue is treated with a cryoprotectant, such as dimethyl sulfoxide (DMSO), propylene glycol, or ethane diol, to curb the detrimental impact of osmosis and diffusion on cells throughout the freezing process [17-20]. Additionally, the cryoprotectant stabilizes the tissue by removing interstitial water. With this method, the required time to generate H&E stainable tissue slides can be reduced from 16 hours to about 10 minutes, allowing rapid evaluation of the dignity of a lesion and the completeness of the resection during ongoing clinical surgery [21-23]. However, the limitations of cryopreservation are the possible formation of ice, entailing a higher risk of tissue destruction, and the shorter storage time of the tissue [24].

1.1.2 Patient-Derived in vitro Tissue Models

The in vivo and ex vivo evaluations of tissues or bodily fluids hold significant importance in refining diagnostic techniques and discovering novel disease biomarkers capable of detecting conditions such as malignant lesions at an initial phase or benign and malignant cellular modifications. Moreover, improved knowledge of cell metabolism, cell microenvironment, and cell-immune system interactions are of great importance to expedite the efficacy of disease therapy, especially from the perspective of patient individualization. In conjunction with in vivo models, comprehensive in vitro models can offer valuable insights into the mechanisms of diseased cells. These models are more cost-effective, easily accessible through molecular imaging techniques, and continuously evolving to replicate human physiology more effectively [25-29]. Hence, they are a good alternative for animal experiments. Since the turn of the 20th century, two-dimensional (2D) cell culture has been the prevailing methodology for culturing cells and a well-established approach for conducting in vitro research. This method has been instrumental in the identification of cellular signaling pathways, the investigation of disease progression, and the advancement of novel therapeutics [30-32]. Nevertheless, cells cultivated in monolayer cultures gradually lose their tumor or cell-specific heterogeneity and are unable to accurately reflect in vivo cell behavior due to the absence of extracellular matrix (ECM) and natural three-dimensional (3D) architecture. As a result, the communication between cell-cell and cell-matrix, the nutrient status, and the physiological or biochemical properties are not accurately portrayed [33-36]. To overcome these limitations, initial attempts to create more complex 3D tissue models were started in the early 1960s. Initial investigations have indicated that fetal organs extracted from the body and disintegrated into individual cells possess a remarkable capability to reassemble and recover the form, tissue structure, and functionality of the parental organ [37-39].

As the potential of stem cells from various organs and tissues to regenerate 3D in vitro models became more apparent, the field of organoids - microscopic, self-assembled 3D reproductions of the parent organs - experienced rapid growth [40-42]. Nowadays, 3D organoids are produced from patient-derived stem or progenitor cells derived from small pieces of surgical patient tissue embedded in an extracellular environment or collagen scaffold such as Matrigel [40,42-45]. These systems yield the great promise of being utilized as patient-derived test platforms for precision pharmacological research and personalized medicine [46-48], as they better replicate cell heterogeneity, cell microenvironments, cell-cell interactions, and the potential simulation of physiological barriers [49-51].

Organoids have now found applications in many research fields (Figure 1). In basic research, organoids can be used to model the development of organs and study the molecular and cellular mechanisms involved in their formation. Moreover, they are suitable tools to mimic human disease development, including genetic, infectious, and malignant diseases [52-55]. There is mounting evidence to support the notion that biobanks containing organoids derived from patients can be immensely valuable for drug development and personalized medicine, especially for cancer and cystic fibrosis [28,56,57]. Furthermore, their ability to maintain a preserved genetic profile allows for gene profiling, which presents exciting opportunities for personalized medicine [58,59]. In addition, organoids are an ideal model for drug screening, as they allow for the assessment of drug responsiveness in various patient populations prior to actual treatment. Standard techniques to analyze the viability of cells upon drug treatment include i.e., fluorescence-based assays [60], tetrazolium or resazurin assays [61,62], or ATP-based and lactate dehydrogenase (LDH)-based assays [63,64]. By coupling patient-derived organoids with organ-on-chip platforms, it is possible to observe interactions between different organoids and cell-to-cell interactions, thereby offering valuable insights into the intricacies of human metabolism [65-68].

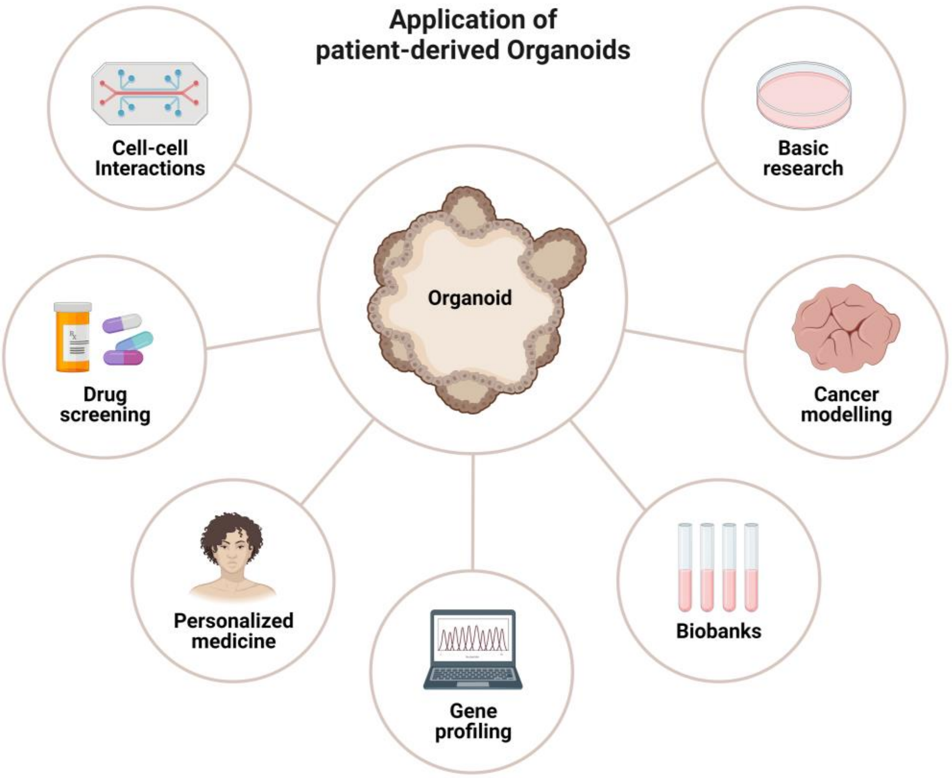

Figure 1: Diverse applications of patient-derived organoids.

1.1.3 Real-Time Imaging

In addition to the used test system, the applied analytical method is another crucial component in the assessment of scientific or medical questions. Identification of structural, phenotypic, molecular, or genetic alterations of cells or tissues usually requires time-consuming and invasive staining methods or destructive procedures with concomitant sacrifice of the sample. The various classical methods each have their own benefits and drawbacks. Although enzymatic labels offer greater sensitivity and require fewer antibodies to achieve sustained long-term staining, they are susceptible to elevated background signals from spillover of the enzymatic reaction products [69,70]. Moreover, tissue and cellular harm due to enzymatic reactions, decreased resolution of delicate structures, and insufficient capability for multiple immunolabeling are further challenges [71-73]. In contrast, fluorescent markers demonstrate high sensitivity and offer a broad selection of fluorochromes, enabling multiple labeling in a single assay. Notably, fluorescence microscopes (such as wide-field and confocal microscopes) can easily resolve intricate structures. However, these methods suffer from high background noise, limited photostability, quenching effects or photobleaching [74,75].

In clinical procedures, such time-consuming techniques are mainly utilized pre- and postoperative. However, they are not suitable for an intraoperative assessment of tissue characteristics. Nowadays, intraoperative decision making such as tumor resection and tissue preservation solely relies on frozen sectioning [23,76]. To assist surgeons with additional information besides pathological assessment of gold standard H&E staining, fast techniques are necessary that can identify characteristic tissue properties. Here, non-invasive, and marker-independent techniques that allow real-time monitoring of cellular processes, cellular metabolism or drug kinetics could be a valuable method to support clinical diagnosis but also to directly evaluate effects of medications. Such label-free techniques are mainly based on the biophysical properties of molecules without the need for conjugated labels. In recent years, especially spectroscopic techniques such as Raman microspectroscopy (RMS), capable to analyze the molecular states of cells or techniques exploiting the autofluorescence of specific proteins or enzymes such as fluorescent lifetime imaging microscopy (FLIM) allowing to identify metabolic alterations of cells has sparked increasing interest [3,77]. In clinical applications, these techniques could either be utilized parallel to histological evaluation of frozen sections or be integrated into an endoscopic setup to investigate tissues in vivo without the need for biopsies.

1.2 Raman Spectroscopy

The identification of tumorous or benign lesions, as well as the evaluation of drug-responsiveness in cancer patients are major challenges in modern biomedical research. Raman spectroscopic techniques rely on the analysis of the interaction between radiation and matter, allowing for the assessment and visualization of molecular and biochemical characteristics of cells or tissues. Therefore, they are an interesting tool for tissue discrimination or in the identification of cellular alterations after drug treatments. Raman spectroscopy provides rapid, marker-independent, non-destructive, and non-invasive data acquisition and is highly sensitive at the molecular level.

1.2.1 The Principle of Raman Scattering

In the quantum mechanical framework, the interaction between photons and molecules involves the assimilation of an incident photon and the instantaneous emission of a scattered photon, a process that is referred to as photon scattering. The molecule is excited into a virtual state, which does not necessarily have to correspond to a real excited state of the molecule [78,79]. Raman scattering is an inelastic process that causes molecular vibrations due to the electromagnetic field of light interacting with matter, which leads to a change in the polarization of the molecule. Rayleigh scattering is the prevailing mechanism in which most photons undergo elastic scattering, as there is no exchange of energy and thus no alteration of frequency [80]. This process is known as Rayleigh scattering. The inelastically scattered fraction, also known as Raman scattering, is about one in 10^7 photons [81]. Both the decrease and the increase of photon energy are possible. In the first case, shown schematically in Figure 2a), the molecule relaxes from the virtual state not back to the ground state, but to a vibrational state. The energy difference between the incident and the scattered photon is then exactly equal to the excitation energy of the oscillation. This process is referred to as Stokes scattering resulting in a loss of energy and a frequency shift to higher wavelengths. In anti-Stokes scattering, the molecule in the excited state absorbs a photon. During emission, the molecule relaxes to the energetically lower state and emits the released energy to the photon at a lower shifted wavelength. This effect was first predicted by Smekal in 1923 and named "Raman effect" after its experimental description by C.V. Raman in 1928 [82,83]. The energy difference after the inelastic light scattering is characteristic for the coordination and the type of atoms present in a molecule [84]. The displacement in wavelength is quantified as wavenumbers, which are computed by subtracting the inverse of the scattered wavelength of light from the inverse of the incident wavelength. The discrepancy is solely attributable to the energetic features of the molecular vibrations and remains unaffected by the wavelength of the laser employed. Raman spectra offer a molecular signature that is particularly unique to each molecule, and capable of detecting variations in the molecule's surroundings and 3D structure [85,86].

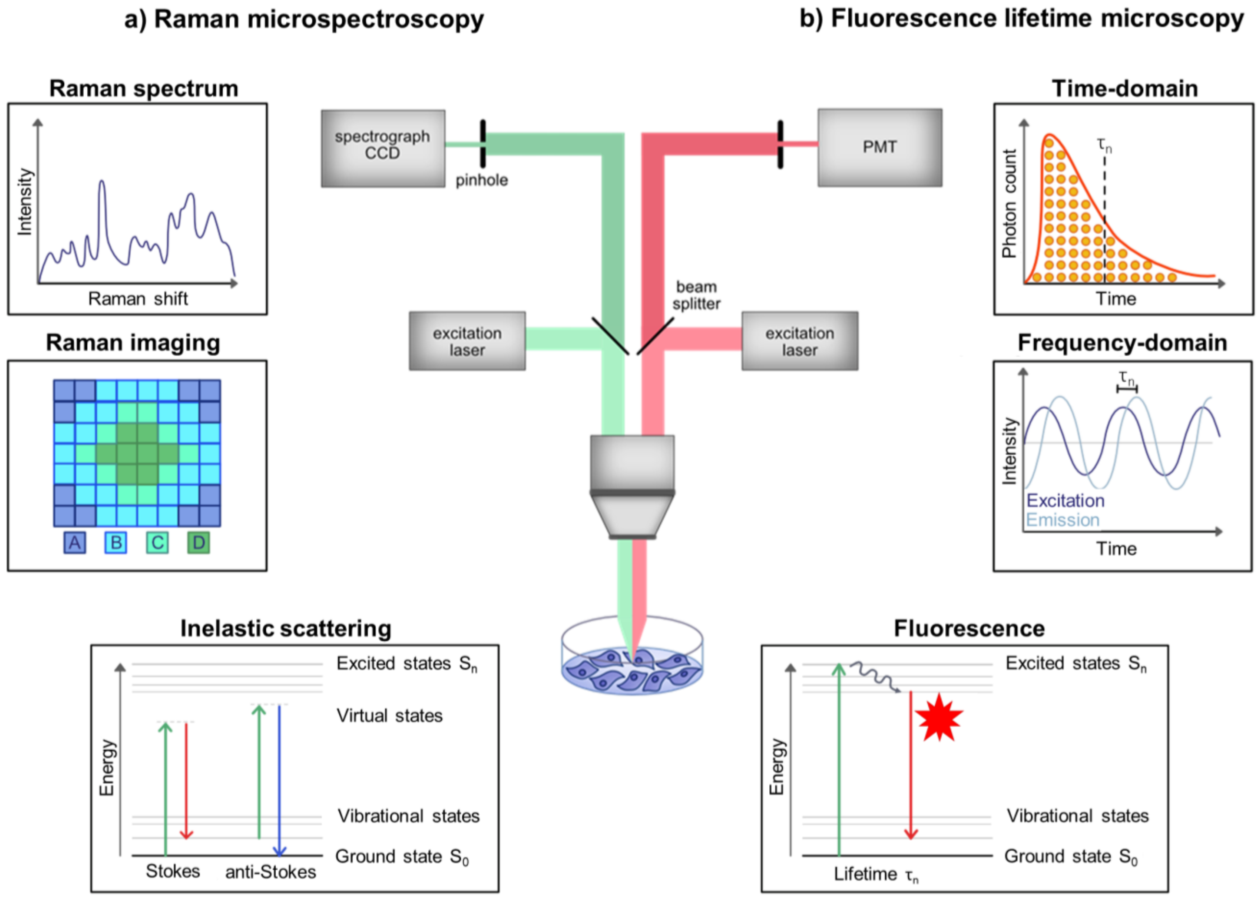

Figure 2: Schematic of Raman microspectroscopy (RMS) and fluorescence lifetime imaging microscopy (FLIM) instrumentation In both techniques laser light is directed on the sample to induce photon-matter interactions. Scattered or emitted light is then transmitted to the detector through a beam splitter and a pinhole. (a) In RMS, energy transfer takes place from the ground state (S_0) to either higher energy levels (anti-Stokes) or lower energy levels (Stokes) through inelastic scattering. A spectrograph coupled e.g., with a charge-couple device (CCD) camera as a detector is required to generate Raman spectra as typical readouts. Raster scanning the laser can be used to generate hyperspectral Raman images, where each pixel corresponds to a particular Raman spectrum. (b) In FLIM, fluorescence lifetimes ($τ_n$) of fluorophores are measured. Photomultiplier tubes (PMT) can be used to detect the accumulated average time a fluorophore spends in the excited state. The most common acquisition methods are photon counting in the frequency domain or in the time domain. Illustration adapted from [3].

Technically, a RMS setup includes a laser light source, a spectrometer, and a detector (Figure 2a). For biological application, the laser utilized for the generation of Raman signals needs to fit specific requirements. Many live cell studies use a laser with an excitation wavelength of 785 nm or 532 nm. The benefit of wavelengths in the infrared region compared to the visible range is that they produce less photodamage and degradation even at high laser power and longer acquisition times. Furthermore, they produce less fluorescence, especially important in fluidic environments i.e., culture medium or blood [87]. Therefore, in studies of sensitive human cells i.e., during surgery where destruction must be avoided at all costs, the near infrared is the laser of choice. This is especially the case in an endoscopic setup where a Raman spectroscope is included in the endoscopic pathway for application in humans. However, when time is a limiting factor, for instance in the analysis of drug distribution over time, visible lasers that require shorter exposure times can be used to generate high quality Raman spectra. The disadvantages of visible lasers include the risk of photodamage and the induction of strong fluorescence signals [88].

After excitation, the inelastically scattered light is directed to the spectrograph where the signal is decomposed into its individual wavelengths [89]. A spectrograph usually consists of a diffraction grating with a specific groove density, which allows the tuning of the spectral resolution. High groove densities in a diffraction grating provide high spectral resolution of closely spaced Raman peaks, as the spectral range decreases and longer exposure times are required [90]. The decomposed signal is then projected to the detector, most commonly a charged-coupled device (CCD) with high quantum efficiency. This CCD is consisting of several small light sensitive photodiodes where the incident photons are converted into an electronic signal [91]. The integration of microscopic objectives for both laser excitation and detection of the scattered light is referred to as Raman microspectroscopy and enables the identification of molecular components and their spatial distribution [92,93].

1.2.2 Raman Microspectroscopy for Analyzing Biological Samples

Since its initial discovery, RMS has advanced into a (bio)analytical technique of notable sensitivity. Raman spectroscopy (RMS) has been widely successful in biological applications owing to two key reasons: Firstly, the weak Raman signal that arises from water in biological samples does not compromise the crucial spectral information obtained from the cells or tissues. Secondly, the non-invasive and marker-independent nature of RMS permits high-resolution subcellular analysis along with real-time data acquisition, thus contributing to its popularity in this field [94,95]. This allows measurements and spectral imaging in phosphate buffered solutions (PBS) or culture medium, not requiring any fixation of cells under physiological conditions without affecting their integrity [73,96-99].

Raman spectra, containing molecular information of complex systems such as cells or tissues, enable the identification of different organelles, i.e., nuclei and mitochondria, or lipids, carbohydrates, and proteins. Having established that RMS is capable of distinguishing between different types of ECM proteins such as collagen fibers and elastic fibers based on their fingerprint Raman spectra, it became clear that this technique is suitable for studying the tissue structures and molecular conformations of ECM components involved in physiological and pathological tissue remodeling [100-107]. Subsequent to its discovery, RMS was employed to tackle the significant clinical requirement of identifying tumor boundaries and infiltration areas during surgical resection, given that the complete removal of tumors is linked to a lower incidence of recurrence and an enhanced survival rate in patients [108-112]. Being sensitive to changes in molecular conformation and cellular environment, RMS has been used to monitor various cellular processes, such as the metabolic and cellular influence of anticancer drugs on tumor cells or organoids [73,113-115]. Certain chemical substances, such as drugs, have highly specific Raman spectra allowing their penetration into cancer cells to be traced by RMS [116,117]. Through the integration of cells obtained from individual patients, RMS may be employed to monitor disparities in drug metabolism and absorption, as well as dose-dependent effectiveness and the emergence of drug resistance, all of which can contribute to improved treatment outcomes and avert the potential for drug toxicity [118-121].

1.3 Fluorescence Lifetime Imaging Microscopy

When compared to conventional intensity-based fluorescence microscopy, fluorescence lifetime imaging microscopy (FLIM) confers the added advantage of a temporal dimension to the fluorescence signal [122]. Conventionally, in fluorescence microscopy, fluorophores are distinguished based on their different spectral properties. Discriminating between fluorophores that possess comparable spectra or elucidating the precise molecular milieu in which a given fluorophore is situated is not feasible by relying exclusively on fluorescence intensity measurement [123]. FLIM represents a robust and non-invasive approach, which operates independently of labeling, and allows for the evaluation of biophysical variations at the molecular level. FLIM is capable of measuring alterations in molecular characteristics, such as temperature, viscosity, and pH, thus enabling the quantification of chemical or physical modifications [124-127].

1.3.1 The Principle of Fluorescence Lifetime Imaging Microscopy

Upon absorption of a photon, a molecule is electronically excited if the energy of the photon is commensurate with the difference between two energetic states of the molecule. Thereafter, the excited molecule may return to the ground state through radiative processes, including fluorescence or phosphorescence, or through nonradiative processes like internal conversion, intersystem crossing, or vibrational relaxation [128]. The fluorescence lifetime pertains to the duration during which a molecule remains in the excited state before it returns to the ground state. Usually, internal conversion transpires prior to emission, given the limited fluorescence lifetime, which normally spans between 10^{-9} to 10^{-8} seconds. FLIM utilizes this fundamental principle and the resulting readout, by detecting the fluorescence lifetime decay processes generated in biomolecules [129].

FLIM operates on two fundamental principles, as depicted in Figure 2b. Time-domain FLIM quantifies the temporal interval between the excitation of a sample through a pulsed laser and the detection of the emitted photons at the photodetector. This setup is referred to as Time-Correlated Single Photon Counting (TCSPC) [122]. By moving the laser beam across a selected area with a system of mirrors, an image of the chosen area can be generated. An alternative approach to determine fluorescence lifetime is by utilizing the phase modulation technique in the frequency domain [130]. When exciting the sample with a sinusoidally modulated continuous wave laser, the emitted fluorescence is also modulated at the same frequency as the incident laser. Information about the phase shift and amplitudes can be obtained as readouts [131].

1.3.2 Metabolic Monitoring of Biological Samples

FLIM allows the analysis of marker-independent readouts based on endogenously autofluorescent molecules, or of targeted probe-based FLIM readouts [3]. Metabolic alterations refer to changes in the cellular metabolism, which primarily affect the production of adenosine triphosphate (ATP) within cells. The generation of ATP can occur through various metabolic pathways, as illustrated in Figure 2. Among the various metabolic processes that occur in cells, glycolysis is one of the most crucial, taking place within the cytosol (Figure 3a). In this process, a single molecule of glucose is transformed into two molecules of pyruvate, ultimately leading to a net production of two molecules each of ATP and nicotinamide adenine dinucleotide (NADH). This process is the first step in the metabolism of glucose, and it provides a small amount of energy to the cell [132,133]. After the formation of pyruvate, it enters the mitochondria where it undergoes pyruvate oxidation, which is catalyzed by the enzyme pyruvate dehydrogenase complex (Figure 3b). This reaction converts the pyruvate molecules into acetyl-coenzyme A (acetyl CoA) [134,135]. Acetyl CoA proceeds to enter the citric acid cycle also referred to as the Krebs cycle taking place in the mitochondria. The citric acid cycle, which is a fundamental metabolic pathway found in all aerobic organisms and integral for most of the energy production, is responsible for the conversion of acetyl-CoA into carbon dioxide and water, thereby liberating energy in the form of ATP, NADH, and $FADH_2$ (Figure 3c) [136-138]. NADH and $FADH_2$ are then utilized during oxidative phosphorylation (OXPHOS), a process that transpires within the inner mitochondrial membrane to generate more ATP (Figure 3d). This is accomplished via the electron transport chain, consisting of a series of protein complexes that actively transport protons across the inner mitochondrial membrane, creating a proton gradient that powers ATP production [139-141]. The endogenous metabolic co-enzymes NADH and flavin adenine dinucleotide (FAD) moreover partake in energy metabolism and the apoptosis pathway by contributing to the production of reactive oxygen species (ROS) [142-144]. Additionally, NADH plays an important role in oxidative stress and the aging process [145,146].

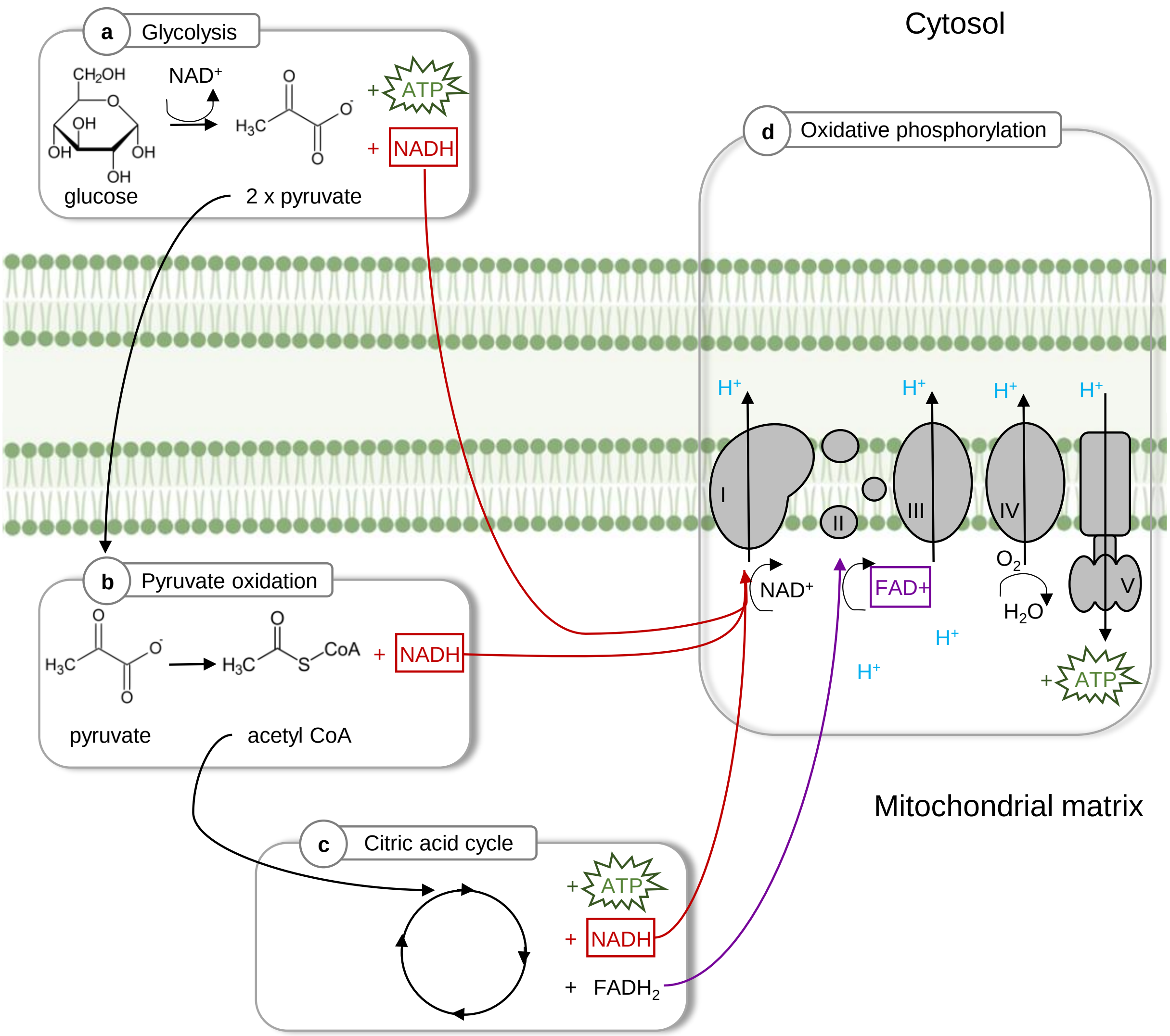

Figure 3: Schematic of metabolic processes. In glycolysis (a), which occurs in the cytosol of cells, one molecule of glucose is converted into two molecules of pyruvate, producing a net gain of two molecules of adenosine triphosphate (ATP) and two molecules of nicotinamide adenine dinucleotide (NADH). After the formation of pyruvate, it enters the mitochondria where it undergoes pyruvate oxidation, where the pyruvate molecules are converted into acetyl-coenzyme A (acetyl CoA) (b). This reaction is catalyzed by the enzyme pyruvate dehydrogenase complex. Acetyl CoA then enters the citric acid cycle (c), which is a series of chemical reactions generating ATP, NADH and $FADH_2$. These molecules are used in the electron transport chain to generate more ATP. The pyruvate molecules can then be further metabolized in the citric acid cycle or converted to lactate under anaerobic conditions. Both NADH and $FADH_2$ generated in the citric acid cycle are used during oxidative phosphorylation (OXPHOS) (d), which takes place in the inner mitochondrial membrane. This process harnesses the energy stored in the electrons of NADH and $FADH_2$ to generate ATP, through the activity of a series of protein complexes that pump protons across the inner mitochondrial membrane, creating a proton gradient that drives the production of ATP.

Upon binding of NADH to its co-enzyme, i.e., during OXPHOS, there is an increase of the fluorescence lifetime from less than 0.4 ns in its free form to about 2 ns in its bound form [147]. Shifting metabolism in cancer cells according to the Warburg effect from OXPHOS to glycolysis, where less NADH and $FADH_2$ are produced, leads to a significant decrease in fluorescence lifetime [148,149]. In different metabolic states, the ratios of free and bound co-enzymes (α1, α2) differ, and therefore both NADH and FAD represent great potential as biomarkers for metabolic pathways [150,151].

Numerous FLIM based studies, especially in the field of cancer metabolism started after the first investigation of fluorescence lifetimes of intrinsic NADH on a yeast model in 1992 by Schneckenburger et al. [152]. FLIM was used to highlight the differences between 2D breast cancer cell lines and 3D models in terms of their metabolic responses to drugs [153-155]. In contrast to 2D cell cultures, in which epithelial plaques formed in response to the drug treatment, 3D cells assembled anastomosing multicellular networks and spherical acini. Next to the assessment of metabolic changes, the potential of FLIM being utilized to trace drug uptake and release in cells has been investigated by observation of changes in fluorescent lifetimes in drug loaded nanoparticles [156,157].

1.4 Machine Learning in Biomedical Research

Numerous industries and scientific areas are currently witnessing a surge in the acquisition of real-time and multimodal data, resulting in an extensive collection of data with multiple characteristics. Nevertheless, such large datasets are prone to encompass features that may provide insignificant information when it comes to comprehending and simulating real-world occurrences. Moreover, the complexity of spectroscopic information, particularly when dealing with biological samples, presents additional challenges. For instance, a singular Raman spectrum can include overlapping information from multiple molecules, making it difficult to identify specific proteins or lipids that share similar functional groups. As a result, machine learning (ML) tools have become increasingly essential for accurate analysis and the identification of novel biomarkers.

1.4.1 Biomarker Identification

A biomarker is a measurable indicator that can be objectively and reproducibly determined, which reflects normal biological or pathological processes or the response to a therapeutic intervention [158]. According to the world health organization (WHO), a biomarker includes “almost any measurement reflecting an interaction between a biological system and a potential hazard, which may be clinical, physical, or biological. The measured response may be functional and physiological, biochemical at the cellular level, or a molecular interaction” [159]. In contrast to a clinical endpoint assessed in clinical trials reflecting how a patient feels, function or survives, a biomarker not necessarily correlates with a patients wellbeing [158,160]. Examples of such biomarkers include blood glucose levels as a molecular biophysical property, the grading and staging of cancers based on histological findings, blood pressure as measure of physiological body processes or bone mineral density obtained from radiographic images [161-166].

A biomarker for clinical application should be non-invasive accessible, easily measurable, and interpretable by clinicians, inexpensive and able to produce rapid results. It also should ideally be derived from available patient sources such as blood or urine. It is essential that a biomarker has high sensitivity with no overlap of values between diseased and healthy patients to minimize the risk of false results, and to allow for high specificity in detecting minute changes. Next, a biomarker should provide insight into the underlying disease mechanism and should vary in response to treatments [158,167]. As new analytical techniques are developed, it becomes possible to discover and evaluate novel biomarkers that possess the various characteristics required for clinical application.

Currently, the gold standard for many disease diagnoses is based on the visual examination of specific patterns on stained tissue sections by trained pathologists. Combinations of traditional H&E staining with stains of several other modalities, where each is offering its own advantages and limitations allows to analyze various biomarkers and is an attractive approach to analyze a patient’s tissue [168]. Semiquantitative scoring systems widely used in the assessment of coronary heart disease, neurologic disease, fibrosis, endometriosis as well as likelihood of malignancy based on an observer assessment have been developed to achieve global agreement in interpretation [169-172]. However, time-consuming and rather expensive staining procedures, storage problems, sample availability, and a certain degree of interobserver and intraobserver variability in reproducibility and accuracy among pathologists was noted. This was rising the question in an era of artificial intelligence (AI) and machine learning (ML) to incorporate computer assisted combination and evaluation of several biomarkers simultaneously [173-175]. A primary constraint of traditional images is their reliance on a limited number of color channels, typically restricted to the visible spectrum. This constraint may hinder the comprehensive characterization of different tissue components, including those that are spectrally complex. Here, spectral methods offer a relatively inexpensive way to gain deeper insight into tissue composition that goes beyond just color information by interrogation of the molecular and metabolic environment.
ML yields the potential to extract quantitative novel biomarkers from medical images or spectral data to avail faster and more efficient automated characterization, monitoring and assessment of drug responses and to provide an objective decision-support tool [168]. However, major hurdles to the successful application of ML in pathology include the biases introduced by the underlying expertise involved in generating the training data and the limitations of scalability due to the restricted availability of pathological annotations, e.g., for identifying specific tissue regions on clinical images or assessing response to treatment [176,177].

1.4.2 Tissue Characterization and Discrimination

The widespread adoption of machine learning (ML) for pattern recognition in intricate datasets can be attributed to its remarkable ability to discern patterns that may elude conventional techniques. This is primarily due to ML models' capacity to identify and extract intricate, nonlinear relationships and patterns within data that would otherwise remain obscured using traditional statistical methods [178]. A dataset represents a compilation of instances, wherein each instance corresponds to a specific case or patient within the study, and is characterized by a set of attributes, also known as features or variables, that are quantitatively described and encoded as numerical values [179]. The combination of many feature vectors is called the feature space. In biological and clinical applications such datasets are for instance genomic data, transcriptomic data, proteomics, clinical parameters, spectroscopic data, or imaging data describing the clinical phenotype of the patient [180-183]. When implementing ML algorithms, the dataset is typically partitioned into two subsets: a training dataset, which serves as the basis for constructing a classifier, and a testing dataset, which is used to evaluate the classifier's performance or estimate its error rate when applied to new, unseen data. This approach, commonly known as train-test split, is a widely used strategy for validating the performance of machine learning models [183,184]. By comparing the predicted output of the model to the actual output, the model's generalization performance can be determined, which is an indicator of how well the model will perform on new, unseen data. This is important for identifying overfitting or underfitting, which are common issues in ML [184,185]. Additionally, by using different validation datasets, it is possible to ensure that the model is robust and can generalize well to different types of data. Furthermore, cross-validation is a common technique that is used to further test the robustness of the model and avoid overfitting by using different subsets of the data for training and testing the model in multiple iterations [186].

Depending on the availability of class labels of the instances, supervised, unsupervised or semisupervised ML algorithms can be applied. While supervised ML algorithms are employed to classify data with full knowledge of class labels, unsupervised ML algorithms are utilized for clustering or dimensionality reduction. Semisupervised ML-algorithms are supervised methods allowing to analyze both labeled and unlabeled datasets. In the case of Raman spectroscopic data, the features of an instance are represented by the intensities of different wavenumbers retaining molecular information. Figure 4 gives an overview of the ML techniques utilized in this thesis. Classically, multivariate data analysis (MVA), such as principal component analysis (PCA), linear discriminant analysis (LDA), or cluster analysis are applied to analyze spectral differences in large Raman data sets not describable by univariate methods. PCA is a statistical technique for reducing the dimensionality of high-dimensional datasets through the linear transformation into a latent variable space, referred to as the scores. PCA is unsupervised and vector-based and seeks to preserve trends and differences in the data while minimizing the number of dimensions. The method is accomplished by solving an eigenvalue problem, which yields a set of uncorrelated and orthogonal principal components (PCs) that establish a new variable space. Furthermore, PCA provides a loading matrix that characterizes the weight of the transformation and a residual matrix that encompasses information that is not significant for the variability of the data [187,188].

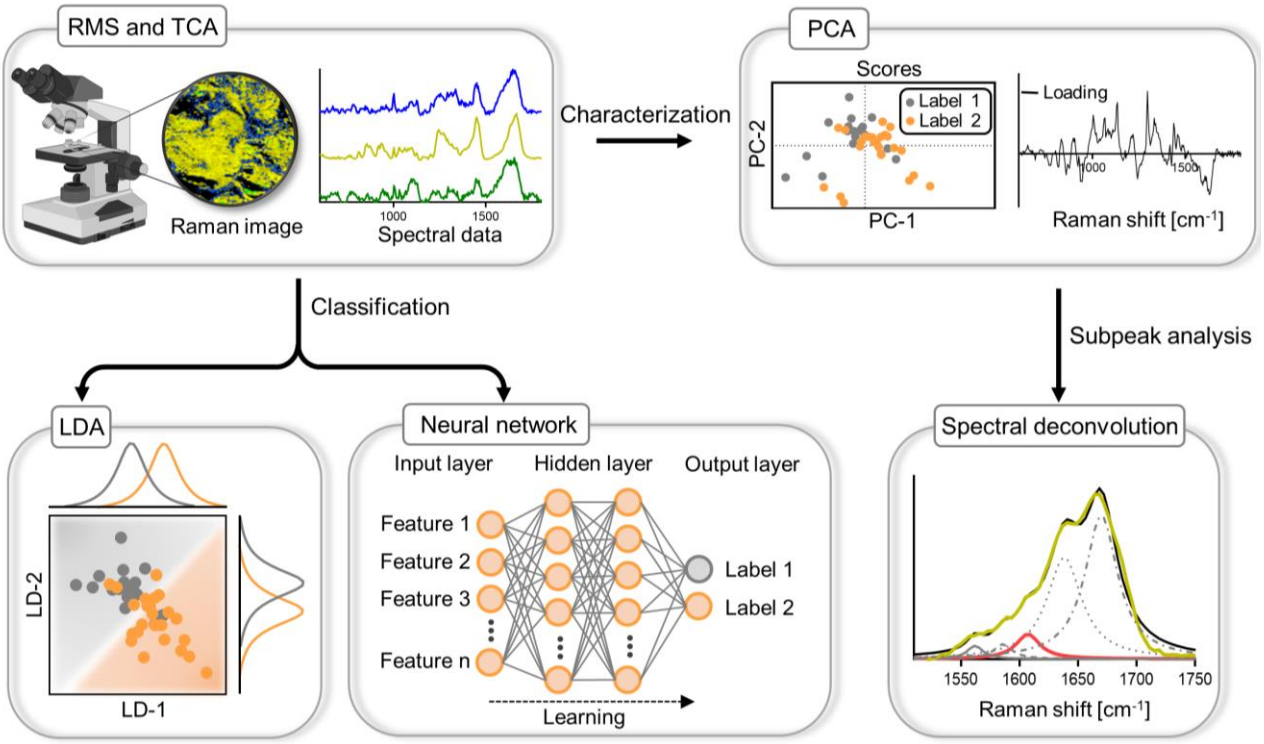

Figure 4: Overview of machine learning (ML) techniques for spectroscopic analysis. Raman microspectroscopy (RMS) and True Component Analysis (TCA) identifies reoccurring Raman spectra in a large area scan to generate a false-color coded Raman image. Extracted spectral data are further processed with principal component analysis (PCA) for molecular characterization. PCA calculates a new coordinate system (scores) explained by the loadings based on the solution of an eigenvalue problem. Relevant peaks are further analyzed by spectral deconvolution, which calculates peak widths and areas of substructural peaks underlying a broad band. Spectral data are classified by linear discriminant analysis (LDA). The colored background in the LDA plot represents the probabilities of a sample belonging to a specific class. Alternatively, spectral data are classified by neural networks involving the use of a multi-layer model to map input data to predefined categories. The input data is processed through hidden layers, which extract relevant features and make predictions based on those features. The final output is a probability distribution over the classes, with the class with the highest probability being the predicted label.

In comparison, LDA is a supervised linear transformation method that aims to maximize the distance between means while minimizing variances within a class. In this method, which requires a class label, the data is mapped to a lower dimension subset to split the data into different classes [189]. Based on such MVA models, it has been demonstrated that the molecular oscillation patterns of Raman spectra are cell type specific and are relatable with dynamic cellular processes such as cell division, differentiation, and cell death [103,190-193]. While PCA and LDA are limited to linear transformations, neural networks employ non-linear activation functions to uncover correlations within datasets. As a result, neural networks have demonstrated superior performance in the classification and retrieval of previously undiscovered and unexplored biomarkers [194]. Furthermore, very deep neural networks can identify complex patterns within signals that would otherwise remain uninterpretable by humans or through traditional statistical analyses, a significant advantage over PCAs and their corresponding loadings plots [73].

However, in the case of Raman spectroscopy all these ML methods analyze large spectroscopic datasets by identification of minute variations in signal intensity or Raman shift. In certain applications, for example when analyzing the secondary structures of proteins, the intensity information alone is no longer sufficient, and a deeper peak analysis is required. Here, a spectral deconvolution can be performed, differentiating several substructural peaks, and evaluating them according to their peak width and peak area [195].

Chapter 2

Objectives of the Thesis

2 Objectives of the Thesis

This PhD thesis explores RMS and FLIM as non-destructive and marker independent tools in combination with various ML techniques and classical histological staining for the detection of drug efficacy, cellular states, fibrotic collagen alteration and epigenetic alteration in various diseases within their 3D environment.

One of the current challenges in modern medicine is to improve patient-specific therapy of benign and malignant diseases, as the efficacy of treatments may be compromised by acquired resistance mechanisms which are not predictable by assessment of standard cell lines or animal models. Conventional techniques utilized for evaluating drug efficacy necessitate the disintegration and concomitant sacrifice of the sample, often in the form of monolayer cell cultures, which lack the ability to reproduce intricate cell-cell interactions present in the native 3D environment. Furthermore, there is an absence of noninvasive methodologies that facilitate the real-time monitoring of drug dynamics in complex cellular networks, which is paramount for evaluating pharmacokinetic properties dictating drug accumulation, metabolism, or release. Therefore, 3D organoids from patients with malignant bladder and colon cancer and benign endometriosis organoids have been used to investigate the effects of different drugs on their cellular and metabolic modes of action over time to assess the general applicability of organoids to identify mechanisms of drug uptake and resistance. Using non-invasive RMS and FLIM in combination with ML techniques, drug-induced effects were evaluated using specific Raman fingerprints of cell nuclei and mitochondria reflecting molecular alterations, and in changes in fluorescence lifetimes of NADH and FAD allowing to assess the metabolic environment.

Another challenge in modern medicine is to improve the pre-, intra-, and postoperative diagnosis of diseases. While pre- and postoperative diagnosis could be improved by the development of sophisticated imaging techniques, intraoperative diagnosis has been based on time-consuming frozen section diagnostics for many years. Here, the use of non-invasive modalities that can be integrated into a sensor in combination with ML methods could provide valuable additional information to further improve tissue differentiation. To holistically understand the pathological changes in a single cell, they must be evaluated in their complex native composition and interplay with the ECM. Therefore, the potential of RMS was tested on various ex vivo human tissues to identify pathological tissue remodeling based on molecular changes in the extracellular environment as well as within DNA. By considering fibrotic tissue changes triggered by a wide variety of inflammatory and cancerous diseases, it was aimed to identify specific biomarkers allowing to classify the pathologies.

Another promising avenue in medical research is the examination of epigenetic modifications. Currently, epigenetic analyses are primarily conducted using destructive and costly genetic testing methods. As such, the potential utility of RMS in identifying specific epigenetic modifications, such as 5-methylcytosine (5mC), was investigated. Additionally, the goal was to correlate fibrotic tissue remodeling with cellular and epigenetic changes, in order to identify a biomarker that may be relevant to a wide range of diseases.

Chapter 3

Results & Discussion

The contents of this chapter are based on:

Becker L., Fischer F., Fleck J. L., Harland N., Herkommer A., Stenzl A., Aicher W. K., Schenke-Layland K., Marzi J.*; Data-Driven Identification of Biomarkers for In Situ Monitoring of Drug Treatment*, Int. J. Mol. Sci. 2022, *23*(13), 6956; https://doi.org/10.3390/ijms23136956

Becker L., Janssen N., Mürdter T., Nies A., Marzi J., Schenke-Layland L.; *Label-free Raman microscopy-based monitoring of anti-cancer drug effects in colorectal cancer organoids towards patient-individualized optimization of treatments*

Becker L.§, Lu C.§, Montes-Mojarro, I. A., Layland S. L., Khalil, S., Nsair A., Fend F., Duffy G. P., Marzi L., Schenke-Layland L.; *Identification of a Raman Marker for Fibrotic Collagen Alteration,* Acta Biomat. 2023; https://doi.org/10.1016/j.actbio.2023.03.016

Becker L.§, Beyer T§., Liebscher S., Carvajal-Berrio D., Bösmüller H., Krämer B., Rall K., Brucker S. Y., Schenke-Layland K., Weiss M., Marzi J., *Marker-independent imaging reveals a correlation of fibrotic and epigenetic alterations in endometriosis*

Becker L., Montes-Mojarro A., Layland S. L., Nsair A., Fend F., Marzi J., Schenke-Layland K., *Exploring the relationship between epigenetic DNA methylation and cardiac fibrosis through Raman microspectroscopy*, Am. J. Physiol. 2023, *325*(1), C332-C343; https://doi.org/10.1152/ajpcell.00209.2023

3 Results & Discussion

3.1 Drug Monitoring in Patient-Derived Organoids

In recent years, there has been an increasing awareness among the scientific community that standardized clinical treatments for similar disorders may not elicit a uniform desired outcome in all patients. This phenomenon is largely attributed to patient-specific acquired drug resistances, which impacts the efficacy of the drugs by altering their uptake and release kinetics. Additionally, it is pertinent to acknowledge that various intrinsic patient characteristics, such as genetic makeup, lifestyle habits, and comorbidities, can influence the treatment response, highlighting the need for personalized medicine approaches [196-200]. To better understand the cellular behavior upon drug treatments, 2D cell culture models have been used for decades. However, it was recognized that they frequently fail to accurately predict the in vivo outcome as cells are dissociated from their native physiological 3D microenvironment, including the ECM and lack blood perfusion [36,201]. This results in a lack of physiological relevance, making it difficult to extrapolate results obtained in 2D culture to in vivo settings.

To circumvent the obstacles of 2D cell culture, we recreated 3D in vitro organoids models from patient-derived bladder cancer and colorectal cancer (CRC), as well as endometrium and endometriosis. The superiority of organoids over 2D standard cell culture has been demonstrated in several studies as they offer the possibility to study the cellular microenvironment potentially evolving into a surrogate tool to predict the response to medication [202-204]. Traditionally, the assessment of the efficacy of drug treatments in cells has relied on techniques that involve lysis of the cells, in order to analyze protein, DNA, RNA, or viability information. Alternatively, researchers have used different staining methods such as IHC and IF staining, which involve the use of fluorophores and fixatives that can alter the native intracellular biochemistry, thus interfering with the results [205,206]. The limitations of destructive methods, such as those previously mentioned, are particularly evident when considering that they only provide a pooled response of the entire specimen, failing to consider the inherent cellular heterogeneity. This ultimately leads to a lack of understanding of the differential response of individual cells within a given sample [207,208]. Additionally, current analytical tools have limited capacity to resolve different modes of cell deaths as for each specific mode different biomarkers are relevant [209,210]. Therefore, we introduced two studies exploring non-invasive RMS and FLIM in combination with ML techniques as promising tools to identify individual drug effects on a molecular and metabolic level as illustrated in Figure 5 (Becker et al., Appendix I, Becker et al., Appendix II).

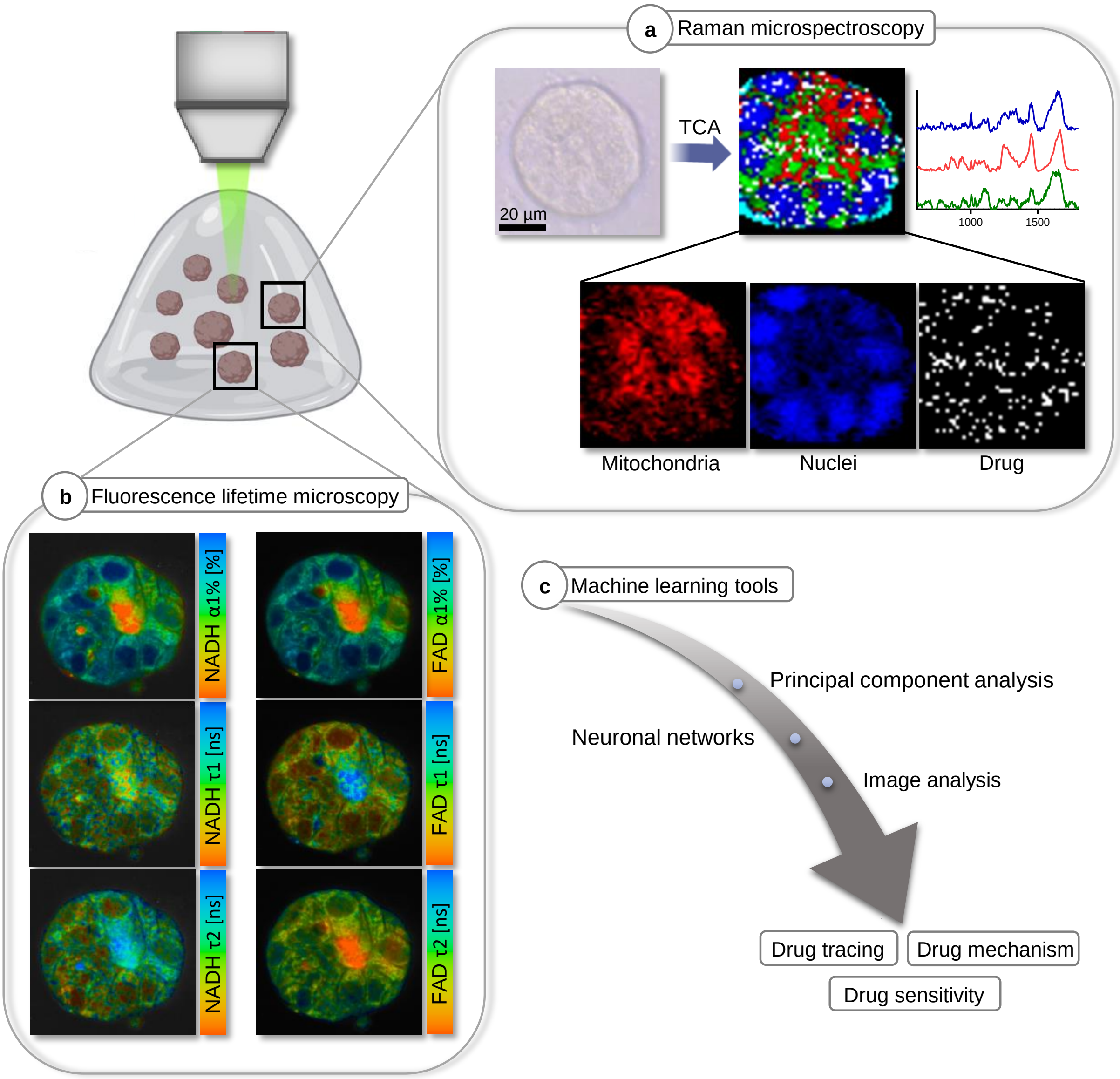

Figure 5: Schematic illustrating the different non-invasive methods used to characterize drug effects in patient-derived organoids in situ. Organoids from patient-derived cells of colorectal cancer, bladder cancer as well as endometrium and endometriosis are cultured in Matrigel and treated with various chemotherapeutics in different concentrations and imaged with RMS (a) and FLIM (b). TCA of Raman images allowed marker-independent visualization of cellular components and drugs based on specific Raman fingerprints. FLIM enabled us to analyze the fluorescence lifetimes of co-enzymes NADH and FAD. (c) Various ML tools were utilized to identify the localization of the drug, the drug mechanism and ultimately the drug sensitivity. TCA: True component analysis; PCA: Principal component analysis; ML: Machine learning.

3.1.1 Marker-Independent Imaging and Drug Tracing of Organoids

We established a non-invasive and marker-independent Raman imaging procedure that can be performed at physiological temperatures (37°C) to differentiate and identify specific cellular components within living bladder cancer and CRC organoids based on specific Raman fingerprints without the need of sacrificing the organoids. RMS and TCA allowed to distinguish between nuclei, mitochondria, lipids, and cytoplasm based on comprehensive comparisons of the Raman spectra to databases, literature, and pre-recorded reference spectra (Becker et al., **Appendix I**, Figure 1; Becker et al., **Appendix II**, Figure 2).

Since a correlation between impaired uptake and efflux of a drug from a cancer cell and its efficacy is suspected [211-213], we asked whether non-invasive monitoring and localization of the drug over time would be possible in patient-derived organoid models to draw conclusions about acquired resistance mechanisms. Organoids express several ATP binding cassette transporters relevant for drug uptake and release which are identified as critical in vivo actors of chemotherapy resistance [214,215]. Several chemotherapeutics such as 5-fluorouracil (5-FU), capecitabine, neratinib, erlotinib and SN-38, all exhibiting specific Raman signals were tested on CRC organoids and visualized by TCA (Figure 6) (Becker et al., **Appendix I**, Figure 1; Becker et al., **Appendix II**, Figure 2). Guided TCA methodology was employed to generate Raman images of CRC organoids. Reference Raman spectra of crystalline drugs were utilized, resulting in the generation of intensity heatmaps that effectively illustrate the localization and distribution of 5-FU (Figure 6a,b), capecitabine (Figure 6c,d), and neratinib (Figure 6e,f) within the organoids. Depending on the position of specific Raman shifts of the drugs the performance of the localization via TCA varies greatly. TCA is a fitting algorithm which assigns pixels within a Raman image to several spectral components to generate a false color-coded image. However, if the reference spectra of the drugs show overlapping peaks with the spectral fingerprint of the biological components between 600-1800 cm^{-1}, the fitting is prone to error. To demonstrate that the generated TCA intensity heatmaps truly reflects the localization of the drug, all Raman spectra in the intensity heat map of the drug were averaged (Figure 6b) and compared to the reference spectra of crystalline drugs. The most dominant peaks in 5-FU (Figure 6b) located at 1235, 1252 and 1353 cm^{-1} showed resemblance between the reference spectra and the averaged TCA drug component of treated CRC organoids. In capecitabin only small peaks located at 896, 1092, 1116, 1450, and 1588 cm^{-1} were displayed (Figure 6d).

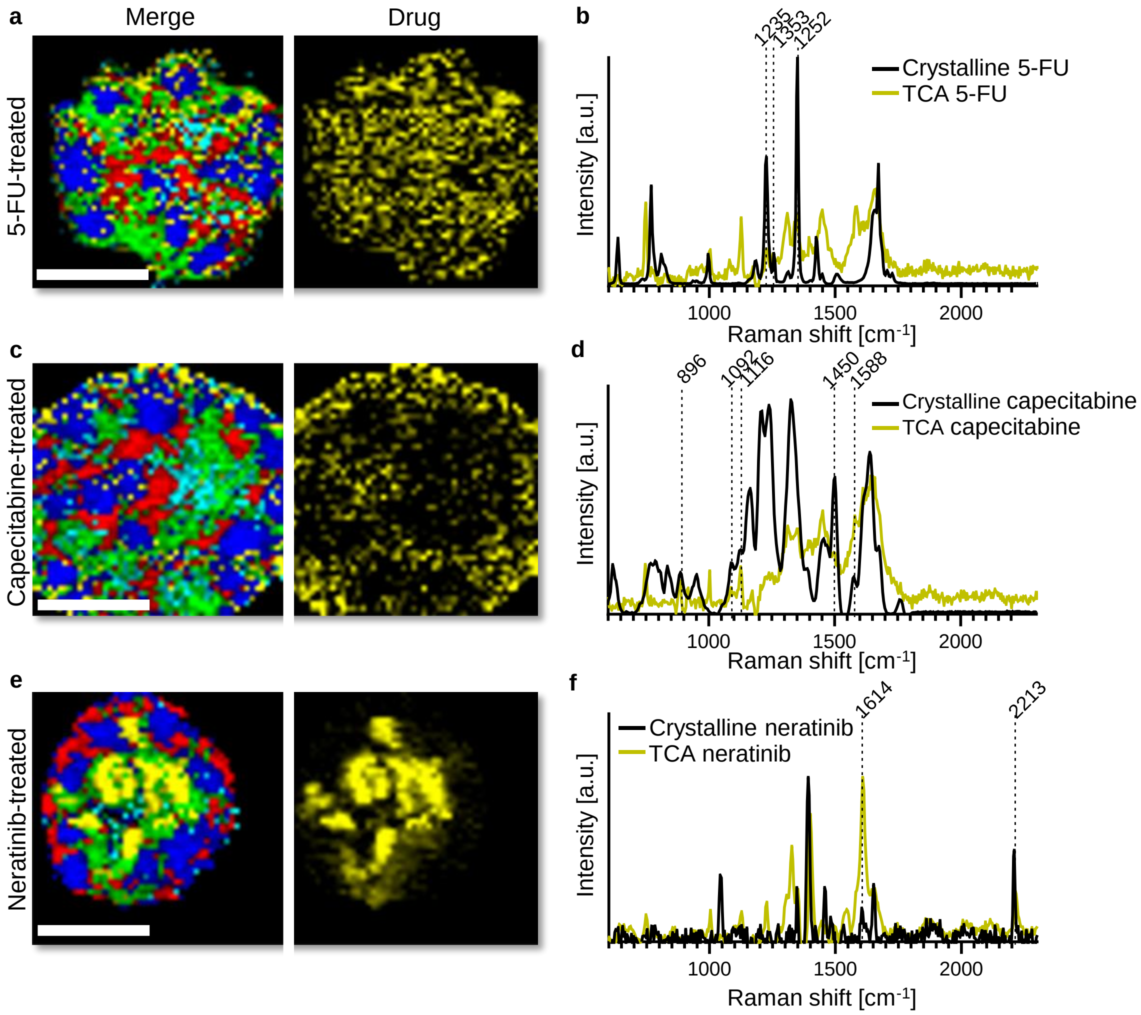

Figure 6: Raman imaging of CRC organoids treated with different chemotherapeutics. TCA images of CRC organoids treated with 5-fluorouracil (5-FU (a), capecitabine (c) and neratinib (e) after 24 hours. Colors: blue: nuclei; red: mitochondria; green: cytoplasm; turquoise: lipids; yellow: drug. Scale bar equals 25 µm. The reference Raman spectra of crystalline 5-FU (b), capecitabine (d), and neratinib (f) are shown in black, and the averaged drug spectra identified by TCA are shown in yellow, demonstrating a resemblance in the location of specific peaks.

These peaks were located directly in the spectral fingerprint of strong Raman scatterers such as amide III and lipids [216,217]. The TCA image generated from the reference spectrum of the capecitabine (Figure 6c) could therefore be disturbed and did not necessarily indicate the localization of the drug. Other drugs that were successfully detected within CRC organoids possess a Raman peak in the silent region of biological samples located between 1800 and 2700 cm^{-1}. These peaks are mostly due to triple bonds between carbons and nitrogen rarely occurring in cells. This makes neratinib and erlotinib perfect candidates for drug tracing as no spectral overlap with biological components occurs [117]. The localization of neratinib by TCA was mainly based on the peak located at 2213 cm^{-1}, clearly visible in the averaged TCA spectra (Figure 6f). This finding is in concordance with previous research where neratinib was identified in SK-BR-3 and NCI-H1975 cells [117].

In the case of erlotinib, a specific peak located at 2110 cm^{-1} was found representative for a C-C triple bond [116]. However, TCA imaging was not able to successfully identify erlotinib in organoids as the averaged spectrum of the intensity heat map did not show the specific peak in the silent region (Figure 7a,b). To further analyze the identified TCA components, PCA was performed on spectra of nuclei and mitochondria for an in-detail molecular assessment. PCA was able to differentiate between untreated and erlotinib treated CRC organoids based on mitochondrial Raman spectra, where also the peak at 2110 cm^{-1} was depicted in the loading plot, however, only at low intensity (Figure 7c, d). Mainly the highest variances in the peaks are shown in the loading plots. If, however, the relevant peaks were generally only of weak intensity and were not represented in large quantities of the molecules, this was also considered to have only a minor influence on the loadings. When using advanced ML-tools such as a neuronal network based FeaSel-Net, which identifies important features in a dataset in a nonlinear approach [218], the erlotinib specific Raman shift at 2122 cm^{-1} was identified as an important discriminator between untreated and erlotinib-treated spectra, where TCA and PCA have failed (Figure 7e).

This result demonstrated the superiority of advanced ML techniques in identifying minute molecular changes in a Raman dataset compared to linear TCA and PCA, but it also reveals the challenges of the spectroscopic approach generating signals of low intensities. To improve signal intensity, either the laser power or the acquisition time must be increased, resulting in additional damage to the cells and longer measurement time, which further hampers time-resolved analysis. To provide faster image acquisition advances of Raman spectroscopy-based methods such as coherent anti-stokes Raman spectroscopy (CARS) or stimulated Raman spectroscopy (SRS) could be employed [93,219,220]. These methods raster a sample at a single wavenumber which drastically increases the speed and contrast of a single scan. Figure 7f shows an exemplary CARS image of dried erlotinib excited at 2110 cm^{-1} allowing to discriminate the drug from glass background by increased CARS intensity.

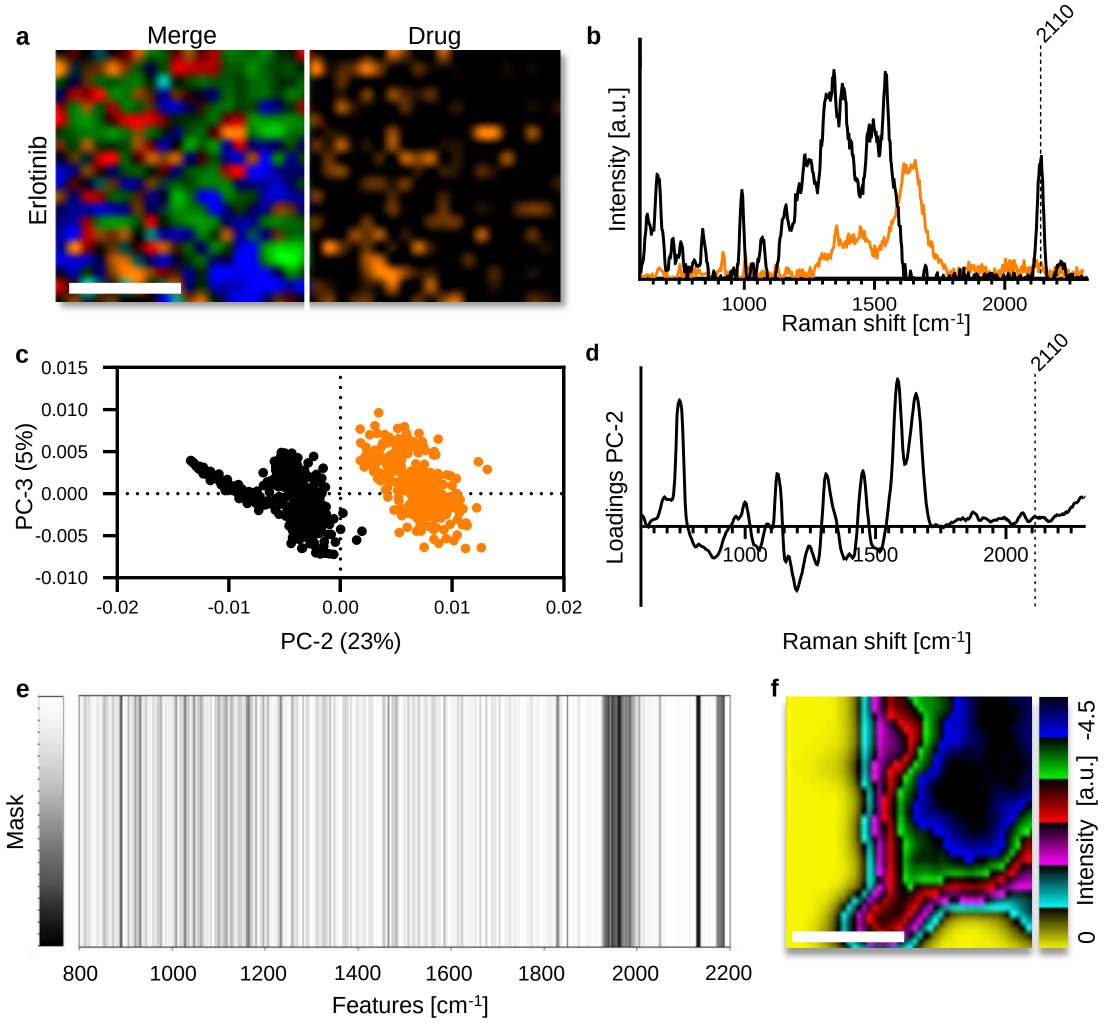

Figure 7: Different approaches for analyzing drug uptake of Raman data. (a) TCA image of a CRC organoid treated with erlotinib. Colors in TCA: blue: nuclei; red: mitochondria; green: cytoplasm; orange: erlotinib. Scale bar equals 25 µm. (b) Raman spectra of erlotinib (black) and the erlotinib TCA component (orange). (c) Principal component analysis (PCA) of erlotinib treated organoids (orange) compared to untreated organoids (black). (d) Corresponding loading plot shows only minor distribution to the erlotinib specific peak in the silent region. (e) FeaSel-Net analysis of Raman data from erlotinib-treated organoids and control samples revealed identified a broad number of peaks in the silent region (1900-2150 cm^{-1}), which are important for the discriminatory ability of the data sets. The results indicate that advanced techniques, particularly those based on ML, show significant improvement over traditional methods in terms of accuracy and computational efficiency. (f) CARS image of erlotinib powder (blue) on a glass substrate (yellow) recorded at 2110 cm^{-1}. Scale bar equals 10 µm.

Another key challenge of drug tracing in organoids or cells arises due to the poor solubility of some chemotherapeutics. For Raman experiments, drugs are preferably dissolved in water, which has a weak Raman signal and is not toxic to cells [94]. However, dissolution in water is often not possible due to the hydrophobic properties of many drugs, and chemical solvents such as dimethyl sulfoxide (DMSO) are required. DMSO solved drugs provide challenges in Raman measurements due to its strong Raman signal overlapping with drug specific peaks as well as with cell culture medium. Even low concentrations of DMSO interfere with the medium and are detectable in all cellular components directly after application to organoids. Hence, for RMS the drugs needs be solubilized differently for instance with non-toxic cyclodextrins, polymeric constructs such as Captisol [221]. A mixture of Captisol and water allowed to solubilize SN-38 which were then applied on CRC organoids allowing the detection of SN-38 specific peak patterns in organoids without interfering signals from the solvent by TCA (Figure 2, Becker et al., **Appendix II**). SN-38 was identified in organoids by drug specific peaks at 1561 cm^{-1}. To identify the sensitivity of SN-38 identification by RMS in CRC organoids, SN-38 resistant and responsive patients (*n*=3) were treated with various concentrations of SN-38 (5 nM, 50 nM, 500 nM, 5 µM, 50 µM and 500 µM) and were analyzed at several time points (2, 4, 24 and 48 hours). Yet, the quantification of the drug via RMS remains challenging as guided TCA image analysis is subject to noise, which requires the usage of additional analytical tools. Therefore, average spectra of the TCA component showing SN-38 of each measured organoid were generated and the peak intensity at 1561 cm^{-1} was compared between treated and untreated organoids cm^{-1} (Figure 8 adapted from Becker et al., **Appendix II**, Figure S2).

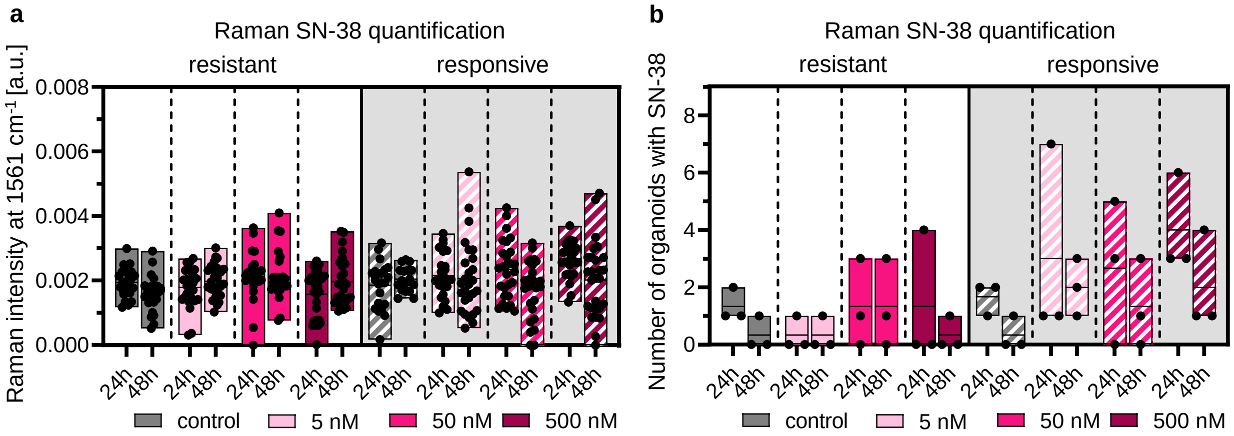

Figure 8: Quantification of SN-38 in CRC organoids based on SN-38 derived Raman spectra display differences between resistant and responsive donors. (a) Raman intensity at 1561 cm^{-1} of SN-38-derived Raman spectra from organoids treated with 5 nM (rose), 50 nM (pink) and 500 nM (bordeaux) of the drug. (b) Quantification of SN-38 in CRC organoids based on the Raman intensity at 1561 cm^{-1}. The presence of SN-38 within the organoids was established through a comparison of the Raman intensity of the treated specimens with the mean intensity of the control group. Adapted from Becker et al., Appendix II, Figure S2.

As depicted in Figure 8a, the intensity distribution of single organoids showed a large distribution in both untreated and treated organoids. Therefore, it is unclear at which intensity threshold it can be assumed that the increased intensity which was identified especially in responsive donors is caused by the drug. Potentially, neuronal networks could be employed to identify the drug, however, here it remains the question to which specific peaks of the reference they need to be compared to that no errors due to overlapping peaks in the biological fingerprint occur.

One additional difficulty in localizing a drug was the limited spatial resolution of the employed measurement technology. According to Abbe's law the limited spatial resolution of RMS is in the range of 200 nm depending on the utilized laser wavelength [222]. In scientific experiments where precise drug localization is crucial, a longer scan time may be necessary to achieve higher lateral resolution in measurements. This is because a higher number of scanning steps are required to obtain more accurate results. However, a long scan time may cause the drug to redistribute during the live experiment, resulting in erroneous snapshots. In addition, if one is interested in the movement of the drug in the same organoid, repeated measurements can lead to cell burn, which significantly weakens the spectral signal.

An alternative method for in vivo analysis of drug uptake is provided by FLIM. FLIM is a method that detects the fluorescence lifetime of autofluorescent molecules such as of the co-enzymes NADH and FAD, both involved in the energy production of the cell. The metabolic effects of SN-38 on CRC organoids are discussed in more detail in section 3.1.2. FLIM images of SN-38 treated organoids showed highly localized regions exhibiting increased fluorescence lifetime signals for FAD. 2-D correlation analysis of fluorescence lifetimes $\tau1$ and $\tau2$ of FAD revealed the existence of one cluster located between 1600-3400 ns in $\tau1$ and 250-600 ns in $\tau2$ in both untreated and SN-38 treated CRC organoids Figure 9a). However, in treated organoids an additional second cluster located between 3000-3400 ns in $\tau2$ and 500-1200 ns in $\tau1$ was detected (Figure 9b), which could be visualized by adjustments of the FLIM image settings (Figure 9c,d) (Becker et al., **Appendix II**, Figure 4).

We proposed that this cluster originated from the autofluorescent property of SN-38 [223]. For quantification of SN-38 inside of CRC organoids, pixels in FLIM images with FAD containing values of $\tau2$ above a threshold of 3150 ns were counted and normalized to the total area of the organoid. The uptake of the drug in organoids was considered if the ratio of pixels with fluorescence lifetimes higher than 3150 ns were above the manual set threshold of 10% of the total organoid area to prevent influences of noise (Becker et al., **Appendix II**, Figure 4). However, as with RMS, the question raised at which threshold an organoid with absorbed SN-38 is considered, since a change in the threshold affects the result.

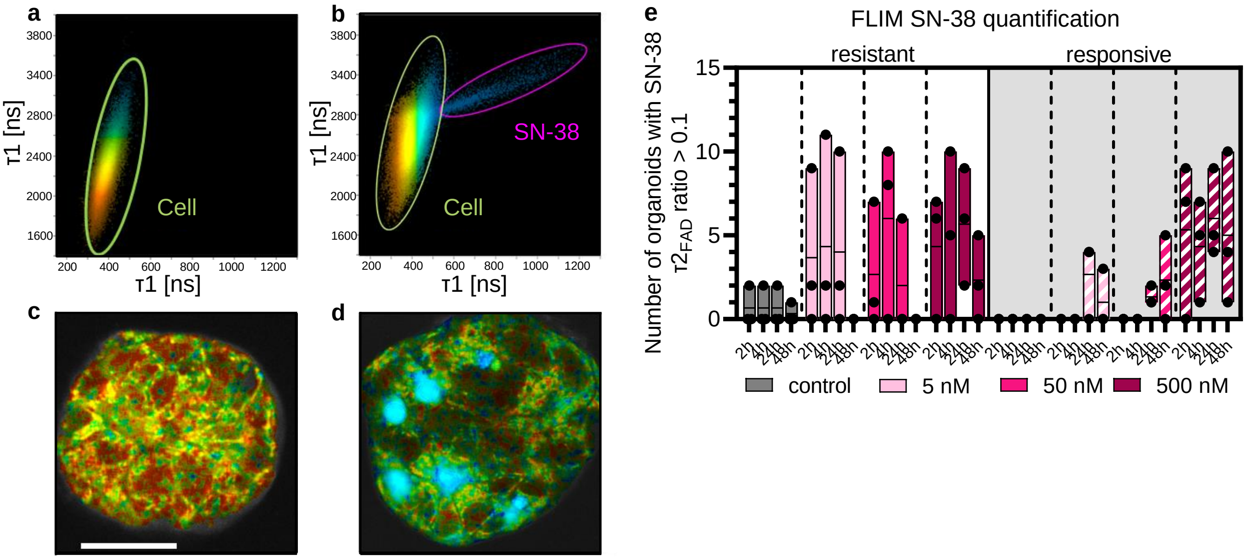

control 2h

500 nM 24h

Figure 9: FLIM enables quantification of SN-38 in CRC organoids. (a) 2D correlation between τ1 and τ2 of a control after 2h and a 500 nM SN-38 treated organoid after 24h (b) shows separation between cellular components (green) and the drug (pink). (c) Corresponding τ2 FLIM image of a control after 2h. (d) τ2 FLIM image of a 500 nM SN-38 treated organoid after 24h. Scale bar equals 20 µm. (e) τ2-based quantification of SN-38 uptake in resistant (solid bars) and responsive donors (striped bars). Adapted from Becker et al., Appendix II, Figure 4.

Applying the threshold at 10%, both untreated SN-38 resistant and responsive organoids displayed in total only six organoids from a total of 360 measured untreated organoids considered with drug throughout all measurements which could be due to artifacts or background signals. Statistical analysis revealed significant differences in SN-38 uptake between resistant and responsive donors. Upon treatment in organoids of two SN-38 resistant donors drug uptake was observed after two hours (Figure 9e). The total amount of organoids with the drug did not change significantly in the following 24 hours, but after 48 hours the number of organoids with the drug decreased to zero organoids at 50 nM and 5 nM drug concentration. Only at 500 nM SN-38 a total of seven organoids still exhibited the drug. In comparison, in organoids of responsive donors the drug was absorbed within the first four hours at a concentration of 500 nM SN-38. When treated with concentrations of 50 and 5 nM SN-38, uptake was observed only after 24 hours. Compared to resistant donors in which the drug was ejected after 48 hours, the number of organoids with absorbed drug increased in organoids of SN-38 responsive donors. A possible explanation for this observation could be that in responsive organoids the cellular uptake of the drug resulted in a direct metabolization via glucuronidation by the enzyme uridine diphosphate glucuronosyltransferase A1 (UGT1A1) with following accumulation, while in resistant donors the drug was not metabolized due to resistance mechanisms [224].

Overall, FLIM allowed to trace drugs in organoids by their autofluorescent properties. Potentially, this FLIM based drug tracing could be employed also for other drugs with autofluorescent properties. In comparison to Raman imaging, FLIM provides faster imaging and time-resolving capabilities as one FLIM measurement requires only 2.7 minutes compared to a Raman measurement requiring approximately 12 minutes for an organoid of the same size.

3.1.2 Metabolic Monitoring and Cellular Assessment

The energy production of a cell provides valuable information of the cellular state and directly reflects the cellular drug response [225]. Non-invasive and marker-independent FLIM measurements of treated organoids allow the analysis of fluorescence lifetime decays of the co-enzymes NADH and FAD both directly involved in the energy metabolism (Figure 3) [142,143], while RMS allows to evaluate the impact of drug treatment on nuclei and mitochondria. To determine whether non-invasive methods can identify the mechanism of drug action in patient-derived organoid models, it is first necessary to discuss whether comparable results can be obtained in organoids derived from standard cell lines. Therefore, we compared organoids from a bladder cancer cell line RT112 to bladder cancer organoids derived from primary tumor tissue of patients (BCO) and organoids derived from patients' urine (UCO). All organoids were treated for two days with various concentrations of cisplatin (*cis)* and venetoclax (*vtx*), drugs used against bladder cancer [226,227]. In Figure 10 the mode of actions of *cis* and *vtx* are visualized. *Cis* intercalates in DNA single strands hampering replication and induces DNA damage. This effect was reflected in PCA of Raman spectra of nuclei by recurrent peak patterns in all three organoid models (Becker et al., **Appendix I**, Figure 2). *Cis* induced effects were mainly detectable by shifts relevant for the structure of DNA, as *cis* intercalate in the DNA backbone ultimately leading to an inhibition of DNA replication. Failed DNA repair activated p53, which induced signal cascades by Fas/FasL, caspase 8 and caspase 7/3 leading to apoptosis of the cell. FLIM allowed us to monitor the induction of apoptosis by increased fluorescent lifetimes of free cytosolic NADH [73,228] (Becker et al., **Appendix I**, Figure S3). Activation of p53 mediated a reduction of glycolysis and lead to lower production of pyruvate [229]. Thus, TCA cycle activity necessitating pyruvate in the energy production was hampered. This resulted in a decrease of bound NADH and an increase of bound FAD. While p53 mediated the reduction of glycolysis, OXPHOS was increased reflected by a decrease in NADH α1% [228-231] (Becker et al., **Appendix I**, Figure S3). *Cis* also induced reactive oxygen species

(ROS) hampering the TCA cycle which lead to a reduction of the mitochondrial membrane potential (MMP) [232]. The loss of MMP resulted in a leakage of cytochrome c and caspase 9 into the cytosol inducing apoptosis [233]. FLIM was also able to detect differences in drug response between the three bladder cancer organoid models for instance in α1% of NADH and FAD in BCO (Becker et al., **Appendix I**, Figure 6) upon *cis* treatment which might be correlated to the switch of energy production or indicated an increased energy consumption of nuclei in preparation for apoptosis [230,231].

In contrast, *vtx* is a drug directly inducing apoptosis. Apoptosis is regularly induced by anti- and pro-apoptotic proteins of i.e., the Bcl-2 family. Upon cellular stress or DNA damage, pro-apoptotic BH3 binds to anti-apoptotic Bcl-2 which recruits pro-apoptotic proteins BAK and BAK to the mitochondrial membrane. BAK and BAX permeabilize the mitochondria with the following release of cytochrome c and induction of caspase cascades resulting in apoptosis. *Vtx* is a BH3 mimetic binding to the BH3 domain of Bcl-2 inducing the BAX/BAK cascade [234]. The induction of apoptosis was reflected by an increase in τ2 of NADH upon *vtx* treatment in all three organoid models [228] (Becker et al., **Appendix I**, Figure 6). In mitochondrial Raman spectra, recurrent peak patterns were only detected after *vtx* treatment (Becker et al., **Appendix I**, Figure 2). This effect was demonstrated by peaks in the loadings relevant for cytochrome c.

Overall, FLIM and RMS allowed to identify drug specific effects on organoids. Organoids derived from the bladder cancer cell line RT112 showed resemblance in their drug induced reaction patterns compared to patient derived organoids from primary tumor tissue as well as urine. These results suggested that on the one hand RMS and FLIM are suitable non-invasive tools to evaluate the mode of action of several drugs in patient-derived organoids. On the other hand, it is of great interest to explore the usability of organoids derived from urine or other body fluids further. Body fluids are easily accessible from patients at an early disease stage without the need for surgery and therefore they provide an ideal early-stage screening platform [235].

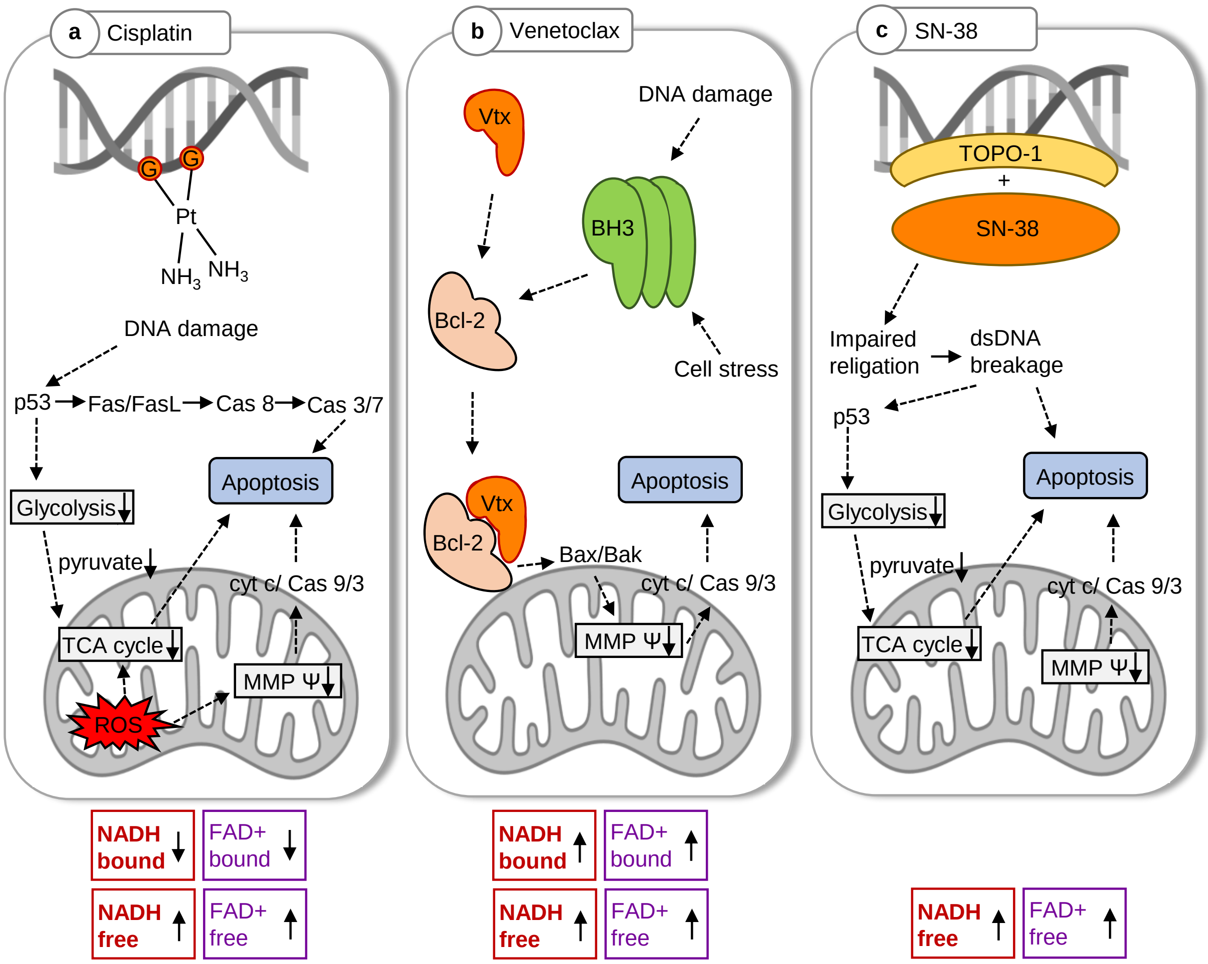

Figure 10: Mode of action of chemotherapeutics studied in this thesis. (a) Cisplatin (*cis*) intercalates in DNA single strands hampering replication and induces DNA damage. Failed DNA repair activates p53 with following signal cascades by Fas/FasL, caspase 8 and caspase 7/3 leading to apoptosis. Activation of p53 also leads to a decreased glycolysis and pyruvate production reducing the tricarboxylic acid (TCA) cycle activity. This results in a decrease of bound NADH and increase of bound FAD+. *Cis* also induces reactive oxygen species (ROS) hampering the TCA cycle and leads to reduction of the mitochondrial membrane potential (MMP). Loss of MMP results in a leakage of cytochrome c and caspase 3/9 into the cytosol inducing apoptosis. Induced apoptosis is reflected by increased free NADH and FAD+. (b) Apoptosis is regulated by pro-apoptotic proteins BAK and BAK permeabilizing the mitochondria with following release of cytochrome c and induction of caspase cascades. BAX and BAK are recruited to mitochondria when pro-apoptotic BH3 bind to anti-apoptotic protein Bcl-2 induced by cell stress and DNA damage. Venetoclax (*vtx*) is a BH3 mimetic which binds to Bcl-2 inducing the BAX/BAK cascade resulting in a loss of MMP, and release of cytochrome c and caspases 3/9. (c) DNA topoisomerase I (TOPO-I) relaxes both positive and negative supercoiled DNA while replication. TOPO-I binds to the 5'-end (phosphate residue) of the strand break via a hydroxy group of a tyrosine residue and rotates the 3'-segments. To release torsional stress TOPO-I causes a single-strand to break without consuming ATP. When it leaves the DNA, it closes the break by ligases. Binding of SN-38 inhibits TOPO-I-mediated relegation of the DNA. The complex containing DNA, TOPO I and SN-38 can collide with replication forks resulting in double-strand breaks in DNA and subsequent induction of apoptosis. SN-38 is also recognized to damage mitochondria by increasing the permeability of the outer mitochondrial membrane, directly associated with MMP disintegration leading to release of cytochrome c and activation of caspase cascades resulting in apoptosis.

Given the success of patient-derived organoids in evaluating drug responses, there is considerable interest in precision medicine to distinguish between drug-resistant and drug-responsive donors. A key obstacle in achieving effective cancer treatment is the restricted efficacy of systemic drug therapies arising from individualized multidrug resistance mechanisms [236]. Evaluating drug efficacy prior to their administration would significantly improve therapy effectiveness and reduce patient's suffering. Therefore, we determined if RMS and FLIM have the potential to identify drug efficacy and to differentiate between sensitivities in SN-38 resistant and responsive CRC patients. Before the measurement with non-invasive RMS and FLIM, the drug sensitivity of six donors was analyzed by fluorometric viability assays (Becker et al., **Appendix II**, Table 2). TCA identified mitochondria, nuclei, cytoplasm, lipids, and SN-38 based on specific Raman signatures (Becker et al., **Appendix II**, Figure 2). Raman spectra of mitochondria and nuclei were extracted from all organoids and were further analyzed by PCA to evaluate the effect of the drug on nuclei and the metabolism. It was reported that SN-38 inhibits DNA topoisomerase I (TOPO-I) which is involved in DNA replication and transcription ultimately leading to DNA breakage. TOPO-I is an enzyme involved in DNA replication by relaxing both positive and negative supercoiled DNA. When bound to the 5'-end (phosphate residue) of the strand by a hydroxy group of a tyrosine residue it rotates the 3' segments. Torsional stress is then released by a single strand break without consuming ATP. After detachment of TOPO-I, the DNA breaks are closed by DNA ligases. SN-38 is the active metabolite of the drug irinotecan and inhibits TOPO-I mediated relegation by forming a complex which collides with the DNA replication forks ultimately resulting in double strand breaks [237-239]. As a consequence, the induction of DNA damage triggers a series of intricate apoptotic signaling pathways, culminating in the initiation of programmed cell death [240,241]. The drug effect within the treated organoids was predominantly discerned through alterations in the loading plot of nuclei Raman spectra, indicative of perturbations in DNA structure (Becker et al., **Appendix II**, Figure S1). Moreover, PCA facilitated the identification of statistically significant discrepancies in drug response between resistant and responsive donors (Becker et al., **Appendix II**, Figure 2). Notably, the dissimilarities between the two groups were primarily attributed to differences in the degree of impact exerted by SN-38 on DNA within the responsive cohort.

SN-38 is also recognized to damage mitochondria by increasing the permeability of the outer mitochondrial membrane, directly associated with MMP disintegration leading to a release of cytochrome c and activation of caspase cascades resulting in apoptosis [242,243]. In Raman spectra of mitochondria of SN-38 responsive donors, PCA identified statistically significant differences between resistant and responsive donors upon drug treatment (Becker et al., **Appendix II**, Figure 2). It was reported that mitochondria may adapt to drug treatments with fusion and fission resulting in a conformational change [244]. PCA of mitochondrial spectra allowed to identify structural changes in mitochondria by shifts responsible for amide I and amide III.

FLIM further allowed metabolic monitoring of drug induced effects in resistant and responsive CRC organoids. Differences between resistant and responsive donors were evaluated by analysis of histograms of different FLIM parameters. Upon drug treatment, FLIM identified alterations in the distribution of bound and free NADH and FAD. In both NADH and FAD a decrease in α1% was identified in responsive donors compared to resistant donors. Additionally, increases in fluorescence lifetime τ2 of FAD were only identified in responsive donors (Becker et al., **Appendix II**, Figure 3). PCA was performed on z-scaled FLIM parameters to identify which parameters are the most relevant for discrimination of responsive and resistant donors. PC-1 identified the main metabolic drug effect of SN-38 in changes of α1% in FAD and NADH detectable in both resistant and responsive donors. PC-2, however, allowed to discriminate between different metabolic effects. While responsive donors reacted with a decrease in score value of PC-2 mainly induced by alterations in τ2 of NADH and α1% of FAD, resistant donors reacted with a slight increase in score values due to τ1 of FAD.

Together, RMS and FLIM allowed us to non-invasively discriminate between resistant and responsive donors upon drug treatment. However, the effects of the treatment could only be determined after the actual treatment and could not be predicted in advance on the untreated organoid by application of both RMS and FLIM. Therefore, experiments must be repeated with a wide variety of chemotherapeutic agents for all donors with simultaneous viability assays. For transition to clinical applications, also the effects of drugs on non-cancerous organoids needs to be tested to evaluate potential side effects. Furthermore, the utilization of diverse chip architectures could be implemented to simulate the flow dynamics of the drug. This approach involves manipulating the physical design of the chip to create an environment that replicates the fluid dynamics of the targeted system. By doing so, the drug's behavior and its effect could be observed and analyzed under conditions that closely mimic those found in vivo [245].

3.1.3 Data-Driven Profiling of Drug Effects

The acquisition of Raman spectra and FLIM images lead to an enormous amount of data requiring the need for ML methods to assess all information and reduce computation time. Utilizing PCA, drug-specific separation within Raman spectra acquired from the nuclei and mitochondria of treated patient-derived cancer organoids were successfully identified. However, these extracted features were not easily interpretable or measurable, as they lose direct reference to the original features [246]. Furthermore, once calculated PCAs are not easily applicable on new datasets, for instance the measurement of patient-derived organoids from a new donor treated with chemotherapeutics. Here, a PCA-projection could be applied to cluster and classify new data on pre-calculated PCA loadings in order to identify the drug response pattern [247]. Another challenge in utilizing PCA arises in the manual selection of the most important principal components that might be affected by bias and errors.

An alternative approach to circumvent these limitations is based on data-driven feature selection. Feature selection, as opposed to preserving information from the entire dataset, focuses only on relevant subsets. These subsets are selected to preserve only the most informative features without affecting the original features in the process. A non-linear feature-selection neuronal network (FeaSel-Net [218]) was utilized to derive a selection of potential biomarkers allowing to classify the different treatments of bladder cancer organoids. FeaSel-Net identified five wavenumbers (Becker et al., **Appendix I**, Table 2) for each dataset (nuclei, mitochondria for RT112, BCO and UCO) capable of classifying the data to their corresponding class with improved accuracy, sensitivity and specificity compared to the classification obtained by PCA (Becker et al., **Appendix I**, Table 3). Some of the wavenumbers identified by FeaSel-Net were also detected in the loadings (e.g., 705 cm^{-1}, 1250 cm^{-1}, 1587 cm^{-1}), but some other important features (e.g., 926 cm^{-1}, 1551 cm^{-1}) showed no overlap. Notably, the peak at 926 cm^{-1} in the BCO nuclei data set was selected in 100% of 50 repeated runs of the neural network, suggesting that even univariate classification is possible, whereas it was not identified in PCA. This comparison showed that unlike PCAs and their associated loading plots, very deep neural networks can find patterns in the signal that were not interpretable by humans or statistical analysis. The question remains whether these results are generalizable due to overfitting and persistence in independent replicates. Here, although a Raman measurement provides large amounts of data, it is quite difficult and time consuming to acquire large data sets of independent spectroscopic data and instances [248].

Utilizing neural network classification, the discrimination of drug sensitivities in SN-38 resistant and responsive CRC organoids was also carried out, yielding favorable classification outcomes (Becker et al., **Appendix II**, Table S1). The results of classifying Raman spectra from cell nuclei and mitochondria, as well as the joint classification of both datasets, demonstrated that the spectral information from mitochondria is of greater importance. This was evident by the increased classification accuracy when only the dataset containing a low concentration of SN-38 (5 nM) in mitochondria was employed.

3.2 Characterization of Fibrotic Collagen Fibers

In the first chapter of the results, the utilization of RMS and FLIM techniques to detect the responsiveness of cancer organoids to various pharmacological agents were discussed. These techniques provided a thorough characterization of the metabolic and nuclear changes that occurred within the organoids upon treatment. Nevertheless, in order to fully comprehend the systemic effects of these medications on the entire human organism, it is necessary to first examine the overall architecture of the tissue and its commonalities. In the following chapter, this holistic perspective will be elaborated and the underlying mechanisms of fibrotic pathogenesis, often associated with neoplastic diseases, will be molecularly investigated.

3.2.1 Histological Gold Standard Fibrosis Identification

The ECM and its multifaceted molecular constituents are vital for maintaining the structural and functional integrity of organs. In the event of tissue damage, biochemical changes occur in the course of normal wound healing, followed by an inflammatory response that causes fibroblasts to differentiate their phenotype into highly specialized synthetic and contractile myofibroblasts (Figure 11) [249]. Myofibroblasts are activated by a variety of mechanisms and a wide range of regulators such as growth factors, chemokines, cytokines, or caspases and are associated with the expression of smooth muscle actin (αSMA) contributing to cell-generated mechanical tension involved in wound contraction [250-252]. In addition, myofibroblasts produce increased fibrillar collagen and matricellular proteins important for preserving the tissue’s structural integrity through the modification of the ECM [249]. After completion of wound healing, the myofibroblasts normally disappear by apoptotic pathways [253]. However, due to influences of a wide range of different diseases such as chronic inflammations or cancer the myofibroblasts can get persistent and stay activated as they develop apoptosis resistance ultimately resulting in an excessive production and deposition of collagens. Such pathological fibrosis can lead to disruption of tissue structure, organ dysfunction and eventually organ failure [250,252,254].

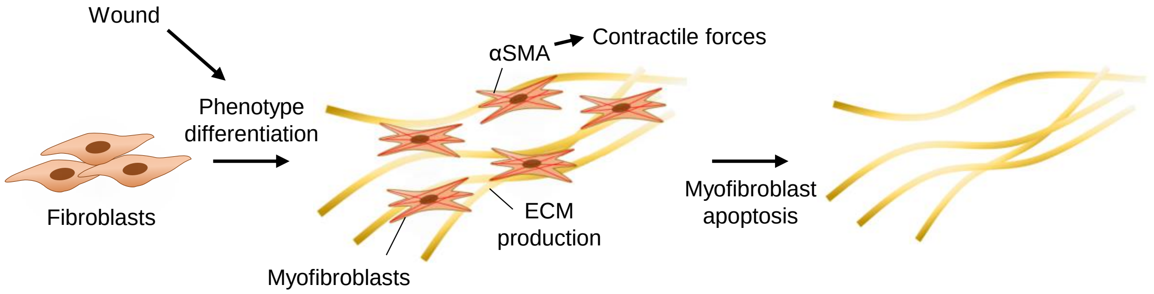

Figure 11: Illustration of myofibroblast differentiation during wound healing. Triggered by a wound, fibroblasts differentiate their phenotype into myofibroblasts. Myofibroblasts express αSMA responsible for the contractile forces required for wound closure. Myofibroblasts are responsible for ECM production such as collagen. After wound healing myofibroblasts undergo apoptosis.

In this thesis the aim was to characterize fibrotic and native collagen fibers in various human ex vivo tissues on a molecular level to gain new insights into the development of pathological tissue alteration. Gold standard histochemical analyses of ECM tissue structures from controls and fibrosis related diseases of liver, colon, breast, lymph nodes and myocardium tissues were performed by Masson's trichrome and Movat-Pentachrome staining allowing to identify the localization of excessive collagen formation. While microscopic evaluation of Masson's trichrome staining primarily identified collagen fibers in blue, Movat-Pentachrome staining allowed to stain for nuclei and elastic fibers (black), collagen fibers (yellow), ground substance and mucin (blue), muscle (red) and fibrin (bright red) (Becker and Lu et al., **Appendix III**, Figure 1). According to histological staining, pathological fibrosis was identified by increased amounts of stained collagen in liver, colon, lymph node, and myocardium. Conversely, identification of fibrosis in connective tissue-dominated organs such as the breast can prove more difficult and requires morphometric examination by experienced pathologists [255]. Occasionally, the clinical diagnosis of fibrotic disease may vary based on individual experience and knowledge, leading to inconsistent diagnostic results showing the lack of deep classification and quantification of collagen fibers by classical stains [256,257]. Furthermore, histological diagnosis is highly dependent on the quality of specimens obtained from biopsies. The quality depends on the inherent variability of the biopsy procedure as well as on the heterogeneity of the disease [258-260].

Picrosirius red staining (PSR) allowed to further characterize collagen fibers by identifying the thickness and maturity due to their birefringent characteristic [261]. However, the maturity and thickness of collagens did not allow to robustly discriminate between control collagen fibers and fibrotic collagen fibers. Moreover, the fiber alignment was not sufficient as discriminant to identify fibrosis when compared among different organs (Becker and Lu et al., **Appendix III**, Figure 2).

All these described histological stains were not specific to identify different collagen subtypes [262]. Therefore, immunofluorescent images of COL I were recorded along with αSMA identifying COL I as an important collagen type in fibrosis. However, the quantification of COL I as well did not lead to uniform conclusions in the identification of fibrosis (Becker and Lu et al., **Appendix III**, Figure 3). In clinical settings, the use of IF staining for fibrosis identification is limited due to a number of factors. These include the high cost of primary antibodies and fluorescence-labelled chemical agents, as well as the lengthy staining procedures involved. Furthermore, the potential for autofluorescence arising from either the tissue or from secondary fluorescence-labelled antibodies presents a further challenge when utilizing IF staining compared to classical histological staining [263]. The main disadvantage of classical and immunofluorescence staining of collagen is that the stains are unable to distinguish pathological fibrotic COL I from native COL I. Similar challenges arise in the application of other imaging techniques such as label-free second harmonic generation (SHG), which allows to identify collagen without the need of staining based on two-photon excitation [264]. While the non-invasive methodology of SHG is very cost effective and does not require sacrifice of the sample, SHG can only provide information on the amount of collagens and arrangement of fibers, which may not be a uniform indicator of fibrosis.

3.2.2 Fibrosis Monitoring by Spectral Deconvolution

Conventional histochemical methods facilitated the recognition and positioning of ECM structures but did not provide molecular-level characterization and lacked the ability to differentiate between various collagen types or distinguish healthy from pathological collagen. To date, 28 distinct collagen types have been identified [265,266]. All collagen types share the presence of tandemly repeated amino acid triplets Gly-Xaa-Yaa, where Gly represents glycine and Xaa as well as Yaa can be any amino acid but are mostly occupied by proline and hydroxyproline [267,268]. In collagen formation, two α1 chains assemble with one α2 chain at the C-terminus to form a triple helix (Figure 12). Binding of the collagen specific chaperon heat shock protein 47 (HSP47) expressed in the rough endoplasmic reticulum (rER) in all collagen-producing cells is involved in the proper folding of the quaternary structure of triple-helical procollagen. Additionally, HSP47 has been identified to block the disintegration of procollagen in the rER prior to its transport to the Golgi apparatus. In the formation of the HSP47 procollagen complex, the aspartic site of two HSP47 chaperons binds to the trailing and leading strand of procollagen by formation of a salt bridge to a Gly-Xaa-Arg triplet while the middle strand is not attached due to steric reasons [269,270]. It was recognized that the overexpression of HSP47 is involved in the development of several fibrosis related diseases [271-273].

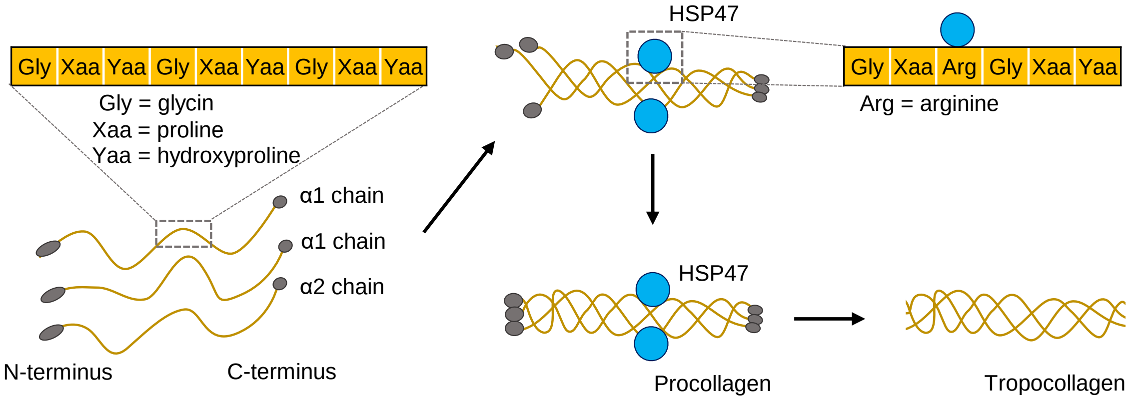

Figure 12: Schematic of collagen fiber folding. The formation of collagen fibers begins with the assembly of three alpha1 chains, each consisting of repetitive glycine-Xaa-Yaa triplets. Xaa and Yaa are typically filled by proline and hydroxyproline, resulting in the establishment of a triple helical conformation. The binding of two heat shock protein 47 (HSP47) to an arginine amino acid in the triple helix results in the formation of procollagen. Upon removal of HSP47 and cleavage of the N- and C-terminus, the final product of tropocollagen is formed.

RMS was utilized to define the biochemical structures of ECM and its pathological changes in fibrosis related diseases. According to Masson’s trichrome staining and pathological evaluation, fibrotic regions of interests were targeted in the bright field mode of the Raman microscope, and visible collagen bundles were analyzed by large-area scans. TCA of the spectral data provided intensity heat maps, identifying nuclei, αSMA, COL I, COL III, and COL IV by distinct spectral fingerprints implicating the potential of RMS being applicable in the non-invasive and marker independent discrimination of different types of collagens as well as biological structures (Becker and Lu et al., **Appendix III**, Figure 4). PCA and score value analysis of 600 single Raman spectra of COL I per patient did not allow to clearly identify fibrotic COL I from controls when comparing liver, colon, breast, lymph node and myocardium together, however, suggested by the loading plot that fibrotic COL I structurally differs COL I fibers of controls. According to the loading plot, the separation between COL I from control and fibrotic diseases were mainly originated by changes in spectral intensities located in the amide I region (1580-1720 cm^{-1}) together with peaks responsible for changes in the amide II and amide III region (Becker and Lu et al., **Appendix III**, Figure S1). [274,275]. The differences between averaged COL I Raman spectra of both control and fibrosis from liver portal triads are displayed in Figure 13a. Examination of the amide I area

(Figure 13b) displayed differences between control and fibrosis. This finding implicated a structural difference between fibrotic and control COL I as in the amide I region most information about the secondary structures such as α-like helices, β-sheets, β-turns and random coils were found. To further analyze the secondary structure of COL I fibers, spectral deconvolution was implemented to evaluate substructural peaks within the amide I region and calculate the peak areas and widths. With spectral deconvolution, five substructural peaks were calculated based on the shape of the averaged amide I region of COL I fibers and literature (Figure 13c,d) [276]. The comparison of peak areas and widths of all substructural peaks among COL I spectra of control and fibrosis of different human organs displayed a consistent increase at the peak located at 1608 cm^{-1} throughout all tissue origins including liver, colon, breast, lymph nodes (Figure 13e) (Becker and Lu et al., **Appendix III**, Figure 4). Comparison of peak widths and areas of other substructural peaks inside the amide I region located at 1563, 1588, and 1636 cm^{-1}, displayed no observable trend between control and fibrotic COL I fibers (Becker and Lu et al., **Appendix III**, Figure S2). Additional to spectral deconvolution developed on average COL I spectra, Raman images containing the entity of single Raman spectra of COL I were analyzed by a filter image approach. Histogram and mode analysis of the ratio of sum-filter images generated at 1667 and 1608 cm^{-1} allowed an image-based evaluation of COL I fibers (Becker and Lu et al., **Appendix III**, Figure 5). Comparing the histograms and modes of sum-filter image ratios between control and fibrotic COL I, a consistent trend with increased values in control COL I was identified throughout all examined tissues except colon. The low values in the control tissue indicated a lower overall signal at wavenumber 1608 cm^{-1} when all COL I spectra in the individual Raman images were considered, further strengthening the identification of a fibrosis-specific biomarker.

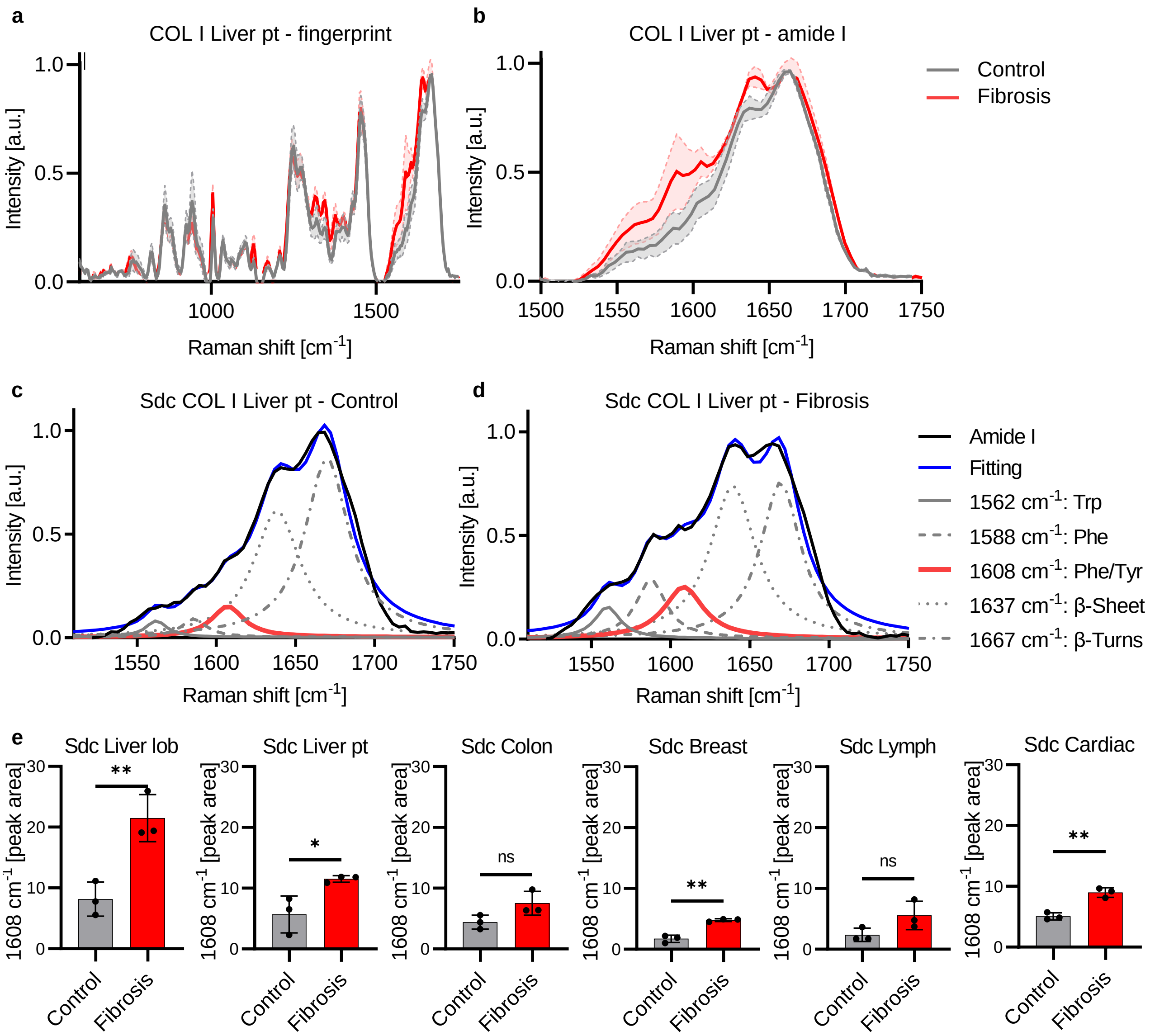

Figure 13: Spectral deconvolution of collagen type I (COL I) Raman spectra displays consistent differences between fibrosis and controls in various human tissues. (a) Average Raman spectra of COL I from control (gray) and fibrotic (red) liver portal triads. (b) Amide I region of control and fibrotic COL I of liver portal triad. The shaded error lines represent the standard deviation. (c) Spectral deconvolution (Sdc) of the amide I region of control liver portal triads. (d) Sdc of the amide I region of fibrotic liver portal triad. (e) Peak areas at 1608 cm^{-1} calculated by Sdc of various human tissues and fibrotic diseases. Statistical analysis: t-test, n=3, *p<0.05, **p<0.01, ns: not significant. Adapted from Becker and Lu et al; Appendix III [277].

The spectral signature located at 1608 cm^{-1} was representative for the amino acids' tyrosine and phenylalanine (Phe) [278,279]. The increased Raman signal in fibrotic COL I located at 1608 cm^{-1} indicated a replacement of the amino acids at Xaa or Yaa to Phe, which was reported to induce alterations in the dissociation constant of the binding of HSP47 to procollagen [268,270]. Therefore, the identified biomarker might have indicated the increased binding affinity of HSP47 contributing to the excessive production and formation of collagen leading to fibrosis [273,280]. If further testing of this hypothesis holds for additional fibrotic diseases and more patients in varying ages, the identified

Raman biomarker for fibrotic COL I might assist pathologists in challenging cases of diagnosis. Furthermore, the fibrosis-specific Raman biomarker could be used in potential Raman-endoscope setups to support intraoperative diagnostics in the future.

We further asked whether it is possible to detect fibrotic COL I changes with the specific Raman biomarker in diseases in which fibrosis is suspected but not yet fully confirmed. Therefore, we compared Raman spectra of COL I from the peritoneum and endometrium and compared them to COL I of endometriosis from the ligamentum sacrouterinum (LiS) and septum rectovaginale (SRV) (Becker and Beyer et al., **Appendix IV**, Figure 2, 4). In endometriosis it is still debated if a fibrotic alteration of collagens is present in endometriotic lesions [281]. We employed RMS and TCA on cryosections of human endometrium and endometriotic glands to identify endoplasmic reticulum, lipids, elastic fibers, COL I and nuclei (Becker and Beyer et al., **Appendix IV**, Figure 1). First, score value analysis of COL I Raman spectra identified a statistically significant difference between endometrium and endometriosis across all menstrual cycle phases (Becker and Beyer et al., **Appendix IV**, Figure 2), where the loading plot indicated alterations in the amide I, II and III regions. Second, the Raman biomarker at 1608 cm^{-1} allowed to identify increases in peak area and width in endometriosis from LiS and SRC compared to endometrium and peritoneum, giving molecular insights that endometriosis might be correlated with fibrosis.

3.3 Disease Diagnostics

3.3.1 Epigenetic Alteration in Endometriosis and Cardiomyopathies

Epigenetic modifications are pivotal in pathological tissue aberrations, as evidenced by their significant role in DNA methylation and histone alterations [282,283]. These dynamic regulators influence cellular proliferation and behavior, thereby exerting an impact on tissue morphology in the pathogenic process [284,285]. For instance, tumor cells often show epigenetic hypomethylation of gene promoter regions, leading to an activation of oncogenes and initiation of chromosome instability [286-289], while DNA hypermethylation initiates the silencing of tumor suppressor genes [290-292]. But also, in cardiomyopathies and other non-cancerous diseases such as endometriosis the influences of epigenetic modifications were identified [293-295]. Therefore, the DNA methylation profile may be relevant for pathogenesis, diagnosis, and prevention/therapy of various oncological and benign diseases [285]. The most common epigenetic alteration is 5-methylcytosine (5mC), accounting for 4% of all cytosines in the human genome [285,296,297]. The main feature of cytosine methylation is its accumulation and specificity in symmetrical cytosine-phosphate-guanine (CpG) islands found in gene promotor regions, in which methylations are present on both DNA strands. The process of de novo methylation is facilitated by the action of DNA cytosine-5-methyltransferases 3A and 3B (DNMT3A/DNMT3B), and subsequently upheld by DNMT1 during DNA replication. During this process, the methylations can be accurately propagated through the copying of the parental strand onto the newly synthesized, unmethylated strand.[285,298,299].

Currently, common methods to identify the epigenetic profile of cells include for instance next-generation sequencing (NGS) or methylation microarrays to characterize single DNA bases. However, these methods have been very time-consuming and require the disruption and sacrifice of tissue and the isolation of cellular DNA [300,301]. Previously it was shown that non-invasive RMS is capable of identifying epigenetic 5mC in mouse models [302]. We therefore applied this promising methodology to several human tissues to on the hand gain new insights in the pathology of different diseases and on the other hand to elucidate the potential of RMS being utilized for disease diagnostic based on epigenetic modifications. RMS and TCA were utilized on cryosections of human endometrium, endometriosis, and peritoneum tissue and FFPE sections of different cardiomyopathies to identify nuclei Raman spectra (Becker and Beyer et al., **Appendix IV**, Figure 1; Becker et al., **Appendix V**, Figure 2). To identify epigenetic alterations between control and diseased tissue, nuclei Raman spectra of endometrium and endometriotic glands, as well as nuclei from cells in areas of fibrosis in cardiomyopathies were investigated by PCA and filter image analysis. Score value analysis identified a statistically significant difference between endometrium and endometriosis glands across all menstrual cycle phases (Becker and Beyer et al., **Appendix IV**, Figure 3). Prominent peaks in the loadings that distinguished endometrial nuclei from endometriosis were depicted at 794 and 1101 cm^{-1}, indicators of PO_2^- in the DNA backbone [190]. Further, in the endometrium shifts were observed at 676, 1341, and 1484 cm^{-1} corresponding to the DNA base guanine [192,303]. In contrast, nucleic Raman spectra of endometriosis displayed increased spectral intensities in structural amide III and amide II at 1239 and 1554 cm^{-1} attributed to changes in histone packing potentially identifying active or inactive genes [304,305] as epigenetic methylations can also occur at various sites in the histones involved in the condensation of DNA. In histones, methylations primarily are located at lysine and arginine residues [306]. The peak at 1285 cm^{-1} corresponded to cytosine or methylene [307]. Further, prominent shifts at 1366 and 1443 cm^{-1} found in endometriosis were related to methylations indicating an increased CH_3 level in DNA of nuclei in endometriotic glands [308-310]. To elucidate if the increased levels of methylation can be attributed to epigenetic 5mC modification, IF imaging of 5mC was performed (Becker and Beyer et al., **Appendix IV**, Figure 3). 3D images of nuclei from endometrium and endometrial glands were acquired and the 5mC signal was evaluated by fluorescence intensity showing increased signal intensity in endometriosis across all menstrual cycle phases compared to endometrium. Additionally, the number of epigenetic foci per nuclei displayed a statistically significant increase in endometriosis, which supported the results obtained by PCA. To further test the potential of RMS in the identification of epigenetic changes, filter images were generated based on the wavenumber representative of methylations located at 1370 cm^{-1}. Mean gray value analysis of filter-images normalized to whole nucleus signal revealed statistically significant increases in endometriosis compared to endometrium. In combination with the result of IF imaging, these findings provided proof of concept that marker-independent Raman imaging of 5mC may hold potential in the epigenetic assessment of endometrial tissue.

Relating the methodology to a more clinically relevant situation, the epigenetic profiles of endometriosis of LiS were compared to those of SRV and healthy peritoneum in which endometriosis can occur [311]. The comparison showed that the weakest epigenetic signal is found in the peritoneum, while both endometrioses were statistically significantly increased (Becker and Beyer et al., **Appendix IV**, Figure 4). This result suggested that the epigenetic profile indeed has the potential to be used for diagnosing tissue alterations. However, it is necessary to examine many more tissues and different localizations of many patients to clinically implement the method. In addition, it is important to examine control tissue from diseased patients to avoid errors due to patient-specific differences. Clinically, however, this is not easy to realize since the excessive removal of healthy tissue from patients must be avoided for health reasons.

5mC staining was also performed on control myocardium and different cardiomyopathies including DCM, hypertrophic cardiomyopathy (HCM) and ischemic heart disease (HCM) (Figure 14a, Becker et al., **Appendix V**) as epigenetic modifications were already reported elsewhere to have an influence in the development of these diseases. Especially it was demonstrated before that DNMT1 is involved in the development of cardiac fibrosis [312,313]. IF staining displayed statistically significant increased amounts of COL I in IHD, HCM and DCM compared to control myocardium (**Figure 14**b). Moreover, statistically significant increased amounts of αSMA were found in DCM (**Figure 14**c) compared to control myocardium. In IHD and HCM the tendency of increased amounts of αSMA was detected. Quantification of the area (Figure 14d) and fluorescence intensity (Figure 14e) of 5mC in fibrotic areas displayed statistically significant increases in IHD and HCM compared to control myocardium, while DCM showed a tendency of increased fluorescence intensity. This result coincided with results from PCA analysis of nuclei Raman spectra. PCA and score value analysis identified statistically significant differences between control myocardium and all three cardiomyopathies (Figure 14f). While increased signals in DNA and DNA backbone were identified in controls at 782, 815 and 1222 cm^{-1}, cardiomyopathies exhibited increased signals in cytosine as well as methylations at 1257 and 1379 cm^{-1} (Figure 14g). Both 5mC analysis of endometriosis and cardiomyopathies implicated that epigenetic methylation of cytosine and following abnormal gene expression play an important role in the so far poorly understood etiology and pathogenesis of fibrotic diseases [314,315].

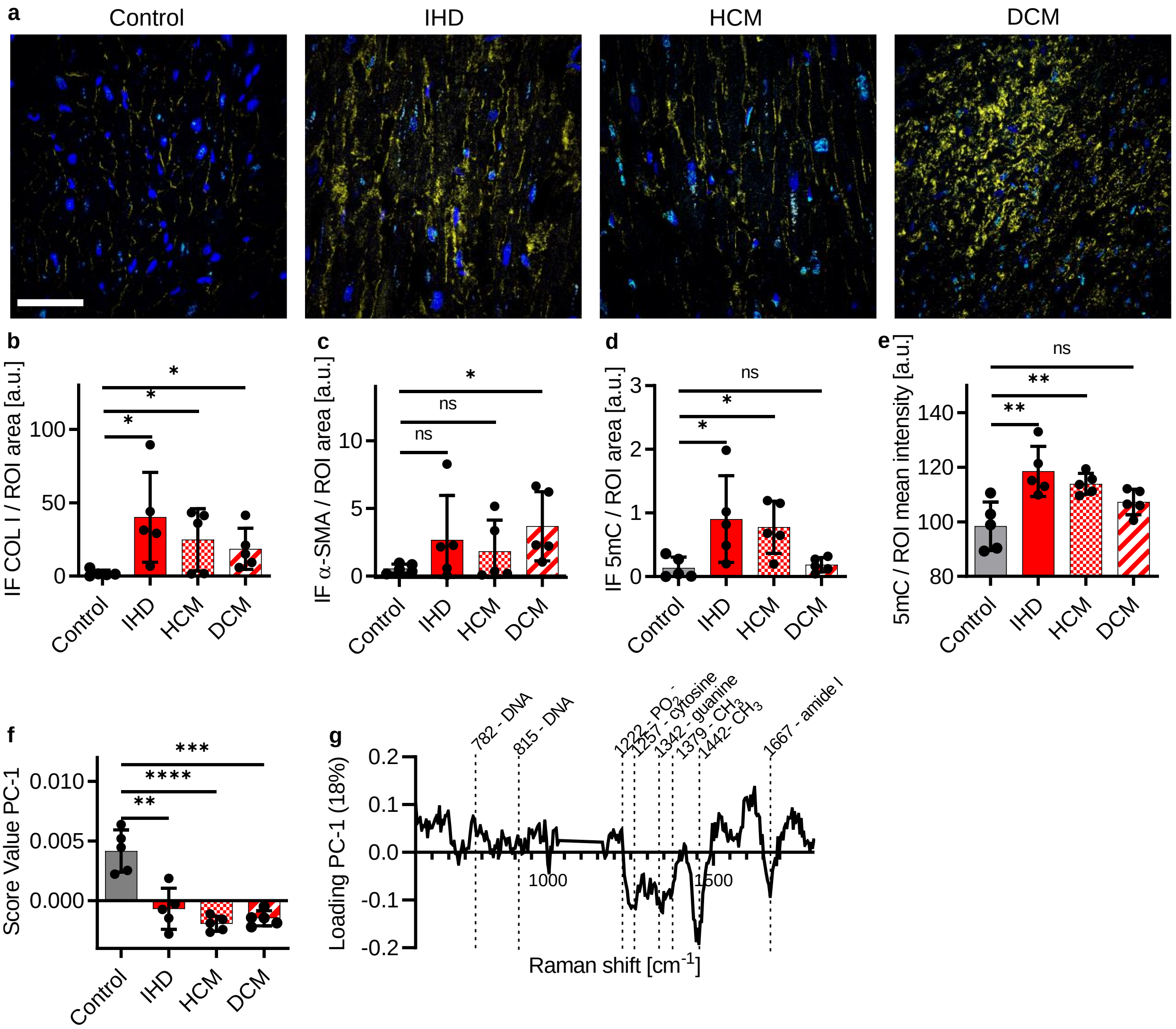

Figure 14: Raman imaging identifies epigenetic alterations in cardiomyopathies.(a) IF images of 5mC staining of control myocardium, ischemic heart disease (IHD), hypertrophic cardiomyopathy (HCM) and dilatated cardiomyopathy (DCM). Colors in IF staining: Nuclei (blue), COL I (yellow), 5mC (turquoise). Scale bar equals 100 µm. (b) Quantification of the amount of 5mC based on IF images normalized by nuclei. (c) Quantification of the fluorescence intensity of 5mC. (d) Score value analysis of PC-1 from nuclei Raman spectra from control myocardium and cardiomyopathies. (e) Corresponding loading plot. Statistical analysis: t-test, *n*=5, **p*<0.05, ***p*<0.01, ****p*<0.001, *****p*<0.0001; ns: not significant. Adapted from Becker et al. **Appendix V**, Figure 3.

As discussed earlier, in normal wound healing, myofibroblasts are removed via apoptotic pathways after secretion of ECM molecules. However, due to influences of epigenetic modifications of DNA the myofibroblasts may get persistent and stay activated as they develop apoptosis resistance ultimately resulting in an excessive production and deposition of collagens (Figure 15) [316,317]. This hypothesis is further supported by the increased expression of αSMA in cardiomyopathies consistent with elevated 5mC levels compared with normal myocardium (**Figure 14**c). Alternatively, the epigenetic modification could also result in an activation of the phenotypical switch of fibroblasts into myofibroblasts secreting ECM molecules even without the presence of a wound [318].

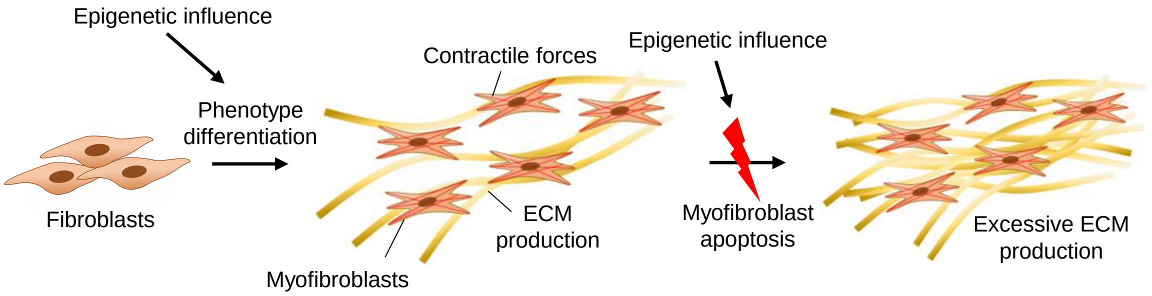

Figure 15: Schematic representation of the epigenetically regulated production of ECM. Phenotypical differentiation of fibroblasts into myofibroblasts is triggered by epigenetic signals. Myofibroblasts expressing αSMA produce extracellular proteins such as collagens. The apoptosis of myofibroblast might be suppressed by epigenetic modifications, resulting in persistent activation and excessive production of ECM.

Overall, it requires further testing of epigenetic expression on more fibrotic diseases and patients to determine if the methylation of cytosine is always a direct indicator of fibrosis. However, IF staining and RMS results showed promising evidence that there is a link between the development of fibrosis and epigenetic modifications of DNA.

3.3.2 Potential and Limitation of Raman Spectroscopy based Tissue Discrimination

RMS allows to resolve different tissue structures by specific spectral fingerprints. Even minute spectral differences can be identified using various ML techniques such as PCA, LDA or neural networks-based algorithms. Compared to histopathology, RMS offers the huge advantage of instantly examining tissue without the need for time-consuming preparation [319]. However, in many applications and in experiments presented in this thesis, Raman spectra were only acquired in a relatively small area (100 µm²) compared to the size of the tissue (several mm²). For small areas, TCA and PCA are very suitable for distinguishing tissue structures, but the recording of large areas is limited by the required time. Should Raman spectroscopy, for instance in the form of an endoscope, eventually find its way into clinical routine i.e., for the intraoperative application of tissue discrimination, the required time for a measurement is an essential health but also economic factor as one minute of operation costs approximately 16€ [320]. In this context, the question arises to what extent a punctual Raman measurement of widely separated points of the tissue is sufficient to capture the tissue morphology in a clinically adequate framework. This problem becomes apparent when a diagnosis is based on rarely occurring and only small features, such as epigenetic modifications that only appear in cell nuclei. Raman measurements of endometrial sections and fibrotic human tissues were performed with a spectral resolution of 0.5 and 1 µm, respectively, while the spot size of 5mC was identified to be approximately 1 µm. Due to the relatively large spot size and the relatively high amount of epigenetic 5mC in cell nuclei (4%) [296], the spectral features of methylations were detected. If a particular epigenetic modification, for example that of a histone subtype, occurs only rarely and has the size of a single protein and additionally overlap with other biological relevant features, it is very likely that the signal of specific epigenetic features is too small to be identified by RMS and PCA. Potentially, advanced ML techniques could help to identify these minute spectral features.

However, in the case of traditional RMS, a coincidental measurement of single epigenetic features in large tissues and the additional measurement of a healthy reference appears very unlikely. This would make the detection of epigenetic changes suitable only for post-operative diagnosis, where time is no longer a critical factor. Alternatively, the physician could delineate and resect a small area during operation, which would then be measured directly afterwards with high spectral resolution. This approach would save the required time for epigenetic staining and money for the needed chemicals and antibodies.

In comparison to epigenetic modifications found in nuclei, COL I fibers are manifold more abundant in human tissues, as COL I is one of the main components of ECM present in all tissues [321,322]. The particular importance of an intact ECM is illustrated by a variety of syndromes ranging from minor to severe disorders, such as invasive cancers and fibrosis, making it an excellent target for disease detection [322]. With the identified fibrosis Raman marker, which allows to detect fibrotic COL I by the peak area at 1608 cm^{-1}, a big improvement in tissue diagnostics could be achieved (Becker and Lu et al., Appendix III). However, it remains the question which Raman parameter is the most robust and easiest one to apply to differentiate between fibrosis and control COL I fibers in a clinical application. In clinical settings, particularly during surgeries, clinicians may rely on single point Raman measurements as they are the most technically feasible. Therefore, the proposed analysis to evaluate the fibrosis biomarker was conducted on only 20 randomly selected single spectra of COL I from each donor Raman image and compared to each other to simulate the smaller number of available spectra in comparison to the performed RMS measurements on over 1000 single Raman spectra per image (Becker and Lu et al., **Appendix III**, Figure 3). Figure 16 showcases the peak area computed through spectral deconvolution at 1608 cm^{-1} (Figure 16a) as well as the mode of the filter-image approach (Figure 16b), when 20 arbitrary Raman spectra are randomly chosen from the pool of available COL I Raman spectra.

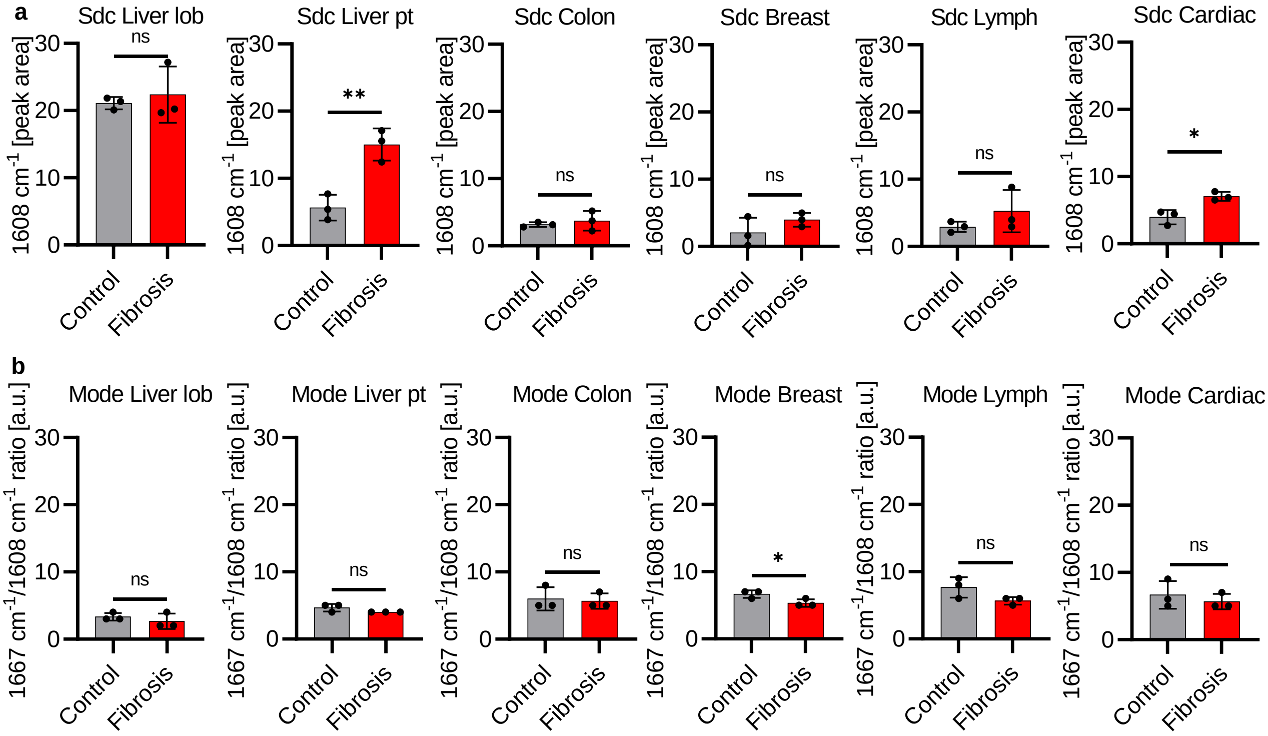

Figure 16: Spectral deconvolution (Sdc) and peak ratio analysis of the amide I region from 20 randomly selected and averaged COL I Raman spectra display similar separation between control and fibrosis through all tissue types. (a) Peak area at 1608 cm^{-1} calculated based on spectral deconvolution of amide I area of 20 randomly selected and averaged COL I spectra from control and fibrotic hepatic lobules (liver lob), liver portal triads (pt), colon, as well as connective tissue of the breast, lymph nodes and myocardium show similar separation through all tissue types. (b) Frequency of modes from filter image ratio at 1608 cm^{-1} normalized by amide I maximum. Statistical analysis: t-test, *n*=3, **p*<0.05, ***p*<0.01, ns: not significant.

The analysis revealed that the tendency towards higher peak areas persisted despite a reduced number of utilized Raman spectra in comparison to the study that examined all available Raman spectra (Becker and Lu et al., **Appendix III**, Figure 4, Figure 5). However, the differences no longer exhibited the same level of statistical significance, as significant increases in peak area in fibrotic COL I spectra were only detected in portal fields of the liver and. In hepatic lobules, colon, breast, and lymph nodes only tendencies of separation were observed. When examining the results of the mode analysis of filter images, the lower number of used Raman spectra becomes even more apparent, as significant differences were only found in the breast. While the tendency for increased modes was detected in portal triads of the lymph nodes, and myocardium, no difference between control and fibrosis were observed in hepatic lobules and colon.

If the quantity of accessible spectra diminishes, there is a propensity for a decline in the quality of the mean spectrum obtained. This could possibly result in noteworthy impediments in the estimation of peak area and width. The deviations from the results acquired by considering all the Raman spectra (~1000 spectra per Raman image) were mainly attributed to the noise in the Raman signals. The noise led to more peaks being present in the averaged COL I spectra, which were eliminated when all the COL I Raman spectra were considered. Spectral deconvolution considered all these individual peaks when determining peak areas and widths, thus influencing the results. In a clinical context, this constraint may be even more prevalent when accounting for the interference of Raman spectra by blood and the auto fluorescence of biological tissues. Here, extra pre-processing and signal enhancing steps are then required, increasing the complexity of data analysis. This problem is not only severe in single Raman spectra of collagen but in general, which makes the tissue classification, i.e., with ML techniques such as deep learning challenging.

Another challenge in this context is the amount of data required for a good classification of the tissue. An important part of data classification is the training of ML models and the preceding data preparation. Techniques such as deep learning require a large amount of data. However, it is challenging to generate a large amount of independent Raman spectroscopic data, since the tissue must first be preserved and additionally evaluated by a pathologist to avoid measuring irrelevant regions. This is especially important for supervised learning algorithms where a class label is mandatory. Furthermore, there is no large open-source database of clinical Raman data to date to pre-train ML models for transfer learning [248]. Finally, it remains questionable whether a pre-trained ML model of a particular dataset can be generalized and used for the classification of another dataset, since poor results might be obtained due to, for example, overfitting. Apart from these questions, a neuronal network-based classification of clinically relevant data provided good results on tailored datasets (Becker et al., **Appendix I**, Table S2; Becker et al., **Appendix II**, Table S1; Becker and Beyer et al., **Appendix IV**, Table S2; Becker and Lu et al., **Appendix III**, Table S1)

Raman spectra of both nuclei and COL I of glands from endometriotic lesions from the LiS and the SRV were compared to control peritoneum with a convolutional neuronal network and classified to the groups *control* and *diseased* (Becker and Beyer et al., **Appendix IV**, Table S2). Classification yielded an accuracy of 98.5%, sensitivity of 98.6%, and a specificity of 98.3% showing the potential of RMS in combination with neuronal networks being applicable for endometriosis detection. However, it is imperative to test this procedure on further donors and other sites of endometriosis such as from genitalia interna (i.e., myometrium), genitalia externa (i.e., vagina, perineum) or extra genitalis (i.e., ureter, retroperitoneum, lung, brain) and to extend it to include other tissue structures, since only the glandular regions have been considered in detail so far. For a clinically robust application, the spectral signatures of endometriosis must be compared to all structures that may be adjacent along the resection pathway. In addition to the peritoneum, these include the stroma, musculature, fascia, or ligaments.

A neural network of similar architecture was also utilized to classify Raman spectra of COL I from both healthy and fibrotic tissue samples taken from various human organs. However, the classification accuracy was found to be only 72%, with a sensitivity of 64% and a specificity of 72% (Becker and Lu et al., **Appendix III**, Table S1). These insufficient results may be due to variations among individual patients or the limited sample size but could also be a result of intrinsic differences between the various organs. Nonetheless, the application of a neural network-based classification still outperformed a classical linear discriminant analysis, which only achieved an accuracy of 62%, with sensitivities and specificities of 62% and 63%, respectively. An expanded dataset could potentially enhance the classification performance. However, if efforts to improve the classification results prove to be ineffective, it may also suggest that the use of COL I Raman spectra alone may not be adequate for a reliable determination of fibrosis.

Other significant challenges must also be addressed when working towards the clinical application of Raman spectroscopy. One significant obstacle in the case of in vivo application is the presence of background autofluorescence caused by various components, such as collagens and red blood cells, under excitation with light in the visible and near-infrared range. [323,324]. Collagens show strong fluorescent signals originated by the amino acids tyrosine and phenylalanine that are especially accumulated in collagen cross-links [325-327]. In comparison, in blood autofluorescence is originated by hemoglobin. Depending on which excitation wavelength is used for RMS, the resulting fluorescence signals vary. In a surgical application, near-infrared lasers are more suitable because they produce less autofluorescence than lasers in the visible range as fewer molecules absorb in near-infrared region. Furthermore, near-infrared lasers produce less photodamage even at high laser powers, which is especially important for the patient's health [87]. Another advantage of longer wavelength light sources is the increased penetration depth of the light in the tissue, since the scattering scales with $\lambda^{-\alpha}$, where λ describes the wavelength and α ranges between 0.2 and 4 [328,329]. It is precisely this increased penetration depth that provides interesting information, as it can reveal molecular changes even below the visible surface. As a result, RMS could be used to detect underlying diseases without the need to remove tissue and. This is particularly interesting in the case of deep infiltrating diseases such as certain types of cancer or endometriosis [330,331]. However, the major limiting factor of near-infrared lasers is the decrease of Raman intensity with increasing wavenumber resulting in a longer exposure time needed. Compared to a 532 nm laser, the excitation efficiency drops by a factor of 4.7 when using a near-infrared 785 nm excitation source [332]. Potentially, signal enhancing techniques such as CARS or SRS could be applied to solve the occurring limitations. These methods raster a sample at a single wavenumber which drastically increases the speed and contrast of a single scan, however, the information of the whole spectral fingerprint is not accessible anymore. These methods are especially useful in acquiring information of C-C and C-H information relevant in lipids. In diseases where increased lipid droplet formation is observed such as CRC and brain cancer, CARS and SRS could be ideal tools to quickly determine at which sites such abnormalities form [333,334]. In combination of CARS or SRS with SHG images of collagen structures and ML techniques, even H&E like images can be created without the need of the actual staining [335]. If this technique finds its way into an endoscope, intraoperative diagnostic could be revolutionized, as the gold standard procedure including biopsy, fast-freezing, cryo-sectioning, H&E staining, and pathological examination could be performed live.

Chapter 4

Conclusion & Outlook

4 Conclusion & Outlook

This thesis reported the establishment of RMS and FLIM in combination with various ML techniques for the tissue discrimination of fibrotic diseases and assessment of drug efficacy in patient-derived cancer organoids. Together, RMS and FLIM are promising tools for the non-invasive in situ monitoring and characterization of drug responses of patient-derived organoids before the treatment is administered to reduce therapy failure and reduce patients suffering. It was successfully demonstrated that RMS and FLIM allow the discrimination between patient-specific differences in drug response by alterations in their metabolic state after drug treatment. In comparison to standard techniques such as protein expression analyses which are currently used to identify the responsiveness of cells, major advantages of RMS and FLIM are their marker-independence, non-invasiveness, and sensitivity on a molecular level, which allowed a real-time monitoring of both drug uptake and cellular response to treatment. For the proposed methodology to be implemented in everyday clinics, it is necessary to undertake extensive efforts to establish robust protocols for RMS and FLIM measurements. This will require the analysis of many patients, as well as a diverse array of cancer organoids in various stages of development. The initial cohort to be evaluated should include individuals of different ethnicities, as genetic variations and environmental factors may impact the cellular response to drugs [336,337]. Furthermore, to achieve a comprehensive pre-investigation of the efficacy of a drug for a specific patient, it is crucial to also investigate the effects of the drugs on healthy cells. This can be accomplished by treating organoids of healthy cells with the drugs and comparing the results to those obtained from the treatment of cancer cells. Through this approach, it will be possible to design an optimally effective medication plan with minimal side effects. To further consider the potential interactions between different organs, the utilization of organ-on-a-chip and human-on-a-chip models may provide valuable insights. These models mimic the in vivo microenvironment and physiological conditions of human organs and organ systems, allowing for the investigation of drug efficacy and toxicity in a more physiologically relevant context. Furthermore, these models can also be used to simulate complex multiorgan interactions and to analyze the systemic effects of drugs, providing a more comprehensive understanding of drug pharmacokinetics and pharmacodynamics. The integration of these cutting-edge technologies into the proposed methodology could enhance the predictive power and accuracy of drug efficacy and safety assessments, ultimately leading to the optimization of treatment plans for individual patients.

Additionally, the experiments need to be repeated with a biobank of different chemotherapeutics and combinations of two or more drugs to identify the best possible treatment for each patient. To be used routinely, the complexity of RMS and FLIM measurements and analysis needs to be decreased as much as possible. Here, an automatized analysis functionality could allow high-throughput screening and analysis. The required measurement time is another hurdle which could be solved in measurement of Raman spectra and fluorescence lifetimes by bimodal probes [338]. An AI-guided and automized analysis of Raman and FLIM data could then lead to an easy accessibly classification of drug efficacy.

In addition to monitoring cellular changes in organoids during drug treatment, RMS for in situ monitoring and characterization of both cellular and extracellular properties show great potential for identifying diseased tissues. RMS in combination with spectral deconvolution was successfully utilized to identify a biomarker for fibrotic COL I fibers compared to controls in various human tissues and diseases. In comparison to standard techniques such as histopathological staining, major advantages of RMS were the non-invasive and marker-independent approach to identify molecular changes allowing a real-time and in-situ characterization of fibrotic diseases. This biomarker for fibrotic COL I has been successfully used in known fibrotic diseases such as Crohn's disease in the colon or fibrosis developed from liver cirrhosis or even cancer in breast and lymph nodes as well as cardiomyopathies, but also showed differences in diseases where the fibrotic pathology is not yet clarified, such as endometriosis. If confirmed in many other fibrotic diseases and in a large number of patients in a wide range of age groups, the discovered biomarker would be useful in answering a variety of medical questions. The biomarker could not only be used to identify fibrous collagen fibers to assist pathologists in difficult cases but could also be used in drug discovery. Until now, drug treatments have only been suitable for alleviating the unpleasant symptoms of fibrosis in order to improve the quality of life. Recently, however, inhibition of interleukin 11 in idiopathic pulmonary fibrosis with a neutralizing antibody was shown to result in reverse myofibroblast activation with subsequent inhibition of fibrotic development [339]. In combination with 3D in vitro models of fibrotic tissue, the developed Raman biomarker could be used to monitor the direct response of the COL I network to drug treatment.

In addition to the pathological evaluation of tissues based on extracellular structures, it has also been successfully demonstrated that different diseases can be distinguished based on their epigenetic profiles. In accordance with IF staining, PCAs and Raman images of cell nuclei identified 5mC as an epigenetic modification in different tissues. Based on the increased intensity of specific spectral signatures of methylations and cytosine, endometriosis could be distinguished from endometrium and peritoneum. In addition, the same result was observed in various cardiomyopathies of the heart compared with controls. The results provide important evidence that characterization of diseased tissue using epigenetic signatures can be accomplished by RMS. In future research, the identification of 5mC as well as other epigenetic changes in different tissues and diseases could be an important key to improve disease detection. Again, the strength of the RMS resides in the non-invasive and marker-independent methodology for identifying molecular changes. In addition to the identification of DNA methylation, the monitoring of acetylation, another important epigenetic feature, could be an interesting target for further research.

In summary, this work demonstrated that RMS has the potential to identify drug-induced effects at the cellular level, as well as provide a method to distinguish diseased tissue from healthy tissue by fibrotic and epigenetic characteristics. If the results obtained can be confirmed in a large number of independent experiments, RMS could be increasingly used in the future to address medically relevant questions. Potentially, if the development of Raman probes suitable for intraoperative usage allows for an in vivo application in the future, the identified Raman biomarkers for fibrosis and epigenetic modification could also be utilized for a live detection of diseases during operation or directly after resection.

5 References

1. Pradipta, A.; Tomonori, T.; Morimoto, K.; Shimazu, K.; Noguchi, S.; Tanaka, K. Emerging Technologies for Real-Time Intraoperative Margin Assessment in Future Breast-Conserving Surgery. *Advanced Science* **2020**, 1901519, doi:10.1002/advs.201901519.
2. Wang, D.; Ma, D.; Wong, M.L.; Wang, Y.X. Recent advances in surgical planning & navigation for tumor biopsy and resection. *Quantitative Imaging in Medicine and Surgery* **2015**, *5*, doi:10.3978/j.issn.2223-4292.2015.10.03.
3. Becker, L.; Janssen, N.; Layland, S.L.; Mürdter, T.E.; Nies, A.T.; Schenke-Layland, K.; Marzi, J. Raman Imaging and Fluorescence Lifetime Imaging Microscopy for Diagnosis of Cancer State and Metabolic Monitoring. *Cancers* **2021**, *13*, 5682, doi:10.3390/cancers13225682.
4. Patil, A.C.; Bosschaart, N.; Keller, M.D.; Leeuwen, T.G.; Mahadevan-Jansen, A. Combined Raman spectroscopy and optical coherence tomography device for tissue characterization. *Optical Letters* **2008**, *33*, 1135-1137, doi:10.1364/OL.33.001135.
5. Bakker Schut, T.C.; Wolthuis, R.; Caspers, P.J.; Puppels, G.J. Real-time tissue characterization on the basis ofin vivo Raman spectra. *Journal of Raman Spectroscopy* **2002**, *33*, 580-585, doi:10.1002/jrs.852.
6. Doroski, D.M.; Brink, K.S.; Temenoff, J.S. Techniques for biological characterization of tissue-engineered tendon and ligament. *Biomaterials* **2007**, *28*, 187-202, doi:10.1016/j.biomaterials.2006.08.040.
7. Ovalle, W.; Nahirney, P. *Netter's Essential Histology With Correlated Histopathology*; Saunders/Elsevier: 2020; Volume 3.
8. Flores Bueso, Y.; Walker, S.P.; Hogan, G.; Claesson, M.J.; Tangney, M. Protoblock - A biological standard for formalin fixed samples. *Microbiome* **2020**, *8*, doi:10.1186/s40168-020-00901-1.
9. Gaffney, E.; Riegman, P.; Grizzle, W.; Watson, P. Factors that drive the increasing use of FFPE tissue in basic and translational cancer research. *Biotechnic & Histochemistry* **2018**, *93*, 373-386, doi:10.1080/10520295.2018.1446101.
10. Van Beers, E.H.; Joosse, S.A.; Ligtenberg, M.J.; Fles, R.; Hogervorst, F.B.L.; Verhoef, S.; Nederlof, P.M. A multiplex PCR predictor for aCGH success of FFPE samples. *British Journal of Cancer* **2006**, *94*, 333-337, doi:10.1038/sj.bjc.6602889.
11. Blow, N. Tissue issues. *Nature* **2007**, *448*, 959-960, doi:10.1038/448959a.
12. Hawes, D.; Shi, S.-R.; Dabbs, D.J.; Taylor, C.R.; Cote, R.J. *Immunohistochemistry*, 2 ed.; Weidner, N., Cote, R.K., Suster, S., Weiss, L.M., Eds.; Modern Surgical Pathology: 2009; Volume 1.
13. Fischer, A.H.; Jacobson, K.A.; Rose, J.; Zeller, R. Hematoxylin and Eosin Staining of Tissue and Cell Sections. *Cold Spring Harbor Protocols* **2008**, *2008*, pdb.prot4986, doi:10.1101/pdb.prot4986.
14. Dwivedi, S.; Purohit, P.; Misra, R.; Pareek, P.; Goel, A.; Khattri, S.; Pant, K.K.; Misra, S.; Sharma, P. Diseases and Molecular Diagnostics: A Step Closer to Precision Medicine. *Indian Journal of Clinical Biochemistry* **2017**, *32*, 374-398, doi:10.1007/s12291-017-0688-8.
15. Bridge, J.A. The role of cytogenetics and molecular diagnostics in the diagnosis of soft-tissue tumors. *Modern Pathology* **2014**, *27*, S80-S97, doi:10.1038/modpathol.2013.179.

16. Lindstrand, A.; Eisfeldt, J.; Pettersson, M.; Carvalho, C.M.B.; Kvarnung, M.; Grigelioniene, G.; Anderlid, B.-M.; Bjerin, O.; Gustavsson, P.; Hammarsjö, A.; et al. From cytogenetics to cytogenomics: whole-genome sequencing as a first-line test comprehensively captures the diverse spectrum of disease-causing genetic variation underlying intellectual disability. *Genome Medicine* **2019**, *11*, doi:10.1186/s13073-019-0675-1.
17. Madfarlane, D.R.; Forsyth, M. Recent insights on the role of cryoprotective agents in vitrification. *Cryobiology* **1990**, *27*, 345-358, doi:10.1016/0011-2240(90)90014-U.
18. Meryman, H.T. Cryoprotective agents. *Cryobiology* **1971**, *8*, 173-183, doi:10.1016/0011-2240(71)90024-1.
19. Brockbank, K.G. Cryoprotective agent and its use in cryopreservation of cellular matter. 1991.
20. Wilson, L.B. A Method for the Rapid Preparation of Fresh Tissues for the Microscope. *JAMA: The Journal of the American Medical Association* **1905**, *XLV*, 1737, doi:10.1001/jama.1905.52510230037003c.
21. Fuller, B.J. Cryoprotectants: the essential antifreezes to protect life in the frozen state. *Cryo Letters* **2004**, *25*, 375-388.
22. Rivenson, Y.; De Haan, K.; Wallace, W.D.; Ozcan, A. Emerging Advances to Transform Histopathology Using Virtual Staining. *BME Frontiers* **2020**, *2020*, 1-11, doi:10.34133/2020/9647163.
23. Jaafar, H. Intra-Operative Frozen Section Consultation: Concepts, Applications and Limitations. *Malaysian Journal of Medical Sciences* **2006**, *13*, 4-16.
24. Hunt, C.J.; Taylor, M.J.; Pegg, D.E. Freeze-substitution and isothermal freeze-fixation studies to elucidate the pattern of ice formation in smooth muscle at 252 K (-21°C). *Jornal of Microscopy* **1982**, *125*, 177-186, doi:10.1111/j.1365-2818.1982.tb00335.x.
25. Katt, M.E.; L, P.A.; D, W.A.; S, X.Z.; C, S.P. In Vitro Tumor Models: Advantages, Disadvantages, Variables, and Selecting the Right Platform. *Front. Bioeng. Biotechnol* **2016**, *4*, doi:doi.org/10.3389/fbioe.2016.00012.
26. Pauli, C.; Hopkins, B.D.; Prandi, D.; Shaw, R.; Fedrizzi, T.; Sboner, A.; Sailer, V.; Augello, M.; Puca, L.; Rosati, R.; et al. Personalized In Vitro and In Vivo Cancer Models to Guide Precision Medicine. *Cancer Discovery* **2017**, *7*, 462-477, doi:10.1158/2159-8290.cd-16-1154.
27. Cunningham, D.; You, Z. In vitro and in vivo model systems used in prostate cancer research. *Journal of Biological Methods* **2015**, *2*, e17, doi:10.14440/jbm.2015.63.
28. Li, Y.; Tang, P.; Cai, S.; Peng, J.; Hua, G. Organoid based personalized medicine: from bench to bedside. *Cell Regeneration* **2020**, *9*, doi:10.1186/s13619-020-00059-z.
29. Harrison, R. Observations on the living developing nerve fiber. *Advances of Patient-Derived Organoids in Personalized Radiotherapy* **1906**, *4*, 140-143, doi:10.3181/00379727-4-98.
30. Tuli, R.; Tuli, S.; Nandi, S.; Huang, X.; Manner, P.A.; Hozack, W.J.; Danielson, K.G.; Hall, D.J.; Tuan, R.S. Transforming Growth Factor-β-mediated Chondrogenesis of Human Mesenchymal Progenitor Cells Involves N-cadherin and Mitogen-activated Protein Kinase and Wnt Signaling Cross-talk. *Journal of Biological Chemistry* **2003**, *278*, 41227-41236, doi:10.1074/jbc.m305312200.
31. Goodspeed, A.; Heiser, L.M.; Gray, J.W.; Costello, J.C. Tumor-Derived Cell Lines as Molecular Models of Cancer Pharmacogenomics. *Molecular Cancer Research* **2016**, *14*, 3-13, doi:10.1158/1541-7786.mcr-15-0189.

32. Ghanemi, A. Cell cultures in drug development: Applications, challenges and limitations. *Saudi Pharm J* **2015**, *23*, 453-454, doi:10.1016/j.jsps.2014.04.002.
33. Scuderio, D.A.; Shoemaker, R.H.; Paull, K.D.; Monks, A.; Tierney, S.; Nofziger, T.H.; Currens, M.J.; Seniff, D. Evaluation of a soluble tetrazolium/formazan assay for cell growth and drug sensitivity in culture using human and other tumor cell lines. *Cancer Res* **1988**, *48*, 4827-4833.
34. Antoni, D.; Burckel, H.; Josset, E.; Noel, G. Three-Dimensional Cell Culture: A Breakthrough in Vivo. *International Journal of Molecular Sciences* **2015**, *16*, 5517-5527, doi:10.3390/ijms16035517.
35. Lai, Y.; Asthana, A.; Kisaalita, W.A. Biomarkers for simplifying HTS 3D cell culture platforms for drug discovery: the case for cytokines. *Drug Disccovery Today* **2011**, *16*, 293-297, doi:10.1016/j.drudis.2011.01.009.
36. Edmondson, R.; Broglie, J.J.; Adcock, A.F.; Yang, L. Three-Dimensional Cell Culture Systems and Their Applications in Drug Discovery and Cell-Based Biosensors. *ASSAY and Drug Development Technologies* **2014**, *12*, 207-218, doi:10.1089/adt.2014.573.
37. Moscona, A.; Moscona, H. The dissociation and aggregation of cells from organ rudiments of the early chick embryo. *J Anat.* **1952**, *86*, 287-301.
38. Weiss, P.; Taylor, A.C. Reconstitution of Complete Organs froms Single-Cell Suspensions of Chick Embryos in Advanced Stages of Differentiation. *Proceedings of the National Academy of Sciences* **1960**, *46*, 1177-1185, doi:10.1073/pnas.46.9.1177.
39. DeLong, G.R. Histogenesis of fetal mouse isocortex and hippocampus in reaggregating cell cultures. *Dev Biol.* **1970**, *22*, 563-583, doi:10.1016/0012-1606(70)90169-7.
40. Sato, T.; Vries, R.G.; Snippert, H.J.; Van De Wetering, M.; Barker, N.; Stange, D.E.; Van Es, J.H.; Abo, A.; Kujala, P.; Peters, P.J.; et al. Single Lgr5 stem cells build crypt-villus structures in vitro without a mesenchymal niche. *Nature* **2009**, *459*, 262-265, doi:10.1038/nature07935.
41. Lancaster, M.A.; Knoblich, J.A. Organogenesis in a dish: modeling development and disease using organoid technologies. *Science (New York, N.Y.)* **2014**, *345*, doi:10.1126/science.1247125.
42. Lancaster, M.A.; Renner, M.; Martin, C.-A.; Wenzel, D.; Bicknell, L.S.; Hurles, M.E.; Homfray, T.; Penninger, J.M.; Jackson, A.P.; Knoblich, J.A. Cerebral organoids model human brain development and microcephaly. *Nature* **2013**, *501*, 373-379, doi:10.1038/nature12517.
43. Ootani, A.; Li, X.; Sangiorgi, E.; Ho, Q.T.; Ueno, H.; Toda, S.; Sugihara, H.; Fujimoto, K.; Weissman, I.L.; Capecchi, M.R.; et al. Sustained in vitro intestinal epithelial culture within a Wnt-dependent stem cell niche. *Nature Medicine* **2009**, *15*, 701-706, doi:10.1038/nm.1951.
44. Taguchi, A.; Kaku, Y.; Ohmori, T.; Sharmin, S.; Ogawa, M.; Sasaki, H.; Nishinakamura, R. Redefining the In Vivo Origin of Metanephric Nephron Progenitors Enables Generation of Complex Kidney Structures from Pluripotent Stem Cells. *Cell Stem Cell* **2014**, *14*, 53-67, doi:10.1016/j.stem.2013.11.010.
45. Huch, M.; Bonfanti, P.; Boj, S.F.; Sato, T.; Loomans, C.J.M.; Van De Wetering, M.; Sojoodi, M.; Li, V.S.W.; Schuijers, J.; Gracanin, A.; et al. Unlimited in vitro expansion of adult bi-potent pancreas progenitors through the Lgr5/R-spondin axis. *The EMBO Journal* **2013**, *32*, 2708-2721, doi:10.1038/emboj.2013.204.
46. Jagga, Z.; Gupta, D. Machine learning for biomarker identification in cancer research - developments toward its clinical application. *Per Med.* **2015**, *12*, 371-387, doi:10.2217/pme.15.5.

47. Flores, M.; Glusman, G.; Brogaard, K.; Price, N.D.; Hood, L. P4 medicine: how systems medicine will transform the healthcare sector and society. *Personalized Medicine* **2013**, *10*, 565-576, doi:10.2217/pme.13.57.
48. Hood, L.; Friend, S.H. Predictive, personalized, preventive, participatory (P4) cancer medicine. *Nature Reviews Clinical Oncology* **2011**, *8*, 184–187, doi:10.1038/nrclinonc.2010.227.
49. Chwalek, K.; Bray, L.J.; Werner, C. Tissue-engineered 3D tumor angiogenesis models: Potential technologies for anti-cancer drug discovery. *Advanced Drug Delivery Reviews* **2014**, *79-80*, 30-39, doi:10.1016/j.addr.2014.05.006.
50. Fong, E.L.S.; Harrington, D.A.; Farach-Carson, M.C.; Yu, H. Heralding a new paradigm in 3D tumor modeling. *Biomaterials* **2016**, *108*, 197-213, doi:10.1016/j.biomaterials.2016.08.052.
51. Gomez, D.P.; Boudreau, D. Organoids and Their Use in Modeling Gut Epithelial Cell Lineage Differentiation and Barrier Properties During Intestinal Diseases. *Frontiers in Cell and Developmental Biology* **2021**, doi:10.3389/fcell.2021.732137.
52. Tang, X.-Y.; Wu, S.; Wang, D.; Chu, C.; Hong, Y.; Tao, M.; Hu, H.; Xu, M.; Guo, X.; Liu, Y. Human organoids in basic research and clinical applications. *Signal Transduction and Targeted Therapy* **2022**, *7*, doi:10.1038/s41392-022-01024-9.
53. Guan, Y.; Xu, D.; Garfin, P.M.; Ehmer, U.; Hurwitz, M.; Enns, G.; Michie, S.; Wu, M.; Zheng, M.; Nishimura, T.; et al. Human hepatic organoids for the analysis of human genetic diseases. *JCI Insight* **2017**, *2*, doi:10.1172/jci.insight.94954.
54. Shpichka, A.; Bikmulina, P.; Peshkova, M.; Heydari, Z.; Kosheleva, N.; Vosough, M.; Timashev, P. Organoids in modelling infectious diseases. *Drug Discovery Today* **2022**, *27*, 223-233, doi:10.1016/j.drudis.2021.08.005.
55. Xu, H.; Jiao, D.; Liu, A.; Wu, K. Tumor organoids: applications in cancer modeling and potentials in precision medicine. *Journal of Hematology & Oncology* **2022**, *15*, doi:10.1186/s13045-022-01278-4.
56. Ramalho, A.S.; Fürstová, E.; Vonk, A.M.; Ferrante, M.; Verfaillie, C.; Dupont, L.; Boon, M.; Proesmans, M.; Beekman, J.M.; Sarouk, I.; et al. Correction of CFTR function in intestinal organoids to guide treatment of cystic fibrosis. *European Respiratory Journal* **2021**, *57*, 1902426, doi:10.1183/13993003.02426-2019.
57. Botti, G.; Bonito, M.D.; Cantile, M. Organoid biobanks as a new tool for pre-clinical validation of candidate drug efficacy and safety. *Int J Physiol Pathophysiol Pharmacol.* **2021**, *13*, 17-21.
58. Weeber, F.; Van De Wetering, M.; Hoogstraat, M.; Dijkstra, K.K.; Krijgsman, O.; Kuilman, T.; Gadellaa-Van Hooijdonk, C.G.M.; Van Der Velden, D.L.; Peeper, D.S.; Cuppen, E.P.J.G.; et al. Preserved genetic diversity in organoids cultured from biopsies of human colorectal cancer metastases. *Proceedings of the National Academy of Sciences* **2015**, *112*, 13308-13311, doi:10.1073/pnas.1516689112.
59. Zhao, Z.; Chen, X.; Dowbaj, A.M.; Sljukic, A.; Bratlie, K.; Lin, L.; Fong, E.L.S.; Balachander, G.M.; Chen, Z.; Soragni, A.; et al. Organoids. *Nature Reviews Methods Primers* **2022**, *2*, doi:10.1038/s43586-022-00174-y.
60. Boyd, V.; Cholewa, O.M.; Papas, K.K. Limitations in the Use of Fluorescein Diacetate/Propidium Iodide (FDA/PI) and Cell Permeable Nucleic Acid Stains for Viability Measurements of Isolated Islets of Langerhans. *Current trends in biotecnology and pharmacy* **2008**, *2*, 66-84.
61. Mosmann, T. apid colorimetric assay for cellular growth and survival: application to proliferation and cytotoxicity assays. *J Immunol Methods* **1983**, *65*, 55-63, doi:10.1016/0022-1759(83)90303-4. PMID: 6606682.
62. Ahmed, S.A.; Gogal Jr, R.M.; Walsh, J.E. A new rapid and simple non-radioactive assay to monitor and determine the proliferation of lymphocytes: an alternative to

[3H]thymidine incorporation assay. *J Immunol Methods* **1994**, *170*, 211-224, doi:10.1016/0022-1759(94)90396-4.

63. Fan, F.; Wood, K.V. Bioluminescent Assays for High-Throughput Screening. *ASSAY and Drug Development Technologies* **2007**, *5*, doi:10.1089/adt.2006.053.
64. Cox, M.C.; Mendes, R.; Silva, F.; Mendes, T.F.; Zelaya-Lazo, A.; Halwachs, K.; Purkal, J.J.; Isidro, I.A.; Félix, A.; Boghaert, E.R.; et al. Application of LDH assay for therapeutic efficacy evaluation of ex vivo tumor models. *Scientific Reports* **2021**, *11*, doi:10.1038/s41598-021-97894-0.
65. Zhu, J.; Ji, L.; Chen, Y.; Li, H.; Huang, M.; Dai, Z.; Wang, J.; Xiang, D.; Fu, G.; Lei, Z.; et al. Organoids and organs-on-chips: insights into predicting the efficacy of systemic treatment in colorectal cancer. *Cell Death Discovery* **2023**, *9*, doi:10.1038/s41420-023-01354-9.
66. Kim, M.; Mun, H.; Sung, C.O.; Cho, E.J.; Jeon, H.-J.; Chun, S.-M.; Jung, D.J.; Shin, T.H.; Jeong, G.S.; Kim, D.K.; et al. Patient-derived lung cancer organoids as in vitro cancer models for therapeutic screening. *Nature Communications* **2019**, *10*, doi:10.1038/s41467-019-11867-6.
67. Pasch, C.A.; Favreau, P.F.; Yueh, A.E.; Babiarz, C.P.; Gillette, A.A.; Sharick, J.T.; Karim, M.R.; Nickel, K.P.; Dezeeuw, A.K.; Sprackling, C.M.; et al. Patient-Derived Cancer Organoid Cultures to Predict Sensitivity to Chemotherapy and Radiation. *Clinical Cancer Research* **2019**, *25*, 5376-5387, doi:10.1158/1078-0432.ccr-18-3590.
68. Manafi, N.; Shokri, F.; Achberger, K.; Hirayama, M.; Mohammadi, M.H.; Noorizadeh, F.; JHong, J.; Liebau, S.; Tsuji, T.; Quinn, P.M.J.; et al. Organoids and organ chips in ophthalmology. *The Ocular Surface* **2021**, *19*, 1-15, doi:10.1016/j.jtos.2020.11.004.
69. Piña, R.; Santos-Díaz, A.I.; Orta-Salazar, E.; Aguilar-Vazquez, A.R.; Mantellero, C.A.; Acosta-Galeana, I.; Estrada-Mondragon, A.; Prior-Gonzalez, M.; Martinez-Cruz, J.I.; Rosas-Arellano, A. Ten Approaches That Improve Immunostaining: A Review of the Latest Advances for the Optimization of Immunofluorescence. *International Journal of Molecular Sciences* **2022**, *23*, 1426, doi:10.3390/ijms23031426.
70. Xu, S.; Ji, X.; Xu, W.; Li, X.; Wang, L.; Bai, Y.; Zhao, B.; Ozaki, Y. Immunoassay using probe-labelling immunogold nanoparticles with silver staining enhancement via surface-enhanced Raman scattering. *The Analyst* **2004**, *129*, 63, doi:10.1039/b313094k.
71. Schultz, S.; Smith, D.R.; Mock, J.J.; Schultz, D.A. Single-target molecule detection with nonbleaching multicolor optical immunolabels. *Proceedings of the National Academy of Sciences* **2000**, *97*, 996-1001, doi:10.1073/pnas.97.3.996.
72. Hyatt, A.D.; Wise, T.G. *Immunocytochemistry and In Situ Hybridization in the Biomedical Sciences* Beesley, J.E., Ed.; Birkhäuser, Boston, MA: 2001.
73. Becker, L.; Fischer, F.; Fleck, J.L.; Harland, N.; Herkommer, A.; Stenzl, A.; Aicher, W.K.; Schenke-Layland, K.; Marzi, J. Data-Driven Identification of Biomarkers for In Situ Monitoring of Drug Treatment in Bladder Cancer Organoids. *International Journal of Molecular Sciences* **2022**, *23*, 6956, doi:10.3390/ijms23136956.
74. Song, L.; Hennink, E.J.; Young, I.T.; Tanke, H.J. Photobleaching kinetics of fluorescein in quantitative fluorescence microscopy. *CellPress* **1995**, *68*, 2588-2600, doi:10.1016/S0006-3495(95)80442-X.
75. Hirano, M.; Ando, R.; Shimozono, S.; Sugiyama, M.; Takeda, N.; Kurokawa, H.; Deguchi, R.; Endo, K.; Haga, K.; Takai-Todaka, R.; et al. A highly photostable and bright green fluorescent protein. *Nature Biotechnology* **2022**, *40*, 1132-1142, doi:10.1038/s41587-022-01278-2.

76. Ratnavelu, N.D.; Brown, A.P.; Mallett, S.; Scholten, R.J.; Patel, A.; Founta, C.; Galaal, K.; Cross, P.; Naik, R. Intraoperative frozen section analysis for the diagnosis of early stage ovarian cancer in suspicious pelvic masses. *Cochrane Database of Systematic Reviews* **2016**, *2016*, doi:10.1002/14651858.cd010360.pub2.
77. Campbell, J.M.; Habibalahi, A.; Mahbub, S.; Gosnell, M.; Anwer, A.G.; Paton, S.; Gronthos, S.; Goldys, E. Non-destructive, label free identification of cell cycle phase in cancer cells by multispectral microscopy of autofluorescence. *BMC Cancer* **2019**, *19*, doi:10.1186/s12885-019-6463-x.
78. Bisht, P.B. *An Introduction to Photonics and Laser Physics with Applications*; IOP Publishing: 2022.
79. Adrian, F.J. Charge transfer effects in surface-enhanced Raman scattering. *J. Chem. Phys.* **1982**, *5302*, doi:10.1063/1.443800.
80. Parson, W.W. *Raman Scattering and Other Multiphoton Processes*; Springer Berlin Heidelberg: 2007.
81. Maiman, T.H. Stimulated Optical Radiation in Ruby. *Nature* **1960**, *187*, 493-494, doi:10.1038/187493a0.
82. Raman, C.V.; Krishnan, K.S. A New Type of Secondary Radiation. *Nature* **1928**, *121*, 501-502, doi:10.1038/121501c0.
83. Smekal, A. Zur Quantentheorie der Dispersion. *Die Naturwissenschaften* **1923**, *11*, 873-875, doi:10.1007/bf01576902.
84. Smith, E.; Dent, G. *Modern Raman Spectroscopy – A Practical Approach*; John Wiley & Sons, Ltd: 2005.
85. Lippert, J.L.; Peticolas, W.L. Laser Raman Investigation of the Effect of Cholesterol on Conformational Changes in Dipalmitoyl Lecithin Multilayers. *Proceedings of the National Academy of Sciences* **1971**, *68*, 1572-1576, doi:10.1073/pnas.68.7.1572.
86. Yu, N.-T.; Liu, C.D.; O'Shea, D.C. Laser Raman spectroscopy and the conformation of insulin and proinsulin. *Journal of Molecular Biology* **1972**, *70*, 117-132, doi:10.1016/0022-2836(72)90167-2.
87. Smith, R.; Wright, K.L.; Ashton, L. Raman spectroscopy: an evolving technique for live cell studies. *The Analyst* **2016**, *141*, 3590-3600, doi:10.1039/c6an00152a.
88. Galli, R.; Uckermann, O.; Andresen, E.F.; Kirsch, M. Intrinsic Indicator of Photodamage during Label-Free Multiphoton Microscopy of Cells and Tissues. *PLoS ONE* **2014**, *9*, e110295, doi:10.1371/journal.pone.0110295.
89. Ciaffoni, L.; Matousek, P.; Parker, W.; McCormack, E.A.; Mortimer, H. Grating Spectrometry and Spatial Heterodyne Fourier Transform Spectrometry: Comparative Noise Analysis for Raman Measurements. *Applied Spectroscopy* **2021**, *75*, 241-249, doi:10.1177/0003702820957311.
90. Adar, F. Considerations of Grating Selection in Optimizing a Raman Spectrograph. *Spectroscopy* **2013**, *28*.
91. Van Der Meiden, H.J.; Al, R.S.; Barth, C.J.; Donné, A.J.H.; Engeln, R.; Goedheer, W.J.; De Groot, B.; Kleyn, A.W.; Koppers, W.R.; Lopes Cardozo, N.J.; et al. High sensitivity imaging Thomson scattering for low temperature plasma. *Review of Scientific Instruments* **2008**, *79*, 013505, doi:10.1063/1.2832333.
92. Adar, F.; Delhaye, M.; DaSilva, E. Evolution of Instrumentation for Detection of the Raman Effect as Driven by Available Technologies and by Developing Applications. *Journal of Chemical Education* **2007**, *84*, 50, doi:10.1021/ed084p50.
93. Delhaye, M.; Dhamelincourt, P. Raman microprobe and microscope with laser excitation. *Journal of Raman Spectroscopy* **1975**, *3*, 33-43, doi:10.1002/jrs.1250030105.

94. Thuriot-Roukos, J.; Khadraoui, R.; Paul, S.; Wojcieszak, R. Raman Spectroscopy Applied to Monitor Furfural Liquid-Phase Oxidation Catalyzed by Supported Gold Nanoparticles. *ACS Omega* **2020**, *5*, 14283-14290, doi:10.1021/acsomega.0c00091.
95. Bell, S.E.J.; Sirimuthu, N.M.S. Surface-Enhanced Raman Spectroscopy as a Probe of Competitive Binding by Anions to Citrate-Reduced Silver Colloids. *The Journal of Physical Chemistry A* **2005**, *109*, 7405-7410, doi:10.1021/jp052184f.
96. Surmacki, J.M.; Woodhams, B.J.; Haslehurst, A.; Ponder, B.A.J.; Bohndiek, S.E. Raman micro-spectroscopy for accurate identification of primary human bronchial epithelial cells. *Scientific Reports* **2018**, *8*, doi:10.1038/s41598-018-30407-8.
97. Votteler, M.; Carvajal Berrio, D.A.; Pudlas, M.; Walles, H.; Schenke-Layland, K. Non-contact, Label-free Monitoring of Cells and Extracellular Matrix using Raman Spectroscopy. *Journal of Visualized Experiments* **2012**, doi:10.3791/3977.
98. Puppels, G.J.; De Mul, F.F.M.; Otto, C.; Greve, J.; Robert-Nicoud, M.; Arndt-Jovin, D.J.; Jovin, T.M. Studying single living cells and chromosomes by confocal Raman microspectroscopy. *Nature* **1990**, *347*, 301-303, doi:10.1038/347301a0.
99. Puppels, G. Laser irradiation and Raman spectroscopy of single living cells and chromosomes: Sample degradation occurs with 514.5 nm but not with 660 nm laser light. *Experimental Cell Research* **1991**, *195*, 361-367, doi:10.1016/0014-4827(91)90385-8.
100. Frushour, B.G.; Koenig, J.L. Raman scattering of collagen, gelatin, and elastin. *Biopolymers* **1975**, *14*, 379-391, doi:10.1002/bip.1975.360140211.
101. Manoharan, R.; Wang, Y.; Feld, M.S. Histochemical analysis of biological tissues using Raman spectroscopy. *Spectrochimica Acta Part A: Molecular and Biomolecular Spectroscopy* **1996**, *52*, 215-249, doi:10.1016/0584-8539(95)01573-6.
102. Manoharan, R.; Baraga, J.J.; Feld, M.S.; Rava, R.P. Quantitative histochemical analysis of human artery using Raman spectroscopy. *J Photochem Photobiol B* **1992**, *30*, 211-233, doi:10.1016/1011-1344(92)80009-k.
103. Jell, G.; Swain, R.; M, S.M. *Raman Spectroscopy: A Tool for Tissue Engineering*; Springer, Berlin, Heidelberg: 2009.
104. Schenke-Layland, K.; Madershahian, N.; Rieman, I.; Starcher, B.; Halhuber, K.; König, K.; Stock, U.A. Impact of cryopreservation on extracellular matrix structures of heart valve leaflets. *Ann Thorac Surg* **2006**, *81*, 918-926, doi:10.1016/j.athoracsur.2005.09.016.
105. Schenke-Layland, K.; Stock, U.A.; Nsair, A.; Xie, J.; Angelis, E.; Fonseca, C.G.; Larbig, R.; Mahajan, A.; Shivkumar, K.; Fishbein, M.C.; et al. Cardiomyopathy is associated with structural remodelling of heart valve extracellular matrix. *European Heart Journal* **2009**, *30*, 2254-2265, doi:10.1093/eurheartj/ehp267.
106. Votteler, M.; Berrio, D.A.C.; Pudlas, M.; Walles, H.; Stock, U.A.; Schenke-Layland, K. Raman spectroscopy for the non-contact and non-destructive monitoring of collagen damage within tissues. *Journal of Biophotonics* **2011**, *5*, 47-56, doi:10.1002/jbio.201100068.
107. Diem, M.; Mazur, A.; Lenau, K.; Schubert, J.; Bird, B.; Miljković, M.; Krafft, C.; Popp, J. Molecular pathologyviaIR and Raman spectral imaging. *Journal of Biophotonics* **2013**, *6*, 855-886, doi:10.1002/jbio.201300131.
108. Alberda, W.; Verhoef, C.; Schipper, M.; Nuyttens, J.; Rothbarth, J.; de Wilt, J.; Burger, J. The Importance of a Minimal Tumor-Free Resection Margin in Locally Recurrent Rectal Cancer. *Diseases of the colon & rectum* **2015**, *58*, 677-685, doi:10.1097/DCR.0000000000000388.

109. Barroso, E.M.; Smits, R.W.H.; Van Lanschot, C.G.F.; Caspers, P.J.; Ten Hove, I.; Mast, H.; Sewnaik, A.; Hardillo, J.A.; Meeuwis, C.A.; Verdijk, R.; et al. Water Concentration Analysis by Raman Spectroscopy to Determine the Location of the Tumor Border in Oral Cancer Surgery. *Cancer Research* **2016**, *76*, 5945-5953, doi:10.1158/0008-5472.can-16-1227.
110. Zhang, J.; Fan, Y.; He, M.; Ma, X.; Song, Y.; Liu, M.; Xu, J. Accuracy of Raman spectroscopy in differentiating brain tumor from normal brain tissue. *Oncotarget* **2017**, *8*, 36824-36831, doi:10.18632/oncotarget.15975.
111. Bakker Schut, T.C.; Caspers, P.J.; Puppels, G.J.; Nijssen, A.; Heule, F.; Neumann, M.H.A.; Hayes, D.P. Discriminating Basal Cell Carcinoma from its Surrounding Tissue by Raman Spectroscopy. *Journal of Investigative Dermatology* **2002**, *119*, 64-69, doi:10.1046/j.1523-1747.2002.01807.x.
112. Marzullo, A.; Neto, O.P.; Bitar, R.A.; Martinho, H.; Martin, A.A. FT-Raman Spectra of the Border of Infiltrating Ductal Carcinoma Lesions. *Photomedicine and Laser Surgery* **2007**, *25*, doi:10.1089/pho.2007.2094.
113. Wang, J.; Lin, K.; Hu, H.; Qie, X.; Huang, W.E.; Cui, Z.; Gong, Y.; Song, Y. In Vitro Anticancer Drug Sensitivity Sensing through Single-Cell Raman Spectroscopy. *Biosensors* **2021**, *11*, 286, doi:10.3390/bios11080286.
114. Qiu, S.; Li, M.; Liu, J.; Chen, X.; Lin, T.; Xu, Y.; Chen, Y.; Weng, Y.; Pan, Y.; Feng, S.; et al. Study on the chemodrug-induced effect in nasopharyngeal carcinoma cells using laser tweezer Raman spectroscopy. *Biomedical Optics Express* **2020**, *11*, 1819, doi:10.1364/boe.388785.
115. Chai, S.; Sun, X.; Fu, C.; Xu, Q.; Ren, Z.; CXie, L.; Ge, J.; Sang, M. Identification and characterization of the inhibitory effect of ART on colorectal cancer cells using Raman spectroscopy. *Journal of Raman Spectroscopy* **2022**, *53*, 191-201, doi:doi.org/10.1002/jrs.6292.
116. El-Mashtoly, S.F.; Petersen, D.; Yosef, H.K.; Mosig, A.; Reinacher-Schick, A.; Kötting, C.; Gerwert, K. Label-free imaging of drug distribution and metabolism in colon cancer cells by Raman microscopy. *The Analyst* **2014**, *139*, 1155, doi:10.1039/c3an01993d.
117. Aljakouch, K.; Lechtonen, T.; Yosef, H.K.; Hammoud, M.K.; Alsaidi, W.; Kötting, C.; Mügge, C.; Kourist, R.; El-Mashtoly, S.F.; Gerwert, K. Raman Microspectroscopic Evidence for the Metabolism of a Tyrosine Kinase Inhibitor, Neratinib, in Cancer Cells. *Angewandte Chemie International Edition* **2018**, *57*, 7250-7254, doi:10.1002/anie.201803394.
118. Chin, L.; Andersen, J.N.; Futreal, P.A. Cancer genomics: from discovery science to personalized medicine. *Nature Medicine* **2011**, *17*, 297-303, doi:10.1038/nm.2323.
119. Diamandis, M.; White, N.M.A.; Yousef, G.M. Personalized Medicine: Marking a New Epoch in Cancer Patient Management. *Molecular Cancer Research* **2010**, *8*, 1175-1187, doi:10.1158/1541-7786.mcr-10-0264.
120. Evron-Levy, T.; Caspi, M.; Wittenstein, A.; Shorer-Arbel, Y.; Shomron, O.; Hirschberg, K.; Kariv, R.; Rosin-Arbesfeld, R. Adenoma-Derived Organoids for Precision Therapy. *Organoids* **2022**, *1*, 54-68, doi:10.3390/organoids1010006.
121. Ergün, S.; Wörsdörfer, P. Organoids, Assembloids and Embryoids: New Avenues for Developmental Biology, Disease Modeling, Drug Testing and Toxicity Assessment without Animal Experimentation. *Organoids* **2022**, *1*, 37-40, doi:10.3390/organoids1010004.
122. Becker, W.; Bergmann, A.; Hink, M.A.; König, K.; Benndorf, K.; Biskup, C. Fluorescence lifetime imaging by time-correlated single-photon counting. *Microsc Res Tech* **2004**, *63*, 58-66, doi:10.1002/jemt.10421.

123. Berezin, M.Y.; Achilefu, S. Fluorescence Lifetime Measurements and Biological Imaging. *Chemical Reviews* **2010**, *110*, 2641-2684, doi:10.1021/cr900343z.
124. Sarder, P.; Maji, D.; Achilefu, S. Molecular Probes for Fluorescence Lifetime Imaging. *Bioconjugate Chemistry* **2015**, *26*, 963-974, doi:10.1021/acs.bioconjchem.5b00167.
125. Benninger, R.K.P.; Koç, Y.; Hofmann, O.; Requejo-Isidro, J.; Neil, M.A.A.; French, P.M.W.; Demello, A.J. Quantitative 3D Mapping of Fluidic Temperatures within Microchannel Networks Using Fluorescence Lifetime Imaging. *Analytical Chemistry* **2006**, *78*, 2272-2278, doi:10.1021/ac051990f.
126. Kuimova, M.K. Mapping viscosity in cells using molecular rotors. *Physical Chemistry Chemical Physics* **2012**, *14*, 12671-12686, doi:10.1039/C2CP41674C.
127. Hille, C.; Berg, M.; Bressel, L.; Munzke, D.; Primus, P.; Löhmannsröben, H.-G.; Dosche, C. Time-domain fluorescence lifetime imaging for intracellular pH sensing in living tissues. *Analytical and Bioanalytical Chemistry* **2008**, *391*, 1871-1879, doi:10.1007/s00216-008-2147-0.
128. Jabłoński, A. Über den Mechanismus der Photolumineszenz von Farbstoffphosphoren. *Zeitschrift für Physik* **1935**, *94*, 38-46, doi:10.1007/bf01330795.
129. Periasamy, A.; Wodnicki, P.; Wang, X.F.; Kwon, S.; Gordon, G.; Herman, B. Time-resolved fluorescence lifetime imaging microscopy using a picosecond pulsed tunable dye laser system. *Review of Scientific Instruments* **1996**, *67*, doi:10.1063/1.1147139.
130. Gadella Jr, T.W.J.; Clegg, R.M.; Jovin, T.M. Fluorescence lifetime imaging microscopy: Pixel-by-pixel analysis of phase-modulation data. *Bioimaging* **1994**, *2*, 139-159, doi:10.1002/1361-6374(199409)2:3<139::AID-BIO4>3.0.CO;2-T.
131. Gratton, E. Fluorescence lifetime imaging for the two-photon microscope: time-domain and frequency-domain methods. *Journal of Biomedical Optics* **2003**, *8*, 381, doi:10.1117/1.1586704.
132. Chaudhry, R.; Varacallo, M. *Biochemistry, Glycolysis*; StatPearls Publishing LLC: 2022.
133. Chandel, N.S. Glycolysis. *Cold Spring Harb Perspect. Biol.* **2021**, *13*, doi:10.1101/cshperspect.a040535.
134. McCommis, K.S.; Finck, B.N. Mitochondrial pyruvate transport: a historical perspective and future research directions. *Biochemical Journal* **2015**, *466*, 443-454, doi:10.1042/bj20141171.
135. Gray, L.R.; Tompkins, S.C.; Taylor, E.B. Regulation of pyruvate metabolism and human disease. *Cellular and Molecular Life Sciences* **2014**, *71*, 2577-2604, doi:10.1007/s00018-013-1539-2.
136. Gasmi, A.; Peana, M.; Arshad, M.; Butnariu, M.; Menzel, A.; Bjørklund, G. Krebs cycle: activators, inhibitors and their roles in the modulation of carcinogenesis. *Archives of Toxicology* **2021**, *95*, 1161-1178, doi:10.1007/s00204-021-02974-9.
137. Akram, M. Citric Acid Cycle and Role of its Intermediates in Metabolism. *Cell Biochemistry and Biophysics* **2014**, *68*, 475-478, doi:10.1007/s12013-013-9750-1.
138. Martínez-Reyes, I.; Chandel, N.S. Mitochondrial TCA cycle metabolites control physiology and disease. *Nature Communications* **2020**, *11*, doi:10.1038/s41467-019-13668-3.
139. Wilson, D.F. Oxidative phosphorylation: regulation and role in cellular and tissue metabolism. *The Journal of Physiology* **2017**, *595*, 7023-7038, doi:10.1113/jp273839.

140. Nolfi-Donegan, D.; Braganza, A.; SHiva, S. Mitochondrial electron transport chain: Oxidative phosphorylation, oxidant production, and methods of measurement. *Redox Biology* **2020**, *37*, doi:10.1016/j.redox.2020.101674.
141. Zheng, J. Energy metabolism of cancer: Glycolysis versus oxidative phosphorylation (Review). *Oncology Letters* **2012**, *4*, 1151-1157, doi:10.3892/ol.2012.928.
142. Chance, B.; Schoener, B.; Oshino, R.; Itshak, F.; Nakase, Y. Oxidation-reduction ratio studies of mitochondria in freeze-trapped samples. NADH and flavoprotein fluorescence signals. *J Biol Chem* **1979**, *254*, 4764-4771.
143. Ghukasyan, V.V.; Kao, F. Monitoring Cellular Metabolism with Fluorescence Lifetime of Reduced Nicotinamide Adenine Dinucleotide. *ACS Publications* **2009**, *113*, 11532–11540, doi:10.1021/jp810931u.
144. Heikal, A.A. Intracellular coenzymes as natural biomarkers for metabolic activities and mitochondrial anomalies. *Biomarkers in Medicine* **2010**, *4*, 241-263, doi:10.2217/bmm.10.1.
145. Chen, L.; Zhang, Z.; Hoshino, A.; Zheng, H.D.; Morley, M.; Arany, Z.; Rabinowitz, J.D. NADPH production by the oxidative pentose-phosphate pathway supports folate metabolism. *Nature Metabolism* **2019**, *1*, 404-415, doi:10.1038/s42255-019-0043-x.
146. Jiang, P.; Du, W.; Wu, M. Regulation of the pentose phosphate pathway in cancer. *Protein & Cell* **2014**, *5*, 592-602, doi:10.1007/s13238-014-0082-8.
147. Lakowicz, J.R.; Szmacinski, H.; Nowaczyk, K.; Johnson, M.L. Fluorescence lifetime imaging of free and protein-bound NADH. *Proceedings of the National Academy of Sciences* **1992**, *89*, 1271-1275, doi:10.1073/pnas.89.4.1271.
148. Warburg, O.; Wind, F.; Negelein, E. The Metabolism of Tumors in the Body. *Journal of General Physiology* **1927**, *8*, 519-530, doi:10.1085/jgp.8.6.519.
149. Awasthi, K.; Moriya, D.; Nakabayashi, T.; Li, L.; Ohta, N. Sensitive detection of intracellular environment of normal and cancer cells by autofluorescence lifetime imaging. *Journal of Photochemistry and Photobiology B: Biology* **2016**, *165*, 256-265, doi:10.1016/j.jphotobiol.2016.10.023.
150. Salmon, J.M.; Kohen, E.; Viallet, P.; Hirschberg, J.G.; Wouters, A.W.; Kohen, C.; Thorell, B. Microspectrofluorometric approach to the study of free/bound NAD(P)H ratio as metabolic indicator in various cell types. *Photochem Photobiol* **1982**, *36*, 583-593, doi:10.1111/j.1751-1097.1982.tb04420.x.
151. Clegg, R.M.; Holub, O.; Gholke, C. Fluorescence lifetime-resolved imaging: Measuring lifetimes in an image. *Methods in Enzymology* **2003**, *360*, 509-549, doi:10.1016/S0076-6879(03)60126-6.
152. Schneckenburger, H.; Koenig, K. Fluorescence decay Kinetics and imaging of NAD(P)H and flavins as metabolic indicators. *Proceedings of SPIE - The International Society for Optical Engineering* **1992**, *31*, 1447-1451, doi:10.1117/12.57704.
153. Cong, A.; Pimenta, R.M.L.; Lee, H.B.; Mereddy, V.; Holy, J.; Heikal, A.A. Two-photon fluorescence lifetime imaging of intrinsic NADH in three-dimensional tumor models. *Cytometry Part A* **2019**, *95*, 80-92, doi:10.1002/cyto.a.23632.
154. Shirshin, E.A.; Shirmanova, M.V.; Gayer, A.V.; Lukina, M.M.; Nikonova, E.E.; Yakimov, B.P.; Budylin, G.S.; Dudenkova, V.V.; Ignatova, N.I.; Komarov, D.V.; et al. Label-free sensing of cells with fluorescence lifetime imaging: The quest for metabolic heterogeneity. *Proceedings of the National Academy of Sciences* **2022**, *119*, e2118241119, doi:10.1073/pnas.2118241119.

155. Alam, S.R.; Wallrabe, H.; Christopher, K.G.; Siller, K.H.; Periasamy, A. Characterization of mitochondrial dysfunction due to laser damage by 2-photon FLIM microscopy. *Scientific Reports* **2022**, *12*, doi:10.1038/s41598-022-15639-z.
156. Romero, G.; Qiu, Y.; Murray, R.A.; Moya, S.E. Study of Intracellular Delivery of Doxorubicin from Poly(lactide-co -glycolide) Nanoparticles by Means of Fluorescence Lifetime Imaging and Confocal Raman Microscopy. *Macromolecular Bioscience* **2013**, *13*, 234-241, doi:10.1002/mabi.201200235.
157. Saari, J.; Rautaniemi, K.; Rojalin, T.; Niemi, L.; Nivaro, O.; Laaksonen, T.; Yliperttula, M.; Vuorimaa-Laukkanen, E. FLIM reveals alternative EV-mediated cellular up-take pathways of paclitaxel. *Jornal of Controlled Release* **2018**, *284*, 133-143, doi:10.1016/j.jconrel.2018.06.015.
158. Group, B.D.w. Biomarkers and surrogate endpoints: preferred definitions and conceptual framework. *Clin Pharmacol Ther* **2001**, *69*, 89-95, doi:10.1067/mcp.2001.113989.
159. WHO International Programme on Chemical Safety Biomarkers and Risk Assessment: Concepts and Principles. Available online: http://www.inchem.org/documents/ehc/ehc/ehc155.htm. (accessed on 09.15.2022).
160. Strimbu, K.; Tavel, J.A. What are biomarkers? *Current Opinion in HIV and AIDS* **2010**, *5*, 463-466, doi:10.1097/coh.0b013e32833ed177.
161. Lou, E.; HJohnson, M.; Sima, C.; onzales-Espinoza, R.; Fleisher, M.; Kris, M.G.; Azzoli, C.G. Serum biomarkers for assessing histology and outcomes in patients with metastatic lung cancer. *Cancer Biomark.* **2014**, *14*, 207-214, doi:10.3233/CBM-140399.
162. Long, J.; Yang, Z.; Wang, L.; Han, Y.; Peng, C.; Yan, C.; Yan, D. Metabolite biomarkers of type 2 diabetes mellitus and pre-diabetes: a systematic review and meta-analysis. *BMC Endocrine Disorders* **2020**, *20*, doi:10.1186/s12902-020-00653-x.
163. Broders, A.C. The grading of carcinoma. *Minn. Med.* **1925**, *8*, 726-730.
164. Shelley, H.S.; Auerbach, S.H.; Classen, K.L. Carcinoma of the Prostate A New System of classification. *AMA Arch Surg.* **1958**, *77*, 751-756, doi:10.1001/archsurg.1958.01290040099012.
165. Desai, M.; Stockbridge, N.; Temple, R. Blood pressure as an example of a biomarker that functions as a surrogate. *The AAPS Journal* **2006**, *8*, E146-E152, doi:10.1208/aapsj080117.
166. Surowiec, R.K.; Ram, S.; Kenneth, M. In Vivo Quantitative Imaging Biomarkers of Bone Quality and Mineral Density using Multi-Band-SWIFT Magnetic Resonance Imaging. *Bone* **2021**, doi:10.1016/j.bone.2020.115615.
167. Bennet, M.R.; Devarajan, P. *Biomarkers of Kidney Disease. Characteristics of an Ideal Biomarker of Kidney Diseases*; Elsevier Inc.: 2011.
168. Gurcan, M.N.; Boucheron, L.E.; Can, A.; Madabhushi, A.; Rajpoot, N.M.; Yener, B. Histopathological Image Analysis: A Review. *IEEE Reviews in Biomedical Engineering* **2009**, *2*, 147-171, doi:10.1109/rbme.2009.2034865.
169. Haas, D.; Shebl, O.; Shamiyeh, A.; Oppelt, P. The rASRM score and the Enzian classification for endometriosis: their strengths and weaknesses. *Acta Obstetricia et Gynecologica Scandinavica* **2013**, *92*, 3-7, doi:10.1111/aogs.12026.
170. Barentsz, J.O.; Weinreb, J.C.; Verma, S.; Thoeny, H.C.; Tempany, C.M.; Shtern, F.; Padhani, A.R.; Margolis, D.; Macura, K.J.; Haider, M.A.; et al. Synopsis of the PI-RADS v2 Guidelines for Multiparametric Prostate Magnetic Resonance Imaging and Recommendations for Use. *European Urology* **2016**, *69*, 41-49, doi:10.1016/j.eururo.2015.08.038.

171. Angulo, P.; Hui, J.M.; Marchesini, G.; Bugianesi, E.; George, J.; Farrell, G.C.; Enders, F.; Saksena, S.; Burt, A.D.; Bida, J.P.; et al. The NAFLD fibrosis score: A noninvasive system that identifies liver fibrosis in patients with NAFLD. *Hepatology* **2007**, *45*, 846-854, doi:10.1002/hep.21496.
172. Bulten, W.; Pinckaers, H.; Van Boven, H.; Vink, R.; De Bel, T.; Van Ginneken, B.; Van Der Laak, J.; Hulsbergen-Van De Kaa, C.; Litjens, G. Automated deep-learning system for Gleason grading of prostate cancer using biopsies: a diagnostic study. *The Lancet Oncology* **2020**, *21*, 233-241, doi:10.1016/s1470-2045(19)30739-9.
173. Elmore, J.G.; Barnhill, R.L.; Elder, D.E.; Longton, G.M.; Pepe, M.S.; Reisch, L.M.; Carney, P.A.; Titus, L.J.; Nelson, H.D.; Onega, T.; et al. Pathologists’ diagnosis of invasive melanoma and melanocytic proliferations: observer accuracy and reproducibility study. *BMJ* **2017**, j2813, doi:10.1136/bmj.j2813.
174. Speight, P.M.; Abram, T.J.; Floriano, P.N.; James, R.; Vick, J.; Thornhill, M.H.; Murdoch, C.; Freeman, C.; Hegarty, A.M.; D'Apice, K.; et al. Interobserver agreement in dysplasia grading: toward an enhanced gold standard for clinical pathology trials. *Oral Surgery, Oral Medicine, Oral Pathology and Oral Radiology* **2015**, *120*, 474-482.e472, doi:10.1016/j.oooo.2015.05.023.
175. Desouza, N.M.; Achten, E.; Alberich-Bayarri, A.; Bamberg, F.; Boellaard, R.; Clément, O.; Fournier, L.; Gallagher, F.; Golay, X.; Heussel, C.P.; et al. Validated imaging biomarkers as decision-making tools in clinical trials and routine practice: current status and recommendations from the EIBALL* subcommittee of the European Society of Radiology (ESR). *Insights into Imaging* **2019**, *10*, doi:10.1186/s13244-019-0764-0.
176. Van Der Laak, J.; Litjens, G.; Ciompi, F. Deep learning in histopathology: the path to the clinic. *Nature Medicine* **2021**, *27*, 775-784, doi:10.1038/s41591-021-01343-4.
177. Waldstein, S.M.; Seeböck, P.; Donner, R.; Sadeghipour, A.; Bogunović, H.; Osborne, A.; Schmidt-Erfurth, U. Unbiased identification of novel subclinical imaging biomarkers using unsupervised deep learning. *Scientific Reports* **2020**, *10*, doi:10.1038/s41598-020-69814-1.
178. Mjolsness, E.; Decoste, D. Machine Learning for Science: State of the Art and Future Prospects. *Science* **2001**, *293*, 2051-2055, doi:10.1126/science.293.5537.2051.
179. Uher, J. Functions of units, scales and quantitative data: Fundamental differences in numerical traceability between sciences. *Quality & Quantity* **2021**, doi:10.1007/s11135-021-01215-6.
180. Zitnik, M.; Nguyen, F.; Leskovec, J.; Goldenberg, A.; Hoffman, M.M. Machine learning for integrating data in biology and medicine: Principles, practice, and opportunities. *Information FUsion* **2019**, *50*, 71-91, doi:10.1016/j.inffus.2018.09.012.
181. Arjmand, B.; Hamidpour, S.K.; Tayanloo-Beik, A.; Goodarzi, P.; Aghayan, H.R.; Adibi, H.; Larijani, B. Machine Learning: A New Prospect in Multi-Omics Data Analysis of Cancer. *Front. Genet.* **2022**, *13*, doi:10.3389/fgene.2022.824451
182. Staziaki, P.V.; Wu, D.; Rayan, J.C.; Santo, I.D.D.O.; Nan, F.; Maybury, A.; Gangasani, N.; Benador, I.; Saligrama, V.; Scalera, J.; et al. Machine learning combining CT findings and clinical parameters improves prediction of length of stay and ICU admission in torso trauma. *European Radiology* **2021**, *31*, 5434-5441, doi:10.1007/s00330-020-07534-w.
183. Willemink, M.J.; Koszek, W.A.; Hardell, C.; Wu, J.; Fleischmann, D.; Harvey, H.; Folio, L.R.; Summers, R.M.; Rubin, D.L.; Lungren, M.P. Preparing Medical

Imaging Data for Machine Learning. *Radiology* **2020**, *295*, 4-15, doi:10.1148/radiol.2020192224.

184. Rácz, A.; Bajusz, D.; Héberger, K. Effect of Dataset Size and Train/Test Split Ratios in QSAR/QSPR Multiclass Classification. *Molecules* **2021**, *26*, 1111, doi:10.3390/molecules26041111.
185. Dobbin, K.K.; Simon, R.M. Optimally splitting cases for training and testing high dimensional classifiers. *BMC Medical Genomics* **2011**, *4*, 31, doi:10.1186/1755-8794-4-31.
186. Raschka, S. Model Evaluation, Model Selection, and Algorithm Selection in Machine Learning. *arXiv* **2018**, doi:10.48550/ARXIV.1811.12808.
187. Jolliffe, I.T. *Principal Component Analysis*; Springer Series in Statistics: 2002.
188. Jolliffe, I.T.; Cadima, J. Principal component analysis: a review and recent developments. *Philosophical Transactions of the Royal Society A: Mathematical, Physical and Engineering Sciences* **2016**, *374*, 20150202, doi:10.1098/rsta.2015.0202.
189. Martinez, A.M.; Kak, A. PCA versus LDA. *EEE Transactions on Pattern Analysis and Machine Intelligence* **2001**, *23*, 228-233, doi:10.1109/34.908974.
190. Nothinger, I.; Hench, L.L. Raman microspectroscopy: a noninvasive tool for studies of individual living cells in vitro. *Expert Rev Med Devices* **2006**, *3*, 215-234, doi:10.1586/17434440.3.2.215.
191. Li, M.; Boardman, D.G.; Ward, A.; Huang, W.E. Single-Cell Raman Sorting. Humana Press: 2014; pp. 147-153.
192. Nothinger, I.; Selvakumaran, J.; Hench, L.L. New detection system for toxic agents based on continuous spectroscopic monitoring of living cells. *Biosens Bioelectron* **2004**, *20*, 780-789, doi:10.1016/j.bios.2004.04.008.
193. Zoladek, A.; Pascut, F.C.; Patelm, P.; Nothinger, I. Non-invasive time-course imaging of apoptotic cells by confocal Raman micro-spectroscopy. *Journal of Raman Spectroscopy* **2011**, *42*, 251-258, doi:10.1002/jrs.2707.
194. Hira, M.T.; Razzaque, M.A.; Angione, C.; Scrivens, J.; Sawan, S.; Sarker, M. Integrated multi-omics analysis of ovarian cancer using variational autoencoders. *Scientific Reports* **2021**, *11*, doi:10.1038/s41598-021-85285-4.
195. Chowdary, M.V.P.; Kalyan Kumar, K.; Mathew, S.; Rao, L.; Krishna, C.M.; Kurien, J. Biochemical correlation of Raman spectra of normal, benign and malignant breast tissues: A spectral deconvolution study. *Biopolymers* **2009**, *91*, 539-546, doi:10.1002/bip.21171.
196. Lange, C.; Abubakar, I.; Alffenaar, J.W.C.; Bothamley, G.; Caminero, J.A.; Carvalho, A.C.C.; Chang, K.C.; Codecasa, L.; Correia, A.; Crudu, V.; et al. Management of patients with multidrug-resistant/extensively drug-resistant tuberculosis in Europe: a TBNET consensus statement. *European Respiratory Journal* **2014**, *44*, 23-63, doi:10.1183/09031936.00188313.
197. Ray, S.; Das, S.; Suar, M. Molecular Mechanism of Drug Resistance. Springer International Publishing: 2017; pp. 47-110.
198. Saha, M.; Sarkar, A. Review on Multiple Facets of Drug Resistance: A Rising Challenge in the 21st Century. *Journal of Xenobiotics* **2021**, *11*, 197-214, doi:10.3390/jox11040013.
199. Roden, D.M.; Wilke, R.A.; Kroemer, H.K.; Stein, C.M. Pharmacogenomics. *Circulation* **2011**, *123*, 1661-1670, doi:10.1161/circulationaha.109.914820.
200. Niederberger, E.; Parnham, M.J. The Impact of Diet and Exercise on Drug Responses. *International Journal of Molecular Sciences* **2021**, *22*, 7692, doi:10.3390/ijms22147692.

201. Abbott, R.D.; Kaplan, D.L. Strategies for improving the physiological relevance of human engineered tissues. *Trends in Biotechnology* **2015**, *33*, 401-407, doi:10.1016/j.tibtech.2015.04.003.
202. Zhou, Z.; Cong, L.; Cong, X. Patient-Derived Organoids in Precision Medicine: Drug Screening, Organoid-on-a-Chip and Living Organoid Biobank. *Front. Oncol.* **2021**, *11*, doi:10.3389/fonc.2021.762184.
203. Kim, J.; Koo, B.-K.; Knoblich, J.A. Human organoids: model systems for human biology and medicine. *Nature Reviews Molecular Cell Biology* **2020**, *21*, 571-584, doi:10.1038/s41580-020-0259-3.
204. Saglam-Metiner, P.; Gulce-Iz, S.; Biray-Avci, C. Bioengineering-inspired three-dimensional culture systems: Organoids to create tumor microenvironment. *Genes* **2019**, *686*, 203-212, doi:10.1016/j.gene.2018.11.058.
205. Marusyk, A.; Polyak, K. Tumor heterogeneity: Causes and consequences. *Biochimica et Biophysica Acta (BBA) - Reviews on Cancer* **2010**, *1805*, 105-117, doi:10.1016/j.bbcan.2009.11.002.
206. Junttila, M.R.; De Sauvage, F.J. Influence of tumour micro-environment heterogeneity on therapeutic response. *Nature* **2013**, *501*, 346-354, doi:10.1038/nature12626.
207. Gong, X.; Lin, C.; Cheng, J.; Su, J.; Zhao, H.; Liu, T.; Wen, X.; Zhao, P. Generation of Multicellular Tumor Spheroids with Microwell-Based Agarose Scaffolds for Drug Testing. *PLOS ONE* **2015**, *10*, e0130348, doi:10.1371/journal.pone.0130348.
208. Gupta, R.K.; Kuznicki, J. Biological and Medical Importance of Cellular Heterogeneity Deciphered by Single-Cell RNA Sequencing. *Cells* **2020**, *9*, 1751, doi:10.3390/cells9081751.
209. Smith, B.A.; Smith, B.D. Biomarkers and Molecular Probes for Cell Death Imaging and Targeted Therapeutics. *Bioconjugate Chemistry* **2012**, *23*, 1989-2006, doi:10.1021/bc3003309.
210. Li, K.; Wu, D.; Chen, X.; Zhang, T.; Zhang, L.; Yi, Y.; Miao, Z.; Jin, N.; Bi, X.; Wang, H.; et al. Current and Emerging Biomarkers of Cell Death in Human Disease. *BioMed Research International* **2014**, *2014*, 1-10, doi:10.1155/2014/690103.
211. Marbeuf-Gueye, C.; Ettori, D.; Priebe, W.; Kozlowski, H.; Garnier-Suillerot, A. Correlation between the kinetics of anthracycline uptake and the resistance factor in cancer cells expressing the multidrug resistance protein or the P-glycoprotein. *Biochimica et Biophysica Acta (BBA) - Molecular Cell Research* **1999**, *1450*, 374-384, doi:10.1016/S0167-4889(99)00060-9.
212. Zisowsky, J.; Koegel, S.; Leyers, S.; Devarakonda, K.; Kassack, M.U.; Osmak, M.; Jaehde, U. Relevance of drug uptake and efflux for cisplatin sensitivity of tumor cells. *Biochemical Pharmacology* **2007**, *73*, 298-307, doi:10.1016/j.bcp.2006.10.003.
213. Namisaki, T.; SCheaeffeler, E.; Fukui, H.; Yoshiji, H.; Najima, Y.; Fritz, P.; Schwab, M.; Nies, A.T. Differential Expression of Drug Uptake and Efflux Transporters in Japanese Patients with Hepatocellular Carcinoma. *Drug Metabolism and Disposition* **2014**, *42*, 2033-2040, doi:10.1124/dmd.114.059832.
214. Gottesman, M.M.; Lavi, O.; Hall, M.D.; Gillet, J. Toward a Better Understanding of the Complexity of Cancer Drug Resistance. *Annu Rev Pharmacol Toxicol* **2016**, *56*, 85-102, doi:10.1146/annurev-pharmtox-010715-103111.
215. Reustle, A.; Fisel, P.; Renner, O.; Büttner, F.; Winter, S.; Rausch, S.; Kruck, S.; Nies, A.T.; Hennenlotter, J.; Scharpf, M.; et al. Characterization of the breast

cancer resistance protein (BCRP/ABCG2) in clear cell renal cell carcinoma. *International Journal of Cancer* **2018**, *143*, 3181-3193, doi:10.1002/ijc.31741.

216. Naumann, D. Infrared and NIR Raman spectroscopy in medical microbiology. *Proceedings SPIE* **1998**, *3257*, 245-257, doi:10.1117/12.306089.
217. Krafft, C.; Sobottka, S.B.; Schackert, G.; Salzer, R. Raman and infrared spectroscopic mapping of human primary intracranial tumors: a comparative study. *Journal of Raman Spectroscopy* **2006**, *37*, 367-375, doi:10.1002/jrs.1450.
218. Fischer, F.; Birk, A.; Frenner, K.; Herkommer, A. FeaSel-Net: A Recursive Feature Selection Callback in Neural Networks. *TechRxiv.* **2022**, doi:10.36227/techrxiv.19803520.
219. Maker, P.; Terhune, R. Study of optical effects due to an induced polarization third order in the electric field strength. *Physical Review* **1965**, *137*, A801.
220. Prince, R.C.; Frontiera, R.R.; Potma, E.O. Stimulated Raman Scattering: From Bulk to Nano. *Chemical Reviews* **2017**, *117*, 5070-5094, doi:10.1021/acs.chemrev.6b00545.
221. Lockwood, S.F.; O'Malley, S.; Mosher, G.L. Improved Aqueous Solubility of Crystalline Astaxanthin (3,3′-dihydroxy-β, β-carotene-4,4′-dione) by Captisol® (Sulfobutyl Ether β-Cyclodextrin). *Journal of Pharmaceutical Sciences* **2003**, *92*, 922-926, doi:10.1002/jps.10359.
222. Abbe, E. Beiträge zur Theorie des Mikroskops und der mikroskopischen Wahrnehmung. *Archiv für Mikroskopische Anatomie* **1873**, *9*, 413-468, doi:10.1007/bf02956173.
223. Robb, R.; Kuo, J.; Liu, Y.; Corrales-Guerrero, S.; Cui, T.; Hegazi, A.; Nagy, G.; Lee, R.J.; Williams, T.M. A novel protein-drug conjugate, SSH20,demonstrates significant efficacy in caveolin-1-expressing tumors. *Molecular Therapy: Oncolytics* **2021**, *22*, doi:10.1016/j.omto.2021.07.013.
224. De Man, F.M.; Goey, A.K.L.; Van Schaik, R.H.N.; Mathijssen, R.H.J.; Bins, S. Individualization of Irinotecan Treatment: A Review of Pharmacokinetics, Pharmacodynamics, and Pharmacogenetics. *Clinical Pharmacokinetics* **2018**, *57*, 1229-1254, doi:10.1007/s40262-018-0644-7.
225. Bencomo-Alvarez, A.E.; Rubio, A.J.; Gonzalez, M.A.; Eiring, A.M. Energy metabolism and drug response in myeloid leukaemic stem cells. *British Journal of Haematology* **2019**, *186*, 524-537, doi:10.1111/bjh.16074.
226. Schardt, J.; Roth, B.; Seiler, R. Forty years of cisplatin-based chemotherapy in muscle-invasive bladder cancer: are we understanding how, who and when? *World Journal of Urology* **2019**, *37*, 1759-1765, doi:10.1007/s00345-018-2544-8.
227. Mandhan, N.; Yassine, F.; Li, K.; Badar, T. Bladder Myeloid Sarcoma with TP53 mutated Myelodysplastic Syndrome/Myeloproliferative Neoplasm Overlap syndrome: Response to Decitabine-Venetoclax regimen. *Leukemia Research Reports* **2022**, *17*, doi:10.1016/j.lrr.2021.100286.
228. Bower, A.J.; Sorrells, J.E.; Li, J.; Marjanovic, M.; Barkalifa, R.; Boppart, S.A. Tracking metabolic dynamics of apoptosis with high-speed two-photon fluorescence lifetime imaging microscopy. *Biomedical Optics Express* **2019**, *10*, 6408, doi:10.1364/boe.10.006408.
229. Puzio-Kuter, A.M. The Role of p53 in Metabolic Regulation. *Genes & Cancer* **2011**, *2*, 385-391, doi:10.1177/1947601911409738.
230. Zbinden, A.; Carvajal Berrio, D.A.; Urbanczyk, M.; Layland, S.L.; Bosch, M.; Fliri, S.; Lu, C.E.; Jeyagaran, A.; Loskill, P.; Duffy, G.P.; et al. Fluorescence lifetime metabolic mapping of hypoxia-induced damage in pancreatic pseudo-islets. *Journal of Biophotonics* **2020**, *13*, doi:10.1002/jbio.202000375.

231. Bower, A.J.; Marjanovic, M.; Zhao, Y.; Li, J.; Chaney, E.J.; Boppart, S.A. Label-freein vivocellular-level detection and imaging of apoptosis. *Journal of Biophotonics* **2017**, *10*, 143-150, doi:10.1002/jbio.201600003.
232. Marullo, R.; Werner, E.; Degtyareva, N.; Moore, B.; Altavilla, G.; Ramalingam, S.S.; Doetsch, P.W. Cisplatin Induces a Mitochondrial-ROS Response That Contributes to Cytotoxicity Depending on Mitochondrial Redox Status and Bioenergetic Functions. *PLoS ONE* **2013**, *8*, e81162, doi:10.1371/journal.pone.0081162.
233. Reiners Jr, J.J.; Caruso, J.A.; Mathieu, P.; Chelladurai, B.; Yin, X.M.; Kessel, D. Release of cytochrome c and activation of pro-caspase-9 following lysosomal photodamage involves bid cleavage. *Cell Death & Differentiation* **2002**, *9*, 934-944, doi:10.1038/sj.cdd.4401048.
234. Bose, P.; Gandhi, V.; Konopleva, M. Pathways and mechanisms of venetoclax resistance. *Leukemia & Lymphoma* **2017**, *58*, 2026-2039, doi:10.1080/10428194.2017.1283032.
235. Hofer, M.; Lutolf, M.P. Engineering organoids. *Nature Reviews Materials* **2021**, *6*, 402-420, doi:10.1038/s41578-021-00279-y.
236. Zhong, L.; Li, Y.; Xiong, L.; Wang, W.; Wu, M.; Yuan, T.; Yang, W.; Tian, C.; Miao, Z.; Wang, T.; et al. Small molecules in targeted cancer therapy: advances, challenges, and future perspectives. *Signal Transduction and Targeted Therapy* **2021**, *6*, doi:10.1038/s41392-021-00572-w.
237. Kciuk, M.; Marciniak, B.; Kontek, R. Irinotecan—Still an Important Player in Cancer Chemotherapy: A Comprehensive Overview. *International Journal of Molecular Sciences* **2020**, *21*, 4919, doi:10.3390/ijms21144919.
238. Voigt, W.; Matsui, S.; Yin, M.B.; Burhans, W.C.; Minderman, H.; Rustum, Y.M. Topoisomerase-I inhibitor SN-38 can induce DNA damage and chromosomal aberrations independent from DNA synthesis. *Anticancer Res.* **1998**, *18*, 3499-9505.
239. Cheng, C.; Kussie, P.; Pavletich, N.; Shuman, S. Conservation of Structure and Mechanism between Eukaryotic Topoisomerase I and Site-Specific Recombinases. *Cell* **1998**, *92*, 841-850, doi:10.1016/s0092-8674(00)81411-7.
240. Hsiang, Y.H.; Lihou, M.G.; Liu, L.F. Arrest of replication forks by drug-stabilized topoisomerase I-DNA cleavable complexes as a mechanism of cell killing by camptothecin. **1989**, *49*, 5077-5082.
241. Sun, X.-F.; Ferreud, L.; Svanvik, J.; Holmlund, B.; Wallin, Å. Anticancer effect of SN-38 on colon cancer cell lines with different metastatic potential. *Oncology Reports* **2008**, doi:10.3892/or.19.6.1493.
242. Maurya, D.K.; Ayuzawa, R.; Doi, C.; Troyer, D.; Tamura, M. Topoisomerase I inhibitor SN-38 effectively attenuates growth of human non-small cell lung cancer cell lines in vitro and in vivo. *Journal of Environmental Pathology, Toxicology and Oncology* **2011**, *30*, 1-10, doi:10.1615/jenvironpatholtoxicoloncol.v30.i1.10.
243. Arnoult, D.; Parone, P.; Martinou, J.-C.; Antonsson, B.; Estaquier, J.R.M.; Ameisen, J.C. Mitochondrial release of apoptosis-inducing factor occurs downstream of cytochrome c release in response to several proapoptotic stimuli. *Journal of Cell Biology* **2002**, *159*, 923-929, doi:10.1083/jcb.200207071.
244. Jin, P.; Jiang, J.; Zhou, L.; Huang, Z.; Nice, E.C.; Huang, C.; Fu, L. Mitochondrial adaptation in cancer drug resistance: prevalence, mechanisms, and management. *Journal of Hematology & Oncology* **2022**, *15*, doi:10.1186/s13045-022-01313-4.

245. Ingber, D.E. Human organs-on-chips for disease modelling, drug development and personalized medicine. *Nature Reviews Genetics* **2022**, *23*, 467-491, doi:10.1038/s41576-022-00466-9.
246. Pearson, K. On lines and planes of closest fit to systems of points in space. *The London, Edinburgh, and Dublin Philosophical Magazine and Journal of Science* **1901**, *2*, 559-572, doi:10.1080/14786440109462720.
247. Kourti, T.; MacGregor, J.F. Process analysis, monitoring and diagnosis, using multivariate projection methods. *Chemometrics and Intelligent Laboratory Systems* **1995**, *28*, 3-21, doi:10.1016/0169-7439(95)80036-9.
248. Luo, R.; Popp, J.; Bocklitz, T. Deep Learning for Raman Spectroscopy: A Review. *Analytica* **2022**, *3*, 287-301, doi:10.3390/analytica3030020.
249. Gibb, A.A.; Lazaropoulos, M.P.; Elrod, J.W. Myofibroblasts and Fibrosis. *Circulation Research* **2020**, *127*, 427-447, doi:10.1161/circresaha.120.316958.
250. Hinz, B.; Phan, S.H.; Thannickal, V.J.; Galli, A.; Bochaton-Piallat, M.-L.; Gabbiani, G. The Myofibroblast. *The American Journal of Pathology* **2007**, *170*, 1807-1816, doi:10.2353/ajpath.2007.070112.
251. Wang, J., Zohar, R; McCulloch, C.A. Multiple roles of alpha-smooth muscle actin in mechanotransduction. *Exp Cell Res* **2006**, *321*, 205-214, doi:10.1016/j.yexcr.2005.11.004.
252. Wynn, T. Cellular and molecular mechanisms of fibrosis. *The Journal of Pathology* **2008**, *214*, 199-210, doi:10.1002/path.2277.
253. Meng, X.; Nikolic-Paterson, D.J.; Lan, H.Y. TGF-β: the master regulator of fibrosis. *Nature Reviews Nephrology volume* **2016**, *12*, 325-338, doi:10.1038/nrneph.2016.48.
254. Chandler, C.; Liu, T.; Buckanovich, R.; Coffman, L.G. The double edge sword of fibrosis in cancer. *Transl Res* **2019**, *209*, 55-67, doi:10.1016/j.trsl.2019.02.006.
255. Fogo, A.B.; Alpers, C.E. Navigating the challenges of fibrosis assessment: land in sight? *J Am Soc Nephrol* **2011**, *22*, 11-13, doi:10.1681/asn.2010111132.
256. Farhoodi, R.; Lansdell, B.J.; Kording, K.P. Quantifying How Staining Methods Bias Measurements of Neuron Morphologies. *Front Neuroinform* **2019**, *13*, 36, doi:10.3389/fninf.2019.00036.
257. Jensen, E.C. Quantitative Analysis of HistologicalStaining and Fluorescence UsingImageJ. *The Anatomical Record* **2ß13**, *296*, 378-381, doi:10.1002/ar.22641.
258. Ratziu, V.; Charlotte, F.; Heurtier, A.; Gombert, S.; Giral, P.; Bruckert, E.; Grimaldi, A.; Capron, F.; Poynard, T. Sampling Variability of Liver Biopsy in Nonalcoholic Fatty Liver Disease. *Gastroenterology* **2005**, *128*, 1898-1906, doi:10.1053/j.gastro.2005.03.084.
259. Ooi, G.J.; Clouston, A.; Johari, Y.; Kemp, W.W.; Roberts, S.K.; Brown, W.A.; Burton, P.R. Evaluation of the histological variability of core and wedge biopsies in nonalcoholic fatty liver disease in bariatric surgical patients. *Surgical Endoscopy* **2021**, *35*, 1210-1218, doi:10.1007/s00464-020-07490-y.
260. Soon, G.; Wee, A. Updates in the quantitative assessment of liver fibrosis for nonalcoholic fatty liver disease: Histological perspective. *Clinical and Molecular Hepatology* **2021**, *27*, 44-57, doi:10.3350/cmh.2020.0181.
261. Woessner, A.E.; McGee, J.D.; Jones, J.D.; Quinn, K.P. Characterizing differences in the collagen fiber organization of skin wounds using quantitative polarized light imaging. *Wound Repair Regen* **2019**, *27*, 711-714, doi:10.1111/wrr.12758.
262. Drifka, C.R.; Loeffler, A.G.; Mathewson, K.; Mehta, G.; Keikhosravi, A.; Liu, Y.; Lemancik, S.; Ricke, W.A.; Weber, S.M.; Kao, W.J.; et al. Comparison of Picrosirius Red Staining With Second Harmonic Generation Imaging for the Quantification of Clinically Relevant Collagen Fiber Features in Histopathology

Samples. *Journal of Histochemistry & Cytochemistry* **2016**, *64*, 519-529, doi:10.1369/0022155416659249.

263. Abraham, E.T.; Oecal, S.; Mörgelin, M.; Schmid, P.W.N.; Buchner, J.; Baumann, U.; Gebauer, J.M. Collagen's primary structure determines collagen:HSP47 complex stoichiometry. *J Biol Chem* **2021**, *297*, 101169, doi:10.1016/j.jbc.2021.101169.
264. Padrez, Y.; Golubewa, L.; Kulahava, T.; Vladimirskaja, T.; Semenkova, G.; Adzerikho, I.; Yatsevich, O.; Amaegberi, N.; Karpicz, R.; Svirko, Y.; et al. Quantitative and qualitative analysis of pulmonary arterial hypertension fibrosis using wide-field second harmonic generation microscopy. *Scientific Reports* **2022**, *12*, 7330, doi:10.1038/s41598-022-11473-5.
265. Ricard-Blum, S. The Collagen Family. *Cold Spring Harbor Perspectives in Biology* **2011**, *3*, a004978-a004978, doi:10.1101/cshperspect.a004978.
266. Miller, E.; Gay, S. Collagen: an overview. *Methods Enzymol.* **1982**, *82*, 3-23, doi:10.1016/0076-6879(82)82058-2.
267. Bella, J.; Eaton, M.; Brodsky, B.; Berman, H.M. Crystal and molecular structure of a collagen-like peptide at 1.9 A resolution. *Science* **1994**, *266*, 75-81, doi:10.1126/science.7695699.
268. Kramer, R.Z.; Bella, J.; Mayville, P.; Brodsky, B.; Berman, H.M. Sequence dependent conformational variations of collagen triple-helical structure. *Nat Struct Biol* **1999**, *6*, 454-457, doi:10.1038/8259.
269. Widmer, C.; Gebauer, J.M.; Brunstein, E.; Rosenbaum, S.; Zaucke, F.; Drögemüller, C.; Leeb, T.; Baumann, U. Molecular basis for the action of the collagen-specific chaperone Hsp47/SERPINH1 and its structure-specific client recognition. *Proceedings of the National Academy of Sciences* **2012**, *109*, 13243-13247, doi:10.1073/pnas.1208072109.
270. Abraham, E.T.; Oecal, S.; Mörgelin, M.; Schmid, P.W.N.; Buchner, J.; Baumann, U.; Gebauer, J.M. Collagen’s primary structure determines collagen:HSP47 complex stoichiometry. *Journal of Biological Chemistry* **2021**, *297*, 101169, doi:10.1016/j.jbc.2021.101169.
271. Razzaque, M.; Hossain, M.; Kohno, S.; Taguchi, T. Bleomycin-induced pulmonary fibrosis in rat is associated with increased expression of collagen-binding heat shock protein (HSP) 47. *Virchows Arch.* **1998**, *432*, 455-460, doi:10.1007/s004280050191.
272. Razzaque, M.; Nazneen, A.; Taguchi, T. Immunolocalization of collagen and collagen-binding heat shock protein 47 in fibrotic lung diseases. *Mod. Pathol.* **1998**, *11*, 1183-1188.
273. Bellaye, P.S.; Burgy, O.; Bonniaud, P.; Kolb, M. HSP47: a potential target for fibrotic diseases and implications for therapy. *Expert Opin Ther Targets* **2021**, *25*, 49-62, doi:10.1080/14728222.2021.1861249.
274. Wen, Z.Q. Raman spectroscopy of protein pharmaceuticals. *J Pharm Sci* **2007**, *96*, 2861-2878, doi:10.1002/jps.20895.
275. Belbachir, K.; Noreen, R.; Gouspillou, G.; Petibois, C. Collagen types analysis and differentiation by FTIR spectroscopy. *Anal Bioanal Chem* **2009**, *395*, 829-837, doi:10.1007/s00216-009-3019-y.
276. Ye, H.; Rahul; Kruger, U.; Wang, T.; Shi, S.; Norfleet, J.; De, S. Burn-related Collagen Conformational Changes in ex vivo Porcine Skin using Raman Spectroscopy. *Scientific Reports* **2019**, *9*, 19138, doi:10.1038/s41598-019-55012-1.
277. Becker, L.; Lu, C.E.; Montes-Mojarro, I.A.; Layland, S.L.; Khalil, S.; Nsair, A.; Duffy, G.P.; Fend, F.; Marzi, J.; Schenke-Layland, K. Raman Microspectroscopy

Identifies Fibrotic Tissues in Collagen-Related Disorders Via Deconvoluted Collagen Type I Spectra. *Acta Biomater.* **2023**, doi:10.1016/j.actbio.2023.03.016.

278. Gullekson, C.; Lucas, L.; Hewitt, K.; Kreplak, L. Surface-sensitive Raman spectroscopy of collagen I fibrils. *Biophys J* **2011**, *100*, 1837-1845, doi:10.1016/j.bpj.2011.02.026.
279. Jyothi Lakshmi, R.; Kartha, V.B.; Murali Krishna, C.; JG, R.S.; Ullas, G.; Uma Devi, P. Tissue Raman spectroscopy for the study of radiation damage: brain irradiation of mice. *Radiat Res* **2002**, *157*, 175-182, doi:10.1667/0033-7587(2002)157[0175:trsfts]2.0.co;2.
280. Taguchi, T.; Nazneen, A.; Al-Shihri, A.A.; Turkistani, K.A.; Razzaque, M.S. Heat shock protein 47: a novel biomarker of phenotypically altered collagen-producing cells. *Acta Histochem Cytochem* **2011**, *44*, 35-41, doi:10.1267/ahc.11001.
281. Foti, P.V.; Farina, R.; Palmucci, S.; Vizzini, I.A.A.; Libertini, N.; Coronella, M.; Spadola, S.; Caltabiano, R.; Iraci, M.; Basile, A.; et al. Endometriosis: clinical features, MR imaging findings and pathologic correlation. *Insights into Imaging* **2018**, *9*, 149-172, doi:10.1007/s13244-017-0591-0.
282. Herceg, Z.; Hainaut, P. Genetic and epigenetic alterations as biomarkers for cancer detection, diagnosis and prognosis. *Molecular Oncology* **2007**, *1*, 26-41, doi:10.1016/j.molonc.2007.01.004.
283. Ogino, S.; Lochhead, P.; Chan, A.T.; Nishihara, R.; Cho, E.; Wolpin, B.M.; Meyerhardt, J.A.; Meissner, A.; Schernhammer, E.S.; Fuchs, C.S.; et al. Molecular pathological epidemiology of epigenetics: emerging integrative science to analyze environment, host, and disease. *Modern Pathology* **2013**, *26*, 465-484, doi:10.1038/modpathol.2012.214.
284. Stoll, S.; Wang, C.; Qiu, H. DNA Methylation and Histone Modification in Hypertension. *International Journal of Molecular Sciences* **2018**, *19*, 1174, doi:10.3390/ijms19041174.
285. Rodenhiser, D. Epigenetics and human disease: translating basic biology into clinical applications. *Canadian Medical Association Journal* **2006**, *174*, 341-348, doi:10.1503/cmaj.050774.
286. Blair, L.P.; Yan, Q. Epigenetic Mechanisms in Commonly Occurring Cancers. *DNA and Cell Biology* **2012**, *31*, S-49-S-61, doi:10.1089/dna.2012.1654.
287. Kazazian, J., H H. Mobile elements: drivers of genome evolution. *Science* **2004**, *303*, 1626-1632, doi:10.1126/science.1089670.
288. Narayan, A.; Ji, W.; Zhang, X.-Y.; Marrogi, A.; Graff, J.R.; Baylin, S.B.; Ehrlich, M. Hypomethylation of pericentromeric DNA in breast adenocarcinomas. *International Journal of Cancer* **1998**, *77*, 833-838, doi:10.1002/(sici)1097-0215(19980911)77:6<833::aid-ijc6>3.0.co;2-v.
289. Gaudet, F.; Hodgson, J.G.; Eden, A.; Jackson-Grusby, L.; Dausman, J.; Gray, J.W.; Leonhardt, H.; Jaenisch, R. Induction of tumors in mice by genomic hypomethylation. *Science* **2003**, *300*, 489-492, doi:10.1126/science.1083558.
290. Garinis, G.A.; Patrinos, G.P.; Spanakis, N.E.; Menounos, P.G. DNA hypermethylation: when tumour suppressor genes go silent. *Human Genetics* **2002**, *111*, 115-127, doi:10.1007/s00439-002-0783-6.
291. Ohm, J.E.; McGarvey, K.M.; Yu, X.; Cheng, L.; Schuebel, K.E.; Cope, L.; Mohammad, H.P.; Chen, W.; Daniel, V.C.; Yu, W.; et al. A stem cell–like chromatin pattern may predispose tumor suppressor genes to DNA hypermethylation and heritable silencing. *Nature Genetics* **2007**, *39*, 237-242, doi:10.1038/ng1972.

292. Lopez-Serra, P.; Esteller, M. DNA methylation-associated silencing of tumor-suppressor microRNAs in cancer. *Oncogene* **2012**, *31*, 1609-1622, doi:10.1038/onc.2011.354.
293. Corbin, L.J.; White, S.J.; Taylor, A.E.; Williams, C.M.; Taylor, K.; Van Den Bosch, M.T.; Teasdale, J.E.; Jones, M.; Bond, M.; Harper, M.T.; et al. Epigenetic Regulation of Associates With Myocardial Infarction and Platelet Function. *Circulation Research* **2022**, *130*, 384-400, doi:10.1161/circresaha.121.318836.
294. Terada, C.I.; Onoue, K.; Fujii, T.; Itami, H.; Morita, K.; Uchiyama, T.; Takeda, M.; Nakagawa, H.; Nakano, T.; Baba, Y.; et al. Histopathological and epigenetic changes in myocardium associated with cancer therapy-related cardiac dysfunction. *ESC Heart Failure* **2022**, doi:10.1002/ehf2.14034.
295. Guo, S. Epigenetics of endometriosis. *Mol Hum Reprod.* **2009**, *15*, 587-607, doi:10.1093/molehr/gap064.
296. Breiling, A.; Lyko, F. Epigenetic regulatory functions of DNA modifications: 5-methylcytosine and beyond. *Epigenetics & Chromatin* **2015**, *8*, doi:10.1186/s13072-015-0016-6.
297. Robertson, K.D. DNA methylation and chromatin – unraveling the tangled web. *Oncogene* **2002**, *21*, 5361-5379, doi:10.1038/sj.onc.1205609.
298. Goll, M.G.; Bestor, T.H. Eukaryotic cytosine methyltransferases. *Annu Rev Biochem* **2005**, *74*, 481-514, doi:10.1146/annurev.biochem.74.010904.153721.
299. Bestor, T.H.; Laudano, A.; Mattaliano, R.; Ingram, V. Cloning and sequencing of a cDNA encoding DNA methyltransferase of mouse cells. The carboxyl-terminal domain of the mammalian enzymes is related to bacterial restriction methyltransferases. *J Mol Biol.* **1988**, *203*, 971-983, doi:10.1016/0022-2836(88)90122-2.
300. Meaburn, E.; Schulz, R. Next generation sequencing in epigenetics: insights and challenges. *Semin Cell Dev Biol.* **2012**, *23*, 192-199, doi:10.1016/j.semcdb.2011.10.010.
301. Schumacher, A.; Kapraniv, P.; Petronis, A. Microarray-based DNA methylation profiling: technology and applications. *Nucleic Acids Research* **2006**, *34*, 528-542, doi:10.1093/nar/gkj461.
302. Daum, R.; Brauchle, E.M.; Berrio, D.A.C.; Jurkowski, T.P.; Schenke-Layland, K. Non-invasive detection of DNA methylation states in carcinoma and pluripotent stem cells using Raman microspectroscopy and imaging. *Scientific Reports* **2019**, *9*, doi:10.1038/s41598-019-43520-z.
303. Chan, J.W.; Taylor, D.S.; Zwerdling, T.; Lane, S.M.; Ihara, K.; Huser, T. Micro-Raman Spectroscopy Detects Individual Neoplastic and Normal Hematopoietic Cells. *Biophysical Journal* **2006**, *90*, 648-656, doi:10.1529/biophysj.105.066761.
304. Mansy, S.; Engstrom, S.K.; Petricolas, W.L. Laser Raman identification of an interaction site on DNA for arginine containing histones in chromatin. *Biochemical and Biophysical Research Communications* **1976**, *68*, 1242-1247, doi:10.1016/0006-291X(76)90330-2.
305. Ó Faoláin, E.; Hunter, M.B.; Byrne, J.M.; Kelehan, P.; McNamara, M.; Byrne, H.J.; Lyng, F.M. A study examining the effects of tissue processing on human tissue sections using vibrational spectroscopy. *Vibrational Spectroscopy* **2005**, *38*, 121-127, doi:10.1016/j.vibspec.2005.02.013.
306. Jambhekar, A.; Dhall, A.; Shi, Y. Roles and regulation of histone methylation in animal development. *Nature Reviews Molecular Cell Biology* **2019**, *20*, 625-641, doi:10.1038/s41580-019-0151-1.
307. Ruiz-Chica, A.J.; Medina, M.A.; Sánchez-Jiménez, F.; Ramírez, F.J. Characterization by Raman spectroscopy of conformational changes on guanine–

cytosine and adenine–thymine oligonucleotides induced by aminooxy analogues of spermidine. *Journal of Raman Spectroscopy* **2004**, *35*, 93-100, doi:10.1002/jrs.1107.

308. Stone, N., Kendall, C., Smith, J., Crow, P., Barr, H. Raman spectroscopy for identification of epithelial cancers. *Faraday Discussions* **2004**, *126*, 141-157, doi:org/10.1039/B304992B.
309. Frank, C.J.; McCreery, R.L.; Redd, D.C. Raman spectroscopy of normal and diseased human breast tissues. *Anal Chem.* **1995**, *67*, 777-783, doi:10.1021/ac00101a001.
310. Nak-Han, J. The Coordination Chemistry of DNA Nucleosides on Gold Nanoparticles as a Probe by SERS. *Bulletin of the Korean Chemical Society* **2002**, *23*, 17900-11800, doi:10.5012/bkcs.2002.23.12.1790.
311. Ferrero, S.; Vellone, V.G.; Barra, F. Pathophysiology of pain in patients with peritoneal endometriosis. *Annals of Translational Medicine* **2019**, *7*, S8-S8, doi:10.21037/atm.2019.01.36.
312. Barcena-Varela, M.; Paish, H.; Alvarez, L.; Uriarte, I.; Latasa, M.U.; Santamaria, E.; Recalde, M.; Garate, M.; Claveria, A.; Colyn, L.; et al. Epigenetic mechanisms and metabolic reprogramming in fibrogenesis: dual targeting of G9a and DNMT1 for the inhibition of liver fibrosis. *Gut* **2020**, gutjnl-2019-2320, doi:10.1136/gutjnl-2019-320205.
313. She, Q.; Shi, P.; Xu, S.-S.; Xuan, H.-Y.; Tao, H.; Shi, K.-H.; Yang, Y. DNMT1 Methylation of LncRNA GAS5 Leads to Cardiac Fibroblast Pyroptosis via Affecting NLRP3 Axis. *Inflammation* **2020**, *43*, 1065-1076, doi:10.1007/s10753-020-01191-3.
314. O'Reilly, S. Epigenetics in fibrosis. *Molecular Aspects of Medicine* **2017**, *54*, 89-102, doi:10.1016/j.mam.2016.10.001.
315. Egger, G.; Liang, G.; Aparicio, A.; Jones, P.A. Epigenetics in human disease and prospects for epigenetic therapy. *Nature* **2004**, *429*, 457-463, doi:10.1038/nature02625.
316. Hu, B.; Gharaee-Kermani, M.; Wu, Z.; Phan, S.H. Epigenetic Regulation of Myofibroblast Differentiation by DNA Methylation. *The American Journal of Pathology* **2010**, *177*, 21-28, doi:10.2353/ajpath.2010.090999.
317. Cisneros, J.; Hagood, J.; Checa, M.; Ortiz-Quintero, B.; Negreros, M.; Herrera, I.; Ramos, C.; Pardo, A.; Selman, M. Hypermethylation-mediated silencing of p14(ARF) in fibroblasts from idiopathic pulmonary fibrosis. *Am J Physiol Lung Cell Mol Physiol.* **2012**, *303*, L295-303, doi:10.1152/ajplung.00332.2011.
318. Felisbino, M.B.; McKinsey, T.A. Epigenetics in Cardiac Fibrosis. *JACC: Basic to Translational Science* **2018**, *3*, 704-715, doi:10.1016/j.jacbts.2018.05.003.
319. Eberhardt, K.; Stiebing, C.; Matthäus, C.; Schmitt, M.; Popp, J. Advantages and limitations of Raman spectroscopy for molecular diagnostics: an update. *Expert Review of Molecular Diagnostics* **2015**, *15*, 773-787, doi:10.1586/14737159.2015.1036744.
320. Wäschle, R.M.; Hinz, J.; Bleeker, F.; Sliwa, B.; Popov, A.S., C E; Bauer, M. *Mythos OP-Minute Leitfaden zur Kalkulation von DRG-Erlösen pro Op-Minute*; Springer Medizin: 2016; Volume 2.
321. Frantz, C.; Stewart, K.M.; Weaver, V.M. The extracellular matrix at a glance. *Journal of Cell Science* **2010**, *123*, 4195-4200, doi:10.1242/jcs.023820.
322. Bonnans, C.; Chou, J.; Werb, Z. Remodelling the extracellular matrix in development and disease. *Nature Reviews Molecular Cell Biology* **2014**, *15*, 786-801, doi:10.1038/nrm3904.

323. Karpishin, T. Reducing Tissue Autofluorescence. *BioTechniques* **2018**, *64*, 131, doi:10.2144/btn-2017-0117.
324. Cao, A.; Pandya, A.K.; Serhatkulu, G.K.; Weber, R.E.; Dai, H.; Thakur, J.S.; Naik, V.M.; Naik, R.; Auner, G.W.; Rabah, R.; et al. A robust method for automated background subtraction of tissue fluorescence. *Journal of Raman Spectroscopy* **2007**, *38*, 1199-1205, doi:10.1002/jrs.1753.
325. Muir, R.; Forbes, S.; Birch, D.J.S.; Vyshemirsky, V.; Rolinski, O.J. Collagen Glycation Detected by Its Intrinsic Fluorescence. *The Journal of Physical Chemistry B* **2021**, *125*, 11058-11066, doi:10.1021/acs.jpcb.1c05001.
326. Nguyen, T.T.; Gobinet, C.; Feru, J.; Pasco, S.B.; Manfait, M.; Piot, O. Characterization of Type I and IV Collagens by Raman Microspectroscopy: Identification of Spectral Markers of the Dermo-Epidermal Junction. *Spectroscopy: An International Journal* **2012**, *27*, 421-427, doi:10.1155/2012/686183.
327. Teale, F.W.J.; Weber, G. Ultraviolet fluorescence of the aromatic amino acids. *Biochemical Journal* **1957**, *65*, 476-482, doi:10.1042/bj0650476.
328. Jacques, S.L. Optical properties of biological tissues: a review. *Phys Med Biol.* **2013**, *58*, R37-61, doi:10.1088/0031-9155/58/11/R37.
329. Hong, G.; Antaris, A.L.; Dai, h. Near-infrared fluorophores for biomedical imaging. *Nature biomedical engineering* **2017**, *1*, doi:10.1038/s41551-016-0010.
330. Li, B.; Wang, Y.; Wang, Y.; Li, S.; Liu, K. Deep Infiltrating Endometriosis Malignant Invasion of Cervical Wall and Rectal Wall With Lynch Syndrome： A Rare Case Report and Review of Literature. *Front. Oncol.* **2022**, *12*, doi:10.3389/fonc.2022.832228.
331. Hegde, P.; Roy, S.; Shetty, U. Tumor Infiltration Depth as a Prognostic Parameter for Nodal Metastasis in Oral Squamous Cell Carcinoma. *International Journal of Applied and Basic Medical Research* **2017**, *7*, 252-257, doi:10.4103/ijabmr.IJABMR_66_17.
332. Zhou, P.; Tek, W. Choosing the most suitable laser wavelength for your Raman application. **2015**, *1*, 1-6.
333. Guerenne-Del Ben, T.; Couderc, V.; Duponchel, L.; Sol, V.; Leproux, P.; Petit, J.-M. Multiplex coherent anti-Stokes Raman scattering microspectroscopy detection of lipid droplets in cancer cells expressing TrkB. *Scientific Reports* **2020**, *10*, doi:10.1038/s41598-020-74021-z.
334. Uckermann, O.; Galli, R.; Tamosaityte, S.; Leipnitz, E.; Geiger, K.D.; Schackert, G.; Koch, E.; Steiner, G.; Kirsch, M. Label-Free Delineation of Brain Tumors by Coherent Anti-Stokes Raman Scattering Microscopy in an Orthotopic Mouse Model and Human Glioblastoma. *PLoS ONE* **2014**, *9*, e107115, doi:10.1371/journal.pone.0107115.
335. Petersen, D.; Mavarani, L.; Niedieker, D.; Freier, E.; Tannapfel, A.; Kötting, C.; Gerwert, K.; El-Mashtoly, S.F. Virtual staining of colon cancer tissue by label-free Raman micro-spectroscopy†. *Analyst* **2017**, *142*, 1207-1215, doi:10.1039/C6AN02072K.
336. Eliason, E. Ethnicity and adverse drug reactions. *BMJ* **2006**, *332*, 1163-1164, doi:10.1136/bmj.332.7551.1163.
337. Fraser, H.S.; Tibbits, R.C. Variation in response to drugs: Part II. Environmental and nutritional variables. *West Indian Med J.* **1983**, *32*, 66-74.
338. Dochow, S.; Fatakdawala, H.; Phipps, J.E.; Ma, D.; Bocklitz, T.; Schmitt, M.; Bishop, J.W.; Margulies, K.B.; Marcu, L.; Popp, J. Comparing Raman and fluorescence lifetime spectroscopy from human atherosclerotic lesions using a bimodal probe. *Journal of Biophotonics* **2016**, *9*, 958-966, doi:10.1002/jbio.201500341.

339. Ng, B.; Dong, J.; D’Agostino, G.; Viswanathan, S.; Widjaja, A.A.; Lim, W.-W.; Ko, N.S.J.; Tan, J.; Chothani, S.P.; Huang, B.; et al. Interleukin-11 is a therapeutic target in idiopathic pulmonary fibrosis. *Science Translational Medicine* **2019**, *11*, eaaw1237, doi:10.1126/scitranslmed.aaw1237.

Acknowledgements

An dieser Stelle möchte ich mich ganz besonders bei meiner Doktormutter Prof. Dr. Katja Schenke-Layland für die fachliche und menschliche Unterstützung, die Aufnahme in ihrer Arbeitsgruppe, sowie die fortwährende Motivation insbesondere bei der Anfertigung der Publikationen bedanken. Ich hätte mir keine bessere Betreuung vorstellen können!

Bei Prof. Dr.-Ing Cristina Tarin möchte ich mich ganz herzlich bedanken für ihre Unterstützung als zweite Berichterstatterin. Außerdem möchte ich mich bei Prof. Dr. Alois Herkommer sowie bei Prof. Dr. med. Sara Y. Brucker für die anregenden Diskussionen im Graduiertenkolleg bedanken.

Ich danke Prof. Dr. med. Falko Fend, Dr. med. Yvonne Aidee Montes Mojarro und Dr. Ali Nsair für die hervorragende und ausdauernde Zusammenarbeit bei der Vervollständigung der Fibrose Studie und insbesondere bei Ihrer Hilfe zur histologischen Begutachtung und der Bereitstellung der Gewebeschnitte.

Ein weiterer Dank gilt Prof. Dr. Wilhelm Aicher und Dr. med. Niklas Harland für die Bereitstellung der Blasenkrebsorganoide, sowie Prof. Dr. med. Matthias Schwab, Prof. Dr. Anne Nies, Dr. Thomas Mürdter und Dr. Nicole Janssen für die Bereitstellung der Darmkrebsorganoide sowie den zahlreichen Diskussionen in unseren Meetings.

Ebenfalls möchte ich Jun. Prof. Dr. med. Martin Weiß für die ausdauernde Bereitstellung der Endometrium und Endometriose Gewebe danken.

Ein großer Dank geht ebenfalls an Dr. Eva-Maria Brauchle und Dr. Julia Marzi für die Betreuung meiner Doktorarbeit und ihrer ständigen Diskussions- und Hilfsbereitschaft und dem Korrekturlesen der Abstracts, Poster und Publikationen. Hier gilt ebenfalls ein großer Dank Shannon Lee Layland für die Unterstützung beim Korrekturlesen der Publikationen.

Daniel Carvajal Berrio und Simone Liebscher danke ich für ihre geduldige Einarbeitung und ständige Unterstützung, insbesondere bei technischen und histologischen, aber auch menschlichen und hundespezifischen Fragen. Ich möchte mich ebenfalls bei Vivien Lehnhardt bedanken, die mich fast seit Beginn der Promotion als Hiwi, aber auch als Freundin unterstützt hat. Auch allen anderen Mitarbeitern der AG Schenke-Layland gilt ein herzlicher Dank für ihre Hilfsbereitschaft, wertvollen Anregungen und die freundschaftliche Arbeitsatmosphäre im Labor und den zahlreichen gemeinsamen Aktivitäten außerhalb der Arbeit.

Bei meinen Kollegen Felix Fischer, Velese Aslani, Carina Veil und Paul Kalva möchte ich mich ganz herzlich für die monatlichen Diskussionen im Graduiertenkolleg und den zahlreichen Aktivitäten außerhalb der Arbeit bedanken.

Bei meinen lieben Freunden und Kollegen Jan-Erik Bredfeldt, Yannick Palmowski, Michael Zimmermann, Tara Beyer, Chuan-En Lu, Max Urbanczyk, Abiramy Jeyagaran, Julia Alber und Emanuel Behling möchte ich mich ganz herzlich für die Motivationsschübe, den anregenden Diskussionen und den Abwechslungen vom Arbeitsalltag bedanken.

Schließlich gilt ein besonderer Dank meiner Familie und meiner Freundin Laura Hasberg für die immerwährende Motivation und uneingeschränkte Unterstützung.

Declaration

Ich erkläre, dass ich die zur Promotion eingereichte Arbeit mit dem Titel: „Raman microscpectroscopy and fluorescence lifetime imaging microscopy based data-driven tissue discrimination and diagnostics” selbstständig verfasst, nur die angegebenen Quellen und Hilfsmittel benutzt und wörtlich oder inhaltlich übernommene Zitate als solche gekennzeichnet habe. Ich erkläre, dass ich die Richtlinien zur Sicherung guter wissenschaftlicher Praxis der Universität Tübingen beachtet wurden. Ich versichere an Eides statt, dass diese Angaben wahr sind und dass ich nichts verschwiegen habe. Mit ist bekannt, dass die falsche Angabe einer Versicherung an Eides statt mit Freiheitsstrafe bis zu drei Jahren oder mit Geldstrafe bestraft wird.

Tübingen, 30.03.2023

Lucas Becker

Appendices

Appendix I: Becker L., Fischer F., Fleck J., Harland N., Stenzl A., Aicher W.K., Schenke-Layland K., Marzi J., *Data-Driven Identification of Biomarkers for In Situ Monitoring of Drug Treatment*, *Int. J. Mol. Sci.* 2022, *23*(13), 6956; https://doi.org/10.3390/ijms23136956

International Journal of
Molecular Sciences

MDPI

Article

Data-Driven Identification of Biomarkers for In Situ Monitoring of Drug Treatment in Bladder Cancer Organoids

Lucas Becker [1,2], Felix Fischer [3], Julia L. Fleck [4], Niklas Harland [5], Alois Herkommer [3], Arnulf Stenzl [5], Wilhelm K. Aicher [6], Katja Schenke-Layland [1,2,7] and Julia Marzi [1,2,7,*]

[1] Department for Medical Technologies and Regenerative Medicine, Institute of Biomedical Engineering, University of Tuebingen, 72076 Tuebingen, Germany; lucas.becker@uni-tuebingen.de (L.B.); katja.schenke-layland@uni-tuebingen.de (K.S.-L.)
[2] Cluster of Excellence iFIT (EXC 2180) "Image-Guided and Functionally Instructed Tumor Therapies", University of Tuebingen, 72076 Tuebingen, Germany
[3] Institute of Applied Optics (ITO), University of Stuttgart, 70569 Stuttgart, Germany; felix.fischer@ito.uni-stuttgart.de (F.F.); alois.herkommer@ito.uni-stuttgart.de (A.H.)
[4] Mines Saint-Etienne, CNRS, UMR 6158 LIMOS, Centre CIS, Université Clermont Auvergne, 42270 Saint Jarez-en-Priest, France; julia.fleck@emse.fr
[5] Department of Urology, University of Tuebingen Hospital, 72076 Tuebingen, Germany; niklas.harland@med.uni-tuebingen.de (N.H.); arnulf.stenzl@med.uni-tuebingen.de (A.S.)
[6] Center of Medical Research, Department of Urology at UKT, University of Tuebingen, 72076 Tuebingen, Germany; aicher@uni-tuebingen.de
[7] NMI Natural and Medical Sciences Institute at the University of Tueingen, 72770 Reutlingen, Germany
* Correspondence: julia.marzi@uni-tuebingen.de

Abstract: Three-dimensional (3D) organoid culture recapitulating patient-specific histopathological and molecular diversity offers great promise for precision medicine in cancer. In this study, we established label-free imaging procedures, including Raman microspectroscopy (RMS) and fluorescence lifetime imaging microscopy (FLIM), for in situ cellular analysis and metabolic monitoring of drug treatment efficacy. Primary tumor and urine specimens were utilized to generate bladder cancer organoids, which were further treated with various concentrations of pharmaceutical agents relevant for the treatment of bladder cancer (i.e., cisplatin, venetoclax). Direct cellular response upon drug treatment was monitored by RMS. Raman spectra of treated and untreated bladder cancer organoids were compared using multivariate data analysis to monitor the impact of drugs on subcellular structures such as nuclei and mitochondria based on shifts and intensity changes of specific molecular vibrations. The effects of different drugs on cell metabolism were assessed by the local autofluorophore environment of NADH and FAD, determined by multiexponential fitting of lifetime decays. Data-driven neural network and data validation analyses (k-means clustering) were performed to retrieve additional and non-biased biomarkers for the classification of drug-specific responsiveness. Together, FLIM and RMS allowed for non-invasive and molecular-sensitive monitoring of tumor-drug interactions, providing the potential to determine and optimize patient-specific treatment efficacy.

Keywords: patient-derived tumor models; personalized medicine; non-invasive molecular imaging; machine learning; drug efficacy testing

check for updates

Citation: Becker, L.; Fischer, F.; Fleck, J.L.; Harland, N.; Herkommer, A.; Stenzl, A.; Aicher, W.K.; Schenke-Layland, K.; Marzi, J. Data-Driven Identification of Biomarkers for In Situ Monitoring of Drug Treatment in Bladder Cancer Organoids. *Int. J. Mol. Sci.* **2022**, *23*, 6956. https://doi.org/10.3390/ijms23136956

Academic Editor: Giuseppe Lucarelli

Received: 20 May 2022
Accepted: 21 June 2022
Published: 23 June 2022

1. Introduction

Patient-derived tumor organoids have emerged as useful in vitro models for the high-throughput screening of drugs for individualized cancer treatment [1–3]. In vitro three-dimensional (3D) organoids, producible in a short time from small amounts of tissue, enable drug testing and the identification of potential diagnostic biomarkers. Such 3D organoids can be generated not only from surgical specimens, but also from endoscopic fine-needle aspirates, biopsy samples or even from patients' body fluids [4,5], allowing for the recapitulation of a wide range of disease stages and clinical conditions. To date, the majority of preclinical bladder cancer research has been conducted with bladder cancer cell lines or mouse models [6,7], poorly representing the features of human bladder tumors. Recently, the generation of mouse and human bladder cancer organoids was reported [8,9], recapitulating the broad histopathological and molecular spectrum of human bladder cancer and suitable for analyses of patient-individualized drug responses. One of the main obstacles in generating organoids is obtaining the patient's tissue, which is typically received from a biopsy. A novel, simplified and non-invasive method is to collect the urine of a patient, eliminating the need for surgery under anesthesia [4,10].

Drug metabolism and uptake, dose-dependent efficacy and the development of drug resistance are key determinants in the treatment of cancer patients. Within the last decade, it has been well recognized that these parameters vary greatly from patient to patient, necessitating personalized options for treatment [11–13]. Pretreatment screening of the dose-dependent potency of chemotherapeutics increases success rates and precludes drug overuse, thereby preventing side effects and additional patient suffering. Moreover, such patient-specific information could make therapies more cost-effective.

Conventional methods to monitor drug-induced effects in cell cultures typically include either cell viability assays or gene and protein expression assays, which allow detailed analysis of total protein or DNA composition [14,15]. Overall, these methods assess the pooled response of a batch of organoids and ignore the cellular heterogeneity that drives resistance to tumor treatment while being time-consuming and requiring lysis of 3D organoids to extract biomolecules [16]. Spatially resolved techniques such as immunofluorescence imaging inherit other limitations such as sample fixation and the incorporation of a fluorophore that could interfere with native intracellular biochemistry. Moreover, each fluorophore probes only one specific biomolecule, limiting the amount of obtainable biochemical information.

Advances in non-destructive imaging techniques have evolved over the past decade, providing time-resolved insight into cellular metabolism and molecular composition. Here, label-free fluorescence lifetime imaging microscopy (FLIM) utilizing the endogenous fluorescence of nicotinamide adenine dinucleotide (NADH) and flavin adenine dinucleotide (FAD) provides new possibilities for gathering information about metabolic pathways. Both coenzymes are involved primarily in the mitochondrial tricarboxylic acid cycle and electron transfer chain, where they are engaged in the formation of adenosine triphosphate and reactive oxygen species (ROS) as part of the energy metabolism and apoptosis pathway [17]. One hallmark of cancer cells is the reprogramed metabolism in their energy production. According to the "Warburg effect", cancer cells are characterized by a dominating aerobic glycolysis metabolism compared to the normally favored oxidative phosphorylation [18]. FLIM possesses the fidelity to identify minute changes in the distribution of bound and free NADH and FAD as a direct measure of the metabolic state [19]. Hence, FLIM is a promising tool for monitoring the direct drug response of chemotherapeutics in organoid models [20].

Complementary to FLIM imaging, non-invasive Raman microspectroscopy (RMS) enables the marker-independent and molecular-sensitive identification and localization of subcellular structures. Molecular fingerprints of Raman active biomolecules such as proteins, lipids, or nucleic acids can reflect a specific tissue state or cellular phenotype [21–24].

These methods yield a large amount of data not describable by conventional univariate models. Therefore, data-driven machine learning tools such as principal component analysis (PCA), k-means clustering, or neural networks have been introduced for the analysis of RMS data to identify the main features of cellular changes after drug treatment in different and complementary approaches [25,26]. Whereas PCA and k-means methods are based solely on linear transformations, neural networks make use of non-linear activation functions and are able to find rather unintuitive and ulterior correlations in the data, which ultimately yields better clustering [27]. Another research-oriented goal is to utilize these machine learning tools to find new, hitherto unknown biomarkers with completely unbiased approaches.

In this study, 3D organoids of the bladder cancer cell line RT112, bladder cancer organoids (BCO) derived from primary tumor biopsy tissue, and urine-derived organoids (UCO) from bladder cancer patients were treated with cisplatin (*cis*) or venetoclax (*vtx*) and evaluated with FLIM and RMS. Herein, we aim to address the molecular and metabolic response of different organoid entities and to develop a multiparametric data-based model that can predict patient-specific treatment efficacies.

2. Results

We characterized three different organoid models derived from a bladder cancer cell line RT112, patient-derived primary bladder cancer tissue (BCO) as well as patient urine (UCO) and compared their direct reaction to anticancer drugs *cis* and *vtx*. RMS and FLIM were implemented for spatially and time-resolved measurements of cellular drug responses.

2.1. Raman Microspectroscopy Allows Label-Free Imaging of Bladder Cancer Organoids

Organoids were derived from a bladder cancer cell line, primary bladder cancer tissue and urine. Immunofluorescence (IF) staining for the epithelial cell markers cytokeratin 5 and cytokeratin 7 and the transcription factor GATA3 was performed to characterize the three cancer organoid models (Figure 1a). IF images served for validation of the cancerogenic phenotype of the cultured urothelial organoids and confirmed successful cultivation. All organoids expressed cytokeratin 7 and GATA3, whereas cytokeratin 5 was not expressed in UCO.

Organoids were treated with different concentrations of *cis* or *vtx*. RMS was performed after 24 and 48 h, respectively. Utilizing true component analysis (TCA), six major cellular components were identified that could be attributed to mitochondria (red), nucleic acids (blue), cytoplasm (green), lipids (yellow), an unknown component (turquoise) and Matrigel (orange) based on their location within the organoids (Figure 1b) and their Raman fingerprint spectra (Figure 1c). To obtain information about the distribution of both drugs in the organoids, acquired reference spectra of solid drugs were included in the TCA calculation. In Raman images, *cis* is represented in pink, while *vtx* is presented in purple.

The assignment of the TCA components to their biological origins is based on the evaluation of individual peaks of the fingerprint spectra. Mitochondria were identified by their pronounced peaks at 747 and 1130 cm^{-1} reported for cytochrome c and b [28,29] and in-house measurement of a reference spectrum. Nuclei are assigned to the peak pair at 798 and 1096 cm^{-1}, indicators for PO_2 occurring in DNA [30], while the cytoplasm is assigned to peaks at 1001 and 1660 cm^{-1}, representative of phenylalanine and amide I bonds found in proteins [31,32]. Lipids are characterized by a peak at 1750 cm^{-1} explaining C=C vibrations in fatty acids [31,33]. The unknown component detected only in UCO demonstrated peaks at 1167 and 1593 cm^{-1}, which might be assigned to C=N and C=C stretching in quinoid rings and C-H in plane bending [32].

2.2. Nuclei Features Identify Spectral Differences between Treated Organoids

To determine the sensitivity of RMS to evaluate drug efficacy in our organoid models, Raman spectra of nuclei were extracted from Raman images. A total number of 20 spectra per organoid and concentration with respect to the acquired timepoint were further analyzed by PCA to investigate the cellular response of the three cancer models. A comparison of PC score values demonstrated trends of separation in dependence on the selected treatment (Figure 2a,c,e). Compared to controls which exhibited score values close to 0, *cis*-treated organoids clustered at opposite score values to *vtx*-treated organoids. Overall, nuclei information was rather influenced by *cis* treatment than *vtx*. Within the group of *cis* treatment, RT112 organoids demonstrated concentration-dependent effects, whereas time-dependent trends were evident for BCO, and no clear time or concentration correlation was visualized for UCOs.

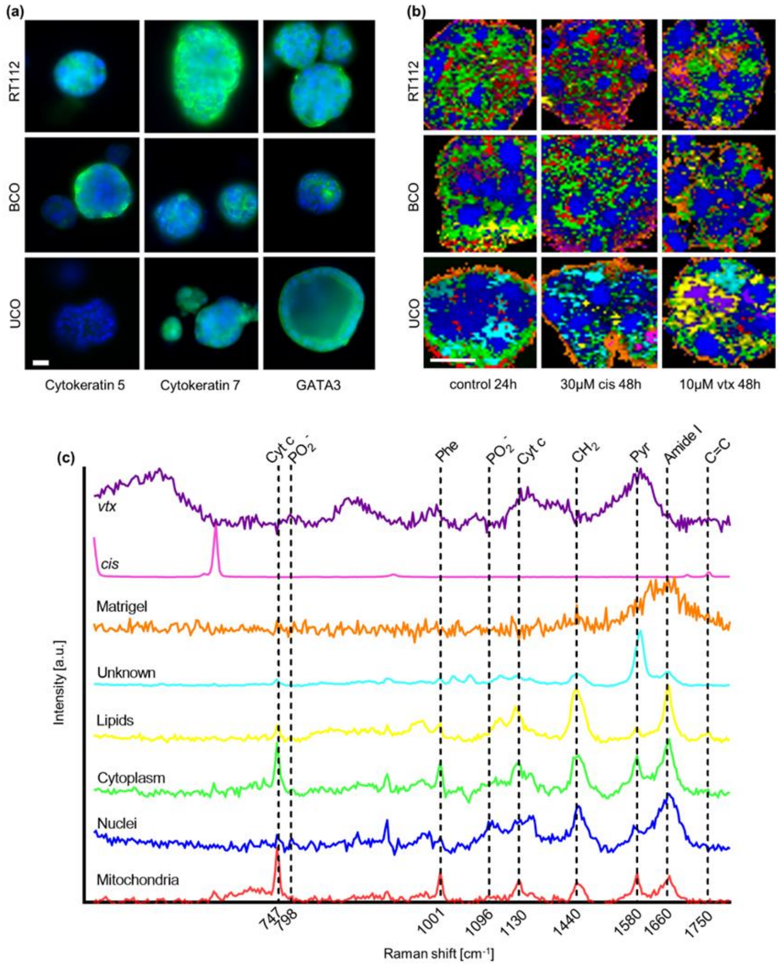

Figure 1. Immunofluorescence (IF) and Raman microspectroscopy (RMS) of different bladder cancer organoid models. (**a**) IF images of untreated RT112, BCO and UCO organoids stained for cytokeratin 5, cytokeratin 7 or GATA3 (green) and DAPI (blue). Scale bar: 25 µm. (**b**) True component analysis (TCA) images of RT112, BCO and UCO organoids. Displayed is one representative scan of untreated and treated organoids (30 µM cisplatin (*cis*) or 10 µM venetoclax (*vtx*)) for each organoid model. Scale bar: 20 µm. (**c**) Relevant TCA spectra for the identified cellular components.

To identify Raman peaks responsible for the separation between *vtx* and *cis* treatment, PC loadings were plotted, and prominent peaks were identified (Figure 2b,d,f). The loadings for each of the three organoid models demonstrated similar band assignments for the separation of *vtx*- and *cis*-induced effects. The shifts to positive loadings in RT112 and BCO as well as to negative loadings in UCO at 702 and 815 cm^{-1} in *cis*-treated organoids might be related to conformational changes from B-form DNA to A-form DNA [34]. Additionally, shifts at 615 and 750 cm^{-1}, representative of changes in the thymidine band, are observed in *cis*-treated organoids. On the opposite, data from non-*cis*-treated organoids demonstrated more pronounced peaks at 1250, 1321, and 1455 cm^{-1}, which represent guanine and

DNA, respectively [30,35]. All relevant peaks and their molecular assignments are listed in Table 1.

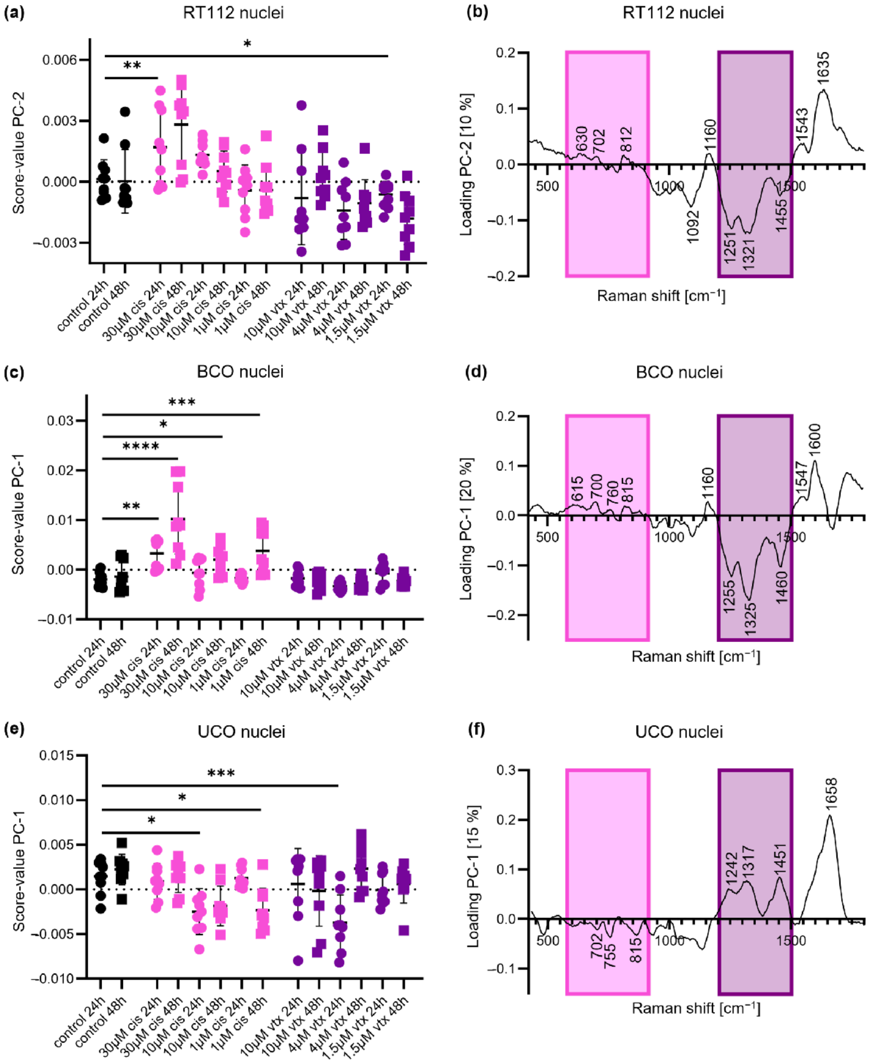

Figure 2. PCA of nuclei-derived Raman spectra reveals similar spectral changes for all organoid models after *cis* (pink) and *vtx* (purple) treatments. (**a**) Score value analysis of the cell line RT112 shows statistically significant differences after *cis* and *vtx* treatment. (**b**) Corresponding loading plot. (**c**) Score value analysis of patient-derived BCOs shows statistically significant differences after *cis* treatment and tendencies of separation after *vtx* treatment. (**d**) Corresponding loading plot. (**e**) Score value analysis of patient-derived UCOs reveals statistically significant differences between controls and *cis* and *vtx* treatment. (**f**) Corresponding loading plot. Black: controls; pink: *cis* treatment; purple: *vtx* treatment; circles: 24 h; square: 48 h; Statistical analysis: One-way ANOVA, $n = 9$, * $p < 0.05$, ** $p < 0.01$, *** $p < 0.001$, **** $p < 0.0001$.

Table 1. Biological assignment of the most relevant wavenumbers.

Wavenumber [cm^{-1}]	Biological Origin	Literature
702	A-form DNA	[34]
705	Cholesterol ester	[36]
747	Cytochrome c	[28]
798	PO_2^-	[30]
815	A-form DNA	[34]
1096	PO_2^-	[30,37]
1125	Cytochrome c	[28]
1250	G	[35]
1315	Cytochrome c	[38]
1321	G	[30,35]
1450	CH_2	[30,31,39]
1455	DNA	[35]
1660	Amide I	[32]
1750	C=C	[33]

2.3. Mitochondrial Spectra Identify Spectral Differences between Organoids after vtx Treatment

PCAs were also performed on extracted mitochondria spectra from the three organoid models to assess cellular responses with regard to cell metabolism. For *cis* treatment, no significant differences in spectral signatures were observed when compared to untreated specimens in all tested organoid systems (Figure 3a,c,e). In contrast, alterations in mitochondrial spectra were observed after *vtx* treatments in patient-derived BCOs and to a smaller extent in UCOs. No significant shift was shown for cell-line-derived organoids. The corresponding loading plots (Figure 3b,d,f) exhibit, similar to the PCAs of nuclei, a recurrent pattern when comparing the individual multivariate analyses with each other. The most prominent peaks in correlation with *vtx* treatment are depicted in purple boxes in the loading plots. The peaks around 1308–1315 cm^{-1}, 1125 cm^{-1} and 747 cm^{-1} can be assigned to cytochrome c [28,38]. The bands in the region between 1447–1450 cm^{-1} are indicative of changes in the CH_2 conformation of proteins [30,31,39]. Interestingly, the cellular response to *vtx* in UCOs demonstrated inverted effects at 742 cm^{-1} and 1455 cm^{-1} when compared to the other organoid systems, presenting the biggest heterogeneity within a group and only a separation at a lower explained variance (PC-5 at 2%).

2.4. Data-Driven Feature Selection Identifies Novel Biomarkers

Neural networks were utilized as a complementary data-driven method to derive potential biomarkers suitable for the evaluation of spectral data and to compare feature output in dependence on the linearity of the transformation method. By using the FeaSel-Net algorithm, we aimed to find spectral biomarkers (i.e., wavenumbers) in the dataset while classifying it into one of the three classes: *cis*, *vtx* and *control*.

In total, six different datasets (*nuclei* and *mitochondria* for each of the three organoid models) were evaluated. Each dataset initially consisted of 350 features (spectral range from 400–1800 cm^{-1} with a sampling interval of 4 cm^{-1}) and was pruned to 10 features after 16 pruning iterations. During preprocessing, Raman spectra were standardized along the feature axis. Their mean spectra can be found in Figure S1. Since neural networks are inherently random in their parameter initialization, a deterministic result cannot be achieved. Thus, we statistically evaluate the resulting masks from 50 executions of the FeaSel-Net algorithm. The five most relevant wavenumbers per dataset are presented in Table 2. The corresponding percentages show how often each wavenumber has been chosen within the 50 executions. Even though the input signal was compressed to less than 3% and an equally likely selection of the features yielded approximately 1.4 selections per feature (2.85%), the algorithm found significantly increased interest in the stated features.

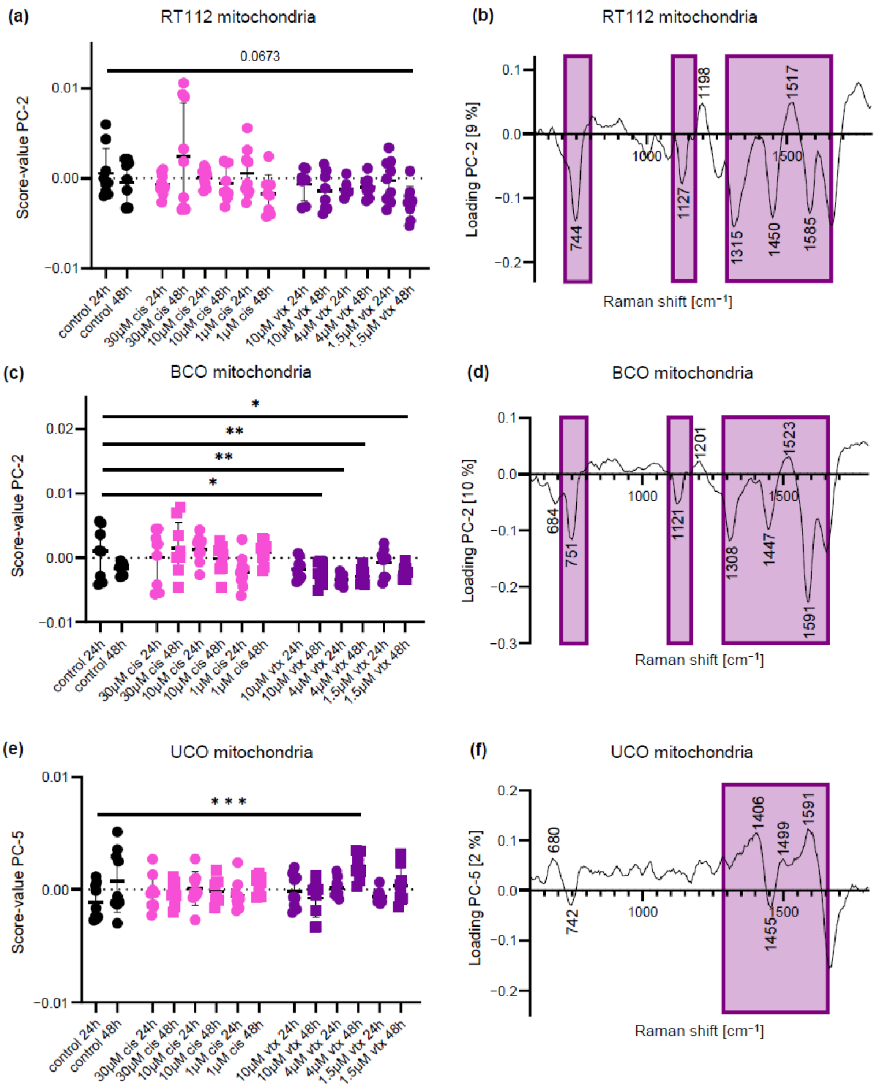

Figure 3. PCA of mitochondria-derived Raman spectra reveals similar spectral for all organoid models after *vtx* (purple) treatment. (**a**) Score value analysis of organoids from the cell line RT112 shows tendencies of separation after *vtx* treatment. (**b**) Corresponding loading plot. (**c**) Score value analysis of patient-derived BCOs show statistically significant differences after *vtx* . (**d**) Corresponding loading plot. (**e**) Score value analysis of patient-derived UCOs reveals statistically significant differences between controls and *vtx* treatment. (**f**) Corresponding loading plot. Black: controls; pink: *cis* treatment; purple: *vtx* treatment; circles: 24 h; square: 48 h; Statistical analysis: One-way ANOVA, $n = 9$, * $p < 0.05$, ** $p < 0.01$, *** $p < 0.001$.

Table 2. Most frequently occurring wavenumbers upon treatment discrimination.

Dataset	ν_1 [cm^{-1}]	ν_2 [cm^{-1}]	ν_3 [cm^{-1}]	ν_4 [cm^{-1}]	ν_5 [cm^{-1}]
Nuclei					
RT112	1551 (76%)	934 (68%)	926 (56%)	1760 (52%)	1688 (50%)
BCO	926 (100%)	1443 (58%)	825 (52%)	1311 (50%)	1535 (44%)
UCO	1479 (84%)	1555 (70%)	813 (68%)	1250 (48%)	404 (40%)
Mitochondria					
RT112	1042 (54%)	697 (52%)	1307 (46%)	460 (46%)	1555 (44%)
BCO	705 (74%)	926 (72%)	476 (72%)	1587 (70%)	693 (48%)
UCO	1259 (82%)	1551 (46%)	1475 (42%)	1287 (38%)	1760 (38%)

The most robust wavenumber eventuated in the nuclei BCO dataset with 50 selections, i.e., a selection in every run. On the other hand, the lowest percentage occurs in the UCO mitochondria dataset with 19 selections, which is still 13.5 times higher than uniformly distributed. Another interesting finding is that there are some overlaps in the resulting features, especially in the nuclei datasets. The spectral area at 1535–1555 cm^{-1} appears to be relevant to all nuclei datasets, and the area around 925–935 cm^{-1} appears to be relevant for RT112 and BCO. These possible biomarkers could be assigned to changes in DNA backbones or α-helix structure [40,41] and to changes in the amide II region [42], all denoting structural alterations of DNA.

Another reoccurring wavenumber emerged in RT112 and BCO mitochondria around 690–705 cm^{-1}. In the PCAs of mitochondria, this wavenumber was not detected in any of the loadings for separation between drug treatments and controls. The wavenumbers at around 700 cm^{-1} could be assigned to cholesterol ester and might display a reaction to drug-induced oxidative stress [36,43]. Another explanation might be the structural-altering effect of *cis* on mitochondrial DNA [33,44].

Furthermore, the interdependencies of the chosen wavenumbers were analyzed, i.e., which wavenumbers are commonly chosen in the same run. To do so, Jaccard coefficients were calculated using the masks that were obtained in 50 runs. The resulting Jaccard coefficient matrices were weighted by the number of feature occurrences in the selection. Figure 4 shows the 10 most selected wavenumbers and their dependencies for each dataset. Especially for the matrices of the BCO mitochondria and the UCO nuclei set, a clustering in the upper left corner is described, indicating a frequent selection of the most common markers at the same time. The simultaneous pick in these BCO and UCO sets cannot be perceived in the other organoid types that exhibit *XOR* behaviors rather than *AND*s, which indicates that even univariate classifications with reasonable results could be possible. In particular, the nuclei BCO set, whose most important wavenumber at 925.5 cm^{-1} is selected every run, is probably able to provide enough information on its own to separate all three classes correctly.

2.5. Classification with Selected Raman Markers

The performance of the biomarkers retrieved from the FeaSel-Net algorithm (Table 2) and from conventional loading analysis of the PCAs (Table S1) was analyzed in the following. Accordingly, the original Raman features were masked and reduced for each dataset and used for classification. The applied classifier for both PCA-derived and FeaSel-Net derived methods was the same fully-connected neural network with an input of five discrete wavenumber values (masked original Raman signal) and an output of the three classes *vtx*, *cis* and *control*. We purposely did not use the classification model from our FeaSel-Net algorithm to ensure equal chances for the two different feature selection methods.

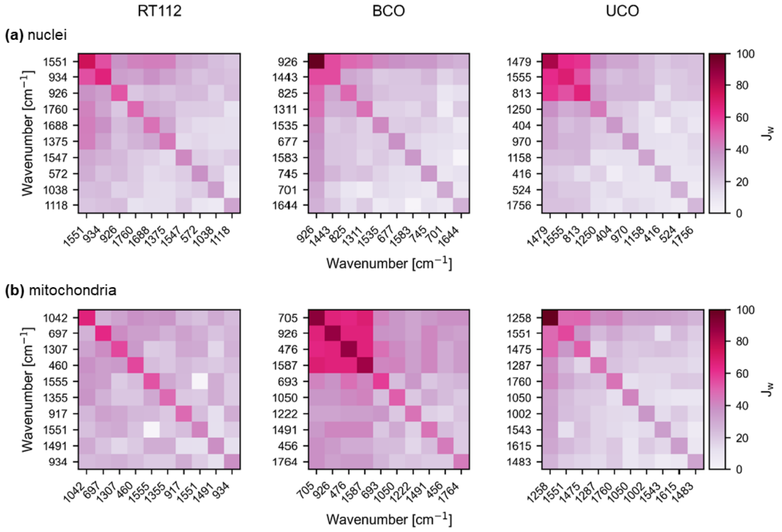

Figure 4. Weighted Jaccard coefficients for the most important wavenumbers evaluated with FeaSel-Net in percent. The plots describe the dependencies within the selected wavenumbers. Darker areas indicate a strong relationship between the features. The selection dependency for the nuclei spectra of each organoid type is shown in (**a**), whereas those of mitochondria are depicted in (**b**).

Table 3 shows the classification results with the performance parameters' accuracy (ACC), sensitivity (SEN), and specificity (SPE) for the neural network trained with the masked RMS data for each of the six datasets. The neural network was trained 10 times for each dataset and feature selection. At first glance, striking classification accuracies between 73 and 87% were demonstrated when taking into account that less than 1% of the overall spectral data points were utilized for the discrimination. In both organelles, the cell line and the BCO model performed slightly better than the UCO.

Table 3. Classification performance of masked Raman data. The presented values (±SD) are the parameters' percentage averages of 10 training runs for each dataset and feature selection method.

	PCA Loadings			FeaSel-Net		
Dataset	**ACC**	**SEN**	**SPE**	**ACC**	**SEN**	**SPE**
Nuclei						
RT112	76.6 ± 1.0	64.9 ± 3.9	82.4 ± 2.4	87.0 ± 1.0	80.4 ± 2.6	90.2 ± 1.3
BCO	79.0 ± 1.1	68.5 ± 3.7	84.2 ± 2.3	84.7 ± 0.8	77.1 ± 2.9	88.5 ± 1.4
UCO	73.1 ± 1.9	59.6 ± 6.4	79.8 ± 4.8	80.1 ± 1.0	70.1 ± 2.8	85.1 ± 1.6
Mitochondria						
RT112	77.9 ± 1.4	66.9 ± 4.6	83.5 ± 3.0	84.4 ± 0.9	76.7 ± 2.9	88.3 ± 1.8
BCO	83.1 ± 0.5	74.6 ± 1.5	87.3 ± 1.0	84.7 ± 0.6	77.0 ± 3.2	88.5 ± 2.0
UCO	72.8 ± 1.0	59.3 ± 3.7	79.6 ± 1.9	76.8 ± 1.2	65.3 ± 4.2	82.6 ± 2.6

When comparing the two biomarker selection methods, Table 3 indicates a difference between the conventional feature selection method (PCA loadings) and the data-driven approach (FeaSel-Net). Throughout all datasets, classification parameters were improved. The overall accuracy increased by 7.3%, whereas improvement in specificity and sensitivity accounted for 5.1% and 12.8%, respectively. These effects correlate in particular to the nuclei-based classification between *control*, *vtx* and *cis* (Table S2 provides a detailed overview).

The previous analysis did not consider differences emerging from the drug concentrations or treatment durations. Thus, classification was repeated on the best-performing pre-trained model (BCO nuclei), and the discrimination was additionally split into concentration and exposure time-dependent subsets. The resulting confusion matrices for different input features are shown in Figure 5. Contrary to the assumption that longer exposure times and higher doses yield better discriminability, a trend that confirms these assumptions cannot be described. This could be since the training has been done with data from all concentrations and durations. However, even though Figure 5 does not show any correlations between drug doses and exposure time, it still shows the influence of the selected biomarker features. The classifier with an input defined by FeaSel-Net (Figure 5a) performs better than a classification with the PCA-derived wavenumbers (Figure 5b).

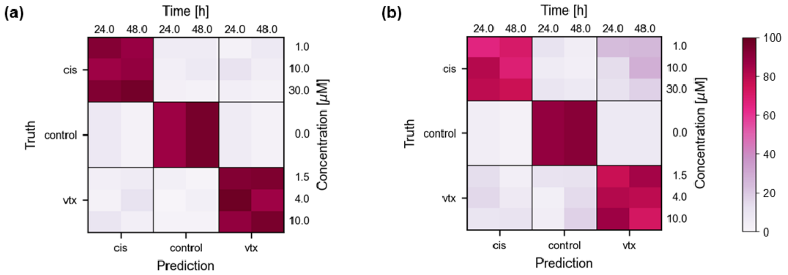

Figure 5. Confusion matrices for the BCO nuclei dataset resolved by drug concentration and exposure time. Classification accuracy (%) with features retrieved from FeaSel-Net (**a**) or PCA loadings (**b**) are shown.

2.6. FLIM Enables Non-Invasive Monitoring of Drug Response Patterns in Bladder Cancer Organoids

Drug treatment with *cis* or *vtx* influences the metabolic pathways in cells [45,46], and it has been shown that FLIM identifies metabolic changes in cell cultures and in vivo [47]. Therefore, FLIM images of endogenous NADH and FAD fluorescence were acquired from RT112, BCOs, and UCOs treated with different concentrations of *cis* and *vtx* for 24 and 48 h. For each treatment, FLIM parameters τ1, τ2, and α1% of the respective coenzymes NADH and FAD were characterized and compared among each other. Exemplarily, differences in FAD α1% and bound NADH fluorescence lifetime τ2 are visualized in representative FLIM images (Figure 6a,c) and mean difference heatmaps (Figure 6b,d). The complete overview of NADH and FAD τ1, τ2, and α1% values can be found in the supplementary material (Figures S2–S4).

Comparing NADH and FAD a1% readouts, representing the redistribution of free vs. bound coenzymes, no significant changes were observed upon *vtx* treatment for any of the organoid models. On the contrary, upon *cis* treatment, a decrease in a1% in both NADH and FAD was observed for BCOs (Figure S2b,e) as well as in FAD a1% in UCOs (Figure 6b). Cell line-derived organoids did not indicate changes in a1% (Figure S2a,d).

FLIM parameters representing the fluorescence lifetime of free (τ1) and bound (τ2) NADH and free (τ2) and bound (τ1) FAD exhibited statistically significant changes for all organoid models after *vtx* treatment and a partial impact of *cis* treatment. Lifetimes τ1 and τ2 of both NADH and FAD increased after *vtx* treatment in all organoid models (Figure S2). In addition, an increase in NADH τ1 after treatment with a high concentration of *cis* was observed in the RT112 and BCO models after 48 h (Figure S3d). In UCO, *cis* lead to a significant decrease in FAD τ1 (Figure S4b). Overall, except for NADH τ1, mean difference heatmaps indicate opposite effects on fluorescence lifetime upon *vtx* and *cis* treatments.

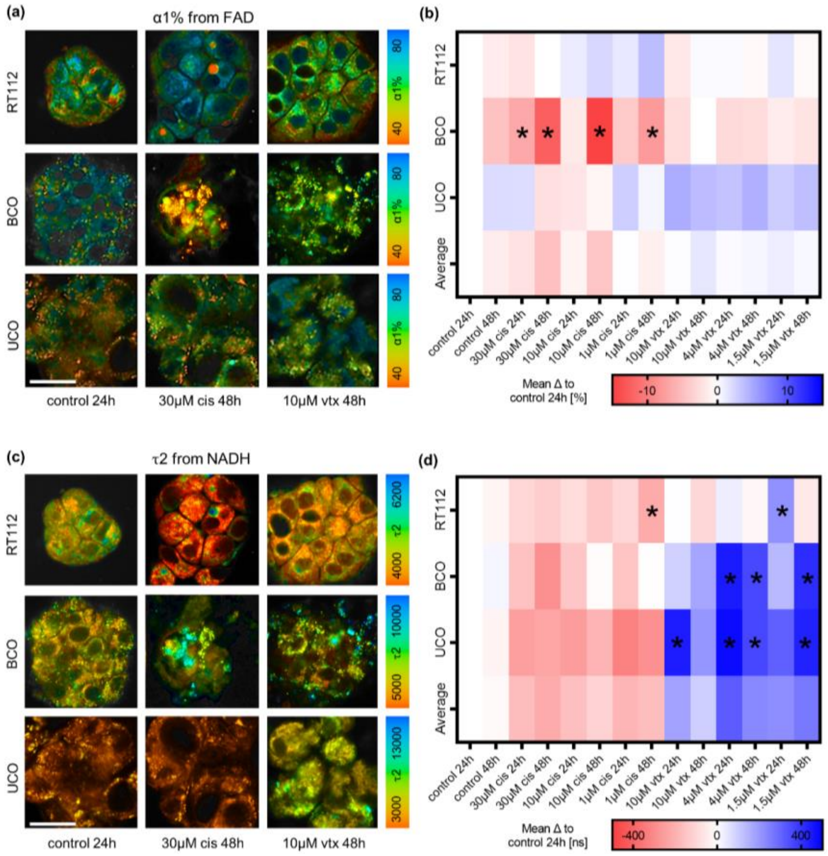

Figure 6. FLIM of bladder cancer organoids. (**a**) Representative FAD α1% images of control RT112, BCO and UCO organoids and 48 h after 30 µM *cis* or 10 µM *vtx* treatment. Scale bar: 25 µm. (**b**) Heatmap of mean differences of NADH α1% to the 24 h control. (**c**) Representative NADH τ2 images of control RT112, BCO and UCO organoids and 48 h after 30 µM *cis* and 10 µM *vtx* treatment. Scale bar: 25 µm. (**d**) Heatmap of mean differences of NADH τ2 to the 24 h control. One-way ANOVA, *n* = 15, * $p < 0.05$.

2.7. *Feature Importance Analysis Automatically Identifies Most Informative FLIM Parameters*

Conventional statistical comparison, i.e., via ANOVA, requires manual interpretation and comparison of each FLIM parameter and is highly dependent on sample heterogeneity or standard deviation. Thus, we were interested in investigating whether a subset of FLIM parameters existed that was sufficiently informative of changes resulting from different drug treatments. To assess the ability of FLIM parameters to automatically discriminate organoids treated with *cis* versus *vtx*, we conducted a feature importance clustering analysis. For this analysis, we considered averaged values of FLIM parameters over all biological replicas or each timepoint/drug/model. We excluded control measurements from this analysis because our focus was on differentiating cells treated with *cis* from those treated with *vtx*. We first verified that FLIM parameter values could be used to automatically separate *cis*-treated organoids from *vtx*-treated ones for each model. Using a k-means clustering analysis (with k = 2), we were able to correctly divide each dataset into two clusters, one containing only *cis*-associated values and the other containing only *vtx*-associated values. These results were consistent across all three models (RT112, BCO and UCO). We then sought to identify which parameters were driving the cluster assignment. To assess the relative importance of each parameter, we conducted a feature importance study. We were able to identify a lower-dimensional subspace of features that offered the correct separation of our datasets. This lower-dimensional subspace contained two out of the six FLIM parameters which were found to be sufficiently informative to discriminate *cis*-treated organoids from *vtx*-treated organoids. Interestingly, the most informative pairs differed across models (Table 4). These results suggest some general trends. First, fluorescence lifetimes seemed to be most informative for cell line and patient-derived models, although different channels were selected for each model. Second, the fluorescence lifetime of τ2 from NADH is the only parameter selected in more than one model, indicating resemblances in patient-derived organoids compared to the cell line.

Table 4. FLIM parameters selected using a feature importance analysis.

Dataset		
RT112	τ1 from FAD	τ1 from NADH
BCO	τ2 from FAD	τ2 from NADH
UCO	α1% of FAD	τ2 from NADH

3. Discussion

In this study, RMS and FLIM were utilized for a comprehensive characterization of the drug effect of *cis* and *vtx* on bladder cancer organoids in different models derived from a cell line as well as patient-derived primary tissue and urine. Our RMS and FLIM measurements suggest that the spectral and endogenous fluorescence information, especially from mitochondria and nuclei, can be useful in situ tools for non-destructive monitoring of drug effects on organoid models.

The promise of patient-derived organoid models in precision medicine relies upon the notion that characterization of their mutational profiles in combination with high-throughput screening with a library of therapeutic compounds can elucidate druggable targets. In the case of bladder cancer, patients are often diagnosed early in disease progression, and patients with non-muscle invasive cancer frequently undergo multiple resections and treatments to avoid cystectomy and its detrimental impact on quality of life. Thus, information on effective drug candidates identified by screening in personalized organoid culture could be utilized to guide intravesical therapies and support decision making for earlier therapy success and better patient compliance by avoiding side effects. In recent years, RMS and FLIM have been established as promising techniques for investigating molecular and metabolic changes in cells. The advantages of these methods are their non-destructive approach with concomitant spatial resolution at the subcellular level [3,23,48].

Therefore, we investigated the capability of these techniques to monitor the metabolic and molecular response of bladder cancer organoids to chemotherapeutic drugs at spatial and temporal resolution. TCA-based image generation enabled the marker-independent discrimination and localization of major subcellular structures within the organoids and even allowed the visualization of accumulations of the drugs. Intensity distribution heatmaps of the single components enabled us to further investigate underlying spectral information. Spectral signatures provided access to changes in molecular composition and identified drug-specific peak patterns in nuclei-derived PCA loadings, which reoccurred in each of the three organoid models. *Cis* treatment-related changes were correlated to alterations in the structure of DNA. Pronounced peaks at 700 and 815 cm^{-1} reported in A-form DNA [34] were present in all organoid models. Multiple studies demonstrate that *cis* results in intrastrand crosslinks (CLs) between adjacent purine bases (1,2-GG or 1,2-AG CLs) or between purine bases separated by a third base, CLs, and monofunctional adducts [49,50].

Additional shifts were observed at 615 and 750 cm^{-1}, which identify C2′-endo/anti conformers of deoxy thymine [34,37] and support our conclusion that RMS has the fidelity to screen for variations in DNA structure.

In addition to DNA damage, *cis* is also known to induce the production of ROS in its target cell [51–53]. Although the intracellular origin of ROS production is still unclear, it was reported that especially *cis*-induced ROS production occurs in mitochondria [54]. Generation of ROS often correlates to loss of the mitochondrial membrane potential [55], leading to inhibition of the TCA cycle [51], which can impact fluorescence lifetimes and is, therefore, a potential reason for alteration upon *cis* treatment. NADH $\tau 1$ denotes the fluorescence lifetime of free, cytosolic NADH, in contrast to bound NADH, which is found in the oxidative phosphorylation chain and is designated by $\tau 2$ [56]. Fluorescent lifetimes are highly sensitive to alterations in the cellular microenvironment, such as pH, solvent polarity, or even viscosity and can, therefore, directly monitor changes in organoids [47,57]. Our data of *cis*-treated organoids indicate similar trends among $\tau 1$ and $\tau 2$ for both NADH and FAD but were only significant for 30 µM *cis* concentration.

In contrast, *vtx* treatment significantly affected both FLIM and Raman results for all organoid models. *Vtx* is a chemotherapeutic drug mimicking the BH3 domain of pro-apoptotic proteins capable of binding to and antagonizing BCL-2 family anti-apoptotic proteins. As a result, the cell undergoes apoptosis mediated by the mitochondrial pathway and initiated by the activation of caspases [58]. This effect was reflected in the Raman data of mitochondria, demonstrating shifts in wavenumbers relevant to cytochrome c. The latter were found mainly in BCOs and UCOs. Utilizing PCAs, nuclei-related alterations were also observed upon *vtx* treatment, which, unlike *cis*, does not directly interact with DNA. We assume that the recurrent changes in the loading plots at 1255, 1325, and 1455 cm^{-1}, all representative of DNA, especially guanine, correlate with the preparation for apoptosis or altered cell metabolism. These shifts might refer to the concomitant denser packing of cell nuclei during the initiation of apoptosis [59].

FLIM was able to detect statistically significant effects on NADH and FAD lifetimes for all three organoid models after *vtx* treatment. In all models, we found increased fluorescence lifetimes as a reaction of cells to *vtx* probably undergoing apoptosis. These findings are consistent with the results of other studies reporting an increase in NADH lifetime associated with apoptosis [60].

In comparison to significant changes in fluorescence lifetimes, minor drug-induced effects were reflected in NADH and FAD $\alpha 1\%$ values and only detected for BCOs treated with *cis*. A decrease in NADH $\alpha 1\%$ is associated with a shift in the ratio of free to bound NADH, which correlates to a switch from glycolysis, favored in cancer cells, to oxidative phosphorylation. Another explanation for the changes in $\alpha 1\%$ might be an increased energy consumption of nuclei as they prepare for apoptosis [61,62], i.e., after DNA bending due to the impact of *cis*.

However, when comparing NADH and FAD $\alpha 1\%$ among all organoid systems, differences in control organoid baseline values were observed. While NADH a1% was at ~78% in non-treated RT112, decreased baseline values were observed in BCOs and UCOs between 60–80% and 50–70%, respectively. These baseline shifts were also visible for $\alpha 1\%$ of FAD to decreased values in BCO and UCO compared to RT112. An explanation for this result might be the stage and type of cancer, which is reflected by the different models. The cell line RT112 is established from a G2 transitional cell carcinoma with untreated primary urinary bladder carcinoma. BCOs were retrieved from a muscle-invasive bladder cancer tumor in stage pT2 in G3, while UCOs were derived from a less aggressive surface tumor in stage pT1 in G2. Because $\alpha 1\%$ is a direct measure of metabolic state indicating the balance between glycolysis and oxidative phosphorylation, baseline shifts in non-treated organoids were in accordance with the metabolic activity and severity of the cancer state.

In addition to the introduction of non-destructive readouts for analyzing the cytotoxic effects of drugs on different types of organoids, we aimed to build data-driven classification models that allow us to identify the most robust and relevant Raman and FLIM parameters enabling the identification of novel biomarkers. Both FLIM and RMS measurements generate large data sets, and automated dimensionality reduction and feature selection can help to translate these methods into a clinical setting and improve the interpretability of the data. The establishment of neural networks allowed us to identify different Raman markers relevant for the separation between controls and treated organoids across the organoid systems. With non-linear optimization and transformation processes that are inherent to neural networks and the recursive feature evaluation provided by FeaSel-Net, the extraction of the most relevant data subsets was enabled in a more complex and yet more accessible approach. The advantage of non-linearity has been confirmed in a deep-learning-based classification with the elaborated features. With Jaccard matrices, the interdependence of the features and the need to apply multivariate analyses on spectral data have been shown. Retrieval of Raman signals from data-driven feature selection results in 12.2% improved sensitivity for discrimination of nuclei-related effects and 6.8% improved sensitivity for drug-induced mitochondrial changes in comparison to Raman bands guided by PCA loadings.

It must be stated that the data-driven and single organoid-based approach presented in this study is very sample-specific, and its finding must not be assumed for bladder cancer in general. To further evaluate the robustness of this method for the assessment of drug response and, in particular, to improve sensitivity to dose-dependent effects, our experiments would need to be repeated on multiple donors with parallel viability assays. Another factor to be considered for this data analysis approach is its virtue: the non-linearity. Compared to PCAs and their assigned loadings plot, very deep neural networks can find patterns in the signal that are not interpretable by humans or statistical analyses. We have specifically chosen the FeaSel-Net approach for feature selection since it offers more possibilities to fine-tune hyper-parameters, which enables us to find better results. Another reason for the neural network approach, in contrast to other feature selection methods such as XGBoost [63], is the capability of further optimizing the machine learning model by adapting the pre-trained weights from our previous feature selection. In terms of generalizability, the neural network approach will perform better when having a bigger dataset and multiple outliers or noisy data.

FLIM measurements obtain multiple parameters of bound and free FAD and NADH, characterizing the metabolic profile of cells. To perform faster and more robust analyses of FLIM data, we investigated whether the identification of different drug effects is reflected in a smaller subset of parameters. All organoid models were subjected to data-driven k-means clustering to identify the FLIM parameters explaining the drug-induced effects. Among organoid models, only one parameter overlap in $\tau 2$ NADH was detected for BCO and UCO organoids. We hypothesize that this indicates similarities in metabolic activities between the patient-derived models but differences in the cell line. Since the RT112 cell line exhibits no overlap in relevant FLIM parameters to the patient-derived organoids, the metabolic and biological difference between the models becomes evident, highlighting the need for patient-specific analyses in drug testing. The overlap of the selected FLIM parameters further corroborates the comparability of the organoid systems, allowing urine-derived organoids to be considered equivalent to organoids derived from primary tissue despite their origin from different donors. K-means clustering also highlights that FLIM parameters displaying the ratios of bound to free NADH and FAD are less important to discriminate the drug effects between *cis* and *vtx* as only in UCO was $\alpha 1\%$ of FAD selected. One possible reason for this result could be that the two drugs tested may have a relatively smaller effect on the redistribution of NADH and FAD than on the change in the microenvironment of the cell, which is detected very sensitively by alterations in the fluorescence lifetimes.

With the novel data-driven methodologies presented in this study, we provide first insights into similar molecular behaviors upon drug treatments between patient-derived organoids produced from primary tissues compared to urine. Interestingly, we found variabilities between the patient-derived organoids and the cell line, especially by clustering the FLIM parameters and thus highlighting the need for patient-specific analysis. These evaluation methods give insights into the distinctness of treated and control organoids, but also provide information on the importance of the specific features of the data, and subsequent filtering allows us to focus on the relevant data. The purpose of the extraction and evaluation of relevant features is to enhance generalizability during discrimination tasks, therefore relieving the process of sample acquisition and improving discriminability. With this knowledge, new sparse sensors and measurement protocols can avail faster and more efficient tumor classifications up to real-time evaluations. This methodology could also be applicable in the future as a tool to identify biomarkers that can be utilized to distinguish tumorous from healthy cells. An important future direction is to conduct Raman and FLIM experiments on additional patient-derived organoids to investigate donor-specific variances. The comparisons between urine- and tissue-derived organoids from the same patient would be of particular interest for further evaluation of both methods. An additional target for subsequent studies is the comparison with patient-derived organoids retrieved from normal bladder tissue. This will allow the identification of the most effective drug concentrations that have a maximum effect on the cancerous tissue and minimum side effects.

The ultimate goal of our study was to establish a multiparametric workflow to rapidly evaluate drug-induced effects on patient-derived tissue models. With our experiments, we provide evidence that RMS and FLIM on organoids can be utilized as a test platform to evaluate the effectiveness of different anticancer drugs as well as their mode of action. In addition, we demonstrated that data-driven approaches can be utilized to reduce data complexity by automated feature selection enabling to improve of classification models and ultimately lead to better prediction accuracy.

4. Materials and Methods

4.1. Cell Culture of Organoids in Matrigel

After informed consent of the patient, tumor cells were retrieved from surgical specimens of a radical cystectomy or rinsing urine for BCO and UCO, respectively. The study was approved by the Ethics Committee (804/2020/B02). An overview of patient-specific pathohistological information is given in Table S3. For the preparation of BCO, the tissue was covered by working medium (DMEM, 2 mM glutamine, 10% FBS, 1% pen-strep (all from Sigma-Aldrich, St. Louis, MO, USA), 100 mM Y-27632 (MecChemExpress, Hölzl GmbH, Cologne, Germany), mechanically cut in cubes of approximately 1 mm^3, suspended in 10 mL working medium and centrifuged (480 g, 10 min, ambient temperature). The sediment was resuspended in 1 mL PBS per 100 mg tissue wet weight. Extracellular matrix components were enzymatically degraded through the addition of 15 µL of a blend of collagenase (3000 U/mL)/hyaluronidase (1000 U/mL; STEMCELL Technologies, Vancouver, Canada) per 1 mL suspension and incubated for 30 min at 37 °C. This step was repeated once. Subsequently, undissolved tissue was removed by a 70 µm cell strainer, and the filtrate was centrifuged (150 g, 7 min, ambient temperature). The vital cells were counted and resuspended at 1×10^6 cells/mL in organoid culture medium and cooled on wet ice [9,64]. The cell suspension (30 µL) and Matrigel (10 µL, BioTechne, Minneapolis, MN, USA) were mixed on ice.

This blend of cells in Matrigel (40 µL) was placed in a 24-well plate. The plate was then turned upside down and incubated for 5 min at 37 °C to generate hanging drops. A total of 500 µL organoid culture medium [9,64] was added per well and incubated at 37 °C, 5% CO_2 and a humidified atmosphere. The organoid culture medium was routinely replaced twice a week after microscopic evaluation of cell growth of the organoids. Before measurements, organoids were transferred into 8 well µ-slides (ibidi GmbH, Gräfelfing, Germany). For the preparation of UCO, cells from urine samples were sedimented by centrifugation, washed twice with PBS, counted, and resuspended at 1×10^6 cells/mL in organoid medium to generate organoids as described above.

4.2. Immunofluorescence Staining

For imaging, organoids were cultured in 8-well chamber slides. Organoids were fixed by 4% formaldehyde (30 min, ambient temperature) and blocked (5% BSA, 0.2% Triton X-100, 0.1% Tween 20, in PBS; 1 h, ambient temperature), and incubated (1 h, 37 °C) with primary antibodies CK5 (BioLegend, Amsterdam, The Netherlands), CK 7 (Abcam, Cambridge, UK) and GATA3 (Abcam). Primary antibodies were incubated with complementary Alexa Fluor 488-labelled (Jackson ImmoResearch Europe, Cambridge, UK) secondary antibodies (1:250, 1 h, ambient temperature). Nuclei were counterstained by DAPI (DAKO), and the expression of the marker genes was visualized by microscopy (Zeiss Axiophot, Carl Zeiss AG, Oberkochen, Germany). Antibody diluent was 1% BSA in PBS. Samples without primary antibodies and samples stained with anti-rabbit IgG antibodies served as controls.

4.3. Sample Preparation for Spectroscopic Raman- and FLIM Measurements

Organoids derived from the RT112 cell line, primary tumor tissue and urine were incubated with 10 µM, 4 µM and 1.5 µM venetoclax (*vtx*, Sellek Chemicals, Houston, TX, USA) or 30 µM, 10 µM and 1 µM cisplatin (*cis*, Sellek Chemicals) in cell culture medium for 24–48 h at 37 °C in 5% CO_2 atmosphere. *Vtx* was dissolved in 20% Captisol (Sellek Chemicals), while *cis* was dissolved in Milli-Q water. Controls were kept in medium. Organoids were first measured with FLIM and afterward with RMS. Prior to FLIM measurements, the samples were washed with PBS to remove phenol red interfering with Raman measurements. Organoids were kept in 200 µL PBS throughout the measurements and immersed in a cell culture medium with or without drugs afterward.

4.4. FLIM Imaging of Organoids

Time-correlated single-photon counting (TCSPC) fluorescence decay measurements were performed with a Zeiss LSM 880 (Zeiss) coupled with a Ti:Sapphire femtosecond laser (MaiTai HP Spectra Physics, Santa Clara, CA, USA) and a two-channel NDD BIG2.0 GaAsP PMT detector (Becker & Hickl GmbH, Berlin, Germany). Autofluorescence of NADH and FAD was excited with two-photon excitation at a wavelength of 700 nm and 5% laser power through a 63×1.4 NA C-plan apochromat objective (Zeiss). Emission light was filtered in the range of 450 to 490 nm for NADH and 500 to 550 nm for FAD. The total image acquisition time was set to 141 s at a resolution of 512 × 512 pixels and a pixel dwell time of 32.77 µs. The instrument response function was recorded at 900 nm from crystalline urea (Sigma-Aldrich). All FLIM measurements were performed at 37 °C using a microscope stage top incubation system (ibidi heating system, ibidi GmbH).

4.5. FLIM Data Analysis

SPCImage (Becker & Hickl GmbH) was utilized to perform biexponential decay fittings with a 30% threshold of maximum photon count to remove the background. The quality of fit was decided based on a mean χ^2 value smaller than 1.15 per image. ASCII images for α1%, τ1 and τ2 were exported for both NADH and FAD for further analysis. α1% explains the ratio of bound to unbound FAD or the ratio of unbound to bound NADH and is a direct measure of cell metabolism. The fluorescence lifetimes τ1 and τ2 describe the fast and slow components of exponential decay.

4.6. Raman Imaging of Organoids

Spectral Raman mapping was performed on a customized inverted WITec alpha300 R Raman system (WITec GmbH, Ulm, Germany) equipped with a green laser (532 nm) and a CCD spectrograph with a grating of 600 g/mm. An incubation chamber (Okolab S.R.L.) was integrated into the setup to keep the organoids constantly at 37 °C. Images were acquired from at least three organoids at a laser power of 58 mW, an integration time per spectrum of 0.2 s and a pixel resolution of 1 × 1 µm at a size of 50 × 50 µm. All measurements were acquired with a 50× objective (Carl Zeiss AG, Oberkochen, Germany). Reference spectra of cytochrome c (derived from bovine heart, Sigma Aldrich), *cis* and *vtx* were recorded as single spectra with an accumulation of 10 spectra and 0.5 s integration time.

4.7. Multivariate Data Analysis

Image analysis of spectral maps was performed with the Project Five 5.2 software (WITec GmbH, Ulm, Germany). RMS data were preprocessed in regard to cosmic ray removal, polynomial baseline correction, cropping to 400–3000 cm^{-1} as well as area intensity normalization. True component analysis (TCA) was performed to analyze Raman images. In brief, TCA is a non-negative matrix factorization-based multivariate data analysis tool elaborating spectral components, which predominantly occur in the data set, allowing us to identify their spectral distribution by false color intensity distribution heatmaps. Based on TCA heatmaps, spectral information (20 spectra/organoid) representing nuclei or mitochondria was extracted for further in-depth analysis of the molecular composition by principal component analysis (PCA) using Unscrambler X10.5 (Camo, Norway). PCA is a gold standard multivariate data analysis tool for spectroscopic data, reducing the dimensionality of a set of spectral data on a vector-based approach. Each vector, the so-called principal component (PC), describes a variation in the spectra. Plotting PC values against each other visualizes a correlation or separation of two or more data sets. The interpretation of the underlying spectral changes can be derived from the PC loadings plot.

4.8. Feature Selection Using FeaSel-Net

We recently developed the neural network architecture FeaSel-Net that is capable of recursively selecting relevant wavenumber areas (features) in the classifier's input signal [65]. It is a combination of a neural network classifier and a feature selection algorithm. Other than dropout methods, this approach does not focus on stochastic pruning of parameters within hidden layers to improve generalizability but on deterministically pruning nodes in the input layer [66]. The package is open-source and can be downloaded from https://pypi.org/project/FeaSel-Net/, (Version 0.0.1). When features are selected, the optimizer in the neural network has to adapt to the fewer input signals and re-optimize the classifier with the new requirements. The selection process itself is a rather complex procedure, where the entropy is measured for every feature being masked, and the features with the highest entropy are kept. Contrarily to the interpretation of PCA loadings, this method provides a completely data-driven and unbiased evaluation of the findings and serves as an extension of the former method. In our recursive feature selection process, every selection was made whenever the threshold of classification accuracy of $\tau_{acc} = 0.98$ was consistently surpassed in the optimization process. The features were reduced by 20% every time the feature evaluation was executed. The reduction was made by masking the initial signal at the input of the neural network. All other parameters can be retrieved from Table S4.

4.9. Neural Network Classifier

Sample discrimination was undertaken by using a simple neural network from the open-source Keras and Tensorflow API (Google Brain). The model had a rhomboidal fully-connected layer structure with $5 - 10 - 20 - 10 - 3$ nodes, where the layer with 5 nodes was the input layer, and the one with 3 nodes was the output layer. The activation functions used were mainly ReLU (Rectified Linear Unit) and one sigmoid function in the last layer for probabilistic output values. The optimizer used was Adam [67], with a learning rate of $\eta = 0.005$. With a batch size of 128, the model was trained for 100 epochs, and a train test split of 0.8 was applied. The model was tested with all validation and training data to obtain the performance parameters in Section 0.

4.10. Feature Importance Clustering Analysis

In total, we curated three model-specific datasets (RT112, BCO and UCO), each with 72 measurements (six FLIM parameter values across 12 timepoints/drug concentration).

We first scaled all data to the z-norm. This was done to ensure that the clustering algorithm can focus on structural similarities and differences instead of amplitude-driven ones. We then performed clustering analysis using the method implemented in the R package *kmeans* for k = 2. Next, we performed a feature importance analysis using the function *FeatureImpCluster* in R by setting the number of true clusters to 2. We repeated the feature importance analysis 20 times using different random seeds. The function *FeatureImpCluster* computes the permutation misclassification rate for each variable of the data. The mean misclassification rate over all iterations can be interpreted as variable importance.

4.11. Statistical Analysis

Statistical analysis was performed using GraphPad Prism version 9.00 for Windows (GraphPad Software). Results are shown throughout the entire article as mean ± standard deviation. All data sets are tested for normal distribution using the Kolmogorov–Smirnov test; outliers were removed using Grubb's test with a confidence interval of 0.05. All n-numbers, applied tests, and corresponding significance for each result are listed in the figure legends. Experiments were performed at least 3 times.

Supplementary Materials: The following supporting information can be downloaded at: https://www.mdpi.com/article/10.3390/ijms23136956/s1.

Author Contributions: Conceptualization, N.H. and J.M.; data curation, L.B.; formal analysis, L.B., F.F. and J.L.F.; funding acquisition, A.H., A.S. and K.S.-L.; methodology, L.B. and F.F.; supervision, A.H., W.K.A. and J.M.; validation, J.M.; visualization, L.B. and F.F.; writing—original draft, L.B., F.F., J.L.F. and J.M.; writing—review & editing, N.H., A.H., A.S., W.K.A. and K.S.-L. All authors have read and agreed to the published version of the manuscript.

Funding: The work described in this paper was conducted in the framework of the Graduate School 2543/1 "Intraoperative Multi-Sensory Tissue-Differentiation in Oncology" (projects A2, A3, C1), funded by the German Research Foundation (DFG—Deutsche Forschungsgemeinschaft). This work was financially supported by the Ministry of Baden-Württemberg for Economic Affairs, Labor and Tourism (3-4332.62-NMI/65), and the Deutsche Forschungsgemeinschaft (INST 2388/33-1, INST 2388/64-1, and Germany's Excellence Strategy—EXC 2180-390900677).

Institutional Review Board Statement: The study was conducted according to the guidelines of the Declaration of Helsinki and approved by the local Ethics Committee (UKT IRB# 804/2020/B02).

Informed Consent Statement: Informed consent was obtained from all subjects involved in the study.

Data Availability Statement: All data are contained within the manuscript or supplementary material. Raw data are available on reasonable request from the corresponding author.

Acknowledgments: The authors thank Christine Mayer (UKT) for her excellent technical support.

Conflicts of Interest: The authors declare no conflict of interest. The funders had no role in the design of the study; in the collection, analyses, or interpretation of data; in the writing of the manuscript, or in the decision to publish the results.

References

1. Moreira, L.; Bakir, B.; Chatterji, P.; Dantes, Z.; Reichert, M.; Rustgi, A.K. Pancreas 3D Organoids: Current and Future Aspects as a Research Platform for Personalized Medicine in Pancreatic Cancer. *Cell. Mol. Gastroenterol. Hepatol.* **2018**, *5*, 289–298. [CrossRef] [PubMed]
2. Walsh, A.J.; Castellanos, J.A.; Nagathihalli, N.S.; Merchant, N.B.; Skala, M.C. Induced Metabolism Changes in Murine and Human Pancreatic Cancer Organoids Reveals Heterogeneous Drug Response. *Pancreas* **2016**, *45*, 863–869. [CrossRef] [PubMed]
3. Sharick, J.T.; Walsh, C.M.; Sprackling, C.M.; Pasch, C.A.; Pham, D.L.; Esbona, K.; Choudhary, A.; Garcia-Valera, R.; Burkard, M.E.; McGregor, S.M.; et al. Metabolic Heterogeneity in Patient Tumor-Derived Organoids by Primary Site and Drug Treatment. *Front. Oncol.* **2020**, *10*, 553. [CrossRef] [PubMed]
4. Lin, V.J.T.; Hu, J.; Zolekar, A.; Yan, L.-J.; Wang, Y.-C. Urine Sample-Derived Cerebral Organoids Suitable for Studying Neurodevelopment and Pharmacological Responses. *Front. Cell Dev. Biol.* **2020**, *8*, 304. [CrossRef]
5. Boj, S.F.; Hwang, C.I.; Baker, L.A.; Chio, I.I.C.; Engle, D.D.; Corbo, V.; Jager, M.; Ponz-Sarvise, M.; Tiriac, H.; Spector, M.S.; et al. Organoid Models of Human and Mouse Ductal Pancreatic Cancer. *Cell* **2015**, *160*, 324–338. [CrossRef]

6. Earl, J.; Rico, D.; Carrillo-De-Santa-Pau, E.; Rodríguez-Santiago, B.; Méndez-Pertuz, M.; Auer, H.; Gómez, G.; Grossman, H.B.; Pisano, D.G.; Schulz, W.A.; et al. The UBC-40 Urothelial Bladder Cancer cell line index: A genomic resource for functional studies. *BMC Genom.* **2015**, *16*, 403. [CrossRef]
7. Kobayashi, T.; Owczarek, T.B.; McKiernan, J.M.; Abate-Shen, C. Modelling bladder cancer in mice: Opportunities and challenges. *Nat. Rev. Cancer* **2015**, *15*, 42–54. [CrossRef]
8. Lee, S.H.; Hu, W.; Matulay, J.T.; Silva, M.V.; Owczarek, T.B.; Kim, K.; Chua, C.W.; Barlow, L.J.; Kandoth, C.; Williams, A.B.; et al. Tumor Evolution and Drug Response in Patient-Derived Organoid Models of Bladder Cancer. *Cell* **2018**, *173*, 515–528.e517. [CrossRef]
9. Mullenders, J.; De Jongh, E.; Brousali, A.; Roosen, M.; Blom, J.P.A.; Begthel, H.; Korving, J.; Jonges, T.; Kranenburg, O.; Meijer, R.; et al. Mouse and human urothelial cancer organoids: A tool for bladder cancer research. *Proc. Natl. Acad. Sci. USA* **2019**, *116*, 4567–4574. [CrossRef]
10. Pollehne, P.; Mojarro, I.A.M.; Schneider, J.; Amend, B.; Fend, F.; Stenzl, A.; Aicher, W.K.; Harland, N. MP06-06 Establishment and Evaluation of a simplified approach to patient derived bladder cancer organoids using urine. *J. Urol.* **2022**, *207*, e79. [CrossRef]
11. Chin, L.; Andersen, J.N.; Futreal, P.A. Cancer genomics: From discovery science to personalized medicine. *Nat. Med.* **2011**, *17*, 297–303. [CrossRef] [PubMed]
12. Diamandis, M.; White, N.M.A.; Yousef, G.M. Personalized Medicine: Marking a New Epoch in Cancer Patient Management. *Mol. Cancer Res.* **2010**, *8*, 1175–1187. [CrossRef] [PubMed]
13. Fenstermacher, D.A.; Wenham, R.M.; Rollison, D.E.; Dalton, W.S. Implementing Personalized Medicine in a Cancer Center. *Cancer J.* **2011**, *17*, 528–536. [CrossRef] [PubMed]
14. Marusyk, A.; Polyak, K. Tumor heterogeneity: Causes and consequences. *Biochim. Biophys. Acta (BBA) Rev. Cancer* **2010**, *1805*, 105–117. [CrossRef]
15. Junttila, M.R.; De Sauvage, F.J. Influence of tumour micro-environment heterogeneity on therapeutic response. *Nature* **2013**, *501*, 346–354. [CrossRef]
16. Gong, X.; Lin, C.; Cheng, J.; Su, J.; Zhao, H.; Liu, T.; Wen, X.; Zhao, P. Generation of Multicellular Tumor Spheroids with Microwell-Based Agarose Scaffolds for Drug Testing. *PLoS ONE* **2015**, *10*, e0130348. [CrossRef]
17. Heikal, A.A. Intracellular coenzymes as natural biomarkers for metabolic activities and mitochondrial anomalies. *Biomark. Med.* **2010**, *4*, 241–263. [CrossRef]
18. Warburg, O.; Wind, F.; Negelein, E. The metabolism of tumors in the body. *J. Gen. Physiol.* **1927**, *8*, 519–530. [CrossRef]
19. Pettit, F.H.; Pelley, J.W.; Reed, L.J. Regulation of pyruvate dehydrogenase kinase and phosphatase by acetyl-CoA/CoA and NADH/NAD ratios. *Biochem. Biophys. Res. Commun.* **1975**, *65*, 575–582. [CrossRef]
20. Fong, E.J.; Strelez, C.; Mumenthaler, S.M. A Perspective on Expanding Our Understanding of Cancer Treatments by Integrating Approaches from the Biological and Physical Sciences. *SLAS Discov.* **2020**, *25*, 672–683. [CrossRef]
21. Niaura, G. Raman Spectroscopy in Analysis of Biomolecules. In *Encyclopedia of Analytical Chemistry: Applications, Theory and Instrumentation*; John Wiley & Sons, Ltd.: Hoboken, NJ, USA, 2014. [CrossRef]
22. Chen, P.; Zhang, F.; Lin, L.; Bai, H.; Zhang, L.; Tang, G.Q.; Fang, H.; Mu, G.G.; Gong, W.; Liu, Z.P.; et al. Raman Spectroscopy for Noninvasive Monitoring of Umbilical Cord Mesenchymal Stem Cells Viability Transitions. In *Stem Cells in Clinic and Research*; IntechOpen: London, UK, 2011.
23. Becker, L.; Janssen, N.; Layland, S.L.; Mürdter, T.E.; Nies, A.T.; Schenke-Layland, K.; Marzi, J. Raman Imaging and Fluorescence Lifetime Imaging Microscopy for Diagnosis of Cancer State and Metabolic Monitoring. *Cancers* **2021**, *13*, 5682. [CrossRef] [PubMed]
24. Hsu, C.-C.; Xu, J.; Brinkhof, B.; Ye, H. A single-cell Raman-based platform to identify developmental stages of human pluripotent stem cell-derived neurons. *Proc. Natl. Acad. Sci. USA* **2020**, *117*, 18412–18423. [CrossRef] [PubMed]
25. González-Solís, J.L.; Martínez-Espinosa, J.C.; Salgado-Román, J.M.; Palomares-Anda, P. Monitoring of chemotherapy leukemia treatment using Raman spectroscopy and principal component analysis. *Lasers Med. Sci.* **2014**, *29*, 1241–1249. [CrossRef] [PubMed]
26. Feizpour, A.; Marstrand, T.; Bastholm, L.; Eirefelt, S.; Evans, C.L. Label-Free Quantification of Pharmacokinetics in Skin with Stimulated Raman Scattering Microscopy and Deep Learning. *J. Investig. Dermatol.* **2021**, *141*, 395–403. [CrossRef] [PubMed]
27. Hira, M.T.; Razzaque, M.A.; Angione, C.; Scrivens, J.; Sawan, S.; Sarker, M. Integrated multi-omics analysis of ovarian cancer using variational autoencoders. *Sci. Rep.* **2021**, *11*, 6265. [CrossRef]
28. Hu, S.; Morris, I.K.; Singh, J.P.; Smith, K.M.; Spiro, T.G. Complete assignment of cytochrome c resonance Raman spectra via enzymic reconstitution with isotopically labeled hemes. *J. Am. Chem. Soc.* **1993**, *115*, 12446–12458. [CrossRef]
29. Brazhe, N.A.; Evlyukhin, A.B.; Goodilin, E.A.; Semenova, A.A.; Novikov, S.M.; Bozhevolnyi, S.I.; Chichkov, B.N.; Sarycheva, A.S.; Baizhumanov, A.A.; Nikelshparg, E.I.; et al. Probing cytochrome c in living mitochondria with surface-enhanced Raman spectroscopy. *Sci. Rep.* **2015**, *5*, 13793. [CrossRef]
30. Notingher, I.; Green, C.; Dyer, C.; Perkins, E.; Hopkins, N.; Lindsay, C.; Hench, L.L. Discrimination between ricin and sulphur mustard toxicity in vitro using Raman spectroscopy. *J. R. Soc. Interface* **2004**, *1*, 79–90. [CrossRef]
31. Malini, R.; Venkatakrishna, K.; Kurien, J.; Pai, K.M.; Rao, L.; Kartha, V.B.; Krishna, C.M. Discrimination of normal, inflammatory, premalignant, and malignant oral tissue: A Raman spectroscopy study. *Biopolymers* **2006**, *81*, 179–193. [CrossRef]
32. Naumann, D. Infrared and NIR Raman spectroscopy in medical microbiology. *Proc. SPIE* **1998**, *3257*, 245–257. [CrossRef]

33. Shetty, G.; Kendall, C.; Shepherd, N.; Stone, N.; Barr, H. Raman spectroscopy: Elucidation of biochemical changes in carcinogenesis of oesophagus. *Br. J. Cancer* **2006**, *94*, 1460–1464. [CrossRef] [PubMed]
34. Thomas, G.J.; Benevides, J.M. An A-helix structure for poly(dA-dT) poly(dA-dT). *Biopolymers* **1985**, *24*, 1101–1105. [CrossRef] [PubMed]
35. Ruiz-Chica, A.J.; Medina, M.A.; Sánchez-Jiménez, F.; Ramírez, F.J. Characterization by Raman spectroscopy of conformational changes on guanine–cytosine and adenine–thymine oligonucleotides induced by aminooxy analogues of spermidine. *J. Raman Spectrosc.* **2004**, *35*, 93–100. [CrossRef]
36. Bik, E.; Mateuszuk, L.; Stojak, M.; Chlopicki, S.; Baranska, M.; Majzner, K. Menadione-induced endothelial inflammation detected by Raman spectroscopy. *Biochim. Et Biophys. Acta (BBA) Mol. Cell Res.* **2021**, *1868*, 118911. [CrossRef]
37. Benevides, J.M.; Wang, A.H.J.; Van Der Marel, G.A.; Van Boom, J.H.; Thomas, G.J. Crystal and solution structures of the B-DNA dodecamer d(CGCAAATTTGCG) probed by Raman spectroscopy: Heterogeneity in the crystal structure does not persist in the solution structure. *Biochemistry* **1988**, *27*, 931–938. [CrossRef]
38. Russo, V.; Candeloro, P.; Malara, N.; Perozziello, G.; Iannone, M.; Scicchitano, M.; Mollace, R.; Musolino, V.; Gliozzi, M.; Carresi, C.; et al. Key Role of Cytochrome C for Apoptosis Detection Using Raman Microimaging in an Animal Model of Brain Ischemia with Insulin Treatment. *Appl. Spectrosc.* **2019**, *73*, 1208–1217. [CrossRef]
39. Lakshmi, R.J.; Kartha, V.B.; Murali Krishna, C.; Solomon, J.G.R.; Ullas, G.; Uma Devi, P. Tissue Raman Spectroscopy for the Study of Radiation Damage: Brain Irradiation of Mice. *Radiat. Res.* **2002**, *157*, 175–182. [CrossRef]
40. Chrobak, E.; Jastrzębska, M.; Bębenek, E.; Kadela-Tomanek, M.; Marciniec, K.; Latocha, M.; Wrzalik, R.; Kusz, J.; Boryczka, S. Molecular Structure, In Vitro Anticancer Study and Molecular Docking of New Phosphate Derivatives of Betulin. *Molecules* **2021**, *26*, 737. [CrossRef]
41. Stone, N.; Kendall, C.; Smith, J.; Crow, P.; Barr, H. Raman spectroscopy for identification of epithelial cancers. *Faraday Discuss.* **2004**, *126*, 141–157. [CrossRef]
42. Ó Faoláin, E.; Hunter, M.B.; Byrne, J.M.; Kelehan, P.; McNamara, M.; Byrne, H.J.; Lyng, F.M. A study examining the effects of tissue processing on human tissue sections using vibrational spectroscopy. *Vib. Spectrosc.* **2005**, *38*, 121–127. [CrossRef]
43. Krafft, C.; Sobottka, S.B.; Schackert, G.; Salzer, R. Raman and infrared spectroscopic mapping of human primary intracranial tumors: A comparative study. *J. Raman Spectrosc.* **2006**, *37*, 367–375. [CrossRef]
44. Aminuddin, A.; Ng, P.Y.; Leong, C.-O.; Chua, E.W. Mitochondrial DNA alterations may influence the cisplatin responsiveness of oral squamous cell carcinoma. *Sci. Rep.* **2020**, *10*, 7885. [CrossRef] [PubMed]
45. Von Stechow, L.; Ruiz-Aracama, A.; Van De Water, B.; Peijnenburg, A.; Danen, E.; Lommen, A. Identification of Cisplatin-Regulated Metabolic Pathways in Pluripotent Stem Cells. *PLoS ONE* **2013**, *8*, e76476. [CrossRef] [PubMed]
46. Liu, H.; Michmerhuizen, M.J.; Lao, Y.; Wan, K.; Salem, A.H.; Sawicki, J.; Serby, M.; Vaidyanathan, S.; Wong, S.L.; Agarwal, S.; et al. Metabolism and Disposition of a Novel B-Cell Lymphoma-2 Inhibitor Venetoclax in Humans and Characterization of Its Unusual Metabolites. *Drug Metab. Dispos.* **2017**, *45*, 294–305. [CrossRef] [PubMed]
47. Chacko, J.V.; Eliceiri, K.W. Autofluorescence lifetime imaging of cellular metabolism: Sensitivity toward cell density, pH, intracellular, and intercellular heterogeneity. *Cytom. Part A* **2019**, *95*, 56–69. [CrossRef]
48. Jamieson, L.E.; Harrison, D.J.; Campbell, C.J. Raman spectroscopy investigation of biochemical changes in tumor spheroids with aging and after treatment with staurosporine. *J. Biophotonics* **2019**, *12*, e201800201. [CrossRef]
49. Eastman, A. The formation, isolation and characterization of DNA adducts produced by anticancer platinum complexes. *Pharmacol. Ther.* **1987**, *34*, 155–166. [CrossRef]
50. Enoiu, M.; Jiricny, J.; Schärer, O.D. Repair of cisplatin-induced DNA interstrand crosslinks by a replication-independent pathway involving transcription-coupled repair and translesion synthesis. *Nucleic Acids Res.* **2012**, *40*, 8953–8964. [CrossRef]
51. Choi, Y.-M.; Kim, H.-K.; Shim, W.; Anwar, M.A.; Kwon, J.-W.; Kwon, H.-K.; Kim, H.J.; Jeong, H.; Kim, H.M.; Hwang, D.; et al. Mechanism of Cisplatin-Induced Cytotoxicity Is Correlated to Impaired Metabolism Due to Mitochondrial ROS Generation. *PLoS ONE* **2015**, *10*, e0135083. [CrossRef]
52. Marzano, C.; Gandin, V.; Folda, A.; Scutari, G.; Bindoli, A.; Rigobello, M.P. Inhibition of thioredoxin reductase by auranofin induces apoptosis in cisplatin-resistant human ovarian cancer cells. *Free. Radic. Biol. Med.* **2007**, *42*, 872–881. [CrossRef]
53. Rybak, L. Dose dependent protection by lipoic acid against cisplatin-induced ototoxicity in rats: Antioxidant defense system. *Toxicol. Sci.* **1999**, *47*, 195–202. [CrossRef] [PubMed]
54. Marullo, R.; Werner, E.; Degtyareva, N.; Moore, B.; Altavilla, G.; Ramalingam, S.S.; Doetsch, P.W. Cisplatin Induces a Mitochondrial-ROS Response That Contributes to Cytotoxicity Depending on Mitochondrial Redox Status and Bioenergetic Functions. *PLoS ONE* **2013**, *8*, e81162. [CrossRef] [PubMed]
55. Sharma, A.; Smith, H.J.; Yao, P.; Mair, W.B. Causal roles of mitochondrial dynamics in longevity and healthy aging. *EMBO Rep.* **2019**, *20*, e48395. [CrossRef]
56. Suhling, K.; Hirvonen, L.M.; Levitt, J.A.; Chung, P.-H.; Tregidgo, C.; Le Marois, A.; Rusakov, D.A.; Zheng, K.; Ameer-Beg, S.; Poland, S.; et al. Fluorescence lifetime imaging (FLIM): Basic concepts and some recent developments. *Med. Photonics* **2015**, *27*, 3–40. [CrossRef]
57. Shimolina, L.E.; Gulin, A.A.; Paez-Perez, M.; López-Duarte, I.; Druzhkova, I.N.; Lukina, M.M.; Gubina, M.V.; Brooks, N.J.; Zagaynova, E.V.; Kuimova, M.K.; et al. Mapping cisplatin-induced viscosity alterations in cancer cells using molecular rotor and fluorescence lifetime imaging microscopy. *J. Biomed. Opt.* **2020**, *25*, 126004. [CrossRef] [PubMed]

Supplementary Materials

Table S1. Most relevant features identified in PCA loadings.

Dataset	**ν_1 [cm^{-1}]**	**ν_2 [cm^{-1}]**	**ν_3 [cm^{-1}]**	**ν_4 [cm^{-1}]**	**ν_5 [cm^{-1}]**
Nuclei					
RT112	744	1315	1450	1585	1660
BCO	751	1308	1447	1591	1660
UCO	680	1406	1499	1591	1666
Mitochondria					
RT112	1092	1251	1321	1635	1700
BCO	1255	1325	1460	1600	1730
UCO	1138	1242	1317	1451	1658

Table S2. Relative improvement [%] of the FeaSel-Net biomarker retrieval compared to the PCA loadings method (accuracy ACC, sensitivity SEN, and specificity SPE).

Dataset	**ACC**	**SEN**	**SPE**
Nuclei (average)	10.1	18.0	7.1
RT112	13.6	23.9	9.5
BCO	7.2	12.6	5.1
UCO	9.6	17.6	6.6
Mitochondria (average)	5.3	9.1	3.6
RT112	8.3	14.6	5.7
BCO	1.9	3.2	1.4
UCO	5.5	10.1	3.8
All Data	7.3	12.8	5.1

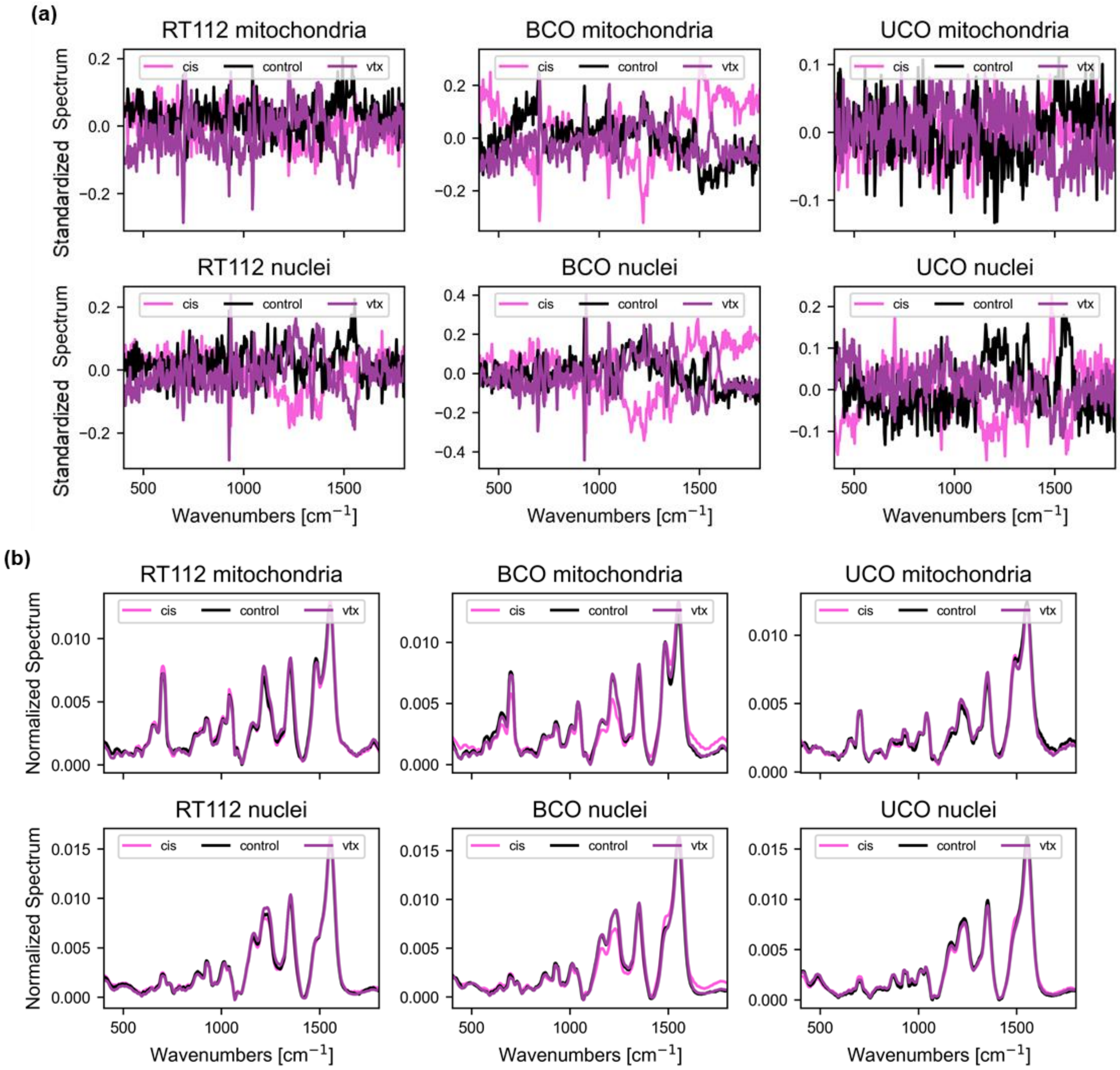

Figure S1. Raman spectra averaged over each class. (a) shows the mean spectra for the standardized spectra along the feature axis whereas **(b)** shows the normalized spectrum along the sample axis.

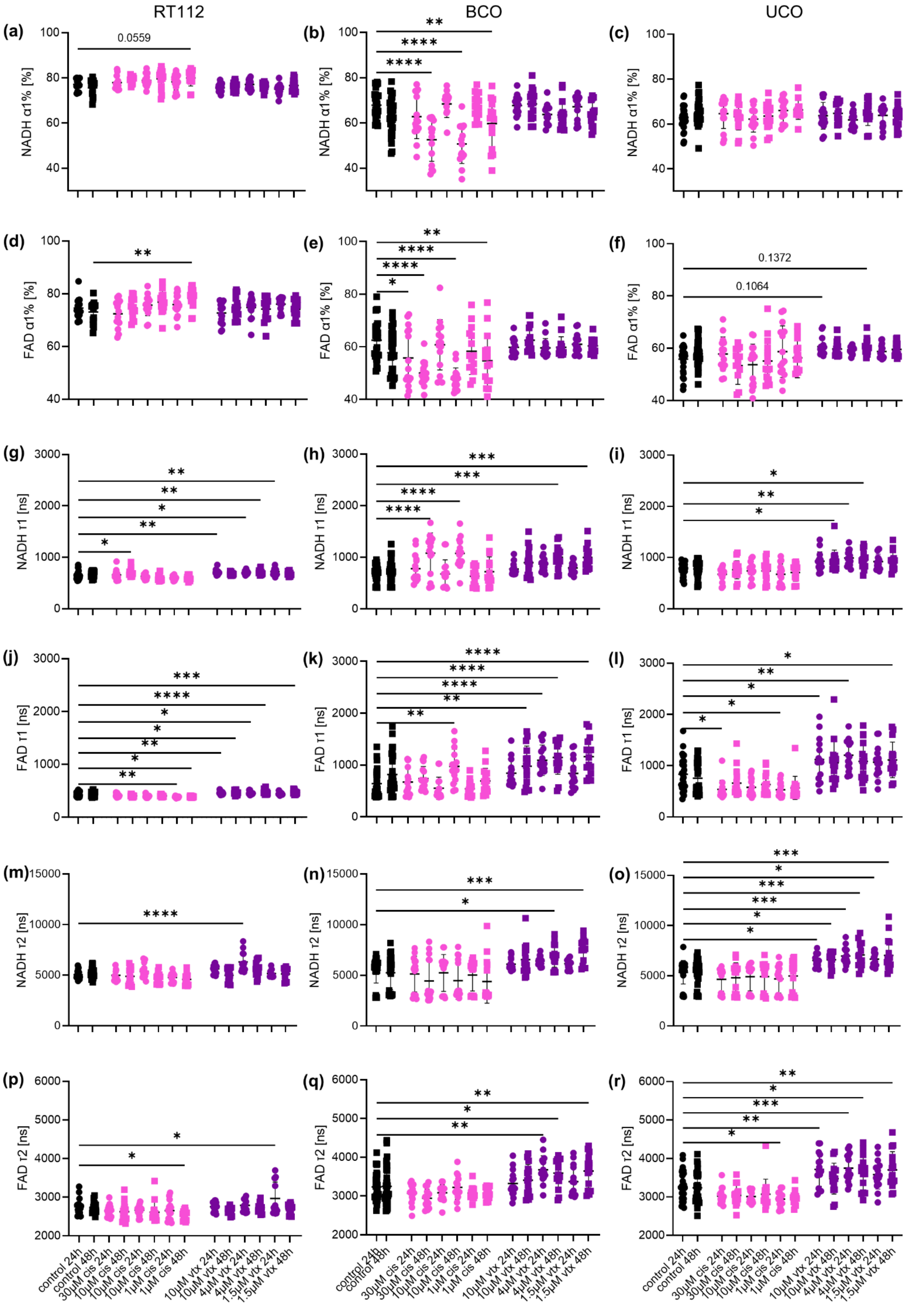

Figure S2. FLIM results for organoids derived from the cell line RT112, BCO and UCO. (a-c) α1% from NADH. **(d-f)** α1% from FAD. **(g-i)** τ1 from NADH. **j-l)** τ1 from FAD. **m-o)** τ2 from NADH. **(p-r)** τ2 from FAD. Data represent average FLIM parameters per organoid, n=15, One-way ANOVA, $p<0.05$.

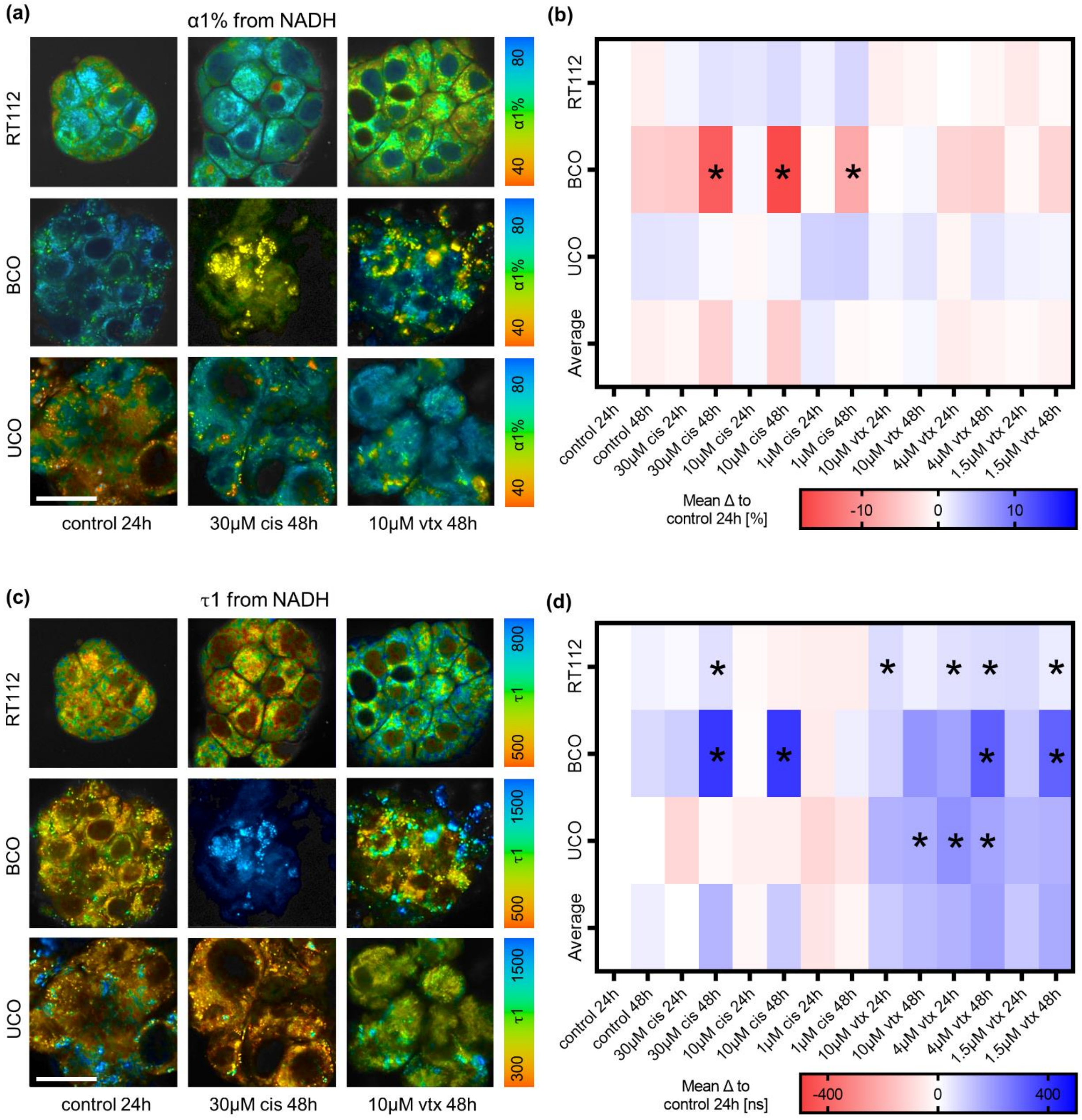

Figure S3. NADH FLIM of bladder cancer organoids. (a) α1% and **(c)** τ1 of RT112, BCO and UCO. Displayed are untreated organoids after 24 hours, 30 µM *cis* treated organoids after 48 hours and 10 µM *vtx* treated organoids after 48 hours. Scale bar: 25 µm. **(b)** Heatmap of mean differences of NADH α1% to the control after 24 hours. **(d)** Heatmap of mean differences of NADH τ2 to the control after 24 hours. One-way ANOVA, n=15, p<0.05.

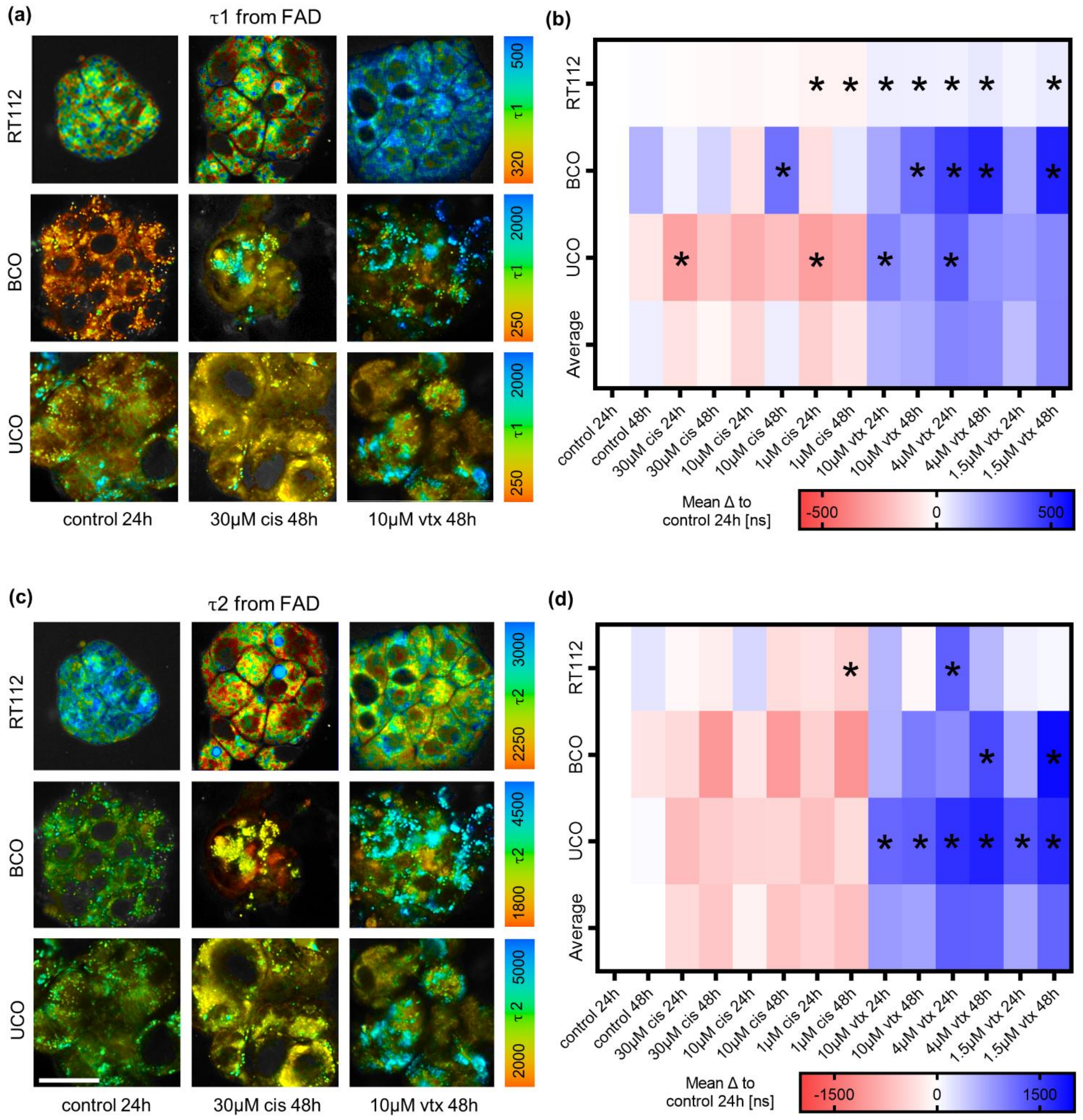

Figure S4. FAD FLIM of bladder cancer organoids. (a) τ1 from FAD and τ2 from FAD **(c)** of RT112, BCO and UCO. Displayed are untreated organoids after 24 hours, 30µM *cis* treated organoids after 48 hours and 10µM *vtx* treated organoids after 48 hours. Scale bar: 25µm. **(b)** Heatmap of mean differences of τ1 from FAD to the control after 24 hours. **(d)** Heatmap of mean differences of τ2 from FAD to the control after 24 hours. Statistical analysis: One-way ANOVA, n=15, $p<0.05$.

Table S3. Information on tumor samples.

Patient	UCO	BCO
Age (years)	85	64
Gender	male	male
Localization	bladder	bladder
Tumor Stage (pT)	pT1	pT2
Tumor Grade (G)	G2	G3
Specimen retrieval	Rinsing urine	Radical cystectomy

Table S4. Parameters for the FeaSel-Net Callback.

Parameter	Symbol	Value
Number of features	n_f	3
Evaluation type	-	accuracy
Threshold value	τ_{acc}	0.98
Threshold decay	σ_{acc}	0.0
Minimum number of epochs	d_{min}	20
Maximum number of epochs	d_{max}	150
Pruning rate	π	0.2
Pruning type	-	exponential
Number of samples per class (eval.)	n_s	10
Normalization of eval. loss	-	min-max norm
Decision metric	-	average

Appendix II: Becker L., Janssen N., Wallisch S., Mürdter T. E., Renner P., Dahlke M. H., Marzi J., Nies A. T., Schwab M., Schenke-Layland K., *Label-free Raman Microscopy-based Monitoring of Anti-cancer Drug Effects in Colorectal Cancer Organoids towards Patient-individualized Optimization of Treatments*

Label-free Raman microscopy and fluorescence lifetime imaging-based monitoring of anti-cancer drug effects in colorectal cancer organoids towards patient-individualized optimization of treatments.

Lucas Becker[a,b], Nicole Janssen[b,c], Svenja Wallisch[c], Thomas E Mürdter[b,c], Philipp Renner[c,d], Marc H Dahlke[c,d], Julia Marzi[a,b,e], Anne T Nies[b,d], Matthias Schwab[b,c,f,g] and Katja Schenke-Layland*[a,b,e]

a Institute of Biomedical Engineering, Department for Medical Technologies and Regenerative Medicine, University of Tübingen, 72076 Tübingen, Germany
b Cluster of Excellence iFIT (EXC 2180) "Image-Guided and Functionally Instructed Tumor Therapies", University of Tübingen, Germany
c Dr. Margarete Fischer-Bosch Institute of Clinical Pharmacology, 70376 Stuttgart, Germany
d Department of Surgery, Robert Bosch Hospital,70367 Stuttgart, Germany
e Natural and Medical Sciences Institute (NMI) at the University of Tübingen, 72770 Reutlingen, Germany
f Department of Clinical Pharmacology, University Hospital Tübingen, 72076 Tübingen, Germany
g Department of Biochemistry and Pharmacy, University of Tübingen, 72076 Tübingen, Germany

Highlights

- No significant mRNA and ABC transporter differences in SN-38 resistant vs responsive CRC organoids
- RMS and FLIM allow molecular and metabolic characterization of CRC organoids
- Molecular and metabolic discrimination of SN-38 resistant vs responsive donors via multivariate analysis of RMS and FLIM data
- FLIM allows time-resolved marker-independent drug tracing in CRC organoids
- The importance of mitochondria should be considered as a critical factor in drug sensitivity

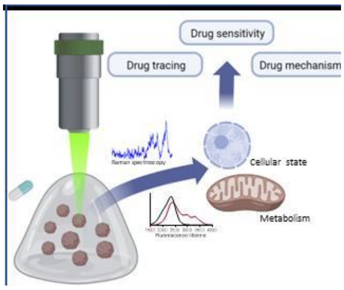

Abstract

Introduction: Primary and acquired therapy resistance of solid tumors are major problems in clinical oncology including different mechanisms such as decreased drug influx and/or increased drug efflux. To study and understand variability of such effects novel models for drug screening are required. Of particular interest are primary patient-derived tumor organoids recapitulating in vivo tumor biology since they represent the interaction of cellular and extracellular environments. Of note, expression of genes encoding to enzymes involved in adsorption, metabolism and excretion of drugs are preserved in such culture systems.

Objectives: In this study, we describe a non-invasive imaging procedure (i.e., Raman-microspectroscopy (RMS), Fluorescence Lifetime Imaging (FLIM)) allowing label-free and real-time cellular analysis as well as monitoring effects of drug treatment.

Methods: A biobank of colorectal cancer (CRC) organoids was established from surgical specimens and cultured in Matrigel. Organoids were exposed to various concentrations of cytotoxic and targeted agents (SN-38) relevant to the treatment of CRC for several days. Real-time cellular response towards drug treatment was analyzed using non-invasive imaging techniques such as RMS. To assess information about metabolic activity FLIM was used to monitor the local fluorophore environment of NADH and FAD. Multivariate data analysis was employed to identify drug responsiveness on continuously monitored CRC organoids.

Results: While mRNA and histological analysis of ABC transporters revealed no statistically significant differences between resistant and responding donors, RMS and FLIM in combination with multivariate data analysis allowed discrimination of drug sensitivity in CRC organoids. RMS and FLIM allow molecular and metabolic assessment of drug effects indicating the importance of mitochondrial activity in drug resistance. In addition, both methods allowed non-invasive tracing of the drug in the living organoid.

Conclusion: Overall, RMS and FLIM are enabling technologies to non-invasively evaluate tumor-drug interactions, with the possibility to screen for patient-individualized effectivity optimizing drug treatment.

Keywords

Organoids; non-destructive imaging; Drug sensitivity; Metabolism; Drug screening

Introduction

Primary and acquired resistance to therapy in solid tumors is a major challenge in clinical oncology and can occur through a variety of mechanisms, including decreased drug influx or increased drug efflux. Colorectal cancer (CRC) is one of the most common cancers and is a leading cause of cancer-related deaths worldwide [1]. Dependent on the cancer stage and location of the tumor at the time of diagnosis, as well as patient specific characteristic, the major treatment options remain chemotherapy and surgery [2]. Given the availability of numerous chemotherapeutic agents, the average survival of advanced colorectal cancer patients has improved significantly in recent years. While treatment response rates to current systemic chemotherapies have been reported to be as high as 50%, multidrug resistance (MDR) evolves in nearly all patients with CRC, reducing the therapeutic efficacy of anticancer drugs and eventually leading to chemotherapy failure and patient death [3]. Consequently, identifying the patient-specific mechanisms of drug efficacy prior to treatment plays an essential function in the successful outcome of chemotherapy and to exclude excessive use of drugs in order to avoid side effects and suffering of patients.

Patient-derived three-dimensional (3D) tumor organoids yield the potential to be valuable personalized in vitro models for high-throughput testing of drugs [4,5]. Organoids that mimic in vivo tumor biology through the interaction of cellular and extracellular milieu can be rapidly produced from small amounts of tissue. Such culture systems preserve the expression of genes encoding enzymes and transporters such as ATP-binding cassettes (ABC) involved in drug adsorption, metabolism, and excretion [6].

The gold standard for monitoring drug-induced effects in cell cultures include cell viability assays or mRNA and protein expression assays allowing accurate assessment of total DNA or protein composition [7,8]. Such time consuming and lysis requiring techniques evaluate the response of a batch of organoids and omit cellular heterogeneity promoting resistance to tumor treatment [9]. Over the years, advances in non-destructive imaging techniques such as Raman spectroscopy (RMS) and fluorescence lifetime imaging microscopy (FLIM) have gained attention in diagnostic applications as they provide insights into molecular composition and cellular metabolism [10].

RMS is an ideal tool for the marker-independent investigation of molecular information and molecular interactions based on the interaction between laser light and the dynamic state of chemical bonds by employing molecule-specific spectral fingerprints as readouts [11]. The latter provide molecule sensitive information enabling the localization of subcellular structures such as nuclei, mitochondria, or lipids [10,12,13]. Complementary to RMS, FLIM is a technique that exploits the endogenous fluorescence of nicotinamide adenine dinucleotide hydride (NADH) and flavin adenine dinucleotide (FAD) to obtain information about intracellular metabolic processes. Endogenous fluorophores are sensitive biomarkers by virtue of their emission properties impacted by alterations in their microenvironment as well as the metabolic state, pathological condition, or morphology of the sample [14].

In this study, patient-derived 3D CRC organoids from SN-38 resistant and responsive donors were compared in their reaction to the drug. RMS and FLIM were implemented for time-resolved and spatially assessment of cellular drug response and drug tracing in dependence of drug concentrations and time points.

Material and Methods

Cell Culture of Organoids in Matrigel

CRC organoids from six patients were obtained and cultured as previously described [15]. Patient specific characteristics and tumor classifications are summarized in Table 1.

EC50 Analysis

Pipetting of tumor organoids/cells was done with BSA-coated tips. Organoids grown in 75%

Matrigel™ domes and tumor organoid medium were harvested by dissolving the matrix with ice-cold PBS. Organoids were washed with ice-cold PBS and resuspended in TrypLE. Enzymatic and mechanical dissociation of organoids was monitored microscopically and stopped by dilution with DMEM/F12. Wells of a 384-well plate were precoated with 8 µL of 15% Matrigel™ in tumor organoid medium and 200 small tumor organoids suspended in 32 µL of 2% Matrigel™ in tumor organoid medium were added. After 1 day, 20 µL of a dilution series of the test drug was added to final concentrations ranging from 10 -10 to 10 -5 M. After another 24 h, 20 µL of prewarmed Celltiter Glo® 3D reagent was added, the plate was incubated at 37°C for 30 min and luminescence was monitored using a multiplate reader (Victor Nivo, PerkingElmer). Each assay comprised as controls 2% Matrigel™ in tumor organoid medium with and without 3% DMSO.

Sample Preparation for Spectroscopic Raman- and FLIM Measurements

For spectroscopic measurements, CRC organoids were transferred to µ-slides with 8 wells (ibidi GmbH, Gräfelfing, Germany). Organoids were incubated with 500 nM, 50 nM and 5 nM of SN-38 (Sellek Chemicals, Houston, USA) in cell culture medium for 0-48 hours at 37°C in 5% CO_2 atmosphere. SN-38 is dissolved in 20% Captisol (Sellek Chemicals, Houston, USA). Controls were kept in cell culture medium. Organoids were measured with RMS and

FLIM. Prior to Raman measurements, the samples were washed with PBS twice to remove phenol red interfering with Raman measurements. Organoids were maintained in 200 µl of imaging medium throughout measurements and then immersed in cell culture medium with or without drug.

Raman Imaging of Organoids

Raman mapping was performed as previously described [5]. Raman maps were acquired from at least three organoids per patient, treatment and timepoint of three independent passages. A reference spectrum of SN-38 (Sigma Aldrich) was recorded as single spectra with an accumulation of 10 spectra and 0.5 s integration time.

Multivariate Data Analysis

Raman data processing was performed as previously described [5]. True component analysis (TCA) was performed to identify different subcellular structures in Raman images. Based on TCA heatmaps spectral information (20 spectra/organoid) representing mitochondria and nuclei were extracted for further in-depth analysis of the molecular composition by principal component analysis (PCA) using Unscrambler X10.5 (Camo, Oslo, Norway).

Neural Network Classification

Binary classification of Raman spectra has been undertaken by using a simple fully connected neural network from the open-source Keras and Tensorflow API (Google Brain). It was aimed to classify the data into one of the two classes: *resistant* and *responsive*. Information about the model architecture can be found in Supplementary S1.

Raman-based SN-38 Quantification

Quantification of SN-38 based on Raman images was acquired from 20 averaged Raman spectra per organoid from TCA heatmaps of SN-38. Peak intensities at 1561 cm^{-1}, providing the highest signal intensity of the drug, were compared among treatments and controls. The uptake of SN-38 in organoids was considered if the intensity of the signal was above the mean + standard deviation of the controls.

FLIM Imaging of Organoids

FLIM imaging was performed as previously described [5]. Images were acquired from at least five organoids from three passages each per patient and treatment.

FLIM Data Analysis

Analysis of FLIM images was performed as previously described [5].

FLIM-based SN-38 Quantification

To quantify the uptake of the drug inside organoids, ASCII images containing $\tau 2$ of FAD were imported in Matlab 2019b. Pixels containing values above 3150 ns were counted and normalized to the total area of organoids. The uptake of SN-38 in organoids was considered if the ratio of pixels 3150 ns was above 10% of the total organoid area.

Statistical Analysis

Statistical analysis was performed using GraphPad Prism version 9.00 for Windows (GraphPad Software). Results are shown throughout the entire article as mean ± standard deviation. All *n*-numbers, applied tests, and corresponding significance for each result are listed in the figure legends. Experiments were performed at least 3 times to obtain a minimum of 9 Raman measurements and 15 FLIM measurements for treatment, timepoint and donor.

Results

In this study, the response of CRC organoids from six different patients to various concentrations of the topoisomerase I inhibitor SN-38 was evaluated. An EC50 evaluation was conducted to determine the drug responsiveness of each donor. The cellular drug responses were then measured using RMS and FLIM, which allowed for spatially and temporally resolved analysis as well as real-time monitoring of drug uptake. Multivariate data analysis and neural network classification were performed to distinguish between responsive and resistant donors in response to SN-38.

EC50 and mRNA characterization

The results of the EC50 evaluation showed that out of six donors tested, three had a high response to the drug (Responsive #1: 25 nM ± 12 nM; Responsive #2: 611 nM ± 398 nM; Responsive #3: 7878 nM ± 2122 nM), while the other three showed a low response after 24 hours (Resistant #1, #2, #3: >10000 nM) (Table 2). The high response donors displayed a significant decrease in cell viability at lower drug concentrations, indicating a higher sensitivity to the drug’s effect. On the other hand, the resistant donors showed only a slight decrease in cell viability even at higher drug concentrations, indicating a lower sensitivity to the drug’s effect. These results provide important insights into the variability of drug response among different individuals and can inform personalized treatment approaches.

Raman Microspectroscopy Allows Label-free Imaging of CRC Organoids

Based on EC50 values, patients were classified into two groups: *responsive* and *resistant*. RMS was performed on CRC organoids 24 and 48 hours after treatment with different concentrations of SN-38 (5 nM, 50 nM, 500 nM), respectively. True Component Analysis (TCA) was utilized to identify five major cellular components assigned to mitochondria (red), nuclei (blue), cytoplasm (green), lipids (turquoise), and SN-38 (pink) based on the location in the organoids (Fig. 2a) and their spectral Raman fingerprint (Fig. 2b). The pronounced peaks at 747 and 1130 cm^{-1} reported for cytochrome c and b [16,17] and the internal measurement of a cytochrome c reference Raman spectrum were used to assign mitochondria [5], while nuclei were identified by their specific peak pair at 798 and 1096 cm^{-1}, indicative for the phosphate backbone of DNA [18]. Cytoplasm is assigned to peaks located at 1001 and 1660 cm^{-1} representative for phenylalanine and amide I bounds found in proteins [19,20], whereas lipids were described by an occurring peak at 1440 cm^{-1} explaining C=C vibrations in fatty acids [19]. The fifth component is attributed to SN-38 by its triple peaks at 1561, 1615 and 1661 cm^{-1} combined with in-house measurement of a reference Raman spectrum.

Mitochondrial Raman Spectra Identify Spectral Differences between Resistant and Responsive Organoids after SN-38 Treatment

To determine the potential of RMS for assessment of SN-38 efficacy in CRC organoid models, Raman spectra of mitochondria were extracted from Raman images and subjected to PCA to further investigate the cellular response in terms of cellular metabolism of the resistant and responsive donors. Variation of the averaged PC score values of PC-2 revealed statistically significant differences after 5 nM (p=0.0408) and 500 nM (p=0.0358) SN-38 treatment between resistant and responsive donors, while for 50 nM treatment the tendency of separation was observed (p=0.1229) (Supplementary Fig. S2a,b). SN-38-resistant and responsive organoids both clustered to higher score values after treatment in comparison to their respective controls. For the identification of differences between resistant and responsive donors in their reaction to the drug, PCA is heavily influenced by the statistically significant difference between controls of responsive and resistant donors (resistant controls 24h: -0.0001 ± 0.0023; responsive controls 24h: -0.0033 ± 0.0025; two-way ANOVA: p=0.0064).

Thus, to accurately evaluate the differences in the drug response, a PCA limited to mitochondria-derived Raman data collected from organoids treated with 5 nM and 500 nM SN-38 was performed (Fig. 2c). Score value analysis of PC-1 exhibited a statistically significant difference (*p*=0.04543) between resistant and responsive organoids treated with 5 nM and 500 nM of SN-38. The corresponding loading plot exhibited Raman peaks contributing to the separation after SN-38 treatment and conspicuous peaks were identified (Fig. 2d). The shifts to positive loadings at 691 cm^{-1} in SN-38-treated organoids as well peaks at 748 and 1127 cm^{-1} were assigned to cytochrome c [16,21,22]. Shifts at 979, 1081, 1281 and 1640 cm^{-1}, were representatives for changes in the structure of mitochondria by alterations in C-C bonds as well as amide III and I [18,23-25]. The peak located at 1602 cm^{-1} was identified to correlate with the release of cytochrome c [26]. All relevant peaks and their molecular assignments are listed in **Error! Reference source not found.**.

Nuclei Features Identify Spectral Differences between SN-38-Resistant and Responsive Organoids

Additionally, PCA was performed on extracted nuclei-derived Raman spectra from SN-38-resistant and responsive CRC organoids. Score value analysis of PC-1 displayed a statistically significant difference between 500 nM (*p*=0.0447) treated responsive and resistant organoids when considering their respective controls (Supplementary Fig. S1c,d). After treatment with 5 nM (p=0.0917) and 50 nM (p=0.3172) tendencies of separation were observed. PCA of nuclei-derived Raman data that incorporated control data, showed differences between resistant and responsive controls evident in PC-1 (resistant controls: 0.0003 ± 0.0008; responsive controls 24h: -0.0009 ± 0.0001; two-way ANOVA: *p*=0.0969). To identify the differences in drug response between resistant and responsive organoids PCA was performed on 5 nM and 500 nM treated nuclei-derived Raman spectra (Fig. 2e). Score value analysis of PC-5 revealed a statistically significant difference between resistant and responsive donors after drug treatment. The corresponding loading plots (Fig. 2f) exhibited peaks for the increase in score values relevant for C-C bonds located at 1581 cm^{-1} [20], C=C bonds at 1656 cm^{-1} [19], as well as CH_2 at 1310 and 1450 cm^{-1} [23] indicating structural changes of DNA backbones. Furthermore, prominent shifts were located at 655 and 752 cm^{-1} representatives for DNA [27,28]. Responsible for lower score values were peaks located at 1102, 1152, 1202 and 1262 cm^{-1} representatives for C-H [11], C-N [29], and CH_2 [30].

Neural Networks Allow to Classify S-38-Resistant and Responsive Organoids

Data-driven neural networks were utilized as a complementary method to classify Raman data to differentiate between SN-38 resistant and responsive donors towards an automatized screening of drug sensitivities. Supplementary **Error! Reference source not found.** shows the classification results with the performance parameters accuracy, sensitivity, and specificity for the neural network trained with the Raman data for each of the 36 datasets. Best accuracies were obtained when classifying only mitochondria-derived Raman spectra (77% ± 4%). The highest accuracy was obtained in the dataset of 5 nM when classifying spectra after 24 and 48 hours together (84%). In comparison, nuclei exhibit accuracies of only 68% ± 3%. The combination of nuclei and mitochondria derived Raman spectra did not result in an improvement of classification accuracy (77% ± 3%).

FLIM Enables Non-Invasive Metabolic Monitoring of Drug Response Patterns in CRC Organoids

FLIM images of endogenous NADH and FAD fluorescence were acquired from SN-38 resistant and responsive CRC organoids treated with different concentrations of SN-38 (5 nM, 50 nM, 500 nM) for 2, 4, 24 and 48 hours. For each treatment, FLIM parameters $\tau 1$, $\tau 2$, and $\alpha 1\%$ of the coenzymes FAD and NADH were analyzed and compared among each other. In

Fig. 3a, exemplary images of α1%, τ1, and τ2 of FAD and NADH of untreated organoids after 2 hours and 500 nM SN-38 treated organoids after 48 hours both from resistant and responsive donors are displayed. Corresponding histograms of resistant and responsive organoids 48 hours after 5 nM and 500 nM SN-38 treatment and untreated controls after 2 hours are shown in Fig. 3b. While α1% of FAD in resistant organoids shifted to slightly lower values two days after SN-38 treatment (resistant control 2h: 91%; resistant 5 nM 48h: 89%; resistant 500 nM 48h: 88%), a small subpeak located at 38% was evident in responsive organoids after treatment. In SN-38 resistant organoids τ1 of FAD shifted to lower fluorescent lifetimes after 500 nM of SN-38, while the treatment with 5 nM led to a small increase (resistant control 2h: 374 ns; resistant 5 nM 48h: 385 ns; resistant 500 nM 48h: 337 ns). In comparison, SN-38 responsive donors reacted with an increase in τ1 of FAD for both concentrations of the drug (responsive control 2h: 370 ns; responsive 5 nM 48h: 388 ns; responsive 500 nM 48h: 380 ns). In τ2 of FAD in resistant organoids, the maximum of the histogram shifted to lower values after treatment compared to the control, while an additional peak located at 3300 ns emerged (resistant control 2h: 2380 ns; resistant 5 nM 48h: 2300 ns; resistant 500 nM 48h: 2307 ns). In contrast, responsive donors showed an increase after drug treatment and a subpeak located at 2950 ns (responsive control 2h: 2382 ns; responsive 5 nM 48h: 2387 ns; responsive 500 nM 48h: 2393 ns). α1% of NADH showed differences between resistant and responsive donors in the controls. While resistant organoids showed a broad band located at 86%, responsive donors showed two peaks located at 80 and 89%. After treatment with 500 nM SN-38, in responsive donors one further peak is displayed at 69%, non-existent in resistant donors. After 5 nM of SN-38, resistant and responsive donors both showed two peaks located at 82, and 88%. In τ1 of NADH, in both resistant and responsive organoids histograms changed to higher values of fluorescence lifetimes after treatment with 500 nM of SN-38 compared to controls, while a subpeak located at 620 ns was evident only in responsive donors (resistant control 2h: 510 ns; resistant 500 nM 48h: 580 ns; responsive control 2h: 512 ns; responsive 500 nM 48h: 535 ns). Treatment with 5 nM of SN-38 led to similar results in τ1 compared to controls. Finally, in τ2 of NADH, controls from resistant donors differed to responsive donors by existence of a peak located at 4750 ns. Treatment with 500 nM of SN-38 showed its maximum in the same range as controls, while after 5 nM the peak shifted to increased fluorescent lifetimes in both resistant and responsive donors (resistant control 2h: 3950 ns; resistant 500 nM 48h: 4073 ns; resistant 5 nM 48h: 4340; responsive control 2h: 4071 ns; responsive 5 nM 48h: 4840; responsive 500 nM 48h: 4065 ns).

For better comparability and comprehensive analysis between differences in drug response, PCA was performed on z-scaled data from α1%, τ1, and τ2 of FAD and NADH for all concentrations and time points. Fig. 3c displays the score value analysis of PC-1, exhibiting statistically significant differences after treatments with 500 nM (p<0.0001) and 50 nM (p=0.249). After treatment with 5 nM of SN-38 a tendency of separation was observable (p=0.1819) when comparing treated and untreated organoids of both resistant and responsive donors. Overall, two distinct reaction patterns were identified by PCA due to SN-38 treatment. In resistant donors, the score value directly increased in the first 2 hours after treatment. For 24 hours the increased score value remained constant until the value decreased below 0 to the untreated level after 48 hours. In responsive organoids, in the first 24 hours no visible variations appeared compared to the untreated organoids, however, after 48 hours the score value increased.

In comparison, score value analysis of PC-2 (Fig. 3d) displayed the differences between the reaction to SN-38 in resistant and responsive donors. While a statistically significant difference between resistant and responsive donors was identified after 500 nM treatment (p=0.447), tendencies of separation were observed after 50 nM (p=0.3172) and 5 nM (p=0917). The corresponding loading plot is visualized in Fig. 3e indicating which FLIM parameter is responsible for shifts in PC-1 and PC-2. According to the loading plot, the increase in score values in PC-1 attributed to the influence of the drug is explained by changes in α1% of both

FAD and NADH. The differences between resistant and responsive donors displayed in PC-2 are mainly explained by differences in τ2 of NADH and α1% of FAD.

FLIM and RMS Enable Marker-Independent Tracing of Drug Uptake in CRC Organoids

Besides evaluating the effect of the drug on cellular components and metabolism in organoids, we were interested in the feasibility of tracing the uptake of SN-38 with FLIM and Raman spectroscopy. By applying 2D correlation between τ1 and τ2 from FAD on untreated (Fig. 4a) and SN-38 treated (Fig. 4b) organoids the existence of a distinct cluster in treated organoids was revealed. While in untreated organoids one cluster between 300-500 ns of τ1 and 1400-3300 ns of τ2 was visible, in SN-38-treated organoids an additional cluster between 600-1300 ns of τ1 and 2800-3500 ns of τ2 was apparent. Corresponding τ2 FLIM images of the untreated and treated organoids (Fig. 4c,d) showed the accumulation of clusters (light blue) inside the SN-38 treated organoid according to τ2 lifetimes above 2800 ns. Fig. 4e) displays the quantification of SN-38 uptake in resistant and responsive organoids based on τ2 of FAD. Resistant donors showed a statistically significant increased drug uptake at 5 nM (p=0.0138) and 50 nM (p=0.0343) of SN-38. Notably, one of the resistant donors displayed a high level of drug uptake (7-11 organoids). At 500 nM of SN-38 no significant difference between resistant and responsive donors is observed (p=0.8388). It is noteworthy that the number of organoids with SN-38 rapidly decreased in resistant donors after 48 hours of treatment. In contrast, responsive donors displayed an upward trend in SN-38 uptake with ongoing treatment.

Raman spectra from SN-38 TCA heatmaps were also subjected to quantification of the drug uptake. The peak intensity at 1561 cm^{-1} was averaged for each organoid and compared to each other (Supplementary Fig. S2a). Successful drug uptake was considered when the peak intensity is above the average + standard deviation of both controls (Supplementary Fig. S2b). In both resistant and responsive donors, the maximum number of organoids containing the drug was reached after 24 hours, which decreased after 48 hours. Overall, more organoids from responsive donors contained the drug compared to resistant donors.

Discussion

The potential of patient-derived organoid models in precision medicine lies in their ability to identify mutational profiles and conduct high-throughput screening with a wide range of therapeutic agents, enabling the pinpointing of effective drug targets prior to patient treatment. Leveraging information on effective drug candidates identified through screening of personalized organoid cultures could improve decision-making for chemotherapeutic therapies and lead to earlier therapeutic success, ultimately resulting in improved patient adherence and prevention of adverse reactions. Although destructive methods or stains were previously necessary to investigate drug responsiveness, the non-destructive techniques of RMS and FLIM have emerged as promising alternatives, allowing for time-resolved analyses [10,31,32]. Therefore, we examined the potential of these techniques to trace chemotherapeutic agent uptake and monitor molecular and metabolic responses in CRC organoids with both spatial and temporal resolution. Employing TCA-based imaging of Raman data, marker-independent discrimination, and localization of important subcellular structures within the organoids was possible and furthermore allowed the visualization of drug accumulations based on specific drug Raman spectra. Analysis of heat maps of intensity distributions of each cellular component allowed further investigation of the associated underlying spectral information using multivariate analyses. Through spectral signatures, changes in molecular composition were detected and drug-specific peak patterns were identified in nuclei-derived PCA loadings that recurred across different drug concentrations in both resistant and sensitive organoids compared to controls. SN-38 treatment related effects on nuclei were correlated to alterations in DNA structure. Shifts at 655 and 752 cm^{-1} reported for changes in DNA [27,28] were present in responsive donors. Together with shifts responsible for changes in C-C, C=C and CH_2 structural differences due to the drug treatment are evident when comparing responsive and resistant donors. Multiple studies demonstrated that SN-38 results in the inhibition of DNA topoisomerase I, an enzyme involved in DNA replication and transcription [33]. By stabilizing cleavable complexes, the ability of the inhibitor to induce DNA damage and transient S-phase arrest results in single-stranded DNA breaks that are subsequently converted to double-stranded DNA breaks (ds). Interestingly, these shifts were observed to be more pronounced in organoids derived from responsive donors, indicating that SN-38 causes a disturbance in the natural DNA, while its effect on organoids from resistant donors is less pronounced.

Induced dsDNA breakage activates a cascade of different apoptotic signaling pathways resulting in apoptotic cell death [33,34]. In addition, SN-38 is recognized to damage mitochondria by increasing the permeability of the outer mitochondrial membrane, directly associated with MMP disintegration [35,36]. This effect was reflected in the Raman data of mitochondria of responsive donors after treatment with SN-38 by demonstrating shifts relevant to cytochrome c. Especially, the shift at 691 cm^{-1} is reported to appear in swollen mitochondria allowing easier release of cytochrome c inducing apoptosis [22]. The release of cytochrome c in responsive donors is also identified by the peak located at 1602 cm^{-1} which has been linked to cytochrome c release in HeLa cells [26].

Effective cancer therapy is often impeded by limited effectiveness of systemic drug therapies caused by patient-specific multidrug resistance. By using Raman data, it is possible to observe how donors respond to a given drug and draw conclusions as to why certain organoids do not respond with induced cell death. Spectral signatures associated with amide I and III indicate structural changes in proteins, which are found in resistant donors and could be linked to adaptive mechanisms such as mitochondrial fusion and fission in cancer cells [37]. These findings suggest that RMS could be useful in directly monitoring the efficacy of chemotherapeutic agents by identifying specific biomarkers of MMP disruption or mitochondrial conformational adjustment that induce apoptosis.

Fluorescence lifetimes are highly sensitive to alterations in the cellular microenvironment and are possible biomarkers to directly monitor the effect of drug treatment [38,39]. NADH $\tau1$ and FAD $\tau2$ designate the fluorescence lifetime of free, cytosolic NADH and FAD, in contrast to bound NADH and FAD, which was found in the oxidative phosphorylation chain and is denoted by $\tau2$ and $\tau1$ [40]. FLIM was able to detect increasing fluorescent lifetimes in FAD and NADH in organoids of responsive donors potentially undergoing apoptosis as it was reported that a loss of the membrane potential is leading to inhibition of the TCA cycle [41]. This is consistent with the results of other studies that have found an increase in the fluorescent lifetime of FAD and NADH associated with apoptosis [5,42]. In contrast, resistant donors reacted with a decrease in fluorescent lifetime potentially indicative for defense mechanism. Additionally, drug-induced effects were identified in FAD and NADH $\alpha1\%$ values in responsive organoids. A reduction of NADH $\alpha1\%$ is associated with an altered ratio between free and bound NADH, which is related to a switch from glycolysis preferred in cancer cells, to OXPHOS. Alternatively, the change in $\alpha1\%$ could be related to increased energy consumption by nuclei in preparation for apoptosis [43,44] i.e., following dsDNA breakage because of SN-38.

Our goal was to improve drug responsiveness categorization in CRC patients through automation. We applied data-driven neural network binary classification of Raman data and achieved best classification accuracies in mitochondria-based Raman spectra. Best classification was obtained after 5 nM treatment with SN-38 mitochondria-based Raman spectra highlighting the impact of metabolic processes on drug sensitivities. The accuracy decreased with all concentrations, indicating that resistant donors respond to treatment at higher concentrations. The combination of nuclei and mitochondria Raman data did not result in an improvement of the classification performance. The utilization of Raman spectroscopy data classification enabled us to assess drug sensitivity merely 24 hours post-treatment. This represents a notable enhancement over conventional EC50 analysis, which necessitates evaluating drug sensitivity over a period of 5 days. Consequently, Raman spectroscopy-based classification has the potential to serve as a surrogate tool for precision medicine drug testing.

The role of ABC transporters and altered drug influx or efflux in acquired multi-drug resistance is suspected [45]. However, SLC and ABC transporter analyses did not show significant alterations between SN-38 resistant and responsive donors. Nonetheless, time-resolved information about drug accumulation in patient-derived organoids could provide valuable insights into drug resistance. FLIM allowed us to trace the drug SN-38 inside organoids. Quantification of SN-38 showed that resistant donors take up the drug within 2 hours and excrete it after 2 days. Uptake and efflux were accompanied by metabolism redistribution visible in changes in a1% levels of NADH and FAD. Increased levels of a1% can be explained by an adaptive mechanism triggered by nucleus-mediated signaling cascades. Reactive donors showed drug detection in organoids after 24 hours, with a maximum after two days, and undetectable within the first four hours. This coincides with a decrease in the $\tau 2$ of NADH and a redistribution to increased free FAD. In contrast, resistant donors showed no decrease in a1% of NADH and FAD and no concomitant changes, suggesting that no adaptation mechanisms against the drugs were induced. An alternative explanation for this observation could be that the cellular uptake of drugs in resistant organoids leads to accumulation. However, the drug is not metabolized via glucuronidation by UGT1A1 due to resistance mechanisms [46].

By TCA-guided analysis, the suitability of RMS to track SN-38 uptake in organoids was also evaluated. Although theoretically feasible, accurate quantification of the drug in the organoids using the strongest Raman shift of the drug was hampered due to overlap with other biological vibrations at 1561 cm^{-1}, the strongest Raman signal of SN-38. To overcome these limitations, using drugs with chemical features such as triple bonds that peak in the spectral silent region, such as erlotinib or neratinib, could be a viable solution [47,48]

Conclusion

In conclusion, this study aimed to establish a multiparametric approach for evaluating the impact of drugs on patient-derived colorectal cancer (CRC) organoids. Our results showed that RMS and FLIM can be employed as a fast and efficient testing platform for evaluating the effectiveness and mode of action of anti-cancer drugs within 48 hours of treatment. Additionally, the study highlighted the potential of automated data-driven analysis to classify complex Raman data and improve the predictability of drug effects.

Data Availability

The experimental data and materials, generated and analyzed during this study, are available from the corresponding authors on reasonable request.

CRediT Statement:

Lucas Becker: Methodology, Validation, Formal analysis, Investigation, Data curation, Software, Visualization, Writing-Original draft preparation. **Julia Marzi:** Supervision, Project administration, Writing-Reviewing and Editing. **Nicole Janssen:** Methodology, Writing-original draft preparation. **Svenja Wallisch:** Resources, Methodology. **Philipp Renner:** Resources, Methodology. **Marc H Dahlke:** Resources, Methodology. **Thomas E Mürdter:** Writing-Reviewing and Editing. **Anne T Nies:** Supervision, Writing-Reviewing and Editing. **Matthias Schwab:** Term, Conceptualization, Project administration, Funding Acquisition, Writing-Reviewing and Editing. **Katja Schenke-Layland:** Term, Conceptualization, Project administration, Funding Acquisition, Writing-Reviewing and Editing. All authors have read and agreed to the published version of the manuscript.

Declaration of Competing Interest

The authors declare no conflict of interest.

Acknowledgements
The work was conducted in the framework of the Graduate School 2543/1 “Intraoperative Multi-Sensory Tissue-Differentiation in Oncology" funded by the German Research Foundation (DFG - Deutsche Forschungsgemeinschaft). Further funding was received by the Deutsche Forschungsgemeinschaft (INST 2388/64-1, INST 2388/33-1 and Germany’s Excellence Strategy, EXC 2180-390900677), the Ministry of Science, Research, and the Arts of Baden-Wuerttemberg (33-729.55-3/214 and SI-BW 01222-91) and the State Ministry of Baden-Wuerttemberg for Economic Affairs, Labour and Housing Construction (3-4332.62-NMI/65) and the Robert-Bosch Stiftung, Stuttgart, Germany.

References

1. Siegel, R.L.; Miller, K.D.; Fuchs, H.E.; Jemal, A. Cancer Statistics, 2021. *CA: A Cancer Journal for Clinicians* **2021**, *71*, 7-33, doi:10.3322/caac.21654.
2. Stein, A.; Atanackovic, D.; Bokemeyer, C. Current standards and new trends in the primary treatment of colorectal cancer. *Eurpoean Journal of Cancer* **2011**, *47*, S312-S314, doi:10.1016/S0959-8049(11)70183-6.
3. Dallas, N.A.; Xia, L.; Fan, F.; Gray, M.J.; Gaur, P.; Van Buren, G.; Samuel, S.; Kim, M.P.; Lim, S.J.; Ellis, L.M. Chemoresistant Colorectal Cancer Cells, the Cancer Stem Cell Phenotype, and Increased Sensitivity to Insulin-like Growth Factor-I Receptor Inhibition. *Cancer Research* **2009**, *69*, 1951-1957, doi:10.1158/0008-5472.can-08-2023.
4. Moreira, L.; Bakir, B.; Chatterji, P.; Dantes, Z.; Reichert, M.; Rustgi, A.K. Pancreas 3D Organoids: Current and Future Aspects as a Research Platform for Personalized Medicine in Pancreatic Cancer. *Cellular and Molecular Gastroenterology and Hepatology* **2018**, *5*, 289-298, doi:10.1016/j.jcmgh.2017.12.004.
5. Becker, L.; Fischer, F.; Fleck, J.L.; Harland, N.; Herkommer, A.; Stenzl, A.; Aicher, W.K.; Schenke-Layland, K.; Marzi, J. Data-Driven Identification of Biomarkers for In Situ Monitoring of Drug Treatment in Bladder Cancer Organoids. *International Journal of Molecular Sciences* **2022**, *23*, 6956, doi:10.3390/ijms23136956.
6. Zhang, L.; Liang, C.; Xu, P.; Liu, M.; Xu, D.; Wang, X. Characterization of in vitro Mrp2 transporter model based on intestinal organoids. *Regulatory Toxicology and Pharmacology* **2019**, *108*, doi:10.1016/j.yrtph.2019.104449.
7. Marusyk, A.; Polyak, K. Tumor heterogeneity: Causes and consequences. *Biochimica et Biophysica Acta (BBA) - Reviews on Cancer* **2010**, *1805*, 105-117, doi:10.1016/j.bbcan.2009.11.002.
8. Junttila, M.R.; De Sauvage, F.J. Influence of tumour micro-environment heterogeneity on therapeutic response. *Nature* **2013**, *501*, 346-354, doi:10.1038/nature12626.
9. Gong, X.; Lin, C.; Cheng, J.; Su, J.; Zhao, H.; Liu, T.; Wen, X.; Zhao, P. Generation of Multicellular Tumor Spheroids with Microwell-Based Agarose Scaffolds for Drug Testing. *PLOS ONE* **2015**, *10*, e0130348, doi:10.1371/journal.pone.0130348.
10. Becker, L.; Janssen, N.; Layland, S.L.; Mürdter, T.E.; Nies, A.T.; Schenke-Layland, K.; Marzi, J. Raman Imaging and Fluorescence Lifetime Imaging Microscopy for Diagnosis of Cancer State and Metabolic Monitoring. *Cancers* **2021**, *13*, 5682, doi:10.3390/cancers13225682.
11. Pezzotti, G. Raman spectroscopy in cell biology and microbiology. *Journal of Raman Spectroscopy* **2021**, *52*, 2348-2443, doi:https://doi.org/10.1002/jrs.6204.
12. Niaura, G. Raman Spectroscopy in Analysis of Biomolecules. *Biomolecules Analysis* **2014**, doi: https://doi.org/10.1002/9780470027318.a0212.pub3.

32. Jamieson, L.E.; Harrison, D.J.; Campbell, C.J. Raman spectroscopy investigation of biochemical changes in tumor spheroids with aging and after treatment with staurosporine. *Journal of Biophotonics* **2019**, *12*, e201800201, doi:10.1002/jbio.201800201.
33. Hsiang, Y.H.; Lihou, M.G.; Liu, L.F. Arrest of replication forks by drug-stabilized topoisomerase I-DNA cleavable complexes as a mechanism of cell killing by camptothecin. **1989**, *49*, 5077-5082.
34. Sun, X.-F.; Ferreud, L.; Svanvik, J.; Holmlund, B.; Wallin, Å. Anticancer effect of SN-38 on colon cancer cell lines with different metastatic potential. *Oncology Reports* **2008**, doi:10.3892/or.19.6.1493.
35. Fulda, S.; Debatin, K. Sensitization for anticancer drug-induced apoptosis by betulinic Acid. *Neoplasia* **2005**, *7*, 162-170, doi:10.1593/neo.04442.
36. Custódio, J.B.A.; Cardoso, C.M.P.; Madeira, V.M.C.; Almeida, L.M. Mitochondrial permeability transition induced by the anticancer drug etoposide. *Toxicology in Vitro* **2001**, *15*, 265-270, doi:10.1016/s0887-2333(01)00019-4.
37. Jin, P.; Jiang, J.; Zhou, L.; Huang, Z.; Nice, E.C.; Huang, C.; Fu, L. Mitochondrial adaptation in cancer drug resistance: prevalence, mechanisms, and management. *Journal of Hematology & Oncology* **2022**, *15*, doi:10.1186/s13045-022-01313-4.
38. Chacko, J.V.; Eliceiri, K.W. Autofluorescence lifetime imaging of cellular metabolism: Sensitivity toward cell density, pH, intracellular, and intercellular heterogeneity. *Cytometry Part A* **2019**, *95*, 56-69, doi:10.1002/cyto.a.23603.
39. Shimolina, L.E.; Gulin, A.A.; Paez-Perez, M.; López-Duarte, I.; Druzhkova, I.N.; Lukina, M.M.; Gubina, M.V.; Brooks, N.J.; Zagaynova, E.V.; Kuimova, M.K.; et al. Mapping cisplatin-induced viscosity alterations in cancer cells using molecular rotor and fluorescence lifetime imaging microscopy. *Journal of Biomedical Optics* **2020**, *25*, doi:10.1117/1.jbo.25.12.126004.
40. Suhling, K.; Hirvonen, L.M.; Levitt, J.A.; Chung, P.-H.; Tregidgo, C.; Le Marois, A.; Rusakov, D.A.; Zheng, K.; Ameer-Beg, S.; Poland, S.; et al. Fluorescence lifetime imaging (FLIM): Basic concepts and some recent developments. *Medical Photonics* **2015**, *27*, 3-40, doi:10.1016/j.medpho.2014.12.001.
41. Choi, Y.-M.; Kim, H.-K.; Shim, W.; Anwar, M.A.; Kwon, J.-W.; Kwon, H.-K.; Kim, H.J.; Jeong, H.; Kim, H.M.; Hwang, D.; et al. Mechanism of Cisplatin-Induced Cytotoxicity Is Correlated to Impaired Metabolism Due to Mitochondrial ROS Generation. *PLOS ONE* **2015**, *10*, e0135083, doi:10.1371/journal.pone.0135083.
42. Bower, A.J.; Sorrells, J.E.; Li, J.; Marjanovic, M.; Barkalifa, R.; Boppart, S.A. Tracking metabolic dynamics of apoptosis with high-speed two-photon fluorescence lifetime imaging microscopy. *Biomedical Optics Express* **2019**, *10*, 6408, doi:10.1364/boe.10.006408.
43. Zbinden, A.; Carvajal Berrio, D.A.; Urbanczyk, M.; Layland, S.L.; Bosch, M.; Fliri, S.; Lu, C.E.; Jeyagaran, A.; Loskill, P.; Duffy, G.P.; et al. Fluorescence lifetime metabolic mapping of hypoxia‐induced damage in pancreatic pseudo‐islets. *Journal of Biophotonics* **2020**, *13*, doi:10.1002/jbio.202000375.
44. Bower, A.J.; Marjanovic, M.; Zhao, Y.; Li, J.; Chaney, E.J.; Boppart, S.A. Label-freein vivocellular-level detection and imaging of apoptosis. *Journal of Biophotonics* **2017**, *10*, 143-150, doi:10.1002/jbio.201600003.
45. Choi, C.-H. ABC transporters as multidrug resistance mechanisms and the development of chemosensitizers for their reversal. *Cancer Cell International* **2005**, *5*, 30, doi:10.1186/1475-2867-5-30.
46. De Man, F.M.; Goey, A.K.L.; Van Schaik, R.H.N.; Mathijssen, R.H.J.; Bins, S. Individualization of Irinotecan Treatment: A Review of Pharmacokinetics, Pharmacodynamics, and Pharmacogenetics. *Clinical Pharmacokinetics* **2018**, *57*, 1229-1254, doi:10.1007/s40262-018-0644-7.
47. El-Mashtoly, S.F.; Petersen, D.; Yosef, H.K.; Mosig, A.; Reinacher-Schick, A.; Kötting, C.; Gerwert, K. Label-free imaging of drug distribution and metabolism in colon cancer cells by Raman microscopy. *The Analyst* **2014**, *139*, 1155, doi:10.1039/c3an01993d.
48. Aljakouch, K.; Lechtonen, T.; Yosef, H.K.; Hammoud, M.K.; Alsaidi, W.; Kötting, C.; Mügge, C.; Kourist, R.; El-Mashtoly, S.F.; Gerwert, K. Raman Microspectroscopic Evidence for the Metabolism of a Tyrosine Kinase Inhibitor, Neratinib, in Cancer Cells. *Angewandte Chemie International Edition* **2018**, *57*, 7250-7254, doi:10.1002/anie.201803394.
49. Thomas, G.J.; Benevides, J.M. An A-helix structure for poly(dA-dT) · poly(dA-dT). *Biopolymers* **1985**, *24*, 1101-1105, doi:10.1002/bip.360240613.

List of Tables

Table 1. Disease origin of included samples.

Donor	**Age**	**Gender**	**Ethnicity**	**Tumor Localization**	**Stage**	**Grade**
Resistant #1	36	Female	Caucasian	Sigma	IIA	G2
Resistant #2	71	Female	Caucasian	Ascending colon	IVC	G2/G3
Resistant #3	52	Male	Caucasian	Rectum	IVA	Low grade
Responsive #1	58	Male	Caucasian	Rectum	IIIC	G2
Responsive #2	74	Female	Caucasian	Ascending colon	IIIC	High grade
Responsive #3	53	Female	Caucasian	Descending colon	IIIB	Low grade

List of Figure Legends

Figure 1. Expression of SLC and ABC membrane transporters implicated in the uptake or efflux of SN-38/irinotecan are not differently expressed in resistant or responsive CRC organoids. RNA was isolated from organoids and Human Transcriptome Arrays 2.0 (HTA 2.0) were carried out. Arrays were RMA normalized per sample and data of 3 SLC (a) and 8 ABC transporter probe sets (b) were extracted.

Figure 2. Raman microspectroscopy (RMS) and principal component analysis (PCA) display statistically significant differences between resistant and responsive colorectal cancer (CRC) organoids after SN-38 treatment. (a) True component analysis (TCA) images of CRC organoids. Displayed is one representative scan of an untreated (control, 0h) and treated organoid (500 nM SN-38, 48h) for both resistant and responsive organoids. Scale bar: 20 µm. **(b)** Relevant TCA spectra for the identified cellular components. **(c)** PCA exhibits separation between controls and SN-38 treated organoids. Score value analysis of mitochondria treated with 5 nM (rose) and 500 nM (bordeaux) of SN-38 display a statistically significant difference in drug response between resistant and responsive organoids. **(d)** Corresponding loading plot. **(e)** Score value analysis of nuclei-derived Raman spectra of CRC organoids treated with 5 nM and 500 nM of SN-38 display a statistically significant difference between resistant and responsive organoids. **(f)** Corresponding loading plot. Statistical analysis: Three-way ANOVA, *n*=3, **p*<0.05.

Figure 3. Fluorescence lifetime imaging microscopy (FLIM) identifies differences in drug response between SN-38 resistant and responsive CRC organoids. (a) Representative FLIM images of untreated controls after 2h and 500 nM SN-38-treated CRC organoids after 48 hours of resistant and responsive donors. Scale bar: 20 µm. **(b)** Corresponding histograms of FLIM parameters α1%, τ1, and τ2 of both FAD and NADH. Histograms of controls and treatments are depicted by black and purple lines. **(c)** Score value analysis of PC-1 displays significant differences in 50 nM, and 500 nM treated organoids of both resistant and responsive donors. **(d)** Score value analysis of PC-2 identifies different

Table 2. EC 50 values for the response variable after 24 hours of treatment with 5 nM SN-38.

Donor	EC 50 at 5 nM of SN-38 (24h)
Resistant #1	>10000
Resistant #2	>10000
Resistant #3	>10000
Responsive #1	25 ± 12
Responsive #2	611 ± 398
Responsive #3	7878 ± 2122

Table 3. Biological assignment of the most relevant wavenumbers.

Wavenumber [cm^{-1}]	Biological origin	Literature
655	DNA	[28]
691	Cytochrome c	[22]
700	A-form DNA	[49]
748	Cytochrome c	[16]
752	DNA	[27]
970	DNA	[24]
979	C-C	[18]
1102	C-H	[11]
1081	C-C	[23]
1127	Cytochrome c	[21]
1152	C-N	[29]
1202	CH2	[30]
1262	CH2	[30]
1281	Amide III	[24]
1310	CH_2	[23]
1450	CH_2, methylene	[23,24]
1581	C-C	[20]
1602	Cytochrome c release	[26]
1640	Amide I	[25]
1656	C=C	[20]

List of Figure Legends

Figure 1. Expression of SLC and ABC membrane transporters implicated in the uptake or efflux of SN-38/irinotecan are not differently expressed in resistant or responsive CRC organoids. RNA was isolated from organoids and Human Transcriptome Arrays 2.0 (HTA 2.0) were carried out. Arrays were RMA normalized per sample and data of 3 SLC (a) and 8 ABC transporter probe sets (b) were extracted.

Figure 2. Raman microspectroscopy (RMS) and principal component analysis (PCA) display statistically significant differences between resistant and responsive colorectal cancer (CRC) organoids after SN-38 treatment. (a) True component analysis (TCA) images of CRC organoids. Displayed is one representative scan of an untreated (control, 0h) and treated organoid (500 nM SN-38, 48h) for both resistant and responsive organoids. Scale bar: 20 µm. **(b)** Relevant TCA spectra for the identified cellular components. **(c)** PCA exhibits separation between controls and SN-38 treated organoids. Score value analysis of mitochondria treated with 5 nM (rose) and 500 nM (bordeaux) of SN-38 display a statistically significant difference in drug response between resistant and responsive organoids. **(d)** Corresponding loading plot. **(e)** Score value analysis of nuclei-derived Raman spectra of CRC organoids treated with 5 nM and 500 nM of SN-38 display a statistically significant difference between resistant and responsive organoids. **(f)** Corresponding loading plot. Statistical analysis: Three-way ANOVA, *n*=3, **p*<0.05.

Figure 3. Fluorescence lifetime imaging microscopy (FLIM) identifies differences in drug response between SN-38 resistant and responsive CRC organoids. (a) Representative FLIM images of untreated controls after 2h and 500 nM SN-38-treated CRC organoids after 48 hours of resistant and responsive donors. Scale bar: 20 µm. **(b)** Corresponding histograms of FLIM parameters $\alpha1\%$, $\tau1$, and $\tau2$ of both FAD and NADH. Histograms of controls and treatments are depicted by black and purple lines. **(c)** Score value analysis of PC-1 displays significant differences in 50 nM, and 500 nM treated organoids of both resistant and responsive donors. **(d)** Score value analysis of PC-2 identifies different

drug reaction patterns between both resistant and responsive organoids. **(e)** Corresponding loading plot. Statistical analysis: Three-way ANOVA, n=3, *p<0.05.

Figure 5. FLIM enables SN-38 tracing in CRC organoids. (a) 2D correlation between τ1 and τ2 of an untreated organoid and **(b)** 500 nM SN-38 treated organoid after 24h showing the existence of a distinct cluster in treated organoids. **(c)** Corresponding τ2 FLIM image of control. **(d)** Corresponding τ2 FLIM image of a 500 nM SN-38 treated organoid after 24h. Scale bar: 20 µm. **(e)** τ2-based quantification of SN-38 uptake.

Figures:

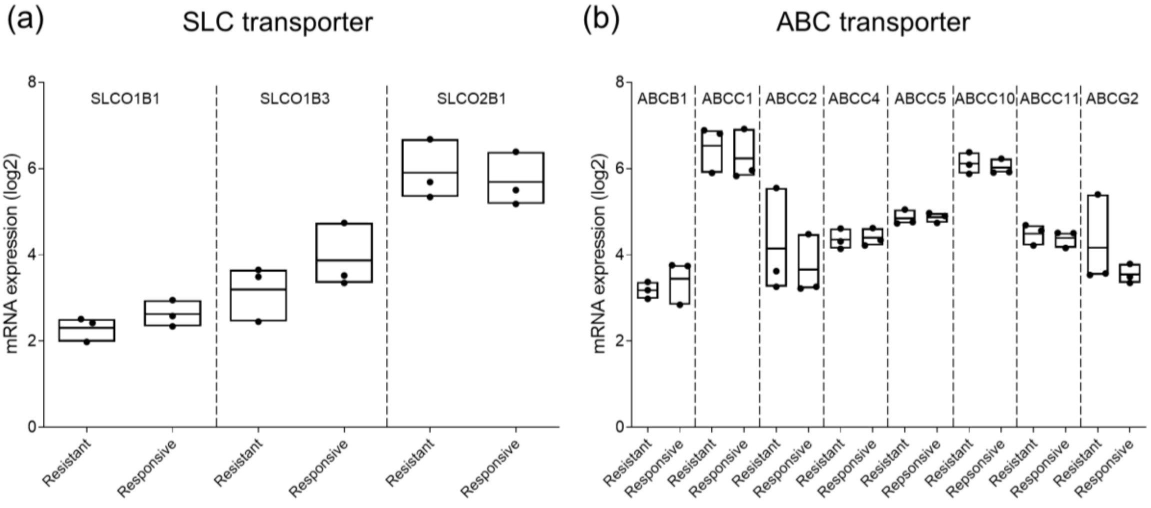
(a)
SLC transporter
mRNA expression (log2)
0
2
4
6
8
SLCO1B1
SLCO1B3
SLCO2B1
Resistant
Responsive
Resistant
Responsive
Resistant
Responsive
(b)
ABC transporter
mRNA expression (log2)
0
2
4
6
8
ABCB1
ABCC1
ABCC2
ABCC4
ABCC5
ABCC10
ABCC11
ABCG2
Resistant
Responsive
Resistant
Responsive
Resistant
Responsive
Resistant
Responsive
Resistant
Repsonsive
Resistant
Repsonsive
Resistant
Responsive
Resistant
Responsive

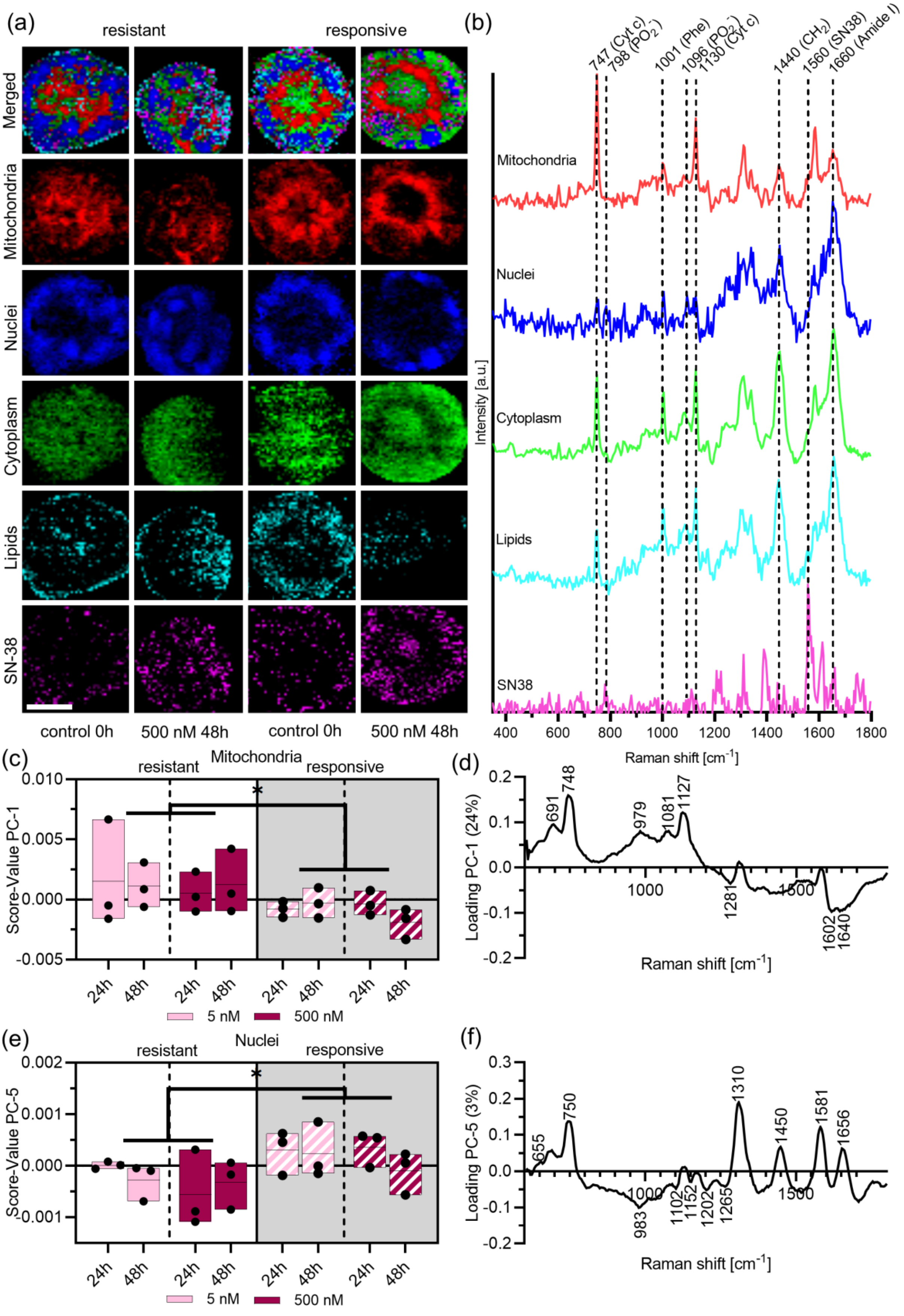
(a)
resistant
responsive
Merged
Mitochondria
Nuclei
Cytoplasm
Lipids
SN-38
control 0h
500 nM 48h
control 0h
500 nM 48h
(b)
747 (Cyt c)
798 (PO2-)
1001 (Phe)
1096 (PO2-)
1130 (Cyt c)
1440 (CH2)
1560 (SN38)
1660 (Amide I)
Mitochondria
Nuclei
Cytoplasm
Lipids
SN38
Intensity [a.u.]
400 600 800 1000 1200 1400 1600 1800
Raman shift [cm-1]
(c)
Mitochondria
resistant
responsive
Score-Value PC-1
0.010 0.005 0.000 -0.005
*
24h 48h 24h 48h 24h 48h 24h 48h
5 nM
500 nM
(d)
Loading PC-1 (24%)
0.2 0.1 0.0 -0.1 -0.2
691 748 979 1081 1127 1281 1602 1640
1000 1500
Raman shift [cm-1]
(e)
Nuclei
resistant
responsive
Score-Value PC-5
0.002 0.001 0.000 -0.001
*
24h 48h 24h 48h 24h 48h 24h 48h
5 nM
500 nM
(f)
Loading PC-5 (3%)
0.3 0.2 0.1 0.0 -0.1 -0.2
655 750 983 1102 1152 1202 1265 1310 1450 1581 1656
1000 1500
Raman shift [cm-1]

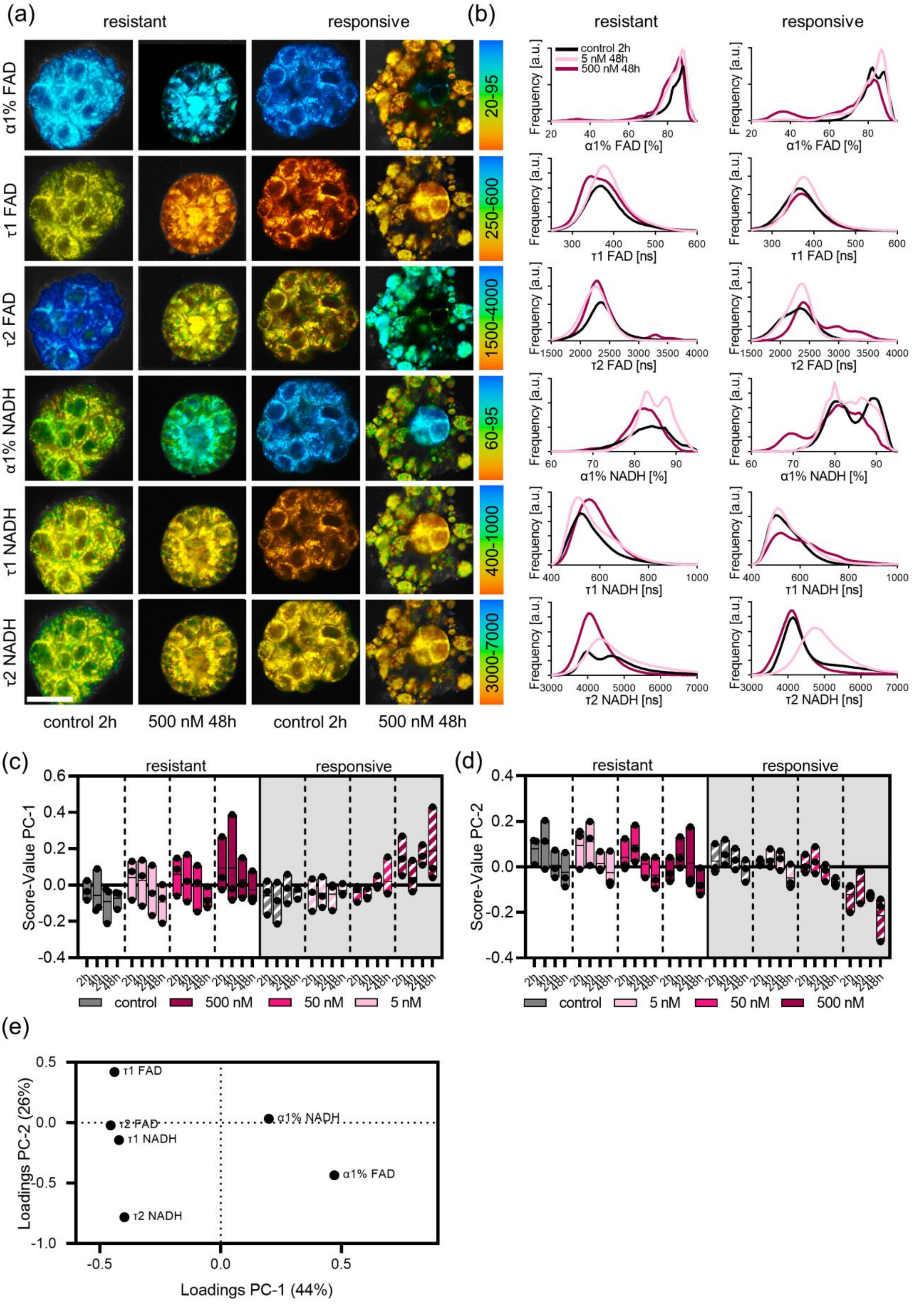
(a)
resistant
responsive
α1% FAD
τ1 FAD
τ2 FAD
α1% NADH
τ1 NADH
τ2 NADH
20-95
250-600
1500-4000
60-95
400-1000
3000-7000
control 2h
500 nM 48h
control 2h
500 nM 48h
(b)
resistant
responsive
control 2h
5 nM 48h
500 nM 48h
Frequency [a.u.]
α1% FAD [%]
τ1 FAD [ns]
τ2 FAD [ns]
α1% NADH [%]
τ1 NADH [ns]
τ2 NADH [ns]
(c)
resistant
responsive
Score-Value PC-1
2h
4h
24h
48h
control
500 nM
50 nM
5 nM
(d)
resistant
responsive
Score-Value PC-2
control
5 nM
50 nM
500 nM
(e)
τ1 FAD
τ2 FAD
τ1 NADH
τ2 NADH
α1% NADH
α1% FAD
Loadings PC-2 (26%)
Loadings PC-1 (44%)

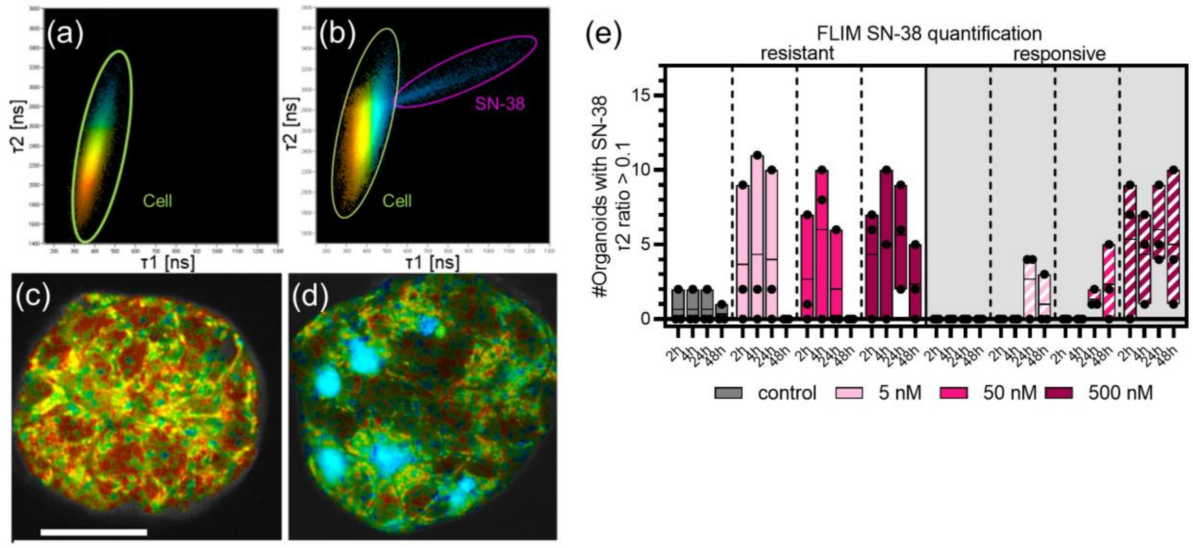
(a)
τ2 [ns]
τ1 [ns]
Cell
(b)
τ2 [ns]
τ1 [ns]
Cell
SN-38
(c)
(d)
(e)
FLIM SN-38 quantification
resistant
responsive
#Organoids with SN-38 τ2 ratio > 0.1
15
10
5
0
2h
4h
24h
48h
control
5 nM
50 nM
500 nM

Supplementary information

Label-free Raman microscopy and fluorescence lifetime imaging-based monitoring of anti-cancer drug effects in colorectal cancer organoids towards patient-individualized optimization of treatments.

Lucas Becker[a,b], Nicole Janssen[b,c], Svenja Wallisch[c], Thomas E Mürdter[b,c], Philipp Renner[c,d], Marc H Dahlke[c,d], Julia Marzi[a,b,e], Anne T Nies[b,d], Matthias Schwab[b,c,f,g] and Katja Schenke-Layland*[a,b,e]

a Institute of Biomedical Engineering, Department for Medical Technologies and Regenerative Medicine, University of Tübingen, 72076 Tübingen, Germany
b Cluster of Excellence iFIT (EXC 2180) "Image-Guided and Functionally Instructed Tumor Therapies", University of Tübingen, Germany
c Dr. Margarete Fischer-Bosch Institute of Clinical Pharmacology, 70376 Stuttgart, Germany
d Department of Surgery, Robert Bosch Hospital,70367 Stuttgart, Germany
e Natural and Medical Sciences Institute (NMI) at the University of Tübingen, 72770 Reutlingen, Germany
f Department of Clinical Pharmacology, University Hospital Tübingen, 72076 Tübingen, Germany
g Department of Biochemistry and Pharmacy, University of Tübingen, 72076 Tübingen, Germany

Supplementary S1. Neural network architecture and classification

The performance of neural network classification was improved by structure modification and hyperparameter tuning of the batch size, the number of epochs, the number of hidden units, the optimizer as well as the learning rate. The network architecture consists of an input layer, several hidden layers, and an output layer. The input layer consists of 400 hidden units and L1 regularization of 0.01 to prevent overfitting. The second hidden layer also consists of 400 hidden units, while the third layer consists of half of the hidden units and the fourth of a quarter of hidden units than the first two hidden layers. To prevent overfitting, two dropout layers with a rate of 0.25 were added after the third and fourth hidden layers. The output layer has 2 units, representing the two classes: *responsive* and *resistant*. The activation functions used are mainly ReLU (Rectified Linear Unit) and one sigmoid function in the last layer for probabilistic output values. The network was compiled with sparse categorical cross entropy loss, optimized using the Adam algorithm [51] with a learning rate of = 0.0001. With a batch size of 512, the model trained for 500 epochs and a train test split of 0.8 is applied.

By using the fully connected neural network, min-max normed Raman data derived from mitochondria and nuclei were classified into one of the two groups: *responsive* and *resistant*. In total 36 datasets containing Raman spectra of mitochondria, nuclei, or a combination of both treated with 5 nM, 50 nM, and/or 500 nM of SN-38 at 24 and/or 48 hours were evaluated.

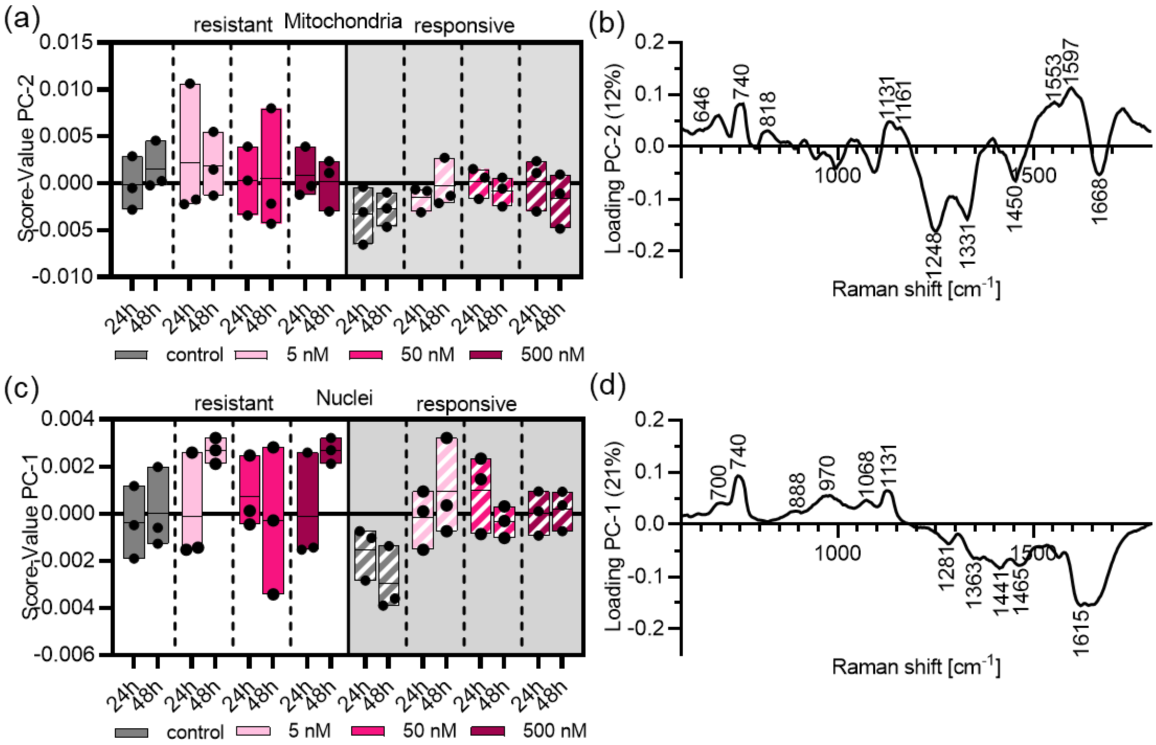

Supplementary Figure S1: PCA of nuclei and mitochondria-derived Raman spectra after SN-38 treatment of CRC organoids reveal differences in drug response between resistant (solid bars) and responsive donors (striped bars). (a) Score value analysis of mitochondria shows statistically significant differences in drug response between resistant and responsive organoids treated with 5 nM (rose) and 500 nM (bordeaux) of the drug. Tendencies of separation were observed in organoids treated with 50 nM SN-38 (pink) (b) Corresponding loading plot. (c) Score value analysis of nuclei reveal statistically significant differences in drug response between resistant and responsive organoids treated with 500 nM SN-38. Tendencies of separation were displayed after 50 nM and 5 nM treatment of the drug. (d) Corresponding loading plot. Statistical analysis: Three-way ANOVA, n=3, *p<0.05.

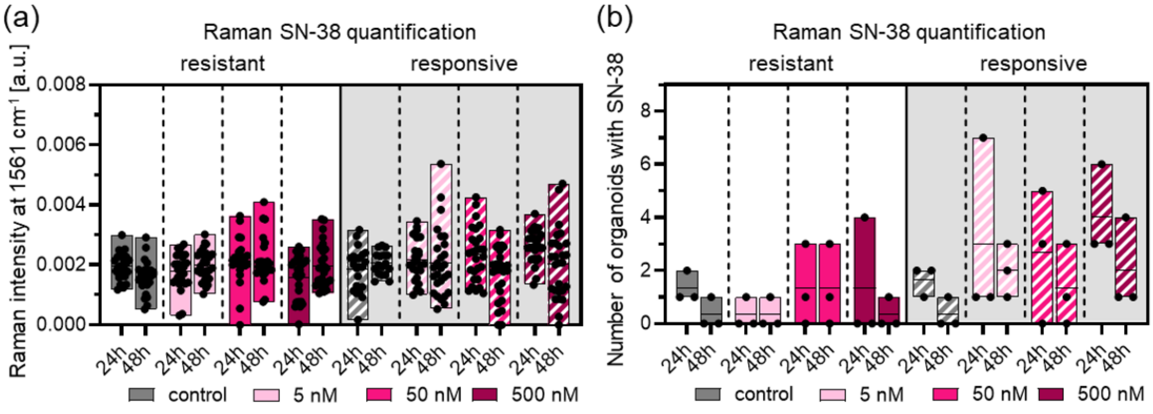

Supplementary Fig. S2: Quantification of SN-38 in CRC organoids based on SN-38-derived Raman spectra display differences between resistant and responsive donors. a) Raman intensity at 1561 cm^{-1} of SN-38-derived Raman spectra from organoids treated with 5 nM (rose), 50 nM (pink) and 500 nM (bordeaux) of the drug. b) Quantification of SN-38 in CRC organoids based on the Raman intensity at 1561 cm^{-1}. The presence of SN-38 within the organoids was established through a comparison of the Raman intensity of the treated specimens with the mean intensity of the control group.

Supplementary Table S1. Classification performance of neural networks on Raman data of treated CRC organoids from SN-38 resistant and responsive donors.

Dataset	Accuracy	Sensitivity	Specificity
Nuclei			
5 nM (24h)	68	68	69
5 nM (48h)	64	68	60
5 nM (24h + 48h)	68	81	58
50 nM (24h)	64	67	61
50 nM (48h)	76	63	90
50 nM (24h + 48h)	66	50	82
500 nM (24h)	70	85	54
500 nM (48h)	70	63	76
500 nM (24h + 48h)	67	77	58
All concentrations (24h)	65	57	73
All concentrations (48h)	69	68	71
All concentrations (24h + 48h)	68	51	64
Mitochondria			
5 nM (24h)	74	79	68
5 nM (48h)	77	82	73
5 nM (24h + 48h)	84	75	75
50 nM (24h)	73	90	57
50 nM (48h)	80	74	85
50 nM (24h + 48h)	76	81	70
500 nM (24h)	82	88	77
500 nM (48h)	77	80	74
500 nM (24h + 48h)	78	78	80
All concentrations (24h)	73	78	69
All concentrations (48h)	75	79	70
All concentrations (24h + 48h)	72	76	69
Mitochondria + Nuclei			
5 nM (24h)	79	81	76
5 nM (48h)	78	92	63
5 nM (24h + 48h)	72	95	51
50 nM (24h)	72	76	70
50 nM (48h)	83	89	78
50 nM (24h + 48h)	75	56	92
500 nM (24h)	76	70	83
500 nM (48h)	81	82	80
500 nM (24h + 48h)	82	83	82
All concentrations (24h)	78	84	71
All concentrations (48h)	75	70	81
All concentrations (24h + 48h)	75	78	73

Appendix III: Becker L., Lu C., Montes-Mojarro I. A., Layland S. L., Khalil S., Nsair A., Duffy G. P., Fend, F., Marzi J., Schenke-Layland K., *Raman Microspectroscopy Identifies Fibrotic Tissues in Collagen-related Disorders Via Deconvoluted Collagen type I Spectra,* Acta Biomater., 2023, 10.1016/j.actbio.2023.03.016.

ARTICLE IN PRESS
JID: ACTBIO [m5G;March 22, 2023;16:15]

Acta Biomaterialia xxx (xxxx) xxx

Contents lists available at ScienceDirect

Acta Biomaterialia

journal homepage: www.elsevier.com/locate/actbio

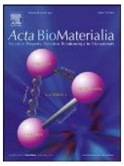

Full length article

Raman microspectroscopy identifies fibrotic tissues in collagen-related disorders via deconvoluted collagen type I spectra

Lucas Becker[a,b,1], Chuan-En Lu[a,1], Ivonne A. Montes-Mojarro[c], Shannon L. Layland[a], Suzan Khalil[d], Ali Nsair[d], Garry P. Duffy[e], Falko Fend[c], Julia Marzi[a,b,f], Katja Schenke-Layland[a,b,f,*]

[a] Institute of Biomedical Engineering, Department for Medical Technologies and Regenerative Medicine, Silcherstr. 7/1, Eberhard Karls University, 72076 Tübingen, Germany
[b] Cluster of Excellence iFIT (EXC 2180) "Image-Guided and Functionally Instructed Tumor Therapies", Eberhard Karls University, Tübingen, Germany
[c] Institute of Pathology and Neuropathology, University Hospital Tübingen, Tübingen, Germany
[d] Department of Medicine/Cardiology, Cardiovascular Research Laboratories, David Geffen School of Medicine at UCLA, 675 Charles E. Young Drive South, MRL 3645 Los Angeles, CA, USA
[e] Anatomy & Regenerative Medicine Institute, School of Medicine, College of Medicine, Nursing and Health Sciences, National University of Ireland Galway, H91 TK33, Galway, Ireland
[f] NMI Natural and Medical Sciences Institute at the University of Tübingen, Markwiesenstr. 55, 72770 Reutlingen, Germany

article info

Article history:
Received 23 November 2022
Revised 28 February 2023
Accepted 9 March 2023
Available online xxx

Keywords:
Pathological tissue remodeling
Non-destructive imaging
Extracellular matrix
Collagen
Spectral deconvolution
Raman microspectroscopy

abstract

Fibrosis is a consequence of the pathological remodeling of extracellular matrix (ECM) structures in the connective tissue of an organ. It is often caused by chronic inflammation, which over time, progressively leads to an excess deposition of collagen type I (COL I) that replaces healthy tissue structures, in many cases leaving a stiff scar. Increasing fibrosis can lead to organ failure and death; therefore, developing methods that potentially allow real-time monitoring of early onset or progression of fibrosis are highly valuable. In this study, the ECM structures of diseased and healthy human tissue from multiple organs were investigated for the presence of fibrosis using routine histology and marker-independent Raman microspectroscopy and Raman imaging. Spectral deconvolution of COL I Raman spectra allowed the discrimination of fibrotic and non-fibrotic COL I fibers. Statistically significant differences were identified in the amide I region of the spectral subpeak at 1608 cm^{-1}, which was deemed to be representative for structural changes in COL I fibers in all examined fibrotic tissues. Raman spectroscopy-based methods in combination with this newly discovered spectroscopic biomarker potentially offer a diagnostic approach to non-invasively track and monitor the progression of fibrosis.

Statement of Significance

Current diagnosis of fibrosis still relies on histopathological examination with invasive biopsy procedures. Although, several non-invasive imaging techniques such as positron emission tomography, single-photon emission computed tomography and second harmonic generation are gradually employed in pre-clinical or clinical studies, these techniques are limited in spatial resolution and the morphological interpretation highly relies on individual experience and knowledge. In this study, we propose a non-destructive technique, Raman microspectroscopy, to discriminate fibrotic changes of collagen type I based on a molecular biomarker. The changes of the secondary structure of collagen type I can be identified by spectral deconvolution, which potentially can provide an automatic diagnosis for fibrotic tissues in the clinical applicaion.

---

[*] Correspondence author at: Institute of Biomedical Engineering, Department for Medical Technologies and Regenerative Medicine, Eberhard Karls University Tübingen, Silcherstraße 7/1, 72076 Tübingen, Germany.

E-mail address: katja.schenke-layland@uni-tuebingen.de (K. Schenke-Layland).

[1] Authors contributed equally.

https://doi.org/10.1016/j.actbio.2023.03.016

Please cite this article as: L. Becker, C.-E. Lu, I.A. Montes-Mojarro et al., Raman microspectroscopy identifies fibrotic tissues in collagen-related disorders via deconvoluted collagen type I spectra, Acta Biomaterialia, https://doi.org/10.1016/j.actbio.2023.03.016

1. Introduction

Fibrosis is the pathological deposition of connective tissue in an organ as a result of extracellular matrix (ECM) remodeling and the excess secretion of collagen type I (COL I). Fibrosis is often caused by chronic inflammation, which over time, progressively remodels and replaces the normal tissue, leaving a biomechanically stiff scar. Stimuli from processes like aging, cancer, autoimmune responses, infections, foreign body response due to implantation, and repetitive tissue damage can lead to chronic inflammation, which is a main driver of fibrosis [1,2]. During fibrosis progression, healthy tissue is replaced by malfunctioning, stiffening scar tissue resulting in organ dysfunction and failure. Almost every organ and tissue in the body can undergo fibrosis [1,3]. In the US, nearly 45%of deaths are highly related to fibrotic diseases [4,5].

Currently, the clinical evaluation of fibrosis mainly relies on the evaluation of tissue biopsies by gold-standard histological analyses (H&E or Masson's trichrome staining), or clinical imaging techniques such as computed tomography, magnetic resonance imaging and ultrasound elastography [6–9]. Potential serum biomarkers were identified as indicators for fibrotic diseases such as the ratio of alanine aminotransferases and aspartate aminotransferases for liver cirrhosis as well as metalloproteases for idiopathic pulmonary fibrosis [10,11]. Nevertheless, these methods mainly allow the diagnosis of late stage, established fibrotic tissues or they assess the malfunctioning organ that is affected by fibrosis, but they cannot detect the early onset or progression of fibrosis [12]. Due to this limitation, proper treatment at an early stage to reduce or slow down the progress of fibrosis is currently not possible.

The primary ECM protein in fibrotic tissues is COL I, which makes it a favorable target for diagnosis [13]. Methods to detect changes in the collagen fiber architecture have been under development for decades; however, the results are difficult to correlate due to data disparity [14,15]. Picrosirius red staining (PSR) was developed for the purpose of characterizing collagen bundles [16]. In combination with polarized microscopy, qualitative and quantitative investigation of histological sections can be conducted, providing information on the thickness and orientation of collagen fibers [17]. However, the morphological interpretation especially from routine histology or histochemistry samples relies on the clinical experience or knowledge of individual pathologists and can generate various diagnostic outcomes [18–20]. Another optical technique, second harmonic generation (SHG), has been employed for characterizing the architecture of fibrillar collagen [19–21]. SHG can offer highly specific optical signals for collagens without any contrast agents or labeling, potentially providing a promising way to conduct non-invasive fibrosis examination [21]. Nevertheless, collagen state examination by PSR and SHG is limited to fiber geometry and morphological changes in the three-dimensional fiber structure.

Over the years, non-invasive spectroscopic techniques have gained attention in diagnostic applications [22–25]. They are suitable for studying molecules based on the interplay between laser light and the dynamic state of chemical bonds [26]. Raman spectral analysis of COL I alteration has been studied for several years. Recently, our group used Raman microspectroscopy (RMS) in combination with multivariate data analysis to identify changes in the sequence of amino acids in COL I of aortic aneurysms [27]. Moreover, RMS has also been used to investigate fibrotic capsules caused by an implantable therapeutic reservoir on streptozotocin-induced rats, demonstrating the capability of RMS to discriminate the existence of advanced glycation end-products in COL I in diabetic animals [28]. RMS has further been successfully implemented for detecting changes in collagen deposition during pathological transformation. Quantification of collagen content was employed to monitor the effectiveness of chemotherapy [25,29,30], diagnosis and characterization of various types of cancer including breast [31], prostate [32], and ovarian [33] cancer, and to monitor cancer progression [22,34]. RMS holds great potential for molecularly differentiating between collagens, particularly in tissues where connective tissue is dominant and the differentiation between fibrotic and native collagen fibers is difficult using traditional diagnostic methods. Its non-invasive nature makes it a valuable alternative to invasive biopsies or other imaging modalities, offering a more accessible and convenient option for patients. In combination with multivariate analysis and classification algorithms, RMS has the potential to provide an automated diagnosis and support pathologists in challenging cases.

In this study, RMS was employed to screen pathological collagen-rich regions ex vivo including liver, colon, breast tissue, lymph nodes and myocardium. ECM compositional differences were identified. COL I spectra were extracted and underwent spectral deconvolution as well as peak-filter and image-based ratio analysis. This study highlights the potential of RMS to be an perioperative tool to decipher the molecular alterations of COL I for fibrosis detection.

2. Materials and methods

2.1. Collection of human tissues samples

Formalin-fixed paraffin-embedded (FFPE) tissues were collected from patients undergoing medically needed surgery at the University Department of General, Visceral and Transplant Surgery, University Hospital Tübingen, and the University of California, Los Angeles (UCLA). Samples were collected after informed consent was obtained. The study was approved by the local ethical committees at UCLA and the University Hospital Tübingen (IRB 177/2014B04). Various fibrotic pathologies of different anatomical regions were analyzed, including liver lobules and portal triads, colon, breast, lymph node and myocardium. Non-fibrotic tissues from respective organs served as controls. A detailed overview of selected tissue samples and how samples were obtained is provided in Table 1. Serial 10 μm cross-sections of the tissues were prepared using a microtome (MICROM HM560, Thermo Scientific, Waltham, MA, USA).

2.2. Deparaffinization

FFPE tissue sections were deparaffinized using a modified protocol where samples were subjected to a thermal treatment at 60°C for 10 minutes, followed by three sequential incubations in xylol for 10 minutes each. The samples were then incubated in a series of ethanol solutions with progressively lower concentrations.

2.3. Masson's trichrome staining

Pathologists evaluated all tissues and confirmed the positions of fibrotic areas based on routine Masson's trichrome staining. Tissue sections were stained using an automated slide stainer Tissue Tek Prisma (Sakura, Finetek, USA) following the manufacturer's protocol.

2.4. Movat's pentachrome staining

FFPE sections were deparaffinized. A modified Movat's pentachrome staining was performed as previously described [35,36].

2.5. Picrosirius red staining

Collagen maturity and directionality analyses were performed via polarized imaging of PSR. First, Weigert's hematoxylin

Table 1
Disease origin of included samples.

Tissue type	Sample 1	Sample 2	Sample 3
Liver lobules & portal triads	Control; liver segmentation Hepatocellular carcinoma and liver cirrhosis (Ishak score 6/6); liver segmentation	Control; liver segmentation Hepatocellular carcinoma and liver cirrhosis (Ishak score 6/6); hepatectomy	Control; liver segmentation Liver cirrhosis associated to biliary atresia (Ishak score 5/6); liver biopsy
Colon submucosa	Control; hemicolectomy Crohn's disease; ileocecal resection	Control; intestine resection Crohn's disease; hemicolon resection	Control; intestine resection Crohn's disease; ileocecal resection
Breast connective tissue	Control; breast reduction surgery Marked fibrocystic changes and duct ectasia of the breast; surgical breast biopsy	Control; mastectomy Sclerosing adenosis; surgical breast biopsy	Control; breast reduction surgery Extensive ductal carcinoma in situ; mastectomy
Lymph nodes	Control; tonsillectomy Nodular sclerosis classical Hodgkin lymphoma; lymph node biopsy	Control; tonsillectomy Nodular sclerosis classical Hodgkin lymphoma; lymph node biopsy	Control; tonsillectomy Nodular sclerosis classical Hodgkin lymphoma; lymphadenectomy
Myocardium	Control; orthotopic heart transplantation Dilated cardiomyopathy; orthotopic heart transplantation	Control; orthotopic heart transplantation Dilated cardiomyopathy; orthotopic heart transplantation	Control; orthotopic heart transplantation Dilated cardiomyopathy; orthotopic heart transplantation

(Waldeck) was utilized to stain the nuclei of deparaffinized sections for 8 mins and washed with tap water for 10 mins. The sections were then treated with 0.1% picrosirius red solution (Morphisto, Frankfurt/Main, Germany) for 60 min. After treatment, the tissues were washed with 0.5% acetic acid and 100% ethanol. The picrosirius red-stained sections were imaged by polarized light microscopy (Axio Observer, Carl Zeiss Microscopy GmbH, Oberkochen, Germany) at 40x magnification followed by ImageJ (Fiji version 2.0.0) processing. The images were transferred to RGB colors. To acquire the area percentages of red and orange (mature collagens), as well as yellow and green (immature collagens) signals, the thresholds were adjusted as follows: red (1-13, 230-256), orange (14-25), yellow (26-52) and green (53-110). The directionality analysis was conducted via Image J by using the plugin “Directionality”. In brief, the method of Fourier components with histogram angles from -90 to 90 degrees were applied to every 32-bit images. Non-parallel fibers were expected to show a flat histogram with various direction; while fibers with similar orientation provide peaks with similar values, representing specific angles on the direction in the histogram [37]. The plugin “OrientationJ” was used to define fiber coherency. OrientationJ evaluates the local orientation of every pixel of an image by a structure-tensor approach. Coherency is calculated as the ratio between the difference and the sum of tensor eigenvalues [38]. Entire images were analyzed and similar settings were used from other literature [15].

2.6 Immunofluorescence staining

The tissue sections underwent antigen retrieval with Tris-EDTA buffer (pH 9, 0.05%) and citrate buffer (pH 6) followed by treatment of goat serum block solution (2%). Afterwards, the tissue sections were incubated overnight with the following primary antibodies: mouse IgG2a monoclonal anti-α smooth muscle actin (αSMA) ($2*10^{-3}$ g/L; Sigma-Aldrich), rabbit polyclonal anti-collagen type I (6.6*10−3 g/L; Acris, Herford, Germany). Secondary antibodies were AlexaFluor 594-conjugated goat anti-mouse (4*10−3 g/L, Thermo Fisher Scientific Life Technologies) and AlexaFluor 488-conjugated goat anti-rabbit (4*10−3 g/L; Thermo Fisher Scientific Life Technologies). Lastly, Drag5 (5 µM; BioLegend, San Diego, USA) was applied on the sections for 15 mins to stain the nuclei. The immunofluorescence (IF)-stained sections were imaged via confocal laser scanning microscopy (LSM 880, Carl Zeiss Microscopy GmbH) with a QUASAR detector. To gain the emission spectrum of the signals, an excitation wavelength of 800 nm was utilized to excite fluorochromes. Several channels representing specific wavelengths of the emission spectra with the range from 406 - 670 nm were created via Lambda stacks (9 nm intervals). Every spectral image was coupled with linear unmixing. Regions of interest were indicated by a pathologist based on pathological examination of the Masson's trichrome staining.

2.7. Raman microspectroscopy and Raman imaging

RMS measurements of tissues were performed on a customized confocal Raman microspectrometer (WITec alpha 300 R, Ulm, Germany), equipped with a 532 nm laser and a CCD camera as described before [39]. For all scans a spectrograph with a grating of 600 g/mm was chosen for spectral detection. The human tissues were deparaffinized and kept humid with PBS during the entire measurement procedure to prevent sample dehydration and burning. Raman maps were measured utilizing a 63x Apochromat water dipping objective (N.A. 1.0; Carl Zeiss Microscopy GmbH). For each tissue section, Raman maps ($n = 3$) were acquired for an area of 100 × 100 µm and at a spatial resolution of 1 µm/pixel. The laser power was set to 50 mW at an integration time of 0.05 s per spectrum for all measurements. Reference spectra of αSMA, COL I, COL III were acquired based on IF images of colon.

2.8 Spectral analysis

With the software WITec project 5 (WITec GmbH, Ulm, Germany), all Raman maps were subjected to cosmic ray removal, polynomial baseline correction, cropping to 400-3000 cm^{-1} and area intensity normalization. With True Component Analysis (TCA), Raman scans were decomposed into spectral components as described previously [40,41]. TCA is a statistical technique that involves the use of a linear combination of spectra or components to describe each pixel in an image. This allows for the separation of different spectra that may be present in the image, and the identification of the materials or substances present based on the unique spectral patterns of the components [42]. Different types of collagens (COL I, COL III, COL IV), nuclei, αSMA, and paraffin were identified as major spectral components and localized in their corresponding intensity distribution in heatmaps resulting in false color-coded Raman images. TCA was employed to eliminate localized paraffin signals from the Raman images, thereby precluding any interferences in the subsequent analyses. Based on TCA heatmaps, spectral information (600 spectra/sample) representing COL I was extracted for further in-depth analysis of the molecular composition by PCA using Unscrambler X10.5 (Camo, Norway).

2.9 Spectral deconvolution

To gain information of peak width and peak area of the substructural bands of the amide I region (1550-1720 cm^{-1}), spectral deconvolution was performed with the software WITec project 5 (WITec). Prior to deconvolution, collagen maps were extracted from the Raman data. Collagen maps were then cropped to the amide region before normalization of the peak at 1667 cm^{-1} to 1. The fitting region was set between 1508 and 1780 cm^{-1}. The initial position of peak calculations was set to 5 wavenumbers based on the shape of the amide I region located at 1565, 1588, 1608, 1637 and 1667 cm^{-1} and information obtained from literature [43]. For spectral deconvolution, the Lorentz fitting algorithm was chosen, with a maximum number of iterations of 1000, while fitting five functions with the shape

$$y = y_0 + \frac{2A}{\pi}\frac{w}{(x - x_0)^2 + w^2} \tag{1}$$

where w describes the width and A the area of the peak. The accuracy of each fit is evaluated with adjusted R^2 values, which is calculated as,

$$R^2{}_{adj} = 1 - \frac{1 - R^2\ (n-1)}{(n-k-1)} \tag{2}$$

where n is the number of points in the data sample and k is the number of variables in the model [43,44]. Information about peak width and peak area was extracted for further analysis. Additionally, peak intensity ratios of mean collagen spectra were calculated by division of the maximum amide I peak at 1667 cm^{-1} by the intensity at 1608 cm^{-1}.

2.10 Raman image ratio analysis

To obtain information about the peak ratios of all the individual collagen spectra within one Raman map, maximum intensity filter images of collagen maps were generated with the software WITec project 5. Sum filter images were acquired at 1667±25 cm^{-1}and at 1608±10 cm^{-1}. Next, image ratios of both filter images were calculated before exporting them to MatLab 2019b. The resulting images contained the value of the peak ratio for each specific pixel position. Filter images were subjected to histogram analysis, in which the distribution of all ratios is represented. Ratios were then rounded to integers before mode analysis.

2.11. Data Classification

Raman spectra were classified using linear discriminant analysis from the open-source Python scikit library [45] and a simple neural network from the open-source Keras and TensorFlow API (Google Brain). The neural network used the whole spectral fingerprints of the Raman spectra for classification. Raman spectra were classified into one of the two classes: control and fibrosis. The fully connected neural network model consists of seven layers. The input layer is a dense layer with 250 hidden units and ReLU (Rectified Linear Unit) activation. The second layer is another dense layer with 1000 hidden units, while the third layer is a dropout layer with a rate of 0.75 used to prevent overfitting. The fourth layer is a dense layer with 500 hidden units, while the fifth layer is another dropout layer with a rate of 0.25. The sixth layer is a dense layer with 62 hidden units. Finally, the seventh layer is a dense layer with 2 units and softmax activation for binary classification. The activation functions used are mainly ReLU and one sigmoid function in the last layer for probabilistic output values. The optimizer used is Adam [46] with a learning rate of 0.001. With a batch size of 128, the model trained for 100 epochs and a train validation test split of 0.6, 0.2, 0.2 is applied.

2.12. Statistical analysis

Statistical comparisons were performed from a minimum of three independent controls and fibrotic patient samples per organ. Statistical analysis was performed using GraphPad Prism version 9.00 (GraphPad Software). Results are shown throughout the entire manuscript as mean ± standard deviation. All n-numbers, applied tests, and corresponding significance for each result are listed in the figure legends.

3. Results

3.1 Histological staining indicates the presence of fibrotic lesions

Fibrosis is characterized by excessive formation of connective tissue. As collagen is the main component of connective tissue, increased collagen (mainly COL I) accumulation is an indicator of fibrotic lesions. Thus, both Masson's trichrome staining and Movat's pentachrome staining are gold standards for histopathological identification of fibrosis in patient biopsies by visualization of collagen fibers. In this study, control tissues of liver hepatocytes, liver portal triads, colon, breast connective tissue, lymph nodes and myocardium were compared to fibrotic pathologies of their respective organ to identify structural and molecular fibrosis patterns in collagen fibers (Fig. 1). Details on investigated tissue samples are provided in Table S1.

Masson's trichrome staining identified major differences in collagens between control and diseased samples. Liver tissues showed hepatic lobules (Liver lob) with small amounts of collagens depicted in blue. In the vertices of the lobes (Liver pt), collagen formations surrounding the proper hepatic artery, hepatic portal vein, bile ducts, lymphatic vessels and branches of the vagus nerve were found. In contrast, cases with liver hepatocellular carcinoma (Ishak score 6) demonstrated an increased amount of collagen that formed collagen bridges between two or more portal triads. The layer of the colon submucosa located between the mucosa (tunica mucosa) and smooth muscle (tunica muscularis) was the focus of the colon sample comparison. Control tissues were compared to samples from patients suffering from Crohn's disease. The diseased sample showed a significant amount of fibrosis and swollen colon tissue when compared to controls. The control breast tissues consisted of varying amounts of fibrous and adipose tissue, and a ductal-lobular secretory system. Masson's trichrome stain identified a large amount of collagen fibers in the control and diseased tissue. Ductal carcinoma, a precancerous invasive breast lesion, were stained showing a similar extent of collagen when compared to the control. Reactive lymph nodes showed reactive follicles and connective tissue septa. Nodular sclerosis classical Hodgkin lymphoma samples were used as the diseased tissue which showed a partial effacement of the nodal architecture with presence of dense collagen bands highlighted by Masson's trichrome staining. Dilated cardiomyopathy samples were compared to control myocardium, which showed significant interstitial collagen infiltrations in the diseased samples. Movat's pentachrome staining provided further information on the composition of the tissues. In consecutive Movat's pentachrome images (Fig. 1b) nuclei and elastic fibers were stained in black, while fibrin and muscles were stained in red. Collagens and reticular fibers were stained in yellow and mucins in blue to green. Like shown with Masson's trichrome staining, Movat's pentachrome-stained samples allowed for the identification of fibrosis based on the amount of collagen. Nevertheless, both stains were unable to discriminate between the different types of collagens and were difficult to quantify due to color overlays.

3.2. Collagen fiber density and orientation differs across tissue types

To determine if collagen fiber orientation is a robust readout when differentiating between control and fibrotic tissues, polarized light images of PSR-stained tissue sections were obtained according to their birefringent characteristics. PSR images of control and fibrotic conditions of all examined tissue types were analyzed

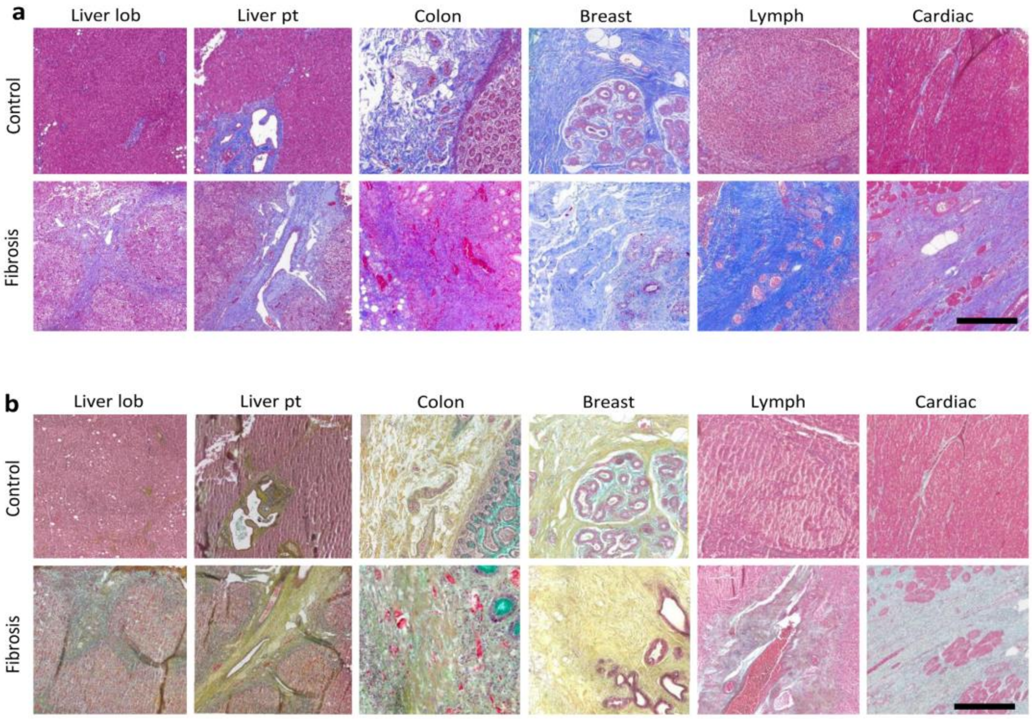

Fig. 1. Histopathology of fibrotic tissue lesions. Masson's trichrome and Movat's pentachrome staining visualize the morphology of control and fibrotic tissues. (a) Masson's trichrome staining of control and fibrotic hepatic lobules (liver lob), liver portal triads (pt), colon, as well as connective tissue of the breast, lymph nodes and myocardium. In Masson's trichrome staining, collagens are stained blue and nuclei are stained brown-black, while cytoplasm is presented in red/pink. (b) In Movat's pentachrome staining, collagens are stained in yellow, nuclei and elastic fibers in black, glycosaminoglycans in blue/green and muscles in red. Scale bars equal 500 µm. (For interpretation of the references to colour in this figure legend, the reader is referred to the web version of this article.)

(Fig. 2a). Quantification of red and green collagens revealed differences between control and fibrotic tissues; however, there was no fibrosis-specific trend observed throughout the different tissue origins (Fig. 2b). According to the calculated ratios, liver hepatocytes and liver portal triads, green collagen fibers prevailed the controls with a shift to red fibers in a fibrotic state (control liver lob: 0.72 arb. u. ± 0.03 arb. u.; fibrotic liver lob: 0.46 arb. u. ± 0.05 arb. u.; $p < 0.0001$; control liver pt: 0.21 arb. u. ± 0.18 arb. u.; fibrotic liver pt: 0.11 arb. u. ± 0.1 arb. u.; $p = 0.0471$). In breast tissue (control: 0.01 arb. u. ± 0.01 arb. u.; fibrosis: 0.07 arb. u. ± 0.10 arb. u.; $p = 0.0112$) and lymph nodes (control: 0.45 arb. u. ± 0.28 arb. u.; fibrosis: 0.81 arb. u. ± 0.06 arb. u.; $p < 0.0001$), more green collagen fibers were observed in the fibrotic state compared with the controls. In colon (control: 0.09 arb. u. ± 0.05 arb. u.; fibrosis: 0.08 arb. u. ± 0.05 arb. u.; $p = 0.4982$) and myocardium (control: 0.26 arb. u. ± 0.14 arb. u.; fibrosis: 0.29 arb. u. ± 0.03 arb. u.: $p = 0.6117$), no significant differences were found when comparing the contribution of red to green collagen fibers.

Collagen fiber alignment was assessed by histograms of fiber orientation. Histograms of collagen fiber direction in control tissues displayed an even distribution on different angles in liver hepatocytes, breast, lymph node and heart, indicating a non-aligned collagen network (Fig. 2c). In liver portal triads and colon, the histogram shifted to a parallel alignment due to naturally structured collagen fibers. In fibrotic collagens, a shift from randomly distributed orientations in controls to a more parallel alignment was found in all tissues except for breast, where most of the fibers were at a similar angle in the histograms (Fig. 2d). The quantification of fiber alignment was performed by coherency analysis indicating the overall percentage of collagens that were parallel aligned (Fig. 2e). The only statistically significant changes in coherency were found in the collagens of lymph nodes (control: 3.2% ± 0.3%; fibrosis: 11.3% ± 3.9%; $p = 0.0406$), while a similar tendency was observed in liver portal triads (control: 36.5% ± 0.2%; fibrosis: 27.8% ± 5.9%; $p = 0.4951$) and myocardium (control: 9.2% ± 3.5%; fibrosis: 17.2% ± 7.0%; $p = 0.2201$). All other tissues did not show statistically significant alterations in the degree of parallelism.

3.3. Raman imaging enables marker-independent visualization of tissue structure states

PSR and histological analyses were not robust enough to determine fibrotic collagen fiber alterations throughout the different tissue types and were not specific for collagen subtypes. Therefore, IF staining and marker-independent RMS were performed to identify and localize COL I and other proteins. IF staining was performed to compare and evaluate the performance of Raman imaging for the identification of distinct tissue structures as well as for the distribution of ECM components in the liver, colon, breast, lymph node and myocardium tissues. IF staining was applied to identify COL I (yellow), αSMA (red), and nuclei (blue) in all tissues (Fig. 3a).

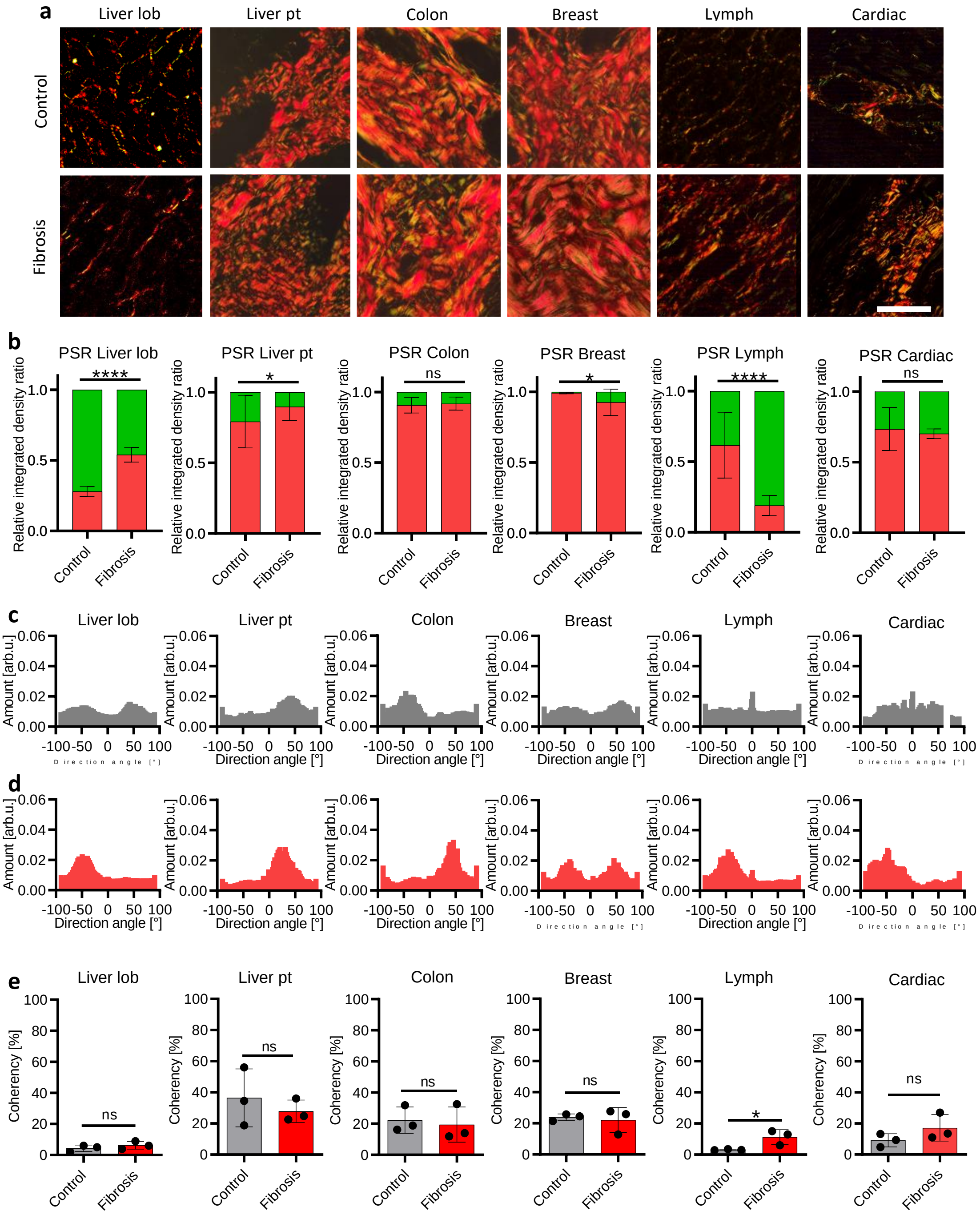

Fig. 2. Analysis of fibrillar collagens via picrosirius red staining (PSR) shows inconsistency throughout fibrotic tissue origin. (a) PSR images of control and fibrotic tissue of different organs. Scale bar equals 100 µm. (b) Quantification of mature/thick collagen (red) and immature/young collagen show inconsistency throughout all tissue origins. Directionality analysis of control collagen fibers (c) shows random distribution in the orientation of collagen fibers. In fibrotic tissues (d), the collagen fibers are more parallel aligned. Overall, the consistency is higher in the fibrosis group. (e) Coherency analysis shows statistically significant differences only in lymph node tissues. Statistical analysis: t-test, $n = 3$, $^{*}p < 0.05$, $^{****}p < 0.0005$. (For interpretation of the references to colour in this figure legend, the reader is referred to the web version of this article.)

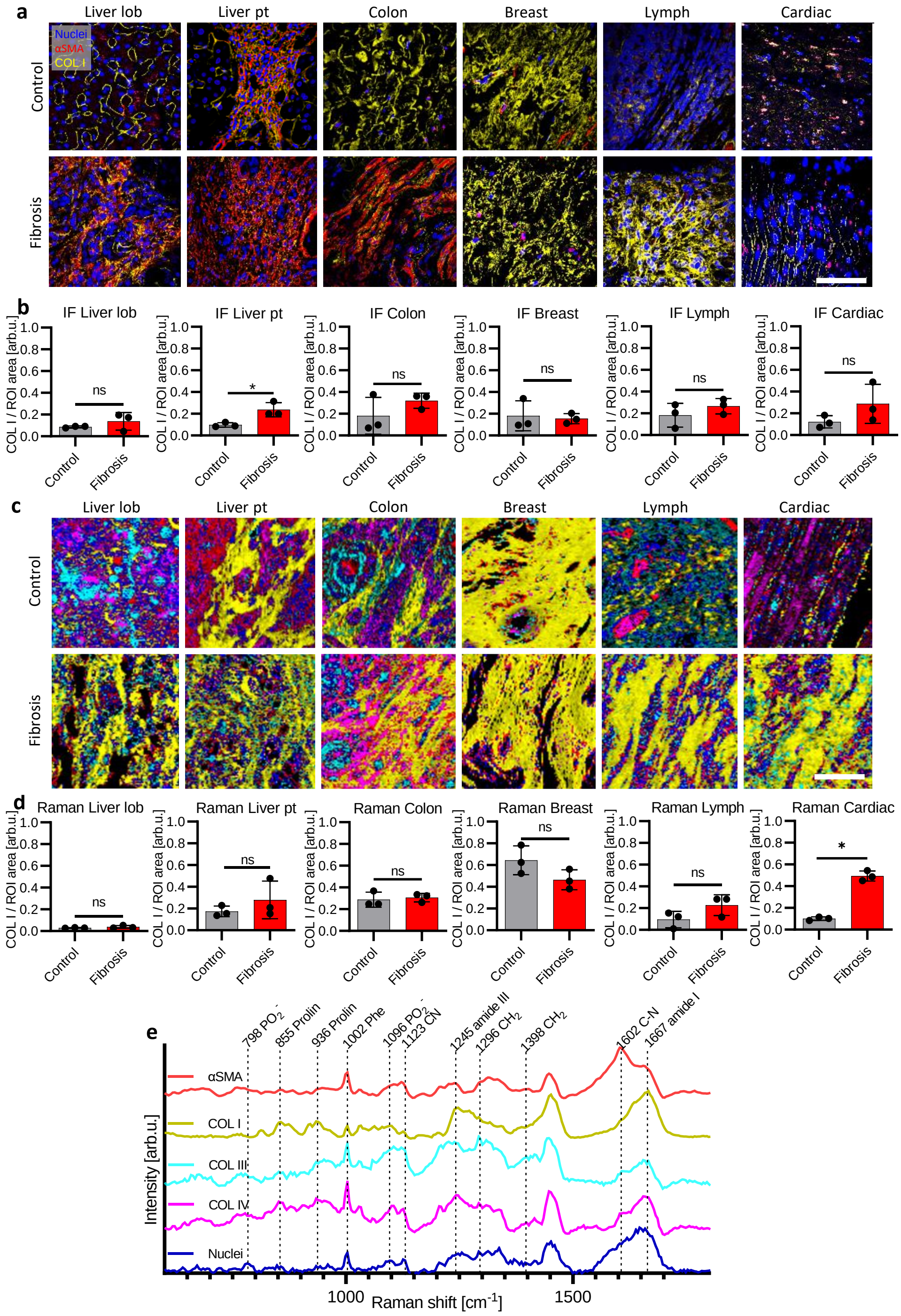

Fig. 3. Comparison of immunofluorescence (IF) staining and marker-independent true component analysis (TCA) of Raman images of control and fibrotic tissue. (a) IF staining and (c) TCA both show the complexity of the different tissue types. Colors in IF staining: nuclei (blue), COL I (yellow), αSMA (red). Scale bar equals 100 µm in IF and 50 µm in TCA images. (b) Quantification of the amount of COL I based on IF images normalized by the whole tissue area. (d) Quantification of the amount of COL I based on Raman maps normalized by the whole tissue area. (e) Spectra identified by TCA: nuclei (blue), COL IV (pink), COL III (turquoise), COL I (yellow) & αSMA (red). Statistical analysis: t-test, $n = 3$. $^{*}p < 0.05$. (For interpretation of the references to colour in this figure legend, the reader is referred to the web version of this article.)

Throughout tissue origins and disease stages, different COL I morphologies were observed. IF staining of control liver hepatocytes demonstrated evenly distributed COL I-composed fibers in circular shape, while in fibrosis, the amount of COL I-composed fibers was slightly increased (Fig. 3b). Apart from COL I, αSMA which is an indicator of mature myofibroblasts, also plays a vital role in ECM remodeling and fibrosis [47]. In hepatocytes, αSMA was randomly distributed in the control tissues, while being colocalized with COL I in tissues affected by fibrosis (Fig. 3a). In the portal triads of the liver, a dense network of COL I was visible in the controls, which increased significantly in fibrosis (Fig. 3b) (control: 0.10 arb. u. ± 0.01 arb. u.; fibrosis: 0.24 arb. u. ± 0.05 arb. u.; p = 0.0246). Both control and fibrosis samples of portal triads showed a colocalization of αSMA with COL I (Fig. 3a). In healthy colon, COL I was distributed throughout the connective tissue, while in the fibrosis samples, although still being distributed throughout the connective tissue, COL I appeared to be embedded particularly between αSMA-positive myofibroblasts. A dense network of COL I-expressing fibers was present in both control and fibrotic breast tissue with no change in the amount (Fig. 3b), whereas αSMA-expressing cells were not detected. No visible differences were identified in control breast tissue compared to fibrosis. In IF images of control lymph nodes, COL I was distributed throughout the tissue (Fig. 3a), slightly increasing in lymph nodes with classical Hodgkin Lymphoma (Fig. 3b) (control: 0.18 arb. u. ± 0.09 arb. u.; fibrosis: 0.27 arb. u. ± 0.06 arb. u.; p = 0.2284). Neither group showed αSMA. In control myocardium, as expected, very little COL I expression was visible, while in fibrotic myocardium an increased amount of parallel aligned COL I fibers was detected (Fig. 3a,b) (control: 0.12 arb. u. ± 0.05 arb. u.; fibrosis: 0.29 arb. u. ± 0.15 arb. u.; p = 0.2003). Interestingly, no αSMA staining was identified in control or fibrotic myocardium.

To characterize the tissue composition of the control and fibrotic samples non-invasively and marker-independently, Raman imaging was performed (Fig. 3c). Large area scans of the regions of interest were analyzed by TCA. The mathematical model identified five major cellular components identified in all tissue types. TCA allowed the visualization of the tissue substructures as false color-coded intensity heatmaps in which each color represented the best fit to one of the identified molecular signatures.

Evaluation of the individual peaks of the fingerprint regions of the Raman spectra (Fig. 3e) in combination with the morphology of the structures allowed the identification of correlating molecular assignments and biological origin. Nuclei (blue) were identified by pronounced peaks at 798 and 1096 cm^{-1}, indicators for PO2− occurring in DNA [48]. COL I (yellow) was assigned to the characteristic peak pair at 855 and 936 cm^{-1} indicatives for proline [49,50]. The collagen type IV (COL IV, pink) Raman spectra shared many spectral features with COL I; however, it showed an increased signal intensity at 1312 cm^{-1}, 1335 cm^{-1}, and 1398 cm^{-1}, which are representatives for CH3/CH2 twisting or wagging modes as well as changes in CH2 deformation [49–51]. Additionally, the band at 1002 cm^{-1}, which is a representative for phenylalanine (Phe), was increased in COL IV as reported before by Nguyen et al [52]. Collagen type III (COL III, turquoise) shares many spectral features with COL I; however, it differed in the amide III region by slightly shifted peaks from 1245 to 1248 cm^{-1} as previously reported [53]. Furthermore, changes in CH2 and CN were found by a band occurring at 1296 cm^{-1} and increased intensities at 1123 cm^{-1} [49,54]. Compared to COL I, the peak pair at 855 and 936 cm^{-1} dropped in intensity in all other collagen types. The spectral assignments to αSMA (red) were based on in-house Raman measurements, which had been acquired and validated by co-localization of the IF signal (Supplementary Fig. S1a). The Raman spectrum of αSMA is mainly distinguished from the Raman spectra of the different collagen types by the shape of the amide I region. In the αSMA Raman spectrum, the maximum of the amide I peak is relocated from 1667 cm^{-1} to 1602 cm^{-1}, wavenumbers which represent C-N bonds [55]. In general, TCA images showed similar morphological features as IF images, indicating the potential of Raman spectroscopy being utilized to image tissues non-invasively. Quantification of the amounts of COL I (Fig. 3d) based on Raman maps solely containing COL I information showed similar results as IF quantification. While there were no observable differences between the control and fibrotic tissues in regard to the amount of COL I in hepatocytes (control liver lob: 0.03 arb. u. ± 0.01 arb. u.; fibrotic liver lob: 0.04 arb. u. ± 0.01 arb. u.; p = 0.3203) or colon (control: 0.10 ± 0.06 arb. u.; fibrosis: 0.23 arb. u. ± 0.08 arb. u.: p = 0.6993), the portal triads of the liver showed a slight increase in fibrotic COL I (control liver pt: 0.17 arb. u. ± 0.04 arb. u.; fibrotic liver pt: 0.28 arb. u. ± 0.14 arb. u.; p = 0.3073). Further, and similar to the IF imaging, in fibrotic lymph nodes the amount of COL I was increased in comparison to the controls (control: 0.10 arb. u. ± 0.06 arb. u.; fibrosis: 0.23 arb. u. ± 0.08 arb. u.; p = 0.1335). A statistically significant increase was identified in fibrotic myocardium (control: 0.10 arb. u. ± 0.01 arb. u.; fibrosis: 0.49 arb. u. ± 0.04 arb. u.; p = 0.0002).

3.4. Fibrotic COL I alterations are identified by Raman analyses at wavenumber 1608 cm^{-1}

In addition to the image-based characterization of tissue patterns, in-depth analysis of the underlaying Raman spectra allowed a molecular-sensitive analysis of tissue structures. For further analysis of collagen fibers from several human tissues, COL I spectra were extracted from large area scans and processed as single or averaged spectra. These Raman spectra were cropped to the fingerprint region (600-1800 cm^{-1}) and peak normalized to 1 for better comparability (Fig. 4a). To determine the sensitivity of Raman spectroscopy to distinguish between control and fibrotic COL I, 200 single spectra per sample were analyzed by principal component analysis (PCA). Comparison of PC score values (Supplementary Fig. S1b) demonstrated trends of separation in PC-2 and PC-3, both mainly explained by shifts in loadings plots (Supplementary Fig. S1c) at the amide I region (1550-1720 cm^{-1}), containing information about the secondary structure of proteins. The secondary structures of collagens were mainly α-like helices, β-sheets, β-turns and random coils (disordered) [56,57].

In addition, LDA and neural network-based classification were utilized to classify the Raman data into one of the two groups control or fibrosis. Supplementary Table S1 shows the classification results with the performance parameters accuracy, sensitivity, and specificity for the LDA, and neural network trained with the entire RMS data. We observed that compared to LDA, the utilization of neural networks resulted in an improvement in classification performance. Specifically, LDA yielded an accuracy of 62% a sensitivity of 60% and a specificity of 64% while the utilization of neural networks resulted in an accuracy of 71% a sensitivity of 64% and a specificity of 72%

For a detailed analysis of the secondary structure of COL I, spectral deconvolution of the amide I peak of averaged control and fibrotic COL I Raman spectra was utilized to separate the broad band into five underlying peaks. The sub-band number and locations were chosen based on the shape of the amide I peak in averaged COL I Raman spectra (Fig. 4b) and according to literature [43]. Fig. 4c and d display the amide I region of control and fibrotic liver portal triads with underlying sub-bands calculated by spectral deconvolution. Spectral deconvolution allowed the analysis of the width and area of sub-peaks occurring at 1562 cm^{-1}, 1588 cm^{-1}, 1608 cm^{-1}, 1637 cm^{-1} and 1667 cm^{-1} which are assigned to tryptophan, phenylalanine, and tyrosine, β-sheets as well as β-turns. The adjusted R2 values were above 0.995 for all the deconvolu-

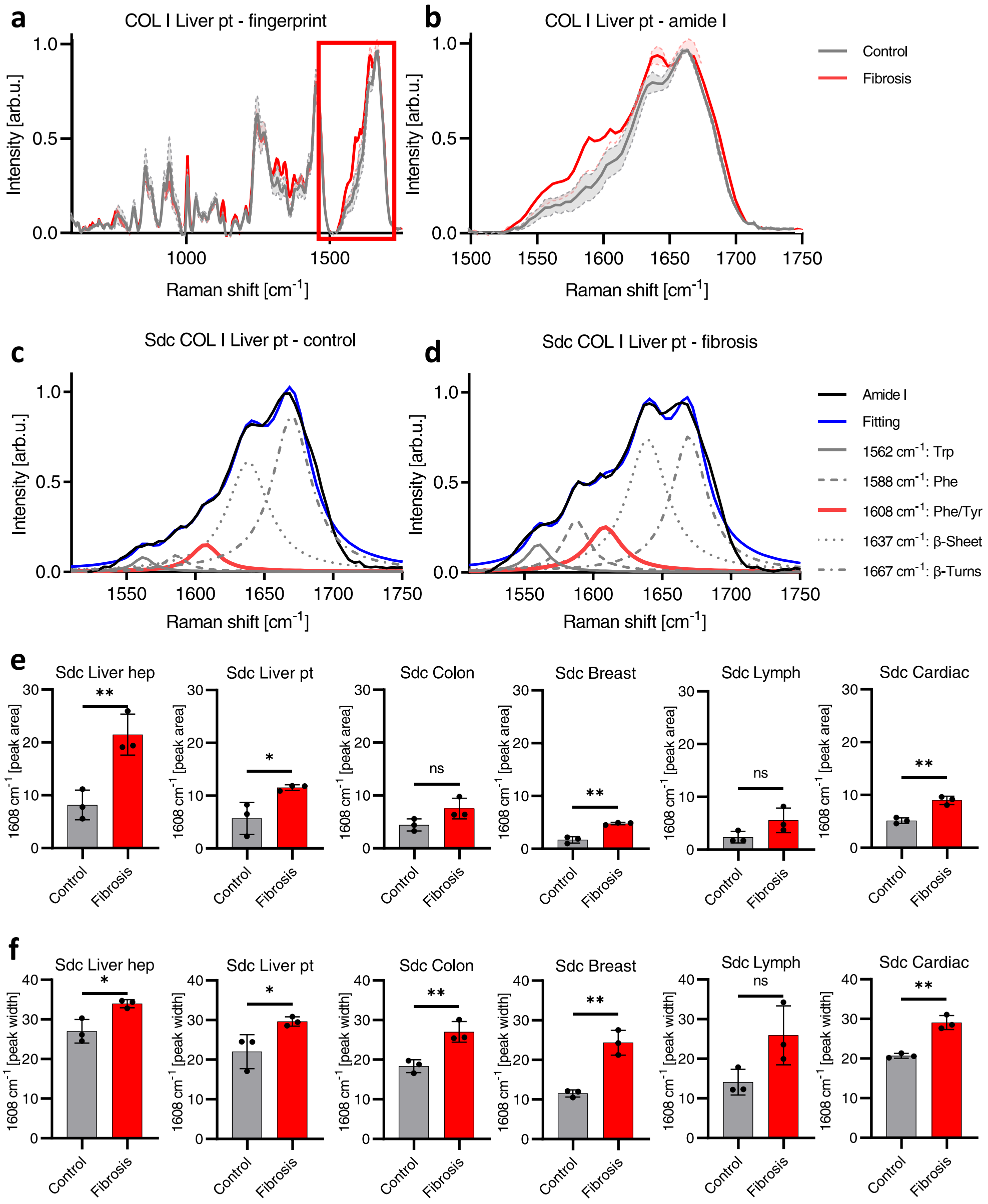

Fig. 4. Spectral deconvolution (Sdc) of the amide I region from averaged COL I Raman spectra display a similar separation between control and fibrosis through all tissue types. (a) Raman fingerprint of control and fibrotic COL I of liver portal triad. (b) Amide I region of control and fibrotic COL I of liver portal triad. The shaded error lines represent the standard deviation. Spectral deconvolution of the amide I band from (c) control and (d) fibrotic liver portal triad. The averaged amide I band is shown by a black solid line and sub-bands at 1562, 1584, 1639 as well as 1667 cm^{-1} are labeled in grey (solid line, dashed, dotted, dash-dot), while the sub-band at 1608 cm^{-1} is marked in red. The fitted amide I band is visualized by a blue solid line. (e) Peak area at 1608 cm^{-1} calculated based on spectral deconvolution of amide I area of averaged COL I spectra from control and fibrotic tissue show similar separation through all tissue types. (f) Peak width at 1608 cm^{-1} calculated based on spectral deconvolution of amide I area of averaged COL I spectra from control and fibrotic tissue show similar separation through all tissue types. Statistical analysis: t-test, n = 3, *p < 0.05, **p < 0.01. (For interpretation of the references to colour in this figure legend, the reader is referred to the web version of this article.)

tions, indicating sufficient fitting accuracy. Area and width of the subpeaks at 1588 cm^{-1}, 1608 cm^{-1} and 1637 cm^{-1} were subjected to statistical analysis. While in peak areas at 1588 cm^{-1} there was a statistically significant increase in fibrotic liver hepatocytes, this increase was inversed in breast tissue samples (Supplementary Fig. S2a). All other tissue types did not show any statistical separation between the control and fibrosis samples. Similar statistical differences were found in the peak width at 1588 cm^{-1} (Supplementary Fig. 2b). Peak analysis of the subpeak at 1637 cm^{-1} did not show any statistically significant difference in all examined tissues in both peak area (Supplementary Fig. S2c) and peak width (Supplementary Fig. S2d). However, analysis of the calculated peak area of the subpeak at 1608 cm^{-1} (Fig. 4e) showed a statistically significant increase in the liver tissues (control liver lob: 8.2 arb. u. ± 2.3 arb. u.; fibrotic liver lob: 21.5 arb. u. ± 3.2 arb. u.; $p = 0.0085$; control liver pt: 5.7 arb. u. ± 2.5 arb. u.; fibrotic liver pt: 11.5 arb. u. ± 0.4 arb. u.; $p = 0.0313$). In colon, the clear tendency of an increased peak area was identified between control and fibrotic tissues (control: 8.2 arb. u. ± 2.3 arb. u.; fibrosis: 21.5 arb. u. ± 3.2 arb. u.; $p = 0.0774$). For COL I in the connective tissue from human breast tissues, spectral deconvolution showed a statistically significant increase in intensity in fibrotic cases for the band at 1608 cm^{-1} (control: 1.7 arb. u. ± 0.5 arb. u.; fibrosis: 4.8 arb. u. ± 0.2 arb. u.; $p = 0.0012$). An increased peak area at 1608 cm^{-1} was also seen when comparing COL I in control and fibrotic lymph nodes (control: 2.4 arb. u. ± 0.9 arb. u.; fibrosis: 5.6 arb. u. ± 1.9 arb. u.; $p = 0.0977$). We further observed a statistically significant increased peak area at 1608 cm^{-1} in the fibrotic myocardium (control: 5.1 arb. u. ± 0.5 arb. u.; fibrosis: 9.0 arb. u. ± 0.7 arb. u.; $p = 0.05$).

In addition to peak areas, spectral deconvolution also enables the calculation of the width of the underlying peaks (Fig. 4f). In all analyzed tissues, statistically significant increases in peak widths were observed in fibrotic COL I compared to control tissue.

As a third parameter of the subpeak at 1608 cm^{-1}, we calculated the peak intensity ratio to the maximum of the highest amide I subpeak located at 1667 cm^{-1} (Fig. 5a). A statistically significant decrease in the peak ratio was identified in fibrotic liver hepatocytes and breast tissues (control liver lob: 2.2 arb. u. ± 0.3 arb. u.; fibrotic liver lob: 1.3 arb. u. ± 0.3 arb. u.; $p = 0.0252$; control breast tissue: 3.5 arb. u. ± 0.9 arb. u.; fibrotic breast tissue: 2.9 arb. u. ± 0.2 arb. u.; $p = 0.0136$). Similar tendencies were demonstrated for the fibrotic tissues of liver portal triad (control: 2.5 arb. u. ± 0.5 arb. u.; fibrosis: 1.7 arb. u. ± 0.3 arb. u.; $p = 0.1543$), colon (control: 2.330 arb. u. ± 0.1 arb. u.; fibrosis: 2.7 arb. u. ± 0.3 arb. u.; $p = 0.1194$), lymph nodes (control: 3.6 arb. u. ± 0.6 arb. u.; fibrosis: 2.2 arb. u. ± 0.8 arb. u.; $p = 0.0699$) and myocardium (control: 2.8 arb. u. ± 0.1 arb. u.; fibrosis: 2.5 arb. u. ± 0.1 arb. u.; $p = 0.0767$). In addition to spectral deconvolution, which evaluated the amide I band of the averaged COL I spectra from Raman maps, a sum filter-based image analysis was employed, evaluating the entity of all COL I spectra of one scan. Here, filter images from COL I maps were created at 1608±10 cm^{-1} and 1667±25 cm^{-1} and divided by each other to assess the peak ratio per pixel in each image. The histograms calculated by filter image-based ratios are displayed in Fig. 5b. Throughout all tissue sections, modes and percentiles showed shifts to lower values in the fibrotic case compared to control. Analysis of the mode (Fig. 5c) revealed the value appearing the most frequent in each image, where a high value was describing ratios with less intense peaks at 1608 cm^{-1}. The analysis of the modes representing the whole COL I maps indicated statistically significant differences for liver hepatocytes (control: 7.8 arb. u. ± 0.3 arb. u.; fibrosis: 4.9 arb. u. ± 0.8 arb. u.; $p = 0.0099$), liver portal triad (control: 9.3 arb. u. ± 0.8 arb. u.; fibrosis: 6.2 arb. u. ± 1.00 arb. u.; $p = 0.0243$) and breast tissues (control: 9.7 arb. u. ± 0.8 arb. u.; fibrosis: 6.3 arb. u. ± 0.9 arb. u.; $p = 0.0162$). Tendencies of separations in modes were found in all other tissue types such as colon (control: 9.4 arb. u. ± 0.8 arb. u.; fibrosis: 8.3 arb. u. ± 0.9 arb. u.; $p = 0.2885$), lymph nodes (control: 16.9 arb. u. ± 2.0 arb. u.; fibrosis: 11.0 arb. u. ± 2.9 arb. u.; $p = 0.0766$) and myocardium (control: 11.3 arb. u. ± 1.6 arb. u.; fibrosis: 8.5 arb. u. ± 1.8 arb. u.; $p = 0.1789$).

4. Discussion

Fibrosis is one consequence of most chronic inflammatory disorders, and COL I-composed fibers are the main component of a fibrotic capsule or scar. Early identification of tissue fibrosis followed by timely treatment could potentially allow the prevention or reversal of organ damage [58]; however, besides indirect diagnosis due to organ malfunction or failure, the current gold standard in fibrosis diagnosis is histopathological assessment of collagen fibers in tissue biopsies [59,60]. This invasive biopsy procedure involves not only time-consuming laboratory work and a potential observer bias [61,62], it is also only possible at a late-stage of the disease. Furthermore, especially in collagen-rich tissues, e.g. the breast tissue, histology-based identification of fibrotic lesions is limited. Here, trained pathologists need to take morphometric observations of histologically-stained tissue sections and perform visual scoring to identify the existence of fibrosis [63]. Clinical diagnosis of fibrotic disease might occasionally be determined differently due to individual experience and knowledge, causing variations of diagnosis results. Also, there exists a limitation of deep collagen fiber characterization, classification, and quantification by classical stains [64,65].

In this study, we demonstrated that non-destructive and marker-independent Raman microspectroscopy and Raman imaging have the potential to detect fibrotic COL I alterations throughout different tissue origins. Tissues from different human organs were investigated, including liver, colon, breast, lymph nodes and myocardium in their respective control stage as well as after the development of fibrotic morphologies. Conventional histological methods were compared to RMS-based approaches. PSR staining was utilized to distinguish between the alignment of collagen fibers in the different tissue types [66,67]. Recently, digital-imaging analysis was used in combination with PSR to evaluate topological alternations in collagen fibers and their compactness in order to gain more understating of fibrosis dynamics [68]. Our results demonstrated that collagen fibers in fibrosis were more frequently aligned in parallel than non-pathological collagen fibers, in which the alignment was randomly distributed. However, the extent to which PSR can be relied upon to assess fibrotic collagen fibers is still controversial. It has been broadly reported that the color of the fibers demonstrates a certain state of collagens [69]. Although it is still under debate whether the colors of the PSR are capable of discerning maturity and thickness of the collagen fibers [70,71], it is believed that in thick/mature collagen fibers, the interaction with polarized light results in a stronger red birefringence and for thinner fibers in a weaker green birefringence [72–74]. The strong positive birefringence of collagen fibers is the result of the superposition of the right-handed superhelix with the left-handed helix, which comprises the three polypeptide chains, leading to an alignment of the amino acid chains approximately parallel to the molecular axis [72]. Moreover, it is also reported that green-yellow collagen fibers may represent procollagen, intermediate collagen, or Col III fibers [66,75,76]. Nevertheless, to date, the exact indication of the colors in PSR staining with polarized light remains debatable and requires complementary validations such as IF staining. In our study, quantification of the presence of red and green fibers revealed statistically significant differences between the control and fibrosis samples in most tissue types except colon and heart. However, shifts in the ratio of red

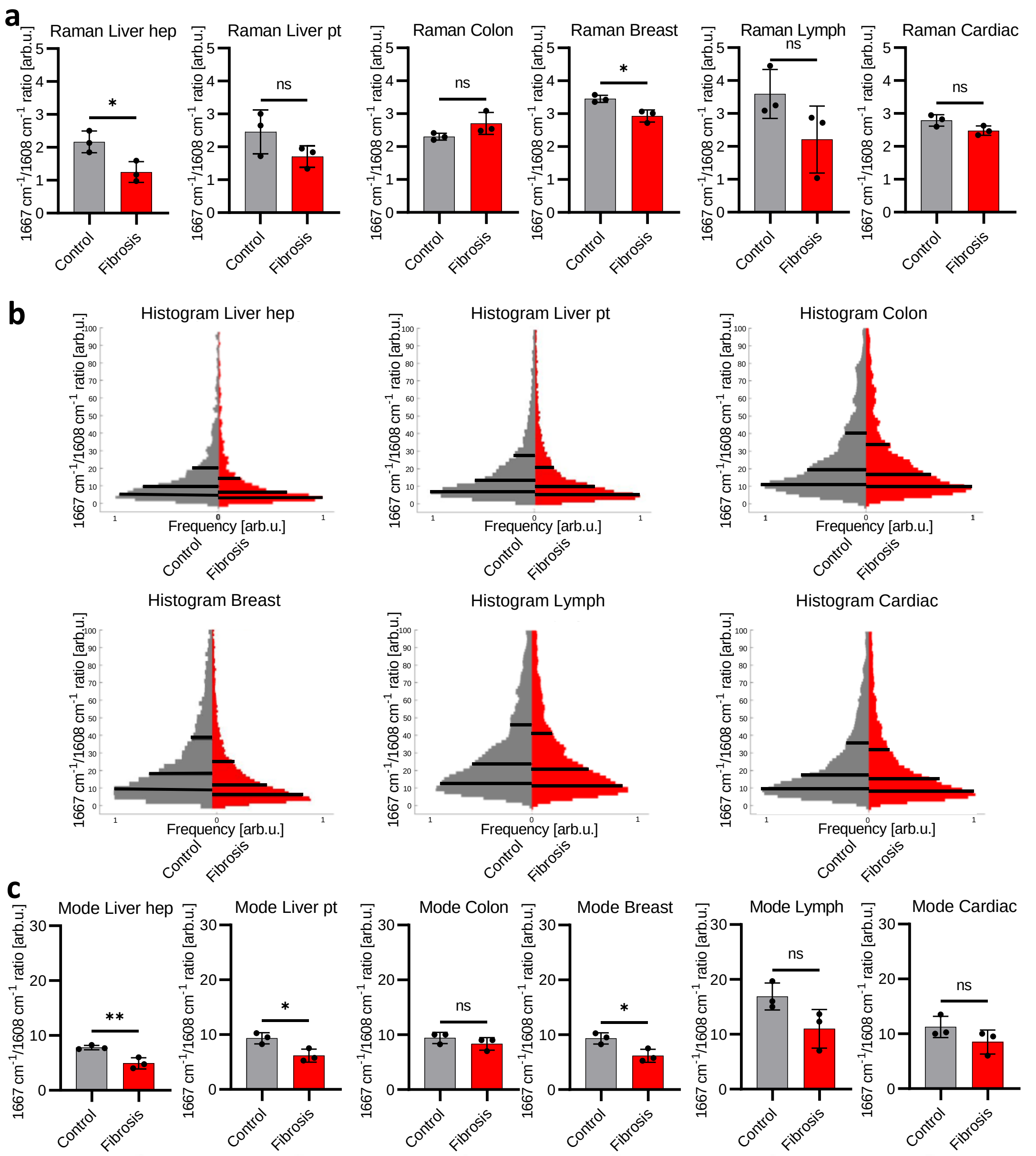

Fig. 5. Peak ratio of amide I region from averaged COL I Raman spectra and Raman image analyses display similar separation between control and fibrosis through all tissue types. (a) Peak ratio of averaged COL I spectra at 1608 cm^{-1} normalized by amide I maximum. (b) Histograms of filter image ratio at 1608 cm^{-1}, normalized by amide I maximum (1667 cm^{-1}). Lines in the histogram represent the 25, 50 and 75 percentiles while the widest position of the histograms is displaying the mode. (c) Frequency of modes from filter image ratio at 1608 cm^{-1} normalized by amide I maximum. Statistical analysis: t-test, $n = 3$, $^{*}p < 0.05$.

and green collagen fibers did not show consistency throughout fibrotic tissues, showing that even though PSR is widely used in pathology and histology labs, several abovementioned uncertainties still exist [77]. Furthermore, some studies also revealed the changes in rotation of the microscope stage can result in color reverse, which lacks robustness for both qualitative and quantitative results [71,78].

IF staining is a powerful tool to detect distinctive signals of specific proteins, which has been widely used to specify collagen subtypes in fibrotic tissue assessment [79]. Nevertheless, limited availability and specificity of primary antibodies, their high costs, and the need for complex staining procedures (especially when using archived FFPE material) favors traditional histological staining as the conventional method for fibrosis diagnosis. Limited possibility of quantitative analysis is another issue with IF staining. Autofluorescence from either the tissue itself or the secondary fluorescence-labelled antibodies can cause variations in image quantification [80]. A main drawback, which is highly relevant to this study, is that the COL I antibodies are unable to differentiate pathological fibrotic COL I from native/healthy COL I. This limitation also applies to SHG imaging since this method, although being non-invasive and marker-independent, does also not allow the discrimination of the different collagen types [81].

To circumvent the obstacles of routine histological and IF staining methods, RMS was used to distinguish diseased COL I from control COL I fibers. Multivariate data analysis tools such as PCA are a common way to provide detailed information about fibrotic COL I alteration contributed by minute shifts in Raman spectra [82]. Nonetheless, in this study, PCA was insufficient to robustly discriminate fibrotic pathologies throughout tissue origins (Supplementary Fig. S1). Moreover, the utilization of both LDA and neural networks for the classification of Raman data failed to yield desirable accuracy levels. Despite LDA yielding an accuracy rate of only 62% when classifying the Raman data of native and fibrotic COL I fibers, an improvement to 71% accuracy was observed when utilizing neural networks (as stated in Supplementary Table 1). The discrepancy in performance could be attributed to the limited sample size utilized during classification as well as the potential impact of variations specific to the organ on the accuracy of classification.

By implementing spectral deconvolution of the amide I signature, information regarding amino acid sequence and secondary structure of specific protein components can be obtained [83,84]. Through spectral deconvolution on averaged COL I Raman spectra, we were able to demonstrate the correlation of the subpeak at 1608 cm^{-1} in the amide I region to fibrotic COL I fibers regardless of the origin of the tissue and disease. Compared with the controls, a larger peak width and peak area were found in most of the examined fibrotic tissues. While these values were statistically significant for liver, breast tissue, and myocardium, a distinct trend was seen in the colon and in lymph nodes. We also found statistically significant differences between controls and fibrotic COL I when comparing histograms and modes of peak ratio images representing single spectra of COL I in whole Raman scans. Whereas other subpeaks at 1588 cm^{-1} and 1638 cm^{-1}, which represent hydroxyproline and β-sheet [85], showed no statistical significance between the control and fibrotic groups. The increase at the Raman shift of 1608 cm^{-1} in fibrotic COL I can be assigned to the amino acid tyrosine and its precursor phenylalanine [86,87]. Recent work from Baumann and Gebauer demonstrated that the primary structure of procollagens has an impact on the binding affinity of heat shock protein 47 (HSP47) at the site of the COLI I triple helix [80]. HSP47 has been widely discussed to be a specific chaperon to procollagen, which might play an important role in COL I folding related to fibrotic diseases [88], making it a potential therapeutic target for anti-fibrotic drugs. The composition of collagens is mainly the repeated triplets Glycine-Xaa-Yaa, where Xaa and Yaa can be any amino acid. Glycine preserves the certain position to maintain the triple helix structure of collagen [89]. For Xaa and Yaa, proline and hydroxyproline are common representatives at the sites [90,91]. Nevertheless, Xaa and Yaa can be also replaced by alternative amino acids such as leucine, arginine, tyrosine or phenylalanine, which has been reported to induce different dissociation constants of the binding of procollagen and HSP47 [91]. Baumann and Gebauer utilized a COL II peptide library to modify new binding sequence motifs with phenylalanine, tyrosine, and leucine, showing a significant decrease in the value of dissociation constant or binding affinity [80]. Increased binding affinity of HSP47 might contribute to the production and formation of excessive amounts of collagen ultimately leading to fibrosis [88,92]. The increased intensity in the fibrotic collagen fibers at the Raman shift of 1608 cm^{-1} might indicate the presence of higher amounts of amino acids with an aromatic ring (phenylalanine and tyrosine) [87,93]. It is hypothesized that procollagens which contain relatively high amounts of aromatic amino acids can bind easier to HSP47 than those without these specific amino acids. Nevertheless, the sequence of fibrotic COL I requires further investigation to provide proper evidence for our findings. An important future direction is to conduct the presented experiments on more fibrosis-related diseases of further tissue origins and collect more tissues from patients. Additionally, the proposed workflow of accessing fibrosis via spectral deconvolution needs to be tested on non-FFPE samples. Successful identification of fibrosis on fresh tissue would allow direct evaluation of pathologic tissue in the surgical room. The identified Raman biomarker could further enable to identify a fibrotic related origin of diseases with unknown pathology.

5. Conclusion

This study demonstrates the potential of RMS as a diagnostic approach to evaluate and identify fibrotic pathologies. We showed the capability of RMS to discern fibrotic COL I in human fibrotic tissues via deconvolution of the amide I band, identifying one specific spectral biomarker robust enough to target fibrotic alterations throughout various tissue origins. This molecular-sensitive approach enables fibrosis monitoring beyond tissue-specific morphological, quantitative, and qualitative differences in collagen patterns. Although only a selection of fibrosis-related diseases was evaluated in this study, this procedure could evolve to a future tool offering pathologists a non-destructive, marker-independent, and potentially automatable way to conduct fibrosis investigation without the need of conventional staining procedures.

Data Availability Statement

The data that support the findings of this study are available from the corresponding author upon reasonable request.

Declaration of Competing Interest

The authors declare no competing financial interests or personal relationships that could have appeared to influence the work reported in this paper.

Acknowledgements

The authors thank the University Department of General, Visceral and Transplant Surgery, University Hospital Tübingen and UCLA for providing the human tissue samples. The work was conducted in the framework of the Graduate School 2543/1 “Intraoperative Multi-Sensory Tissue-Differentiation in Oncology" funded by the German Research Foundation (DFG). Further funding was received by the European Union (H2020-EU, 812865, DELIVER), DFG (INST 2388/64-1, INST 2388/33-1 and Germany’s Excellence Strategy, EXC 2180-390900677), the Ministry of Science, Research, and the Arts of Baden-Wuerttemberg (33-729.55-3/214 and SI-BW 01222-91) and the State Ministry of Baden-Wuerttemberg for Economic Affairs, Labor and Tourism (3-4332.62-NMI/65).

Supplementary materials

Supplementary material associated with this article can be found, in the online version, at doi:10.1016/j.actbio.2023.03.016.

References

[1] T.A. Wynn, Cellular and molecular mechanisms of fibrosis, J. Pathol. 214 (2) (2008) 199–210.
[2] C. Chandler, T. Liu, R. Buckanovich, L.G. Coffman, The double edge sword of fibrosis in cancer, Transl. Res. 209 (2019) 55–67.
[3] D.M. Dolivo, Anti-fibrotic effects of pharmacologic FGF-2: a review of recent literature, J. Mol. Med. 100 (6) (2022) 847–860.
[4] T.A. Wynn, Fibrotic disease and the T(H)1/T(H)2 paradigm, Nat. Rev. Immunol. 4 (8) (2004) 583–594.

[5] L.A. Murtha, M.J. Schuliga, N.S. Mabotuwana, S.A. Hardy, D.W. Waters, J.K. Burgess, D.A. Knight, A.J. Boyle, The processes and mechanisms of cardiac and pulmonary fibrosis, Front. Physiol. 8 (2017) 777.

[6] R. Rasotto, D. Berlato, M.H. Goldschmidt, V. Zappulli, Prognostic significance of canine mammary tumor histologic subtypes: an observational cohort study of 229 cases, Vet. Pathol. 54 (4) (2017) 571–578.

[7] C.C. Choong, S.K. Venkatesh, E.P. Siew, Accuracy of routine clinical ultrasound for staging of liver fibrosis, J. Clin. Imaging Sci. 2 (2012) 58.

[8] L. Petitclerc, G. Gilbert, B.N. Nguyen, A. Tang, Liver fibrosis quantification by magnetic resonance imaging, Top. Magn. Reson. Imaging. 26 (6) (2017) 229–241.

[9] S.M. Humphries, J.J. Swigris, K.K. Brown, M. Strand, Q. Gong, J.S. Sundy, G. Raghu, M.I. Schwarz, K.R. Flaherty, R. Sood, T.G. O'Riordan, D.A. Lynch, Quantitative high-resolution computed tomography fibrosis score: performance characteristics in idiopathic pulmonary fibrosis, Eur. Respir. J. 52 (3) (2018).

[10] T. Liu, X. Wang, M.A. Karsdal, D.J. Leeming, F. Genovese, Molecular serum markers of liver fibrosis, Biomark. Insights 7 (2012) 105–117.

[11] A. Stainer, P. Faverio, S. Busnelli, M. Catalano, M.Della Zoppa, A. Marruchella, A. Pesci, F. Luppi, Molecular biomarkers in idiopathic pulmonary fibrosis: state of the art and future directions, Int. J. Mol. Sci. 22 (12) (2021).

[12] S.B. Montesi, P. Désogère, B.C. Fuchs, P. Caravan, Molecular imaging of fibrosis: recent advances and future directions, J. Clin. Invest. 129 (1) (2019) 24–33.

[13] R. Urtasun, N. Nieto, Hepatic stellate cells and oxidative stress, Rev. Esp. Enferm. Dig. 99 (4) (2007) 223–230.

[14] L.B. Mostaço-Guidolin, A.C. Ko, F. Wang, B. Xiang, M. Hewko, G. Tian, A. Major, M. Shiomi, M.G. Sowa, Collagen morphology and texture analysis: from statistics to classification, Sci. Rep. 3 (2013) 2190.

[15] T.D. Clemons, M. Bradshaw, P. Toshniwal, N. Chaudhari, A.W. Stevenson, J. Lynch, M.W. Fear, F.M. Wood, K.S. Iyer, Coherency image analysis to quantify collagen architecture: implications in scar assessment, RSC Adv. 8 (18) (2018) 9661–9669.

[16] P. Whittaker, R.A. Kloner, D.R. Boughner, J.G. Pickering, Quantitative assessment of myocardial collagen with picrosirius red staining and circularly polarized light, Basic Res. Cardiol. 89 (5) (1994) 397–410.

[17] A.E. Woessner, J.D. McGee, J.D. Jones, K.P. Quinn, Characterizing differences in the collagen fiber organization of skin wounds using quantitative polarized light imaging, Wound Repair Regen. 27 (6) (2019) 711–714.

[18] M. Brereton, B. De La Salle, J. Ardern, K. Hyde, J. Burthem, Do we know why we make errors in morphological diagnosis? An analysis of approach and decision-making in haematological morphology, EBioMedicine 2 (9) (2015) 1224–1234.

[19] K.G.M. Brockbank, R W, J. Xie, S.F. Hamm-Alvarez, Z.Z. Chen, K. Schenke-Layland, Quantitative second harmonic generation imaging of cartilage damage, Cell Tissue Bank. 9 (4) (2008) 299–307.

[20] K. Schenke-Layland, J. Xie, E. Angelis, B. Starcher, K. Wu, I. Riemann, W.R. Maclellan, S.F. Hamm-Alvarez, Increased degradation of extracellular matrix structures of lacrimal glands implicated in the pathogenesis of Sjögren's syndrome, Matrix Biol. 27 (1) (2008) 53–66.

[21] K. Schenke-Layland, I. Riemann, U.A. Stock, K. König, Imaging of cardiovascular structures using near-infrared femtosecond multiphoton laser scanning microscopy, J. Biomed. Opt. 10 (2) (2005) 024017.

[22] L. Becker, N. Janssen, S.L. Layland, T.E. Mürdter, A.T. Nies, K. Schenke-Layland, J. Marzi, Raman imaging and fluorescence lifetime imaging microscopy for diagnosis of cancer state and metabolic monitoring, Cancers 13 (22) (2021) 5682.

[23] K. Eberhardt, C. Stiebing, C. Matthäus, M. Schmitt, J. Popp, Advantages and limitations of Raman spectroscopy for molecular diagnostics: an update, Expert Rev. Mol. Diagn. 15 (6) (2015) 773–787.

[24] M.G. Martinez, A.J. Bullock, S. Macneil, I.U. Rehman, Characterisation of structural changes in collagen with Raman spectroscopy, Appl. Spectrosc. Rev. 54 (6) (2019) 509–542.

[25] G.W. Auner, S.K. Koya, C. Huang, B. Broadbent, M. Trexler, Z. Auner, A. Elias, K.C. Mehne, M.A. Brusatori, Applications of Raman spectroscopy in cancer diagnosis, Cancer Metast. Rev. 37 (4) (2018) 691–717.

[26] G. Pezzotti, Raman spectroscopy in cell biology and microbiology, J. Raman Spectrosc. 52 (12) (2021) 2348–2443.

[27] K. Sugiyama, J. Marzi, J. Alber, E.M. Brauchle, M. Ando, Y. Yamashiro, B. Ramkhelawon, K. Schenke-Layland, H. Yanagisawa, Raman microspectroscopy and Raman imaging reveal biomarkers specific for thoracic aortic aneurysms, Cell Rep. Med. 2 (5) (2021) 100261.

[28] R. Beatty, C.E. Lu, J. Marzi, R.E. Levey, D. Carvajal Berrio, G. Lattanzi, R. Wylie, R. O'Connor, E. Wallace, G. Ghersi, M. Salamone, E.B. Dolan, S.L. Layland, K. Schenke-Layland, G.P. Duffy, The foreign body response to an implantable therapeutic reservoir in a diabetic rodent model, Tissue Eng. Part C 27 (10) (2021) 515–528.

[29] S.K. Paidi, J.R. Troncoso, M.G. Harper, Z. Liu, K.G. Nguyen, S. Ravindranathan, L. Rebello, D.E. Lee, J.D. Ivers, D.A. Zaharoff, N. Rajaram, I. Barman, Raman spectroscopy reveals phenotype switches in breast cancer metastasis, Theranostics 12 (12) (2022) 5351–5363.

[30] J. Depciuch, A. Stanek-Widera, M. Warchulska, D. Lange, K. Sarwa, A. Kaziorowska, M. Kula, J. Cebulski, Identification of chemical changes in healthy breast tissue caused by chemotherapy using Raman and FTIR spectroscopy: a preliminary study, Infrared Phys. Technol. 102 (2019).

[31] D. Lazaro-Pacheco, M.A. Shaaban, N.A. Titiloye, S. Rehman, I.U. Rehman, Elucidating the chemical and structural composition of breast cancer using Raman micro-spectroscopy, EXCLI J. 20 (2021) 1118–1132.

[32] F. Gaba, W.J. Tipping, M. Salji, K. Faulds, D. Graham, H.Y. Leung, Raman spectroscopy in prostate cancer: techniques, applications and advancements, Cancers 14 (6) (2022) 1535.

[33] K. Viswanathan, K. Soumya, K. Gurusankar, S. Jeyavijayan, Raman spectroscopic analysis of ovarian cancer tissues and normal ovarian tissues, Laser Phys. 29 (2019).

[34] L. Becker, F. Fischer, J.L. Fleck, N. Harland, A. Herkommer, A. Stenzl, W.K. Aicher, K. Schenke-Layland, J. Marzi, Data-driven identification of biomarkers for in situ monitoring of drug treatment in bladder cancer organoids, Int. J. Mol. Sci. 23 (13) (2022) 6956.

[35] H. Russell Jr, A modification of Movat's pentachrome stain, Arch. Pathol. 94 (2) (1972) 187–191.

[36] K. Schenke-Layland, I. Riemann, U.A. Stock, K. König, Imaging of cardiovascular structures using near-infrared femtosecond multiphoton laser scanning microscopy, J. Biomedic. Opt. 10 (2) (2005) 024017.

[37] W. Liu, E. Ralston, A new directionality tool for assessing microtubule pattern alterations, Cytoskeleton 71 (4) (2014) 230–240.

[38] R. Rezakhaniha, A. Agianniotis, J.T. Schrauwen, A. Griffa, D. Sage, C.V. Bouten, F.N. van de Vosse, M. Unser, N. Stergiopulos, Experimental investigation of collagen waviness and orientation in the arterial adventitia using confocal laser scanning microscopy, Biomech. Model. Mechanobiol. 11 (3-4) (2012) 461–473.

[39] A. Zbinden, S.L. Layland, M. Urbanczyk, D.A. Carvajal Berrio, J. Marzi, M. Zauner, A. Hammerschmidt, E.M. Brauchle, K. Sudrow, S. Fink, M. Templin, S. Liebscher, G. Klein, A. Deb, G.P. Duffy, G.M. Crooks, J.A. Eble, H.K.A. Mikkola, A. Nsair, M. Seifert, K. Schenke-Layland, Nidogen-1 mitigates ischemia and promotes tissue survival and regeneration, Adv. Sci. 8 (4) (2021) 2002500.

[40] M. Holl, M.L. Rasch, L. Becker, A.L. Keller, L. Schultze-Rhonhof, F. Ruoff, M. Templin, S. Keller, F. Neis, F. Keßler, J. Andress, C. Bachmann, B. Krämer, K. Schenke-Layland, S.Y. Brucker, J. Marzi, M. Weiss, Cell type-specific anti-adhesion properties of peritoneal cell treatment with plasma-activated media (PAM), Biomedicines 10 (4) (2022).

[41] A. Zbinden, J. Marzi, K. Schlünder, C. Probst, M. Urbanczyk, S. Black, E. Brauchle, S.L. Layland, U. Kraushaar, G.P. Duffy, K. Schenke-Layland, P. Loskill, Non-invasive marker-independent high content analysis of a microphysiological human pancreas-on-a-chip model, Matrix Biol. 85-86 (2020) 205–220.

[42] J. Marzi, E. Brauchle, K. Schenke-Layland, M.W. Rolle, Non-invasive functional molecular phenotyping of human smooth muscle cells utilized in cardiovascular tissue engineering, Acta Biomater. 89 (2019) 193–205.

[43] H. Ye, U.Kruger Rahul, T. Wang, S. Shi, J. Norfleet, S. De, Burn-related collagen conformational changes in ex vivo porcine skin using raman spectroscopy, Sci. Rep. 9 (1) (2019) 19138.

[44] X. Li, Y. Zhang, P. Yu, Association of bio-energy processing-induced protein molecular structure changes with CNCPS-based protein degradation and digestion of co-products in dairy cows, J. Agric. Food Chem. 64 (20) (2016) 4086–4094.

[45] F. Pedregosa, G. Varoquaux, A. Gramfort, V. Michel, B. Thirion, O. Grisel, M. Blondel, P. Prettenhofer, R. Weiss, V. Dubourg, J. Vanderplas, A. Passos, D. Cournapeau, M. Brucher, M. Perrot, E. Duchesnay, Scikit-learn: Machine Learning in {P}ython}, J. Mach. Learn. Res. 12 (2011) 2825–2830.

[46] D.B. Kingma, Adam: A method for stochastic optimization, CoRR (2014) abs/1412.6980.

[47] A.V. Shinde, C. Humeres, N.G. Frangogiannis, The role of α-smooth muscle actin in fibroblast-mediated matrix contraction and remodeling, Biochim. Biophys. Acta Mol. Basis Dis. 1863 (1) (2017) 298–309.

[48] I. Notingher, C. Green, C. Dyer, E. Perkins, N. Hopkins, C. Lindsay, L.L. Hench, Discrimination between ricin and sulphur mustard toxicity in vitro using Raman spectroscopy, J. R. Soc. Interface 1 (1) (2004) 79–90.

[49] Z. Huang, A. McWilliams, H. Lui, D.I. McLean, S. Lam, H. Zeng, Near-infrared Raman spectroscopy for optical diagnosis of lung cancer, Int. J. Cancer 107 (6) (2003) 1047–1052.

[50] W.T. Cheng, M.T. Liu, H.N. Liu, S.Y. Lin, Micro-Raman spectroscopy used to identify and grade human skin pilomatrixoma, Microsc. Res. Tech. 68 (2) (2005) 75–79.

[51] D.P. Lau, Z. Huang, H. Lui, C.S. Man, K. Berean, M.D. Morrison, H. Zeng, Raman spectroscopy for optical diagnosis in normal and cancerous tissue of the nasopharynx-preliminary findings, Lasers Surg. Med. 32 (3) (2003) 210–214.

[52] T.T. Nguyen, C. Gobinet, J. Feru, S.B. Pasco, M. Manfait, O. Piot, Characterization of type I and IV collagens by raman microspectroscopy: identification of spectral markers of the dermo-epidermal junction, Spectroscopy 27 (2012) 686183.

[53] J. Cárcamo-Vega, A. Aliaga, R. Clavijo, B. Manuel, M. Vallette, Raman study of the shockwave effect on collagens, Spectrochim. Acta Part A 86 (2011) 360–365.

[54] E. Ó Faoláin, M.B. Hunter, J.M. Byrne, P. Kelehan, M. McNamara, H.J. Byrne, F.M. Lyng, A study examining the effects of tissue processing on human tissue sections using vibrational spectroscopy, Vibr. Spectrosc. 38 (1) (2005) 121–127.

[55] N. Nakamura, P. Moënne-Loccoz, K. Tanizawa, M. Mure, S. Suzuki, J.P. Klinman, J. Sanders-Loehr, Topaquinone-Dependent amine oxidases: identification of reaction intermediates by Raman spectroscopy, Biochemistry 36 (38) (1997) 11479–11486.

[56] Z.Q. Wen, Raman spectroscopy of protein pharmaceuticals, J. Pharm. Sci. 96 (11) (2007) 2861–2878.

[57] K. Belbachir, R. Noreen, G. Gouspillou, C. Petibois, Collagen types analysis and differentiation by FTIR spectroscopy, Anal. Bioanal. Chem. 395 (3) (2009) 829–837.

[58] M. Sisto, D. Ribatti, S. Lisi, Organ fibrosis and autoimmunity: the role of inflammation in TGFβ-dependent EMT, Biomolecules 11 (2) (2021).

[59] S. Seger, M. Stritt, E. Vezzali, O. Nayler, P. Hess, P.M.A. Groenen, A.K. Stalder, A fully automated image analysis method to quantify lung fibrosis in the bleomycin-induced rat model, PLoS One 13 (3) (2018) e0193057.

[60] L.C. Testa, Y. Jule, L. Lundh, K. Bertotti, M.A. Merideth, K.J. O'Brien, S.D. Nathan, D.C. Venuto, S. El-Chemaly, M.C.V. Malicdan, B.R. Gochuico, Automated digital quantification of pulmonary fibrosis in human histopathology specimens, Front. Med. 8 (2021) 607720.

[61] S.A. Taqi, S.A. Sami, L.B. Sami, S.A. Zaki, A review of artifacts in histopathology, J. Oral. Maxillofac. Pathol. 22 (2) (2018) 279.

[62] R.H. Hübner, W. Gitter, N.E. El Mokhtari, M. Mathiak, M. Both, H. Bolte, S. Freitag-Wolf, B. Bewig, Standardized quantification of pulmonary fibrosis in histological samples, BioTechniques 44 (4) (2008) 514–517 507-11.

[63] A.B. Fogo, C.E. Alpers, Navigating the challenges of fibrosis assessment: land in sight? J. Am. Soc. Nephrol. 22 (1) (2011) 11–13.

[64] R. Farhoodi, B.J. Lansdell, K.P. Kording, Quantifying how staining methods bias measurements of neuron morphologies, Front. Neuroinform. 13 (2019) 36.

[65] E.C. Jensen, Quantitative analysis of histological staining and fluorescence using ImageJ, Anatom. Rec. 296 (3) (2013) 378–381.

[66] J. Liu, M.Y. Xu, J. Wu, H. Zhang, L. Yang, D.X. Lun, Y.C. Hu, B. Liu, Picrosirius-polarization method for collagen fiber detection in tendons: a mini-review, Orthop. Surg. 13 (3) (2021) 701–707.

[67] F.E.-Z. Yassin, R. El-Dawela, M. Kerim, Picrosirius red staining assessment of collagen after dermal roller application: A minimally invasive percutaneous collagen induction therapy, Indian J. Dermatopathol. Diagn. Dermatol. 1 (2) (2014) 68–74.

[68] G.E. Courtoy, I. Leclercq, A. Froidure, G. Schiano, J. Morelle, O. Devuyst, F. Huaux, C. Bouzin, Digital image analysis of picrosirius red staining: a robust method for multi-organ fibrosis quantification and characterization, Biomolecules 10 (11) (2020).

[69] M.G. Monaghan, M. Holeiter, E. Brauchle, S.L. Layland, Y. Lu, A. Deb, A. Pandit, A. Nsair, K. Schenke-Layland, Exogenous miR-29B delivery through a hyaluronan-based injectable system yields functional maintenance of the infarcted myocardium, Tissue Eng.g Part A 24 (1-2) (2018) 57–67.

[70] C.M. López De Padilla, M.J. Coenen, A. Tovar, R.E. De la Vega, C.H. Evans, S.A. Müller, Picrosirius red staining: revisiting its application to the qualitative and quantitative assessment of collagen type I and type III in tendon, J. Histochem. Cytochem. 69 (10) (2021) 633–643.

[71] R. Lattouf, R. Younes, D. Lutomski, N. Naaman, G. Godeau, K. Senni, S. Changotade, Picrosirius red staining: a useful tool to appraise collagen networks in normal and pathological tissues, J. Histochem. Cytochem. 62 (10) (2014) 751–758.

[72] M. Wolman, F.H. Kasten, Polarized light microscopy in the study of the molecular structure of collagen and reticulin, Histochemistry 85 (1) (1986) 41–49.

[73] S.Y. Yu, C.A. Tozzi, J. Babiarz, P.C. Leppert, Collagen changes in rat cervix in pregnancy–polarized light microscopic and electron microscopic studies, Proc. Soc. Exp. Biol. Med. 209 (4) (1995) 360–368.

[74] B. Patel, Z. Xu, C.B. Pinnock, L.S. Kabbani, M.T. Lam, Self-assembled collagen–fibrin hydrogel reinforces tissue engineered adventitia vessels seeded with human fibroblasts, Sci. Rep. 8 (1) (2018) 3294.

[75] P.B. Jahagirdar, A.D. Kale, S. Hallikerimath, Stromal characterization and comparison of odontogenic cysts and odontogenic tumors using picrosirius red stain and polarizing microscopy: a retrospective and histochemical study, Indian J. Cancer 52 (3) (2015) 408–412.

[76] L.C. Junqueira, G. Bignolas, R.R. Brentani, Picrosirius staining plus polarization microscopy, a specific method for collagen detection in tissue sections, Histochem. J. 11 (4) (1979) 447–455.

[77] C.R. Drifka, A.G. Loeffler, K. Mathewson, G. Mehta, A. Keikhosravi, Y. Liu, S. Lemancik, W.A. Ricke, S.M. Weber, W.J. Kao, K.W. Eliceiri, Comparison of picrosirius red staining with second harmonic generation imaging for the quantification of clinically relevant collagen fiber features in histopathology samples, J. Histochem. Cytochem. 64 (9) (2016) 519–529.

[78] P.G.B. Coelho, M.V. Souza, L.G. Conceição, M.I.V. Viloria, S.A.O. Bedoya, Evaluation of dermal collagen stained with picrosirius red and examined under polarized light microscopy, An. Bras. Dermatol. 93 (3) (2018) 415–418.

[79] X. Lin, M. Barravecchia, R. Matthew Kottmann, P. Sime, D.A. Dean, Caveolin-1 gene therapy inhibits inflammasome activation to protect from bleomycin-induced pulmonary fibrosis, Sci. Rep. 9 (1) (2019) 19643.

[80] E.T. Abraham, S. Oecal, M. Mörgelin, P.W.N. Schmid, J. Buchner, U. Baumann, J.M. Gebauer, Collagen's primary structure determines collagen:HSP47 complex stoichiometry, J. Biol. Chem. 297 (6) (2021) 101169.

[81] Y. Padrez, L. Golubewa, T. Kulahava, T. Vladimirskaja, G. Semenkova, I. Adzerikho, O. Yatsevich, N. Amaegberi, R. Karpicz, Y. Svirko, P. Kuzhir, D. Rutkauskas, Quantitative and qualitative analysis of pulmonary arterial hypertension fibrosis using wide-field second harmonic generation microscopy, Sci. Rep. 12 (1) (2022) 7330.

[82] K. Sugiyama, J. Marzi, J. Alber, E.M. Brauchle, M. Ando, Y. Yamashiro, B. Ramkhelawon, K. Schenke-Layland, H. Yanagisawa, Raman microspectroscopy and Raman imaging reveal biomarkers specific for thoracic aortic aneurysms, Cell Rep. Med. 2 (5) (2021) 100261.

[83] N.C. Maiti, M.M. Apetri, M.G. Zagorski, P.R. Carey, V.E. Anderson, Raman spectroscopic characterization of secondary structure in natively unfolded proteins: α-Synuclein, J. Am. Chem. Soc. 126 (8) (2004) 2399–2408.

[84] G. Pezzotti, W. Zhu, Y. Hashimoto, E. Marin, T. Masumura, Y.-I. Sato, T. Nakazaki, Raman fingerprints of rice nutritional quality: a comparison between japanese koshihikari and internationally renowned cultivars, Foods 10 (12) (2021) 2936.

[85] H. Ye, F. Rahul, U. Kruger, T. Wang, S. Shi, J. Norfleet, S. De, Burn-related collagen conformational changes in ex vivo porcine skin using Raman spectroscopy, Sci. Rep. 9 (2019) 19138.

[86] C. Gullekson, L. Lucas, K. Hewitt, L. Kreplak, Surface-sensitive Raman spectroscopy of collagen I fibrils, Biophys. J. 100 (7) (2011) 1837–1845.

[87] R. Jyothi Lakshmi, V.B. Kartha, C. Murali Krishna, R.S. JG, G. Ullas, P. Uma Devi, Tissue Raman spectroscopy for the study of radiation damage: brain irradiation of mice, Radiat. Res. 157 (2) (2002) 175–182.

[88] P.S. Bellaye, O. Burgy, P. Bonniaud, M. Kolb, HSP47: a potential target for fibrotic diseases and implications for therapy, Expert Opin. Ther. Targets 25 (1) (2021) 49–62.

[89] A.V. Persikov, R.J. Pillitteri, P. Amin, U. Schwarze, P.H. Byers, B. Brodsky, Stability related bias in residues replacing glycines within the collagen triple helix (Gly-Xaa-Yaa) in inherited connective tissue disorders, Hum. Mutat. 24 (4) (2004) 330–337.

[90] J. Bella, M. Eaton, B. Brodsky, H.M. Berman, Crystal and molecular structure of a collagen-like peptide at 1.9 A resolution, Science 266 (5182) (1994) 75–81.

[91] R.Z. Kramer, J. Bella, P. Mayville, B. Brodsky, H.M. Berman, Sequence dependent conformational variations of collagen triple-helical structure, Nat. Struct. Biol. 6 (5) (1999) 454–457.

[92] T. Taguchi, A. Nazneen, A.A. Al-Shihri, K.A. Turkistani, M.S. Razzaque, Heat shock protein 47: a novel biomarker of phenotypically altered collagen-producing cells, Acta Histochem. Cytochem. 44 (2) (2011) 35–41.

[93] C. Gullekson, L. Lucas, K. Hewitt, L. Kreplak, Surface-sensitive Raman spectroscopy of collagen I fibrils, Biophys. J. 100 (7) (2011) 1837–1845.

Supporting Information

Raman Microspectroscopy Identifies Fibrotic Tissues in Collagen-related Disorders via Deconvoluted Collagen Type I Spectra

Lucas Becker [a,b§], Chuan-En Lu [a§], Ivonne A. Montes-Mojarro [c], Shannon L. Layland [a], Suzan Khalil [d], Ali Nsair [d], Garry P. Duffy [e], Falko Fend [c], Julia Marzi [a,b,f], Katja Schenke-Layland [a,b,f]

[a]***Institute of Biomedical Engineering***, *Department for Medical Technologies and Regenerative Medicine, Silcherstr. 7/1, Eberhard Karls University, 72076 Tübingen, Germany*
[b]***Cluster of Excellence iFIT (EXC 2180) "Image-Guided and Functionally Instructed Tumor Therapies"***, *Eberhard Karls University, Tübingen, Germany*
[c]***Institute of Pathology and Neuropathology,*** *University Hospital Tübingen, Tübingen, Germany*
[d]***Department of Medicine/Cardiology***, *Cardiovascular Research Laboratories, David Geffen School of Medicine at UCLA, 675 Charles E. Young Drive South, MRL 3645 Los Angeles, CA, USA*
[e]***Anatomy & Regenerative Medicine Institute***, *School of Medicine, College of Medicine, Nursing and Health Sciences, National University of Ireland Galway, H91 TK33, Galway, Ireland*
[f]***NMI Natural and Medical Sciences Institute at the University of Tübingen***, *Markwiesenstr. 55, 72770 Reutlingen, Germany*

§ Authors contributed equally.

Correspondence:
Prof. Dr. Katja Schenke-Layland
Institute of Biomedical Engineering
Department for Medical Technologies and Regenerative Medicine
Eberhard Karls University Tübingen
Silcherstraße 7/1
72076 Tübingen, Germany
Phone: +49 7071 2985205
E-Mail: katja.schenke-layland@uni-tuebingen.de

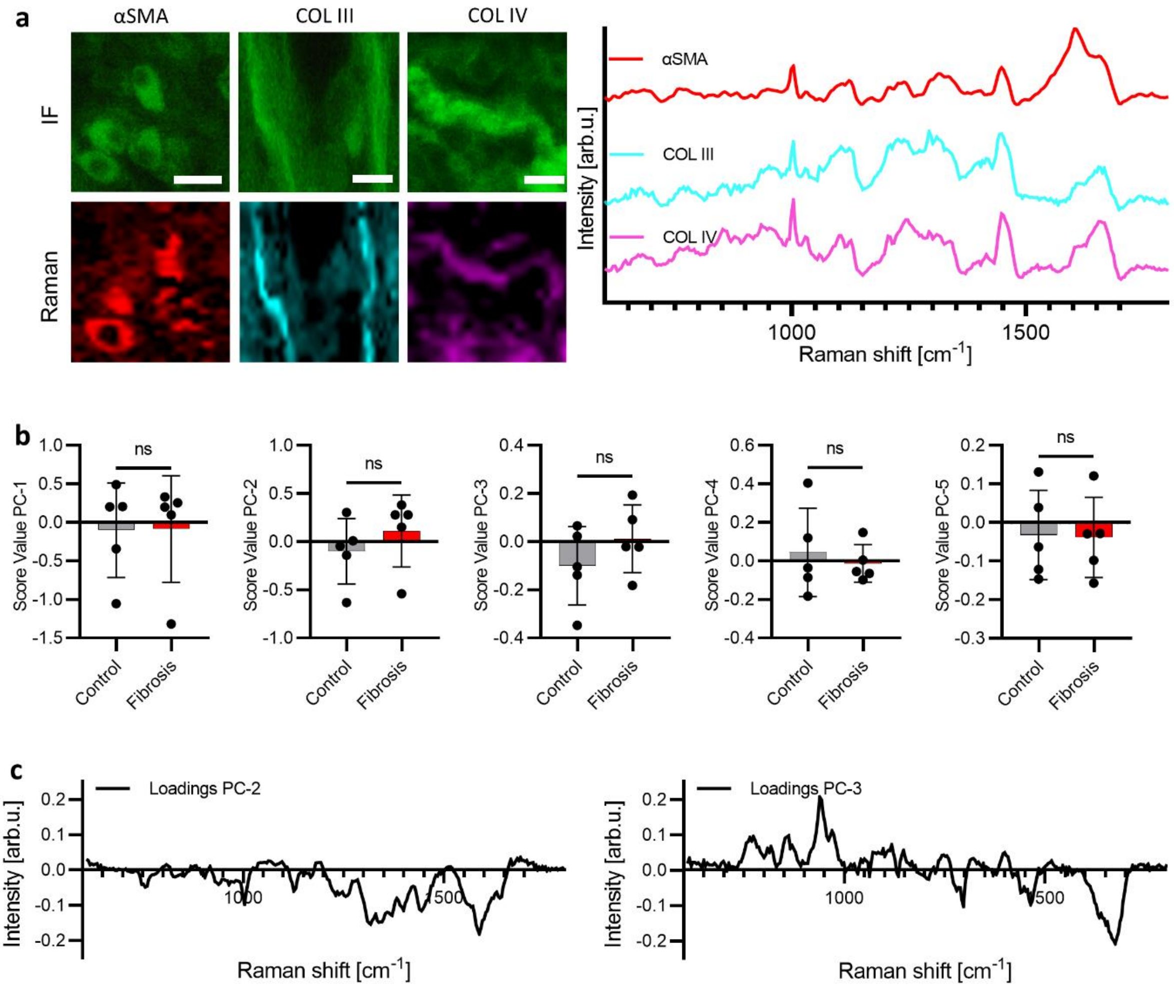

Supplementary Figure S1: (a) Comparison of immunofluorescence staining and marker-independent true component analysis of Raman images of human colon identifies αSMA (red), COL III (turquoise) and COL IV (pink). Scale bars equal 7 µm. (b) Score value analysis of fibrotic and control COL I spectra from all tissue types shows no statistically significant differences. (c) Loading plots of PC-2 and PC-3. Statistical analysis: t-test, *n*=3, **p*<0.05.

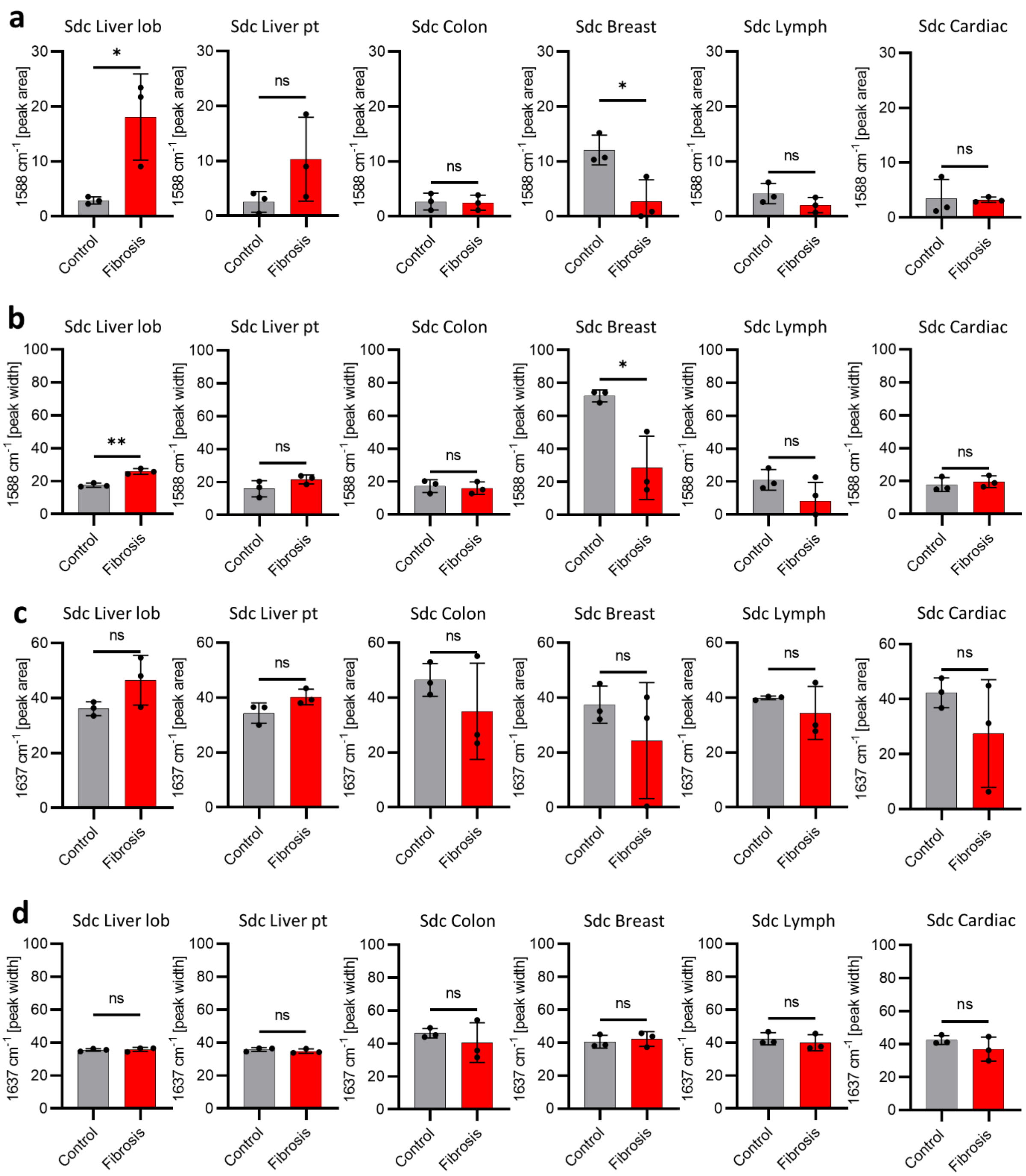

Supplementary Figure S2: Spectral deconvolution (Sdc) of amide I region from averaged COL I Raman spectra. (a) Peak **area** at 1588 cm^{-1} calculated based on spectral deconvolution of amide I area of averaged COL I spectra from control and fibrotic tissue. (b) Peak **width** at 1588 cm^{-1} calculated based on spectral deconvolution of amide I area of averaged COL I spectra from control and fibrotic tissue. (c) Peak **area** at 1637 cm^{-1} calculated based on spectral deconvolution of amide I area of averaged COL I spectra from control and fibrotic tissue. (d) Peak **width** at 1637 cm^{-1} calculated based on spectral deconvolution of amide I area of averaged COL I spectra from control and fibrotic tissue. Statistical analysis: t-test, n=3, *p<0.05.

Supplementary Table S1: Classification performance of COL I Raman data. The presented values display classification parameters for linear discriminant analysis (LDA) as well as neural network-based classification.

	LDA	Neural network
Accuracy	62%	71%
Sensitivity	60%	64%
Specificity	64%	72%

Appendix IV: Becker L., Beyer T., Liebscher S., Carvajal-Berrio D., Bösmüller H., Rall K., Brucker S. Y., Schenke-Layland K., Weiss M., Marzi J., *Marker-independent imaging reveals a correlation of fibrotic and epigenetic alterations in endometriosis*

Marker-independent imaging reveals a correlation of fibrotic and epigenetic alterations in endometriosis

Lucas Becker[a,b§], Tara Beyer[a§], Simone Liebscher[a], Daniel A Carvajal-Berrio[a,b], Hans Bösmüller[c], Bernhard Krämer[d], Katharina Rall[d], Sara Y Brucker[d] , Katja Schenke-Layland[a,b,e], Martin Weiss[d,e] and Julia Marzi*[a,b,e]

[a] Institute of Biomedical Engineering, Department for Medical Technologies and Regenerative Medicine, University of Tübingen, 72076 Tübingen, Germany
[b] Cluster of Excellence iFIT (EXC 2180) "Image-Guided and Functionally Instructed Tumor Therapies", University of Tübingen, Germany
[c] Institute of Pathology and Neuropathology, University Hospital Tübingen and Eberhard Karls University Tübingen, 72076, Tübingen, Germany
[d] Department of Women's Health, Research Institute for Women's Health, Eberhard Karls University Tübingen, 72076 Tübingen, Germany
[e] NMI Natural and Medical Sciences Institute at the University of Tübingen, 72770 Reutlingen, Germany

§ Authors contributed equally

*Correspondence: Julia Marzi, University of Tübingen, Institute of Biomedical Engineering, Silcherstr. 7/1, 72076 Tübingen; Julia.marzi@uni-tuebingen.de, +4970712985204

Abstract

Endometriosis can cause various symptoms such as chronic pelvic pain, hypermenorrhea, and infertility. To date, the average time until diagnosis consumes several years and requires invasive laparoscopy. The aim of this study was to molecularly characterize endometrium and endometriosis using Raman microspectroscopy to identify potential biomarkers and test its diagnostic potential. Raman microspectroscopy was used to identify the major subcellular structures of the glands present in human endometrium and endometriosis of the ligamentum sacrouterinum and septum rectovaginale, followed by principal component analysis. Distinct differences in collagen type I and nuclear signatures were identified in endometrium and endometriosis samples. Spectral deconvolution allowed identification of a Raman biomarker indicative of fibrotic changes in endometriosis. Additionally, a significant increase in epigenetic 5mC foci and signal intensity relevant for methylations was detected in nuclei of endometriosis. The neural network-based classification of Raman data resulted in high accuracies and therefore shows great potential for the detection of diseases such as endometriosis.

Keywords

Raman microspectroscopy; benign tissue remodeling; glands; ECM; machine learning

Introduction

Endometriosis is a benign disease affecting 10-15% of women in childbearing age; although the number of unreported cases is estimated to be much higher [1,2]. The severity of the disease varies from patient to patient. While about 6-10% of the women suffer from symptoms like dysmenorrhea, dyspareunia, dysuria, dyschezia, pelvic or bowel pain and abdominal bloating others are not aware of their condition until they encounter infertility disorder [3,4]. The determining feature of endometriosis is the appearance of endometrial tissue, which includes glands and stroma at an ectopic site, outside the uterus [5]. Due to the unclear and heterogeneous pathogenesis and symptoms, there is still a lack of sensitive biomarkers for investigating and diagnosing endometriosis. Invasive procedures by laparoscopy and histopathological assessment of biopsies remain the standard of care for endometriosis diagnosis. It is estimated that it takes approximately nine years to diagnose endometriosis [6].

One major obstacle is the indeterminate pathogenesis of endometriosis. Hitherto, there are several theories but none of them fully captures the manifold clinical appearances and disease patterns [7]. It is likely that there is either a combination of the theories or other factors involved, such as inflammatory processes, hormone levels or genetic predisposition, which might play an important, yet undiscovered role [7]. Sampson's theory about retrograde menstruation and consecutive ectopic implantation is the most supported in literature until today [8,9]. In the genetic-epigenetic theory, endometriosis is not solely based on genetic changes, but is at least partially epigenetically determined [10]. Examples of causative factors are oxidative stress in the uterus during menstruation and in the abdominal cavity after the onset of retrograde menstruation, inflammation or immunological influences [11]. This theory is consistent with all observations in endometriosis and would also explain that lesions respond differently to estrogen, progestins, and pregnancy. Glands in ectopic locations can remain inactive for long periods without alteration [12].

Tissue from patients suffering from endometriosis has also shown features of fibrosis [5,13], which plays a pivotal role in the progression and worsening of the symptoms due to stiff lesions distorting the uterine anatomy [13,14]. This has resulted in a proposed revision of the definition and potential therapeutic targets of endometriosis, suggesting to focus on the fibrotic pathology [15,16].

Furthermore, the last decade witnessed advances in non-destructive imaging techniques providing spatially and temporally resolved insights into tissue alterations. Besides clinical imaging such as transvaginal ultrasound, magnetic resonance imaging or computed tomography scans, novel, marker-independent imaging techniques gain relevance in complementary histopathological analyses and tissue discrimination [17,18]. Raman microspectroscopy (RMS) enables marker-independent and molecular-sensitive identification and localization of subcellular structures by analyzing molecular fingerprints of Raman-active biomolecules such as lipids, collagens, or nucleic acids reflecting a specific tissue state or cellular phenotype [19,20].

In this study, fibrotic and epigenetic characteristics of endometrium and endometriosis tissues from the sacrouterine ligament (LiS) and rectovaginal septum (SRV) were analyzed utilizing conventional histology and complementary non-destructive RMS. The objective of this study was to gain a deeper understanding of modifications in nuclei and collagens at a molecular level and to identify endometriosis-relevant biomarkers. RMS was combined with machine learning-based techniques to recognize disease pathomechanisms and to develop a multiparametric data-based model capable of differentiating between normal and diseased states across all phases of the menstrual cycle (Figure 1a).

Results

Histological staining indicates the presence of glands in endometrium and endometriosis

H&E and CD10 immunohistochemical staining were employed to identify endometrial gland positions in tissue sections. Samples from all phases of menstrual cycle were investigated. In H&E stains, extracellular matrix, cytoplasm (pink) and nuclei (blue) were visualized. Endometrium glands in control tissues in proliferative phase showed a typical single-layer high prismatic morphology (Figure 1b). Control tissue in the luteal phase showed a typical saw-blade shaped morphology with extended lumina. The CD10 staining confirmed the presence of endometrial stroma cells. Stroma around glands appeared brown, while nuclei of glands were stained in blue (Figure 1b). In dependence of the orientation of the tissue during sample processing into cryo-sections, glands appeared in sagittal shape. Using the H&E and CD10 staining as reference, gland positions were localized in consecutive, non-stained tissue section and investigated by RMS.

Raman imaging enables marker-independent visualization of tissue structures

To characterize the biomolecular composition of glands and surrounding ECM, non-destructive and marker-independent Raman imaging and multivariate data analysis were implemented on control endometrium and endometriosis derived from LiS. Raman scans of glands were analyzed by true component analysis (TCA) and enabled to identify and localize major tissue structures (Figure 1c). Based on the identified Raman spectra, TCA allowed visualizing the glands as false color-coded intensity heatmaps in which each color represents the best fit to one of the identified molecular signatures. Raman spectra and morphology of structures visualized by TCA, were applied to assign tissue structures to their biological origin which were nuclei (blue), lipids (yellow), collagen I (COL I, green) and endoplasmic reticulum (ER, pink). In endometriosis tissue sections, additionally to the spectral components found in control sections a further fiber-like structure was found (red), which was attributed to elastin as validated by resorcin-fuchsin staining (Fig. S1a) and literature reference spectra [19]. Nuclei were identified by their typical peaks related to the phosphate stretching of the backbone of DNA located at 798 and 1096 cm^{-1} [21]. Collagens were characterized by peaks at 855 and 936 cm^{-1} indicative for proline [22]. The collagen component demonstrated a fibrillar distribution in the stroma. Lipids were identified by peaks located at 1442 and 1775 cm^{-1} explaining methylene groups and C=C vibrations in fatty acids [23,24]. Lipids are in close proximity to gland positions in both endometrium and endometriosis. Table 1 gives an overview of the identified Raman shifts and their corresponding biological explanation.

Table 1. Biological assignment of the most relevant wavenumbers.

Wavenumber [cm^{-1}]	**Biological origin**	**Wavenumber [cm^{-1}]**	**Biological origin**
676	Guanine[25]	1366	CH_3[26]
794	PO_2^- [21]	1370	CH_3[27,28]
798	PO_2^- [21]	1397	C=O[29]
855	Proline[22]	1442	C=C[23]
936	Proline[22]	1443	CH_3[28]
1091	C-N[22]	1484	Guanine[21]
1096	PO_2^- [21]	1486	Amide II[30]
1163	Amide III[30]	1554	Amide II[29]
1236	Tyrosine[22]	1557	Tryptophan[31]
1239	Amide III[29]	1592	Amide II[29]
1256	Amide III[27]	1628	C=C[31]
1285	Cytosine[32]	1666	Amide I[29]
1320	Amide III[33]	1730	C=O, ester[34]
1341	Guanine[21]	1775	C=C[24]
1363	Guanine[32]		

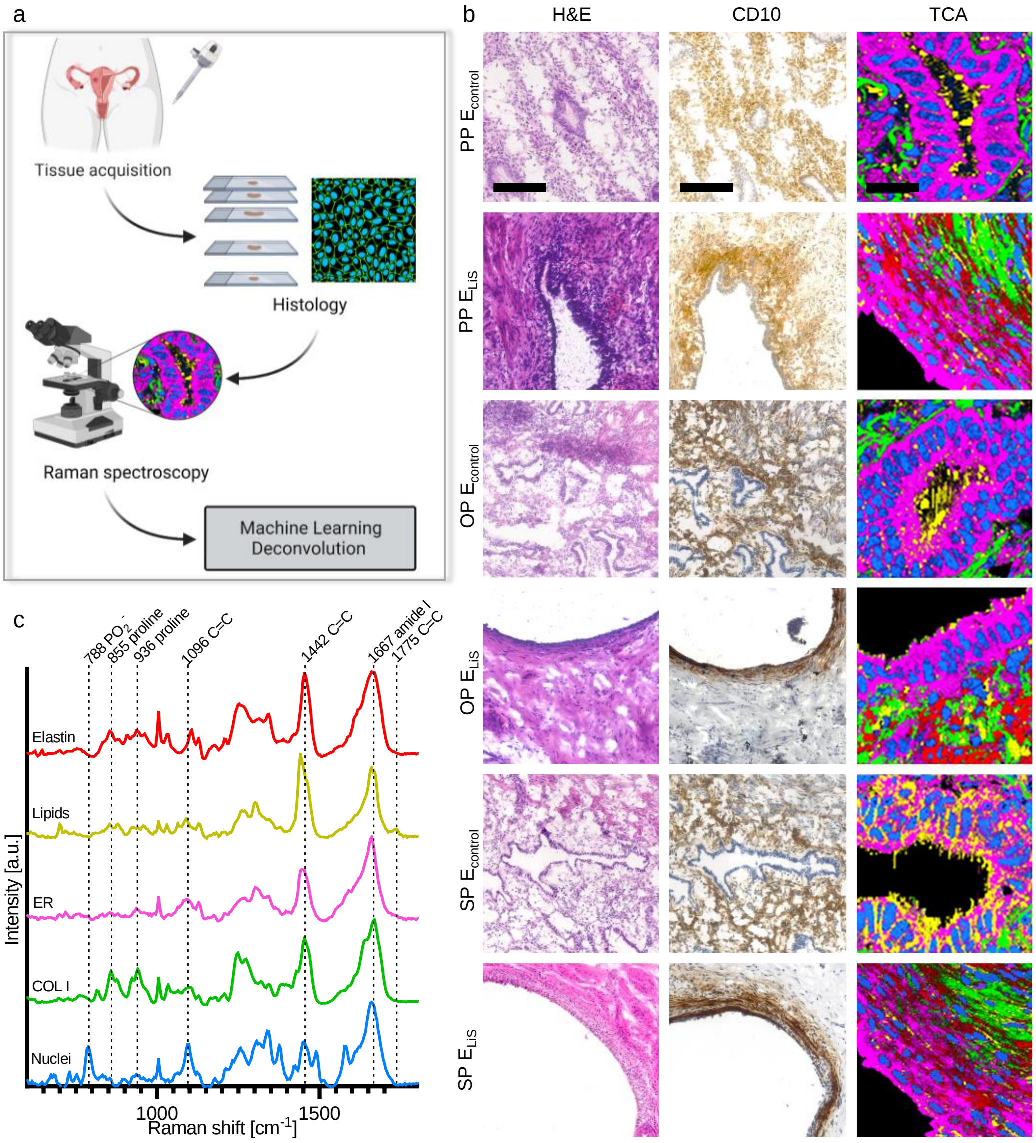

Figure 1. Conventional and Raman-based histopathology of endometrium and endometrial glands in different menstrual cycle phases. (a) Workflow of histopathological and Raman spectroscopy-based diagnosis of endometrium and endometrial lesions. (b) Histology of endometrium (E$_{control}$) and endometriosis from ligamentum sacrouterinum (E$_{LiS}$) in proliferative phase (PP), ovulation phase (OP) and secretory phase (SP). H&E and consecutive CD10, displays endometrial glands and surrounding stromal cells. Scale bar equals 130 µm. Raman images of glands generated by true component analysis of Raman heatmaps. Scale bar equals 20 µm. (c) Raman spectra identified by TCA: nuclei (blue), collagen type I (COL I, green), endoplasmic reticulum (ER, pink), lipids (yellow), elastin (red).

Picrosirius-red staining identifies differences in collagen fiber density and orientation

To investigate collagen fibers more specifically, polarized light images of picrosirius red (PSR) stained tissue sections were obtained according to their birefringent characteristics. PSR images of endometrium and endometriosis were obtained for all menstrual cycle phases (Figure 2a). Regardless of the menstrual cycle phases, the quantification of the presence of dense or mature (red/orange) and thinner (yellow, green) fibers showed statistically significant differences between endometrium and endometriosis from LiS (Figure 2b). In endometrium, less mature and more immature collagen fibers were found in comparison to endometriosis tissues. This overall trend between endometrium and endometriosis was observed regardless of the menstrual cycle phases. However, for endometrium a decrease in red-polarized contribution is observed over the course of the menstruation cycle. While in PP more green fibers were present, OP and SP of endometrium showed an increase in red fibers (two-way ANOVA, $p < 0.05$). In contrast, no changes were observed across the menstrual cycle phases in endometriosis (two-way ANOVA, $p > 0.05$). Furthermore, quantification of collagen fiber alignment was performed by coherency analysis indicating the overall percentage of collagens that are parallelly aligned (Figure 2c). Non-statistically significant increases in coherency were found in endometriosis across all menstrual cycle phases compared to endometrium (two-way ANOVA, $p > 0.05$).

COL I signatures differ between endometrium and endometriosis

In addition to image-based histopathological characterization of the tissues, in-depth analysis of the underlying Raman spectra allows for molecular-sensitive analysis of tissue structures. For submolecular analysis, principal component analysis (PCA) was performed on extracted COL I spectra (fingerprint range 400-180 cm^{-1}). Despite impacts of the cycle phase in endometriosis derived collagens, significant differences were identified in COL I features between endometrium and endometriosis. Score value analysis of PC-3 showed decreased score values of endometriosis from LiS across all menstrual cycle phases (two-way ANOVA, $p < 0.01$) (Figure 2d). The loading plots identified prominent Raman peaks accounting for the separation (Figure 2e). Based on the loading of PC-3, increased spectral intensities correlating to endometrium were found at 1666 cm^{-1}, representative for changes in amide I. The increased signal at 1091 cm^{-1} in endometrium is attributed to C-N or C-C vibrations [22], while the peak at 1486 cm^{-1} is assigned to amide II [30]. The most prominent peaks in correlation to endometriosis were depicted at 1557, 1592 and 1628 cm^{-1}, related to tryptophan or amide II and C=C bonds [29,31,35]. Additional peaks assigned to the separation of endometriosis were located at 1397 cm^{-1}, representative for C=O stretching [29] or CH_2 deformations [22], 1236 cm^{-1} corresponding to changes in amide III and CH_2 wagging [30] and 1163 cm^{-1} assigned to tyrosine [22].

Spectral Deconvolution Identifies Fibrotic COL I Alterations in Endometriosis

Continuing the analysis of COL I fibers from endometrium and endometriosis, Raman maps containing solely COL I spectra were extracted from large area scans and averaged. These Raman spectra were cropped to the amide I region (1520 - 1780 cm^{-1}) that was utilized for the analysis of protein secondary structures. Spectral deconvolution was utilized to investigate underlying peaks of the amide I band (Figure 2f-h). The secondary structures of collagens are mainly α-like helices, β-sheets, β-turns, and random coils (disordered). The number and location of sub bands were selected by the shape of the amide I peak in COL I and as described previously [36]. Comparison of the area under the curve at 1563 cm^{-1} (two-way ANOVA, $p < 0.01$(Figure 2i) as well as 1608 cm^{-1} (two-way ANOVA, $p < 0.05$) (Figure 2j) showed statistically significant changes between endometrium and endometriosis across all menstrual cycle phases. Peak areas at 1588 cm^{-1} (two-way ANOVA, $p > 0.05$) (Figure S2a) as well as 1636 cm^{-1} sub bands (two-way ANOVA, $p > 0.05$) (Figure S2b) showed no separation between endometrium and endometriosis. In one of our previous studies, calculating peak ratios (in an image-based approach) has been demonstrated to be a robust fibrosis biomarker [36], which could also be confirmed for the endometriosis tissues (two-way ANOVA, $p < 0.05$) (Figure 2k).

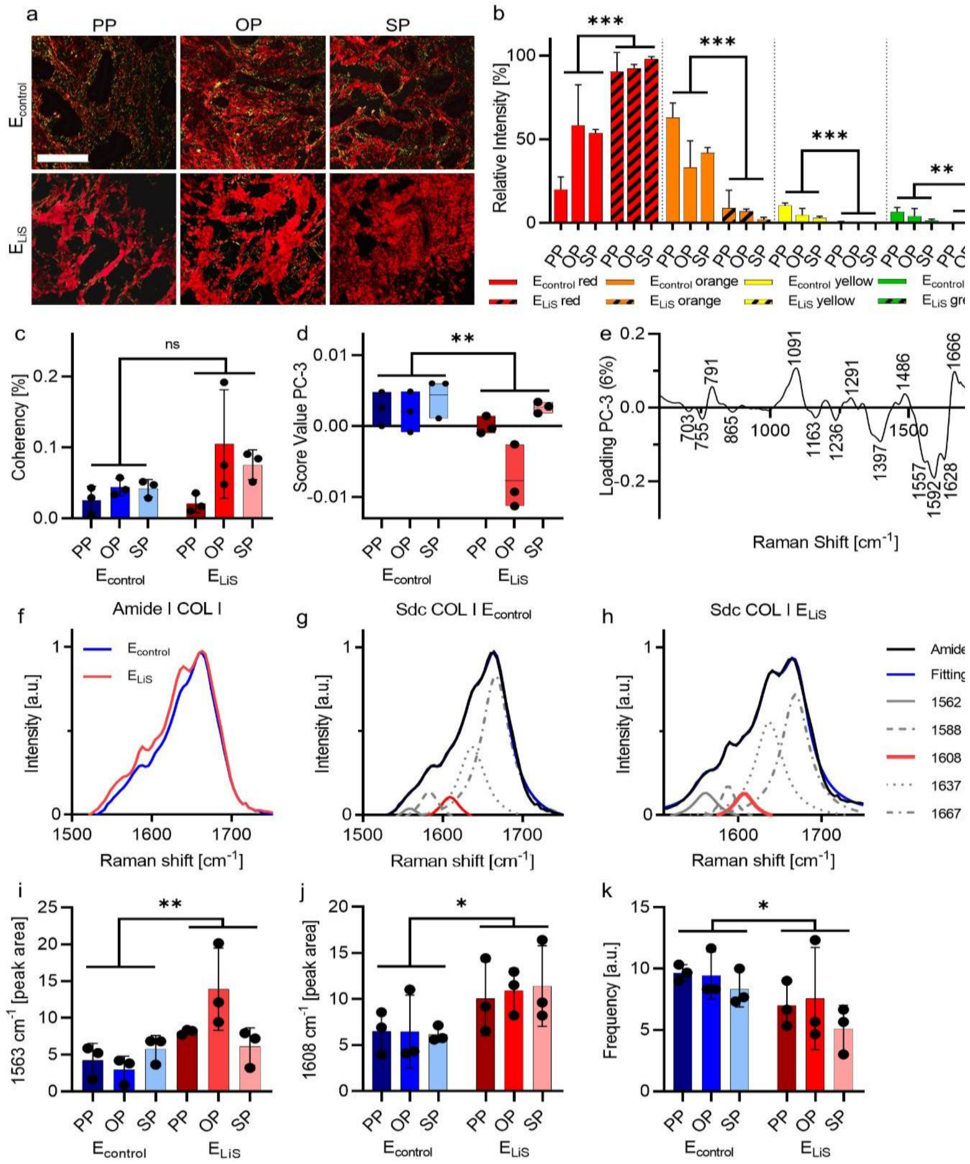

Figure 2. Collagen analysis by picrosirius red (PSR) staining and RMS reveal fibrotic changes in endometriosis. (a) PSR staining of endometrium *in loco typico* and endometriosis from LiS. Scale bar equals 100 µm. (b) Quantification of collagen fiber density using PSR color scales displays differences in collagen fiber structure in endometrium compared to endometriosis. (c) Fiber alignment of collagen fibers display a trend towards more parallel aligned fibers in endometriosis. (d) PCA score value analysis of COL I Raman spectra and (e) corresponding PC-3 loadings plot. (f) Amide I band of averaged COL I spectra from endometrium (blue) and endometriosis (red) were subjected to spectral deconvolution: (g) endometrium; (h) endometriosis. Peak area of subpeaks at (i) 1563 cm^{-1} and (j) 1608 cm^{-1}

show differences between endometrium and endometriosis. (k) Frequency of modes from filter image ratio at 1608 cm^{-1} normalized by amide I maximum. Data are presented as a mean ± SD. Statistical differences between the groups were determined by two-way ANOVA ($^{*}p < 0.05$, $^{**}p < 0.01$, $^{***}p < 0.001$, ns: not significant); n=3. $E_{control}$: endometrium; E_{LIS}: endometriosis of ligamentum sacrouterinum.

PCA identifies differences in nuclei between endometrium and endometriosis

In addition to analysis of collagen structures, Raman spectra of nuclei from endometrial glands were extracted and analyzed by PCA, resulting in significant differences in PC-1 (two-way ANOVA, $p < 0.001$) (Figure 3a). Particularly pronounced peaks in the loadings (Figure 3b) separating nuclei features from endometrium and endometriosis were located at 794 and 1101 cm^{-1}, indicating the phosphate backbone in DNA [37]. Additionally, shifts at 676, 1341 and 1484 cm^{-1} corresponding to the DNA base guanine [25,38], were observed in endometrium features. In endometriosis-derived spectra, increased intensities were found for amide III and amide II bands (1239 and 1554 cm^{-1}) [29], cytosine (1285 cm^{-1}) [32] as well as methyl-groups (1366 and 1443 cm^{-1}) [26-28].

5mC staining demonstrates epigenetic influences in endometriosis

The differences observed in the Raman analysis of the nuclei, especially for peaks representative for methyl-groups and cytosine, encouraged to further elaborate methylation patterns of the tissues. Subsequently, our objective was to determine epigenetic foci in Raman images of endometrium and endometriosis. In order to identify spectral bands indicative for epigenetic methylation, reference spectra of both cytidine and 5mC were recorded (Figure 3c). Comparison of both spectra revealed a peak assigned to CH_3 at 1370 cm^{-1} only detected in 5mC [27,28]. IF staining of 5mC was utilized to identify epigenetic 5mC foci within nuclei (Figure 3d). Three-dimensional fluorescence images were analyzed to determine foci counts (two-way ANOVA, $p < 0.01$) and intensities (two-way ANOVA, $p < 0.001$), which were both found to be increased in endometriosis (Figure 3e,f). According to the generated 5mC reference spectra, sum-filter images at 1370 cm^{-1} were generated and combined with nuclei heatmaps recorded at 788 cm^{-1} (Figure 3g). Raman-based 5mC MGV was increased in nuclei of glands in endometriosis (two-way ANOVA, $p < 0.001$) (Figure 3h).

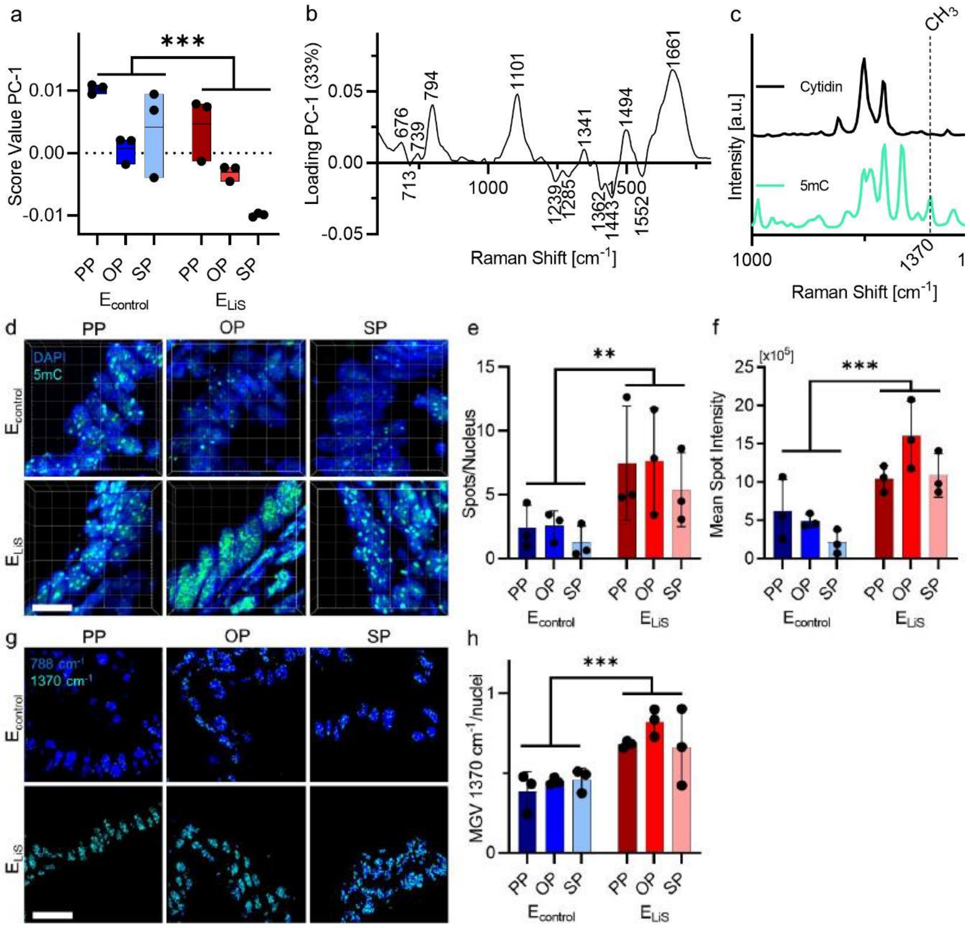

Figure 3. RMS and 5mC staining identify alterations in nuclei of endometriosis. (a) PCA of nuclei spectra indicate differences between endometrium and endometriosis. (b) Corresponding loadings plot. (c) Raman spectra of isolated cytidine and 5mC. (d) 5mC immunofluorescence staining (green) of endometrium and endometriosis. Scale bar equals 10 µm. (e) Mean spot intensity of 5mC foci and (f) 5mC foci per nucleus were determined. (g) Overlay of Raman filter images at 1370 cm^{-1} (green) and 788 cm^{-1} (blue) Scale bar: 30 µm. (h) An increase in 1370 cm^{-1} assigned mean gray value intensity (MGV) per nucleus is found in endometriosis. Data are presented as a mean ± SD. Statistical differences between the groups were determined by two-way ANOVA (*$p < 0.05$, **$p < 0.01$, ***$p < 0.001$); n=3.

Fibrotic and epigenetic features discriminate endometriosis and surrounding tissue

RMS integrated in an endoscopic system offers the great perspective being utilized intraoperatively to classify diseased tissue sites during a surgery without the need for biopsies and conventional histopathological staining. To elucidate the potential of RMS to identify endometriosis from surrounding tissues, glands from the LiS and a second ectopic position – SRV - were compared to healthy peritoneum. Therefore, the established analyses and extracted spectral features for COLI and 5mC were additionally performed on RMS data of peritoneum ($P_{control}$) and endometriosis from SRV (E_{SRV}) (Figure 4a). The quantification of PSR color scales revealed similarities between endometriosis of LiS and SRV as well as peritoneum (one-way ANOVA, $p > 0.05$) (Figure 4b). Overall, more mature fibers were detected in endometriosis and peritoneum compared to endometrium (one-way ANOVA, $p < 0.001$). Coherency analysis of collagen fibers (Figure 4c) displayed no statistically significant differences between endometrium, peritoneum and endometriosis (one-way ANOVA, $p > 0.05$). However, a tendency towards more parallel aligned collagen fibers was visible by increased coherency in endometriosis. In contrast, spectral deconvolution of the amide I band of extracted COL I spectra revealed significant increases at peak areas of the 1608 cm^{-1} subpeak between control peritoneum and endometriosis of both LiS (one-way ANOVA, $p < 0.01$) and SRV (one-way ANOVA, $p < 0.05$) (Figure 4d). Comparison within endometriosis showed no significant difference (one-way ANOVA, $p > 0.05$). Similar results were found in the analysis of the mode of filter images at 1608 cm^{-1} normalized by the amide I maximum in COL I spectra (Figure 4e). Assessment of epigenetic alterations by 5mC foci demonstrated a significant discrimination between nuclei in glands of endometriosis from the LiS (one-way ANOVA, $p < 0.01$; $p < 0.05$; $p < 0.01$) and SRV (one-way ANOVA, $p > 0.05$; $p < 0.05$; $p > 0.05$) and peritoneum tissue for both, IF as well as RMS-based localization (Figure 4f-h).

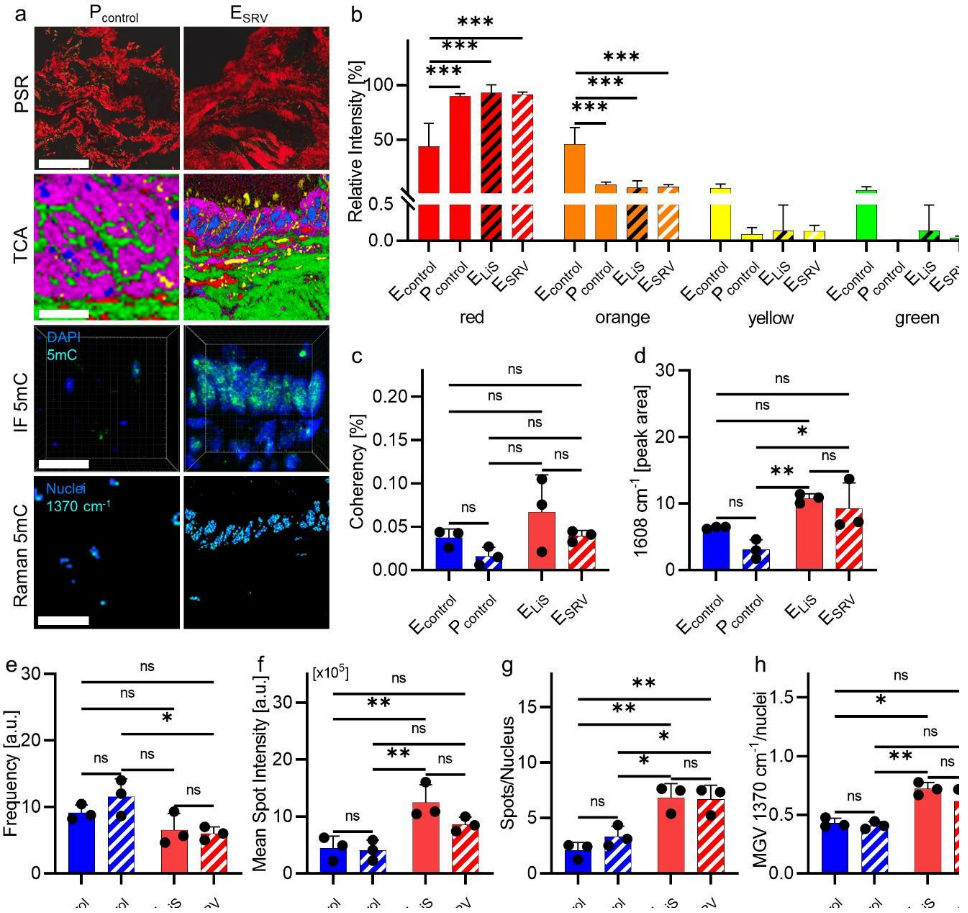

Figure 4. Fibrotic and epigenetic spectral biomarkers enable a discrimination between endometriosis and peritoneum. (a) Representative images of PSR, TCA, 5mC IF and combined Raman images at 1370 and 788 cm^{-1} of control peritoneum ($P_{control}$) and endometriosis from the SRV (E_{SRV}). Scale bars: 100 µm (PSR), 20 µm (TCA), 10 µm (5mC IF), 30 µm (5mC Raman). (b) PSR displays no statistically significant differences in collagen maturity/thickness between peritoneum and endometriosis from both LiS and SRV. (c) Fiber coherency of collagen fibers show no differences between peritoneum and endometriosis from both LiS and SRV. (d) Spectral deconvolution of the amide I region of averaged COL I spectra allow discrimination between peritoneum and endometriosis from both LiS and SRV. (e) Frequency of modes from filter image ratio at 1608 cm^{-1} normalized by amide I maximum of COL I. (f) Mean spot intensitiy from 5mC IF staining. (g) Spots per nucleus based on 5mC IF staining. (h) MGV analysis from Raman filter images at 1370 cm^{-1} normalized by whole nuclei signal. Quantitative data were presented as a mean ± SD. Statistical differences between the groups were determined by ordinary one-way ANOVA ($^{*}p < 0.05$, $^{**}p < 0.01$, $^{***}p < 0.001$, ns; not significant); n=3.

Neuronal Networks classify Raman signatures of endometriosis and peritoneum

To discuss the potential clinical suitability of Raman spectroscopy, the Raman spectra of nuclei and COL I of control peritoneum were compared to endometriosis from LiS and SRV and classified using a CNN. Applying a training-validation-test set split of 60-20-20 to the CNN lead to a test set error of 0.15% and test set loss of 0.64% at an accuracy of 98.9% with a validation loss of 0.64% and validation accuracy of 98.4% (Fig. S3). The corresponding training set accuracy and test set accuracy as well as training set loss and test set loss across all epochs is displayed in Tab. S2. Applying the trained CNN to the unknown test dataset yielded a prediction accuracy of 98.5%, sensitivity of 98.6%, and a specificity of 98.3%.

Discussion

This study used non-invasive label-free Raman spectroscopy to analyze the peritoneum, endometrium, and endometriosis of the LiS and the SRV. The results suggest that the epigenetic and fibrotic factors may play a role in the development of endometriosis, as demonstrated through Raman measurements, IF imaging of epigenetic 5mC staining, PSR staining, and a novel Raman biomarker for fibrotic COL I analysis.

Collagen, the most prevalent and frequently modified constituent of the extracellular matrix (ECM), is fundamental for tissue formation and is linked to various diseases. Accurate control of ECM synthesis and remodeling is critical for human well-being. Aberrations in ECM remodeling can impact the progression of different pathological conditions, influencing disease course. Fibrosis is characterized by excessive ECM production with consecutive tissue stiffening, seen in cancer and skin ailments [39]. Histological PSR staining was used for determining collagen fiber status. Despite controversial opinions, it is generally reported that the color of stained collagen fibers can indicate a certain degree of maturity, which in turn correlates with birefringence properties [40]. PSR results indicated that during the proliferative phase of the menstrual cycle, the stratum functionale of the endometrium synthesized new collagen fibers, demonstrated by an increase in immature collagen fibers (yellow/green). During the transition to ovulation and the secretory phase, a simultaneous increase in red and orange fibers and a decrease in green and yellow fibers was detected, indicating the maturation of collagen fibers. The loss of previously formed collagen fibers occurred during subsequent menstruation. Collagen fibers in the stroma of endometriosis were thicker and more mature than those in the endometrium. Due to their atypical location, the degree of maturity of the collagen fibers did not change during the menstrual cycle, and neither detachment nor new formation occurred. Fibrotic ECM remodeling is associated not only to collagen maturation but also to collagen fiber alignment. Parallel alignment of myofibroblasts, essential for collagen fiber synthesis, has been observed in the fibrotic phenotype in vitro and in vivo. This results in the synthesis of parallel-aligned collagen fibers [41] with concomitant increase in tissue stiffness [42].

Raman spectroscopy can be used to further elucidate the molecular changes of COL I in the endometrium and endometriosis. The differences are mainly due to variations in C-N, C-C, C=O, and C=C bonds, accompanied by changes in amides I, II, and III and different proportions of tyrosine and tryptophan. These results suggest a change in the secondary structure of COL I. Recently, we analyzed fibrotic diseases of several human organs by spectral deconvolution of the amide I band of COL I Raman spectra. All tissues showed fibrotic COL I alteration by an increase in the peak area at 1608 cm^{-1}. Application of this analytical tool showed evidence of the fibrotic COL I modification in endometriosis compared to endometrium as well as peritoneum [36].

We aimed to link the fibrosis-related pathogenesis in endometriosis with alteration on the nuclear level. Raman spectroscopy allowed differentiation of endometriosis and endometrium based on shifts in the phosphate scaffold of DNA, and based on changes in prominent DNA bases, indicative of an altered chromatin structure. While spectral signatures for guanine are observed in the endometrium, cytosine signals dominate in endometriosis. In addition, signals related to increased CH_3 content are found in endometriosis, while increased spectral intensities for amide III and amide II are observed in the endometrium, possibly indicating changes in the histone packing of DNA. To investigate the increased levels of CH_3 and cytosine levels in endometriosis we analyzed the tissues by their epigenetic 5mC profile. Both IF staining and Raman spectroscopy epigenetic analysis showed an increase in methylation and 5mC foci in endometriosis. These results suggest an alteration in chromatin packing affecting normal cellular activity. Epigenetic changes in methylation are reflected in lower proliferative activity of endometriosis compared with endometrium according to ki67 staining (Supplementary S6b).

In a recent study, epigenetic DNA methylation patterns were associated with the Heat Shock protein 47 (HSP47) gene expression [43]. HSP47 has been reported to mediate TGFβ1-induced collagen deposition leading to fibrosis [41,44]. This finding agrees well with the increased peak area at the spectral position of 1608 cm^{-1} of COL I, which is associated with increased phenylalanine content found in COL I fibers increasing the binding affinity of HSP47 ultimately leading to fibrotic COL I alteration [36,45,46].

To further evaluate the robustness for assessing fibrotic and epigenetic alteration with Raman spectroscopy, we examined additional sites of endometriosis i.e., the SRV as well as the peritoneum. The latter served as a more realistic control, since endometriosis is by definition not localized in the endometrium. While histological PSR analysis was not sufficient to determine endometriosis from peritoneum, as the connective tissue is largely composed of mature collagen fibers, spectral deconvolution of COL I Raman spectra allowed to discriminate the tissues. Moreover, epigenetic differences in nuclei were observable by RMS.

Until now, the detection of endometriosis that had to be solved mainly by laparoscopic surgery, is still challenging. Since 2000, Raman endoscope systems suitable for in vivo disease detection have been developed and expanded to preclinical investigations [47]. In future applications, such endoscopes could be used in everyday clinical practice. This necessitates an automatized real-time classification of gathered Raman data to support the surgeon’s decision making. Using a neural network-based classification of Raman data from nuclei and COL I from peritoneum and endometriosis from the LiS and the SRV, we provide evidence for successful identification of the disease in an ex vivo model. It should be noted that the data-driven classification approach presented in this study is highly sample-specific, and its results may not apply to endometriosis and other control tissue in general due to the small number of patients involved. To further evaluate the robustness of this method for the detection of endometriosis, experiments would need to be performed with multiple donors and endometriosis lesions at other tissue sites such as from genitalia interna (i.e., myometrium), genitalia externa (i.e., vagina, perineum) or extra genitalis (i.e., ureter, retroperitoneum, lung, brain).

This study demonstrated the potential of RMS as a diagnostic approach to characterize and identify endometriosis. We showed the capability of RMS to discern endometriosis beyond influences of the menstrual cycle phase. Fibrotic COL I alterations were identified in endometriosis tissues. Moreover, RMS was able to detect 5mC-related epigenetic differences between endometriosis and endometrium as well as peritoneum. In combination with neural network-based classification, accurate tissue dicrimination is enabled. The established spectral signatures allow to target structural and epigenetic alterations in a non-destructive manner and, in the future, could serve as novel biomarkers not only for investigations of endometrial pathogenesis but also as diagnostic markers. The presented approach could evolve to offer pathologists a complementary tool for non-destructive, marker-independent, and automated diagnosis of endometriosis with the potential to be implemented minimally-invasive by usage of Raman endoscopic systems.

Material and Methods

Ethics statement

After informed consent was obtained, endometrium, endometriosis and peritoneal tissues were retrieved from surgical specimens.

The Ethical Committee of the Medical Faculty of the Eberhard Karls University Tübingen approved the scientific use of the tissue of the Medical Faculty of the Eberhard Karls University Tübingen (152/2018BO2, approval: 29.03.2018)

Collection of human tissue samples

Samples of endometrium, endometriosis from the LiS and the SRV, as well as peritoneum were acquired by the Women's Hospital at the University Hospital Tübingen. Endometrium was procured through hysterectomy, while the endometriosis tissues were obtained via minimally invasive laparoscopic surgery. Only patients that were not taking contraceptives and had not yet reached menopause were included in the study. Specimens were stored in DPBS until cryo-preservation using Tissue Tek O.C.T. (Tissue Tec, Sakura Finetek Europe B.V., Alphen aan den Rijn, Netherlands). According to their size and density, they were left at room temperature until soaked and stored at -80°C until further processing. Serial 10 µm thick cross sections of endometrium, endometriosis and peritoneum tissue were prepared utilizing a cryotome (MICROM HM560, Thermo Scientific, Waltham, USA). Tissue sections were collected on objective slides (SUPERFROST PLUS, Menzel, Braunschweig, Germany) for histochemical and immunofluorescence staining, as well as Raman microspectroscopy. Overall, female patients with and without endometriosis (LiS) in all menstrual cycle phases (proliferative phase (PP), ovulation phase (OP) and secretory phase (SP)) were included (n = 3). Additionally, SRV endometriosis and peritoneum were acquired (n = 3). An overview of patient specific information is given in Table S1.

Histological Tissue Characterization

For characterization of cryosections from endometrium, endometriosis and peritoneum, routine immunohistochemical stains were performed. To determine general cellular and tissue morphology, cryosections were stained with hematoxylin-eosin (H&E) according to standard protocols. Consecutive CD10 staining served as confirmation stain to identify the localization of endometriosis. Ki67 staining was implemented to identify the proliferation of cells, while resorcin-fuchsin staining identified microfibrils and elastic fibers in tissues. Picrosirius-red (PSR) staining was implemented to visualize collagen maturity/thickness. Detailed protocols are available in the supplements.

5mC Staining

Immunofluorescence (IF) 5mC staining was adapted from Daum et al [48].

Brightfield and Immunofluorescence Imaging

Brightfield tile scans of H&E, CD10, resorcin-fuchsin and Ki67 stained tissue sections were performed on an Axio Observer using a 63x1.4 NA C-plan apochromat objective (Zeiss Microscopy GmbH).

3D image acquisision and analysis

IF stains were imaged utilizing a Zeiss LSM 880 (Zeiss microscopy GmbH). Images were acquired as z-stacks with 2 tracks through a C Plan-Apochromat 63x/1.4. An oil DIC UV-VIS-IR M27 objective at a bit depth of 16 bit, scaling of 0.07 x 0.07 µm per pixel and image size of 476 x 476 pixel, resulting in 33.74 x 33.74 µm large images was utilized to acquire images. Z-stack images were analyzed with Imaris 9.7.2. Detailed information of image processing can be found in the supplements.

Raman Imaging

Raman scans were acquired on a customized setup as previously described [49]. For each sample, glandular regions were measured according to ROIs defined by CD10 staining. Three spectral maps containing one spectrum per 0.5 µm were generated of an area of 80×80 µm, at an acquisition time of 0.05 s per spectrum and a laser power of 50 mW. To guarantee measurements in focus, the in-built TrueSurface module was utilized, allowing to measure large coarsely-textured samples.

Spectral Analyses

Image analyses of spectral maps were performed with the Project Five 5.2 software (WITec GmbH). Raman data were subjected to cosmic ray removal, polynomial baseline correction, cropped to 400 - 3000 cm^{-1} and area normalized to 1 prior to analysis by true component analysis (TCA). TCA identified spectral components that were most prevalent in the data set and enabled a visualization based on the generation of intensity distribution images for each identified component. Gray value intensities were determined in the intensity distribution images for quantitative assessment of each component in endometrium and endometriosis. Sum-filter images at the spectral positions 1370 cm^{-1} and 1395 cm^{-1} with a spectral width of 30 cm^{-1} were extracted from nuclei Raman spectra and combined with filter images recorded at 788 cm^{-1} depicting the whole nuclei. For image combination, the color top-value of the 5mC sum filter image was set to 0.1 with a bottom-value of 0, while the top-value of the nuclei filter image was set to 1 with a bottom-value of 0. Next, combined images were transferred to ImageJ 1.52. Prior to assessing mean gray values (MGV), the combined images were transferred to RGB stack images. MGV of both green and blue channels were calculated.

Principal Component Analysis

For in-depth analysis of endometrium and endometriosis-derived spectral signatures, principal component analysis (PCA) was performed with the Unscrambler software (Unscrambler X10.5, CAMO, Oslo, Norway) on 200 extracted single spectra per Raman image from nuclei COL I masks. Briefly, PCA is a multivariate data analysis tool reducing the dimensionality of a set of spectral data on a vector-based approach, in which each vector, so-called principal component (PC), describes a variation in the spectra. Plotting PC values against each other visualizes a correlation or separation of two or more data sets.

Deconvolution

For in-depth analysis of protein secondary structures, spectral deconvolution on the amide I region (1580-1720 cm^{-1}) was performed on averaged COL I Raman spectra as described previously [36].

Neural Network Classifier

Sample classification was undertaken by using a neural network from the open-source Keras and Tensorflow API (Google Brain). Information about the model architecture can be found in the supplements. It was aimed to classify the data into one of the two classes: *control* and *diseased*. For classification, one dataset including both nuclei and COL I spectra was evaluated. The dataset consisted of 740 features (spectral range from 600-1800 cm^{-1} with a sampling interval of 4 cm^{-1} for both nuclei and COL I spectra) and 600 spectra per patient. The performance of CNN classification was improved by structure modification and hyperparameter tuning of the batch size, the number of epochs, the number of hidden units, the optimizer as well as the learning rate.

Statistical Analysis

Statistical comparisons were performed from a minimum of three independent patients per menstrual cycle phase. Statistical analysis was performed using GraphPad Prism version 9.00 for Windows (GraphPad Software). Results are shown throughout the entire manuscript as mean ± standard deviation. Statistical significance was determined by one-way ANOVA or two-way ANOVA for multiple comparisons and grouped comparisons. Values of $p < 0.05$ were considered significant ($^{*}p < 0.05$; $^{**}p < 0.01$; $^{***}p < 0.001$). All *n*-numbers, applied tests and corresponding significance for each result are listed in the figure legends.

Data availability

The experimental data and materials, generated and analyzed during this study, are available from the corresponding authors on reasonable request.

CRediT Statement:

L.B., T.B., K.R., S.Y.B., K.S-L. and J.M. designed and conducted the study. B.K., K.R. and M.W. provided the clinical samples. L.B, T.B, S.L. and D.A.C-B. performed the tissue staining. H.B. performed the pathological examination of the tissues. L.B. and T.B. performed statistical analyses. L.B. established neural network models. L.B. and T.B. were responsible for data processing and graphing. L.B., T.B. and J.M. wrote the manuscript. S.Y.B., K.S-L., M.W. and J.M. supervised the project. All authors reviewed the manuscript.

Acknowledgements

The work was conducted in the framework of the Graduate School 2543/1 “Intraoperative Multi-Sensory Tissue-Differentiation in Oncology" funded by the German Research Foundation (DFG - Deutsche Forschungsgemeinschaft). Further funding was received by the Deutsche Forschungsgemeinschaft (INST 2388/64-1, INST 2388/33-1 and Germany’s Excellence Strategy, EXC 2180-390900677), the Ministry of Science, Research, and the Arts of Baden-Wuerttemberg (33-729.55-3/214 and SI-BW 01222-91) and the State Ministry of Baden-Wuerttemberg for Economic Affairs, Labour and Tourism (3-4332.62-NMI/65).

Declaration of Competing Interest

The authors declare no conflict of interest.

Supplementary material

Supplementary data to this article can be found online.

References

1 Ferrero, H. *et al.* A novel homologous model for noninvasive monitoring of endometriosis progression. *Biol. Reprod.* **96**, 302-312, doi:10.1095/biolreprod.116.140756. (2017).

2 Shafrir, A. L. *et al.* Risk for and consequences of endometriosis: A critical epidemiologic review. *Best Practice & Research Clinical Obstetrics & Gynaecology* **51**, 1-15, doi:10.1016/j.bpobgyn.2018.06.001 (2018).

3 Zeng, X. *et al.* NR4A1 is Involved in Fibrogenesis in Ovarian Endometriosis. *Cellular Physiology and Biochemistry* **46**, 1078-1090, doi:10.1159/000488838 (2018).

4 Pezzuto, A., Pomini, P., Steinkasserer, M., Nardelli, G. B. & Minelli, L. Patient with pelvic pains: retroperitoneal fibrosis or pelvic endometriosis? A case report and review of literature. *Fertility and Sterility* **92**, 1497.e1499-1497.e1491, doi:10.1016/j.fertnstert.2009.07.982 (2009).

5 Kurman, R. J., Ellenson, L. H. & Ronnett, B. M. *Blaustein's Pathology of the Female Genital Tract*. 7 edn, (Springer Cham, 2019).

6 Cox, H., Henderson, L., Wood, R. & Cagliarini, G. Learning to take charge: women's experiences of living with endometriosis. *Complementary Therapies in Nursing & Midwifery* **9**, 62-68, doi:10.1016/S1353-6117(02)00138-5 (2003).

7 Parasar, P., Ozcan, P. & Terry, K. L. Endometriosis: Epidemiology, Diagnosis and Clinical Management. *Current Obstetrics and Gynecology Reports* **6**, 34-41, doi:10.1007/s13669-017-0187-1 (2017).

8 Sampson, J. Heterotopic or misplaced endometrial tissue. *American Journal of Obstetrics and Gynecology* **10**, 649-664, doi:10.1016/S0002-9378(25)90629-1 (1925).

9 Sourial, S., Tempest, N. & Hapangama, D. K. Theories on the Pathogenesis of Endometriosis. *International Journal of Reproductive Medicine* **2014**, 1-9, doi:10.1155/2014/179515 (2014).

10 Koninckx, P. R. *et al.* Pathogenesis of endometriosis: the genetic/epigenetic theory. *Fertility and Sterility* **111**, 327-340, doi:10.1016/j.fertnstert.2018.10.013 (2019).

11 Acién, P. & Velasco, I. Endometriosis: A Disease That Remains Enigmatic. *ISRN Obstetrics and Gynecology* **2013**, 1-12, doi:10.1155/2013/242149 (2013).

12 Bruner-Tran, K., Ding, T. & Osteen, K. Dioxin and Endometrial Progesterone Resistance. *Seminars in Reproductive Medicine* **28**, 059-068, doi:10.1055/s-0029-1242995 (2010).

13 Zhang, Q., Duan, J., Liu, X. & Guo, S. Platelets drive smooth muscle metaplasia and fibrogenesis in endometriosis through epithelial-mesenchymal transition and fibroblast-to-myofibroblast transdifferentiation. *Mol Cell Endocrinol.* **15**, 1-16, doi:10.1016/j.mce.2016.03.015. (2016).

14 Zheng, Y., Khan, Z., Zanfagnin, V., Correa, L. F. & Delaney, A. A. Epigenetic Modulation of Collagen 1A1: Therapeutic Implications in Fibrosis and Endometriosis. *Biol Reprod.* **94**, 87, doi:10.1095/biolreprod.115.138115 (2016).

15 Vigano, P. *et al.* Time to redefine endometriosis including its pro-fibrotic nature. *Hum Reprod.* **33**, 347-352, doi:10.1093/humrep/dex354. (2018).

16 Nishimoto-Kakiuchi, A. *et al.* A long-acting anti–IL-8 antibody improves inflammation and fibrosis in endometriosis. *Science Translational Medicine* **15**, eabq5858, doi:doi:10.1126/scitranslmed.abq5858 (2023).

17 Bocklitz, T. W. *et al.* Pseudo-HE images derived from CARS/TPEF/SHG multimodal imaging in combination with Raman-spectroscopy as a pathological screening tool. *BMC Cancer* **16**, 534, doi:10.1186/s12885-016-2520-x (2016).

18 Huang, L. *et al.* Rapid, label-free histopathological diagnosis of liver cancer based on Raman spectroscopy and deep learning. *Nature Communications* **14**, 48, doi:10.1038/s41467-022-35696-2 (2023).

19 Sugiyama, K. *et al.* Raman microspectroscopy and Raman imaging reveal biomarkers specific for thoracic aortic aneurysms. *Cell Reports Medicine* **2**, 100261, doi:10.1016/j.xcrm.2021.100261 (2021).

20 Marzi, J., Brauchle, E. M., Schenke-Layland, K. & Rolle, M. W. Non-invasive functional molecular phenotyping of human smooth muscle cells utilized in cardiovascular tissue engineering. *Acta biomaterialia* **89**, 193-205 (2019).

21 Notingher, I. *et al.* Discrimination between ricin and sulphur mustard toxicity in vitro using Raman spectroscopy. *Journal of The Royal Society Interface* **1**, 79-90, doi:10.1098/rsif.2004.0008 (2004).

22 Cheng, W.-T., Liu, M.-T., Liu, H.-N. & Lin, S.-Y. Micro-Raman spectroscopy used to identify and grade human skin pilomatrixoma. *Microscopy Research and Technique* **68**, 75-79, doi:10.1002/jemt.20229 (2005).

23 Shetty, G., Kendall, C., Shepherd, N., Stone, N. & Barr, H. Raman spectroscopy: elucidation of biochemical changes in carcinogenesis of oesophagus. *British Journal of Cancer* **94**, 1460-1464, doi:10.1038/sj.bjc.6603102 (2006).

24 Malini, R. *et al.* Discrimination of normal, inflammatory, premalignant, and malignant oral tissue: A Raman spectroscopy study. *Biopolymers* **81**, 179-193, doi:10.1002/bip.20398 (2006).

25 Chan, J. W. *et al.* Micro-Raman Spectroscopy Detects Individual Neoplastic and Normal Hematopoietic Cells. *Biophysical Journal* **90**, 648-656, doi:10.1529/biophysj.105.066761 (2006).

26 Frank, C. J., McCreery, R. L. & Redd, D. C. Raman spectroscopy of normal and diseased human breast tissues. *Anal Chem.* **67**, 777-783, doi:10.1021/ac00101a001. (1995).

27 Stone, N., Kendall, C., Smith, J., Crow, P., Barr, H. Raman spectroscopy for identification of epithelial cancers. *Faraday Discussions* **126**, 141-157, doi:org/10.1039/B304992B (2004).

28 Nak-Han, J. The Coordination Chemistry of DNA Nucleosides on Gold Nanoparticles as a Probe by SERS. *Bulletin of the Korean Chemical Society* **23**, 17900-11800, doi:10.5012/bkcs.2002.23.12.1790 (2002).

29 Ó Faoláin, E. *et al.* A study examining the effects of tissue processing on human tissue sections using vibrational spectroscopy. *Vibrational Spectroscopy* **38**, 121-127, doi:10.1016/j.vibspec.2005.02.013 (2005).

30 Dukor, R. Vibrational spectroscopy in the detection of cancer. *Biomedical Applications* **5**, 3335-3359, doi:10.1002/0470027320.s8107 (2002).

31 Naumann, D. Infrared and NIR Raman spectroscopy in medical microbiology. *Proceedings SPIE* **3257**, 245-257, doi:10.1117/12.306089 (1998).

32 Ruiz-Chica, A. J., Medina, M. A., Sánchez-Jiménez, F. & Ramírez, F. J. Characterization by Raman spectroscopy of conformational changes on guanine–cytosine and adenine–thymine oligonucleotides induced by aminooxy analogues of spermidine. *Journal of Raman Spectroscopy* **35**, 93-100, doi:10.1002/jrs.1107 (2004).

33 Lakshmi, R. J. *et al.* Tissue Raman Spectroscopy for the Study of Radiation Damage: Brain Irradiation of Mice. *Radiation Research* **157**, 175-182, doi:10.1667/0033-7587(2002)157[0175:trsfts]2.0.co;2 (2002).

34 Krafft, C., Sobottka, S. B., Schackert, G. & Salzer, R. Raman and infrared spectroscopic mapping of human primary intracranial tumors: a comparative study. *Journal of Raman Spectroscopy* **37**, 367-375, doi:10.1002/jrs.1450 (2006).

35 Huang, Z. *et al.* Near-infrared Raman spectroscopy for optical diagnosis of lung cancer. *International Journal of Cancer* **107**, 1047-1052, doi:10.1002/ijc.11500 (2003).

36 Becker, L. *et al.* Raman Microspectroscopy Identifies Fibrotic Tissues in Collagen-Related Disorders Via Deconvoluted Collagen Type I Spectra. *Acta Biomater.*, doi:10.1016/j.actbio.2023.03.016 (2023).

37 Nothinger, I. & Hench, L. L. Raman microspectroscopy: a noninvasive tool for studies of individual living cells in vitro. *Expert Rev Med Devices* **3**, 215-234, doi:10.1586/17434440.3.2.215 (2006).

38 Nothinger, I., Selvakumaran, J. & Hench, L. L. New detection system for toxic agents based on continuous spectroscopic monitoring of living cells. *Biosens Bioelectron* **20**, 780-789, doi:10.1016/j.bios.2004.04.008 (2004).

39 Muschler, J. & Streuli, C. H. Cell-Matrix Interactions in Mammary Gland Development and Breast Cancer. *Cold Spring Harbor Perspectives in Biology* **2**, a003202-a003202, doi:10.1101/cshperspect.a003202 (2010).

40 Rich, L. & Whittaker, P. Collagen and picrosirius red staining: a polarized light assessment of fibrillar hue and spatial distribution. *Biology* (2005).

41 Ng, C. P., Hinz, B. & Swartz, M. A. Interstitial fluid flow induces myofibroblast differentiation and collagen alignment in vitro. *Journal of Cell Science* **118**, 4731-4739, doi:10.1242/jcs.02605 (2005).

42 Brauchle, E. M. *et al.* Biomechanical and biomolecular characterization of extracellular matrix structures in human colon carcinomas. *Matrix Biology* **68**, 180-193, doi:10.1016/j.matbio.2018.03.016 (2018).

43 Letsiou, S., Letsiou, K., Athanasios, A. & Athanasios, T. Transcriptional and epigenetic effects of Vitis vinifera L. leaf extract on UV-stressed human dermal fibroblasts. *Molecular Biology Reports* **47**, doi:10.1007/s11033-020-05645-7. (2020).

44 Xiao, H. *et al.* HSP47 regulates ECM accumulation in renal proximal tubular cells induced by TGF-β1 through ERK1/2 and JNK MAPK pathways. *Am J Physiol Renal Physiol.* **303**, F757-F765, doi:10.1152/ajprenal.00470.2011. (2012).

45 Abraham, E. T. *et al.* Collagen's primary structure determines collagen:HSP47 complex stoichiometry. *Journal of Biological Chemistry* **297**, 101169, doi:10.1016/j.jbc.2021.101169 (2021).

46 Taguchi, T., Nazneen, A., Al-Shihri, A. A., A. Turkistani, K. & Razzaque, M. S. Heat Shock Protein 47: A Novel Biomarker of Phenotypically Altered Collagen-Producing Cells. *ACTA HISTOCHEMICA ET CYTOCHEMICA* **44**, 35-41, doi:10.1267/ahc.11001 (2011).

47 Hollon, T. C. *et al.* Near real-time intraoperative brain tumor diagnosis using stimulated Raman histology and deep neural networks. *Nature medicine* **26**, 52-58 (2020).

48 Daum, R., Brauchle, E. M., Berrio, D. A. C., Jurkowski, T. P. & Schenke-Layland, K. Non-invasive detection of DNA methylation states in carcinoma and pluripotent stem cells using Raman microspectroscopy and imaging. *Scientific Reports* **9**, doi:10.1038/s41598-019-43520-z (2019).

49 Becker, L. *et al.* Raman Imaging and Fluorescence Lifetime Imaging Microscopy for Diagnosis of Cancer State and Metabolic Monitoring. *Cancers* **13**, 5682, doi:10.3390/cancers13225682 (2021).

Supplementary Information

Marker-independent imaging reveals a correlation of fibrotic and epigenetic alterations in endometriosis

Lucas Becker[a,b§], Tara Beyer[a,c§], Simone Liebscher[a], Daniel Carvajal-Berrio[a,b], Hans Bösmüller[c], Katharina Rall[d], Sara Y Brucker[d] , Katja Schenke-Layland[a,b,e], Martin Weiss[c,e] and Julia Marzi*[a,b,e]

Supplementary Tables

Table S1. Patient characteristics. PP: proliferative phase; OP: ovulation phase; SP: secretory phase.

Sample	**Donor 1**	**Donor 2**	**Donor 3**
Endometrium PP	41	40	49
Endometrium OP	38	45	42
Endometrium SP	37	44	42
Endometriosis LiS PP	31	41	36
Endometriosis LiS OP	40	29	38
Endometriosis LiS SP	31	43	40
Endometriosis SRV	31, PP	41, PP	32, OP
Peritoneum	25	31	31

Table S2. Performance of CNN classification of nuclei and COL I Raman spectra from endometriosis from both LiS and SRV and peritoneum.

Training	CNN
Test set error	0.015
Test set loss	0.065
Training accuracy	0.984
Validation loss	0.064
Validation accuracy	0.985
Test	
Accuracy	0.985
Sensitivity	0.985
Specificity	0.983

Supplementary Methods

Detailed protocols of histological stains.

Hematoxylin-Eosin (H&E) Staining

Cryo-sections were washed twice with DPBS for 10 min and fixed with 4% paraformaldehyde (PFA) for 20 min. Mayer's hemalum solution (Roth, Karlsruhe, Germany) (8 min) was used as a stain for the nuclei and eosin (Roth) (3.5 min) served as the counterstain. Differentiation was reached by rinsing the section with distilled water. Sections were then dehydrated in an ascending ethanol series ending with 100% isopropanol and consecutive mounting with Isomount 2000 (VWR Chemicals, Radnor, USA).

CD10 Staining

Cryosections were washed and fixed. Endogenous peroxidase activity was quenched with 1.5 ml 30% H_2O_2 (Sigma Aldrich, St. Louis, USA) in 50 ml methanol (Thermo Fisher Scientific, Waltham, USA) in the dark (20 minutes). Unspecific binding sites were blocked with horse serum (vector R.T.U Normal horse serum 2.5% 50 ml (Thermo Fisher Scientific) (30 min). After washing with DPBS$^-$, anti-CD10 mouse IgG1 (1: 100, Leica Biosystems, Nußloch, Germany) was applied overnight at 4°C. Sections were rinsed three times with DPBS$^-$, then ImmPRESS™ Reagent anti-mouse IgG ready-to-use solution (Thermo Fisher Scientific) was applied (30 min). Sections were then incubated with ImmPACT™ DAB kit (Abcam, Cambridge, GB) under continuous light microscope control. After washing with DPBS$^-$, nuclei were stained with hematoxylin QS (Vector Laboratories, Newark, USA). Finally, sections were mounted with Dako Faramount aqueous mounting medium (Agilent, Santa Clara, USA).

Ki67 Staining

Cryo-sections were washed and fixed. Slides were permeabilized with 1% Triton X-100 (Sigma Aldrich) for 30 min. After 10 min of washing with PBS, unspecific binding sites were blocked with ImmPRESS horse serum (Thermo Fisher Scientific) for 30 min. Ki67 primary antibody (1:1000, Abcam) was applied and incubated overnight at 4°C. Cryo-sections were washed three times with 0.01% Tween in PBS before applying ImmPRESS-AP Horse Anti-Rabbit IgG Polymer Kit+Alkaline Phosphatase Polymer Reagent (Thermo Fisher Scientific) for 30 min. After washing three times with 0.01% Tween in PBS ImmPACT Vector Red Substrate Kit (Thermo Fisher Scientific) was applied for 15 min in the dark. Finally, sections were mounted with Dako Faramount aqueous mounting medium.

Resorcin Fuchsin Staining

Cryo-sections were prepared as usual. Sections were placed in resorcinol-fuchsin staining solution (Sigma Aldrich) for 15 minutes. Nuclei were stained with red aluminum sulfate for 8 minutes. Sections were then rinsed with water for 1 minute. Differentiation was performed with 0.5% HCl in ethanol. Finally, the slides were mounted with Dako Faramount aqueous mounting medium.

Picrosirius Red Staining

Collagen maturity and directionality analyses were performed via picrosirius red staining. Firstly, Weigert's hematoxylin was used to stain nuclei of cryosections for 8 minutes and washed with tap water for 10 minutes. The sections were then treated with 0.1% picrosirius red solution (Morphisto, Frankfurt/Main, Germany) for 60 minutes. After the treatment, the tissues were washed with 0.5% acetic acid and 100% ethanol. The picrosirius red stained sections were imaged by polarized light microscopy (Axio

Observer, Zeiss Microscopy GmbH, Oberkochen, Germany) at 40x magnification followed by image J (Fiji version 2.0.0) processing. The images were transferred to RGB colors. In order to acquire the area percentages of red, orange (mature collagens), yellow and green (immature collagens) signals, the thresholds were adjusted as follows: Red (1-13, 230-256), orange (14-25), yellow (26-52) and green (53-110). For morphological assessment of collagen fibers, we utilized methods based on curvelet transform and Fourier transformation. CURVE Align, an open-source software package, was used to calculate alignment of collagen fibers. Alignment was represented on a scale from 0–1, where 1 displayed the highest degree of parallelism.

3D-image analysis

5mC and DAPI channels were analyzed separately with Imaris 9.7.2. The DAPI channel was processed individually for optimal visibility and contrast as it serves for general identification of nuclei. First, image layers negative for DAPI were truncated. Layers were then intensity normalized to 1. For calculation of nuclei volumes, the “Surfaces” tool was utilized to create artificial solid objects of a specified gray value range. Gaussian smoothing was set to 10^{-4} µm. To separate individual nuclei, “Region growing” was set to 0.1 µm. A threshold of a minimum of 10 voxels was applied for final filtering. Non-glandular nuclei volumes were deleted manually. The remaining surfaces were unified. To determine the number of glandular nuclei in a z-stack, “ClearView-GPU Deconvolution” with standard parameters utilizing the “Robust” algorithm with a maximum of 25 iterations was utilized. Resolved nuclei were independently counted manually three times. For 5mC analysis, histogram values were set between 1500 and 15000. First, control stains with no primary antibody were analyzed to determine the background noise. The “Threshold cutoff” was set to an intensity of 1500. For analysis of intensity of 5mC within nuclei, previously calculated surfaces of glandular nuclei were utilized. In the statistics tab of the created surface mean intensity, summed intensity and volume within the surface of 5mC were acquired. To identify 5mC spots, the “Spots” function was utilized. “Classify Spots” as well as “Region Growing” was disabled for classification. The estimated spot size was set to 1 µm. “Background Object Subtraction” was enabled for spot detection. Created spots were filtered with a quality above 1500. All spots that were not distributed within the glandular nuclei surface were deleted.

Neural network architecture

The neural network model had a fully-connected layer structure with 512-256-128-2 nodes, where the layer with 512 nodes was the input layer and the one with 2 nodes the output layer. The activation functions used were mainly ReLU (Rectified Linear Unit) and one softmax function in the last layer for probabilistic output values. Hyperparameter tuning was performed to identify optimal parameters for classification. The used hyperparameters were batch size: 128, epochs: 100, number of hidden units: 512, optimizer: Adam, learning rate: η=0.001. A training-validation-test split of 0.6-0.2-0.2 was applied. In our data assessment we compared dense neural networks with different amounts of layers as well as different amounts of dropouts in between the layers. The best classification results were obtained with a dropout of 75% after the first and after the second hidden unit.

Supplementary Figures

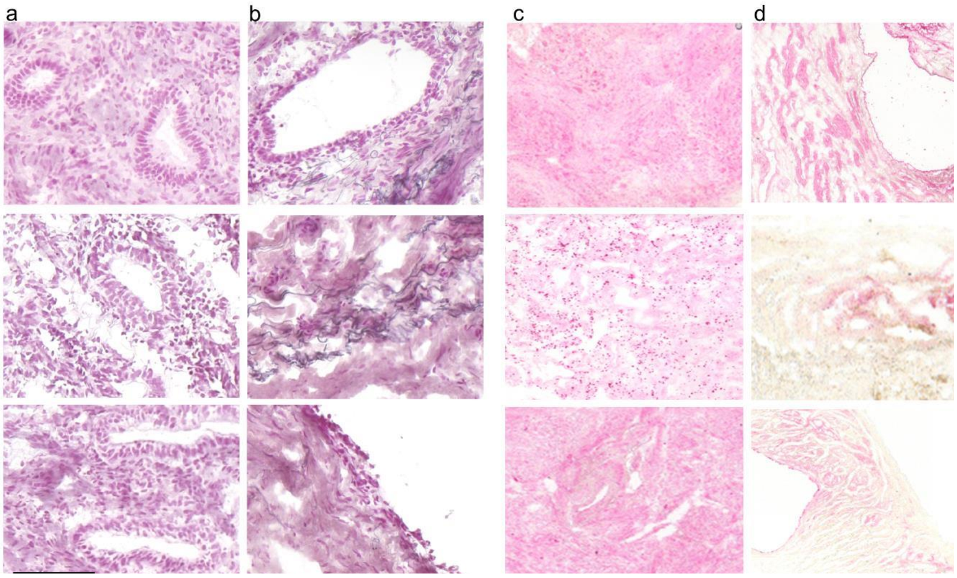

Figure S1: Resorcin Fuchsin staining for detection of elastic fibers and ki67 staining for identification of proliferation. (a) Resorcin fuchsin stains of the endometrium in different menstrual cycle phases. (b) Tissue next to glands of endometriosis of LiS in different menstrual cycle phases. Scale bar: 100 µm. (c) Ki67 staining of endometrium in different menstrual cycle phases. (d) Ki67 staining of endometriosis of LiS. Proliferative cells are visible by pink staining. While endometrium shows staining in the whole tissue, in endometriosis, proliferation takes place near glands.

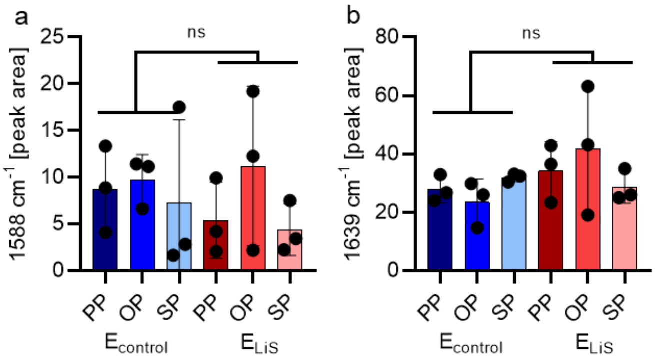

Figure S2: Spectral deconvolution (Sdc) of the amide I region from averaged COL I Raman spectra display differences between endometrium ($E_{control}$) and endometriosis from the LiS (E_{LiS}). (c) Peak area at 1563 cm^{-1} calculated based on spectral deconvolution of amide I area of averaged COL I spectra show differences between endometrium and endometriosis from the LiS. Peak areas at 1588 cm^{-1} (d) and 1639 cm^{-1} (e) calculated by spectral deconvolution display no difference between endometrium and endometriosis from the LiS.

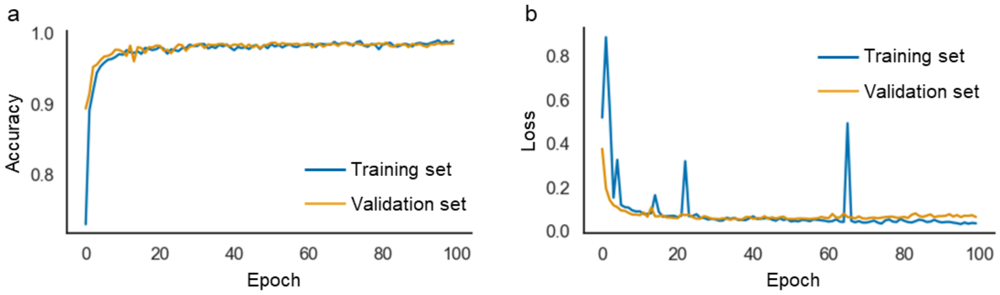

Figure S3: Training and validation curves of neural network classification. (a) Accuracy of training and validation set classifying endometriosis form both LiS and SRV and peritoneum based on combined COL I and nuclei Raman data. (b) Loss of training and validation set.

Appendix V: Becker L., Montes-Mojarro A., Layland S. L., Nsair A., Fend F., Marzi J., Schenke-Layland K., *Exploring the relationship between epigenetic DNA methylation and cardiac fibrosis through Raman microspectroscopy*, Am. J. Physiol*.* 2023, *325*(1), C332-C343; https://doi.org/10.1152/ajpcell.00209.2023

Am J Physiol Cell Physiol 325: C332–C343, 2023.
First published June 19, 2023; doi:10.1152/ajpcell.00209.2023

american physiological society®
AMERICAN JOURNAL OF PHYSIOLOGY
CELL PHYSIOLOGY®

RESEARCH ARTICLE

Decoding Fibrosis

Exploring the relationship between epigenetic DNA methylation and cardiac fibrosis through Raman microspectroscopy

Lucas Becker,[1,2] Ivonne A. Montes-Mojarro,[4] Shannon Lee Layland,[1] Ali Nsair,[3] Falko Fend,[4] Julia Marzi,[1,2,5] and Katja Schenke-Layland[1,2,5]

[1]Department for Medical Technologies and Regenerative Medicine, Institute of Biomedical Engineering, University of Tübingen, Tübingen, Germany; [2]Cluster of Excellence iFIT (EXC 2180) "Image-Guided and Functionally Instructed Tumor Therapies", University of Tübingen, Tübingen, Germany; [3]Division of Cardiology, Department of Medicine, Cardiovascular Research Laboratories, David Geffen School of Medicine at UCLA, Los Angeles, California, United States; [4]Institute of Pathology and Neuropathology, University Hospital Tübingen, Tübingen, Germany; and [5]NMI Natural and Medical Sciences Institute at the University Tübingen, Reutlingen, Germany

Abstract

Cardiomyopathies are associated with fibrotic remodeling of the heart, which is characterized by the excessive accumulation of collagen type I (COL I) due to chronic inflammation and suspected epigenetic influences. Despite the severity and high mortality rate of cardiac fibrosis, current treatment options are often inadequate, underscoring the importance of gaining a deeper understanding of the disease's underlying molecular and cellular mechanisms. In this study, the extracellular matrix (ECM) and nuclei in fibrotic areas of different cardiomyopathies were molecularly characterized by Raman microspectroscopy and imaging and compared with the control myocardium. Patient samples were obtained from heart tissue affected by ischemia, hypertrophy, and dilated cardiomyopathy and analyzed for fibrosis through conventional histology and marker-independent Raman microspectroscopy (RMS). Prominent differences between control myocardium and cardiomyopathies were revealed by spectral deconvolution of COL I Raman spectra. Statistically significant differences were identified in the amide I region of spectral subpeak at 1,608 cm^{-1}, which is a representative endogenous marker for alterations in the structural conformation of COL I fibers. Moreover, epigenetic 5mC DNA modification was identified within cell nuclei by multivariate analysis. A statistically significant increase in signal intensities of spectral features indicative of DNA methylation was detected in cardiomyopathies in accordance with immunofluorescence 5mC staining. Overall, RMS is a versatile technology in the discrimination of cardiomyopathies based on molecular evaluation of COL I and nuclei while providing insights into the pathogenesis of the diseases.

NEW & NOTEWORTHY Cardiomyopathies are associated with severe fibrotic remodeling of the heart, which is characterized by the excessive accumulation of collagen type I (COL I). In this study, we used marker-independent Raman microspectroscopy (RMS) to gain a deeper understanding of the disease's underlying molecular and cellular mechanisms.

collagen; extracellular matrix; non-destructive imaging; pathological tissue remodeling; Raman spectroscopy

INTRODUCTION

Cardiomyopathies comprise a heterogeneous group of myocardial diseases characterized by mechanical or electrical dysfunction (1). Myocardial infarction is defined as a muscle failure caused by a blocked blood vessel (ischemia) resulting in an anoxic state of the heart muscle (2). Spasms of the coronary artery, restricting the arterial lumen (3) or intravascular aggregation of lipids, and white blood cells inducing myocardial damage by inflammatory processes (4) are additional causes of ischemia. Most common primary diseases are diabetes, hypertension, hyperlipidemia, overweight, and obesity (5, 6). Although genetic predisposition plays a minor role in pathological development, epigenetic alterations were linked to fibrotic tissue modification in ischemia (7). Epigenetics refer to the mechanisms that result in heritable changes in the structure and function of chromatin without modifying the underlying DNA nucleotide sequences (8). Epigenetic mechanisms include, for example, transcriptional silencing of methylated DNA regions by DNA methylation, opening or closing of chromatin by histone modifications, initiation of repair mechanisms, or elongation of transcription

Correspondence: K. Schenke-Layland (katja.schenke-layland@uni-tuebingen.de).
Submitted 16 May 2023 / Revised 9 June 2023 / Accepted 9 June 2023

(9). The initiation of these mechanisms is mainly based on reversible changes in DNA in the form of methylation of cytosine and histone changes such as methylation, acetylation, phosphorylation, or ubiquitination (10).

In contrast, cardiac hypertrophy is an adaptive process of the myocardium in response to a variety of intrinsic and extrinsic stimuli, including left ventricular dilation, decreased systolic function, cardiomyocyte loss, and the development of fibrosis ultimately leading to heart failure and death (11, 12). Finally, dilatated cardiomyopathy is characterized by the presence of left ventricular dilatation and contractile dysfunction. Common causes of dilated cardiomyopathy are genetic mutations, or myocarditis (13).

The determining feature of these cardiomyopathies is the appearance of fibrotic tissue. In normal wound healing, fibroblasts are activated and transform into myofibroblasts. Hallmarks of myofibroblasts are the expression of contractile a smooth muscle actin (aSMA) and the secretion of extracellular matrix (ECM) proteins such as collagen type I (COL I) (14). Normally, myofibroblasts are removed by apoptotic pathways after completion of the wound healing process, however, epigenetic modifications could lead to resistance mechanisms, resulting in an excessive production of COL I (14).

Clinical evaluation of fibrosis currently relies primarily on the examination of tissue biopsies by standard histological analyses (H&E and Masson trichrome staining) or imaging techniques such as computed tomography, magnetic resonance imaging, and ultrasound elastography (15–18). In contrast, epigenetic evaluation often requires the disruption of tissue and the isolation of cellular DNA to perform next-generation sequencing (NGS) or methylation microarrays (19, 20). In recent years, noninvasive spectroscopic methods such as Raman microspectroscopy (RMS) have emerged as an alternative to conventional staining protocols (21–24). Recently, our group used Raman microspectroscopy to identify epigenetic 5mC alterations in human colon carcinoma cells (25). Furthermore, it has recently been demonstrated that fibrotic collagen changes can be identified by spectral deconvolution in various human tissues (22).

In this study, RMS was used to monitor collagen-rich regions of ex vivo tissues of cardiomyopathies including ischemic heart disease (IHD), hypertropic cardiomyoopathy (HCM), and dilatative cardiomyopathy (DCM). COL I spectra were extracted and underwent spectral deconvolution as well as peak-filter and image-based ratio analysis, whereas nuclei spectra were analyzed by principal component analysis (PCA) in comparison with 5mC immunofluorescence (IF) imaging.

MATERIALS AND METHODS

Collection of Human Tissue Samples

Formalin-fixed paraffin-embedded (FFPE) blocks were collected from patients undergoing medically indicated orthotopic heart transplantation at the University Department of General, Visceral and Transplant Surgery at the University of California (UCLA). Cases with different cardiomyopathies where fibrosis is accumulated in tissues were investigated including cases diagnosed as IHC, HCM, and DCM. For comparison, human control tissue from myocardium without fibrosis was analyzed ($n = 5$). All samples were collected after informed consent. The study was approved by the local ethical committee at UCLA. A microtome (MICROM HM560, Thermo Scientific, Waltham, MA) was used to obtain serial 10-l m cross sections of the tissue. A pathologist evaluated all tissues and confirmed the location of fibrotic areas using routine Masson trichrome staining.

Masson Trichrome Staining

Tissue sections were stained by utilizing the automatic slide stainer Tissue Tek Prisma (Sakura, Finetek) following the manufacturer’s protocol. The sections were scanned and imaged using an Axio Observer (Carl Zeiss Microscopy GmbH, Oberkochen, Germany) at 63 magnification.

Deparaffinization

FFPE tissue sections were deparaffinized using a modified protocol where samples were subjected to a thermal treatment at 60 C for 10 min, followed by three sequential incubations in xylol for 10 min each. The samples were then incubated in a series of ethanol solutions with progressively lower concentrations.

Picrosirius Red Staining

Weigert’s hematoxylin was applied for 8 min and washed with tap water for 10 min to stain nuclei. Afterward, tissue sections were treated with 0.1% picrosirius red solution (Morphisto, Frankfurt/Main, Germany) for 60 min and washed with 0.5% acetic acid and 100% ethanol for 5 min. Picrosirius red (PSR)-stained heart tissues were imaged by polarized light microscopy utilizing an Axio Observer at 63 magnification. Alterations in the amounts of red/orange and yellow/green were recorded. To identify red, orange, yellow, and green fibers, the images were transferred to Hue, Saturation, Value (HSV) color space in MATLAB 2019 b. The percentages of red (0–9, 230–256), orange (10–38), yellow (39–51), and green (52–128) pixels were analyzed for each image. Three images were analyzed for each sample. PSR images were additionally used to identify collagen fiber alignment. Angles of collagen were measured with ImageJ (Fiji version 2.0.0, National Institutes of Health, NIH). Utilizing the “OrientationJ” plugin collagen fiber coherency was defined for each image. In brief, coherency is calculated as the ratio between the difference and the sum of tensor eigenvalues describing the directionality of fibers (26).

COL I and aSMA Immunofluorescence Staining

Antigen retrieval was performed with Tris-EDTA buffer (pH 9, 0.05%) and citrate buffer (pH 6) followed by treatment of goat serum block solution (2%). Tissue sections were then incubated overnight with the following primary antibodies: rabbit polyclonal anti-Collagen I (6.6 mg/L; Acris, Herford, Germany) and mouse IgG2a monoclonal anti-a smooth muscle actin (aSMA) (2 mg/L; Sigma-Aldrich). Secondary antibodies AlexaFluor 488 conjugated goat anti-rabbit (4 mg/L; Thermo Fisher Scientific Life Technologies) and AlexaFluor 594 conjugated goat anti-mouse (4 mg/L, Thermo Fisher Scientific Life Technologies, Sindelfingen, Germany) were used as fluorescence labels. Afterward, Drag5 (5 µM; BioLegend, San Diego) was applied to the tissue sections for 15 min to stain nuclei. IF stains were imaged utilizing a Zeiss LSM 880 (Zeiss microscopy

GmbH). Images were acquired through a C Plan-Apochromat 63x/1.4. Oil DIC UV-VIS-IR M27 objective at a bit depth of 16 bit, scaling of 0.07 0.07 l m per pixel, and image size of 476 476 pixel, resulting in 33.74 33.74 l m large images. Image analysis was performed using ImageJ. For each tissue, three images were analyzed.

5mC Immunofluorescence Staining

Antigen retrieval was performed with Tris-EDTA buffer (pH 9, 0.05%) and citrate buffer (pH 6) followed by treatment of goat serum block solution (2%). Tissue sections were then placed in 88% of methanol for 30 min. After washing twice with DPBS for 10 min, 1 M HCl was applied for 90 min. Slides were then neutralized with 0.1 M sodium tetraborate (pH = 8.5) for 30 min. Then, unspecific binding sites were blocked with a 2% goat-blocking solution for 30 min. Tissue sections were then incubated overnight with the following primary antibodies: 5mC mouse monoclonal IgG primary antibody (1 l g/mL, Sigma Aldrich) and rabbit polyclonal anti-Collagen I (6.6 mg/L) at 4 C overnight. Secondary antibodies AlexaFluor 488 conjugated goat anti-rabbit (4 mg/L) and AlexaFluor 594 conjugated goat anti-mouse (4 mg/L) were used as fluorescence labels. After washing twice with DPBS for 10 min, autofluorescence was quenched with Vector TrueView autofluorescence quenching Kit (Vektor Laboratories, Newark). Afterward, Drag5 (5 µM) was applied on the tissue sections for 15 min to stain nuclei before mounting with ProLong gold antifade reagent. IF images were acquired utilizing a Zeiss LSM 880 at 63 magnification. Analysis was performed using ImageJ. For each tissue, three images were analyzed.

Raman Microspectroscopy

RMS measurements of tissue sections were performed with a customized confocal Raman microspectrometer (WITec alpha 300 R, Ulm, Germany) equipped with a 532 nm laser, a charge-coupled device (CCD) camera, and a 600 g/mm grating. Prior to Raman measurement, heart tissue samples were deparaffinized and kept humid with PBS during the entire measurement. Three Raman maps per sample with a size of 100 100 l m at a resolution of 1 l m/pixel at an integration time of 0.05 s were acquired utilizing a 63 apochromat water dipping objective (N.A. 1.0; Carl Zeiss Microscopy GmbH). For all measurements, the laser power was set to 50 mW.

Spectral Analysis

All Raman maps were subjected to cosmic ray removal, polynomial baseline correction, cropping to 400–3,000 cm ^{1}, and area intensity normalization with the software WITec project 5 (WITec GmbH). True component analysis (TCA) was used to decompose Raman maps into five major spectral components including nuclei, COL I, COL III, myosin, and aSMA to generate false color-coded Raman images.

PCA

For in-depth analysis of differences in control myocardium and different cardiomyopathies, PCA was performed on 200 extracted spectra from nuclei and COL I per patient with Unscrambler software (Unscrambler X10.5, CAMO, Oslo, Norway).

Spectral Deconvolution

Spectral deconvolution was performed as previously described (22). In short, with the software WITec project 5, spectral deconvolution was used to calculate the peak width and peak area of the substructural bands of the amide I region (1,550–1,720 cm ^{1}) of COL I. Collagen maps were extracted from the Raman data and then cropped to the amide I region before normalization to the peak at 1,667 cm ^{1} to 1. Inside the fitting region between 1,508 and 1,780 cm ^{1} the initial position of calculations was set to five wavenumbers based on the shape of the amide I region located at 1,563, 1,588, 1,608, 1,637, and 1,667 cm ^{1}. For spectral deconvolution, the Lorentz fitting algorithm was chosen, with a maximum number of iterations of 1,000, whereas fitting five functions (27, 28). Furthermore, peak intensity ratios of averaged COL I spectra were calculated by division of the maximum of the amide I peak located at 1,667 cm ^{1} by the intensity at 1,608 cm ^{1}.

Raman Image Ratio Analysis

To provide information on peak ratios of all individual collagen spectra within one Raman map, sum filter images of collagen maps were created using WITec project 5 software as previously described (22). Sum filter images were collected at 1,667 ± 25 cm ^{1} and at 1,608 ± 10 cm ^{1} and then divided before exporting them to MATLAB 2019 b. The obtained filter images were subjected to histogram analysis showing the distribution of all individual ratios. The ratios were rounded to integers before mode analysis.

Statistical Analysis

Statistical comparisons were performed from a minimum of five independent patient samples per pathology. Statistical analysis was performed using GraphPad Prism version 9.00 (GraphPad Software). Results are shown throughout the entire manuscript as mean ± standard deviation. All n numbers, applied tests, and corresponding significance for each result are listed in the figure legends.

RESULTS

Histological Staining Identifies Fibrotic Lesions

Fibrosis is a condition characterized by excessive collagen formation, leading to tissue remodeling and the development of persistent scar tissue, although the reason for this overproduction may vary in different cardiomyopathies (29, 30). Therefore, histological stains such as Masson's trichrome staining are utilized to diagnose and localize fibrotic lesions by visualizing excessive amounts of collagen fibers. In this study, the control tissue of myocardium was compared with fibrotic pathologies of myocardium derived from coronary ischemia, hypertrophy, and dilatation to identify structural and molecular patterns describing fibrotic collagen fibers.

Figure 1A shows exemplary Masson's trichrome stains of control myocardium, IHD, HCM, and DCM. Although control myocardium displayed scattered network-forming collagen fibers depicted in blue between muscles, infarcted fibrotic lesions are identified by excessive amounts of interstitial collagens in IHD, HCM, and DCM.

Collagen Fiber Maturity and Orientation Differs across Cardiomopathies

Picrosirius red (PSR) staining of tissues allowed the assessment of collagen maturity due to their birefringent characteristics. In Fig. 1B, exemplary PSR images under bright-field illumination of control myocardium, and the infarcted conditions of IHD, HCM, and DCM are displayed with collagen fibers stained in red. Corresponding polarized light images of the respective areas are displayed in Fig. 1C. Color threshold analysis of the percentage of red/orange collagen fibers and yellow/green collagen fibers varied strongly between the different heart diseases (Fig. 1E). Although the ratio of control and DCM showed no statistically significant difference ($P = 0.3202$), IHD exhibited significantly more red/orange fibers compared with the control ($P = 0.0403$). In HCM, the tendency of increased amount in red/orange fibers was detected ($P = 0.0851$). Conclusive differences between control and fibrotic heart tissues were not identified between the investigated samples. The quantification of fiber alignment in PSR images was performed by coherency analysis, which indicates the overall percentage of parallel aligned collagen fibers (Fig. 1F). Only in collagens of IHD ($P = 0.0402$) statistically significant increases in coherency were found while collagens were more randomly oriented in HCM ($P = 0.6226$) and DCM ($P = 0.5273$) as controls.

Immunofluorescence Staining Display the Complexity of Heart Tissues

Masson's trichrome and PSR staining are not specific for collagen subtypes. Therefore, IF staining was performed to particularly identify and localize COL I. IF images of control myocardium, IHD, HCM, and DCM identified COL I (yellow), aSMA (red), and nuclei (blue) in all tissues (Fig. 1D). Different COL I morphologies were observed depending on the origin of the tissue and disease. Little amounts of COL I were detected in the control myocardium, whereas an increased number of parallelly aligned COL I fibers was observed in IHD, HCM, and DCM. Colocalization of aSMA with cell nuclei was shown in IF images visualized by purple colors. Area quantification of COL I in IF images (Fig. 1G) showed statistically significant increased amounts of collagen fibers in IHD ($P = 0.0239$), HCM ($P = 0.0439$), and DCM ($P = 0.0308$). For aSMA identified by IF imaging (Fig. 1H), a statistically significant increase in DCM was found ($P = 0.0269$) while increases in IHD ($P = 0.1899$) and HCM ($P = 0.2583$) were not statistically significant.

Raman Imaging Allows Marker-Indepentent Visualization of Tissue Structures

Although histological and IF staining can identify fibrotic heart diseases based on collagen staining, these methods are time-consuming and require the usage of expensive chemicals. Consequently, marker-independent RMS was implemented to characterize the biomolecular composition of the myocardium and different cardiomyopathies. Raman maps of myocardium and infarcted areas were analyzed by True Component Analysis (TCA), a type of multivariate data analysis. Raman imaging and TCA (Fig. 2A) identified and localized five different components in myocardium tissues based on their spectral fingerprint (Fig. 2B). Peaks related to DNA (798, 1,096 cm^{-1}) (31), could define the structures, that were detected in one component of the TCA (blue). Another component showed peak assignments reported before to proline in COL I (yellow) located at 855 and 936 cm^{-1} (32, 33). The Raman spectra of collagen type III (COL III, turquoise) shared many spectral features with COL I, however, exhibited increased intensities at 1,123 and 1,296 cm^{-1}, and representatives for CN and CH_2 (32, 34) displayed a shifted amide III peak from 1,245 to 1,248 cm^{-1} (35). In contrast, myosin (pink) was assigned by its morphology and increased Raman intensities at 827 and 853 cm^{-1} representatives for C-C in proline and ring-breathing mode in tyrosine (33, 36). Based on in-house Raman measurements validated by colocalization of IF signals, aSMA was assigned to the fifth spectral component identified by TCA (red) (22). The potential of RMS being utilized for noninvasive, and marker-independent imaging of tissue structures was identified as Raman images and IF images showed similar morphological features and comparable results in the quantification of the amounts of COL I and aSMA. Quantification of COL I by Raman imaging (Fig. 2C) identified statistically significant increases in all myopathies [IHD ($P = 0.0005$), HCM ($P = 0.0032$), and DCM ($P = 0.0019$)]. For aSMA detected by Raman imaging (Fig. 2D), a statistically significant increase in the amount was found in HCM ($P = 0.0186$), whereas the tendency of increase was found in DCM ($P = 0.0758$). Similar amounts of aSMA compared with controls were found in IHD ($P = 0.7363$).

PCA Identifies Differences Between Healthy Myocardium and Cardiomyopathies

To determine the potential of RMS for assessment of different pathological alterations in myocardium, Raman spectra of COL I were extracted from Raman images and subjected to PCA to further investigate similarities or differences between the diseases. PC-3 score values (Fig. 2E) revealed statistically significant increases in HCM ($P = 0.0330$) as well as DCM ($P = 0.0232$) compared with control myocardium, whereas for IHD ($P = 0.0642$) only a tendency toward increased score values was found. The shifts in the score values were explained by the corresponding loading plot (Fig. 2F), which mainly indicated changes in the amide I region (1,550–1,720 cm^{-1}) responsible for alteration in the secondary structure of proteins. In COL I, the secondary structure is defined mainly by a-like helices, b-sheets, b-turns, and random coils (disordered) (37, 38). Further COL I structure-related peaks were found in

Figure 1. Histological staining allows the localization of fibrosis. A: Masson's trichrome staining of control myocardium, ischemic heart disease (IHD), hypertrophic cardiomyopathy (HCM), and dilated cardiomyopathy (DCM) identify fibrosis by excessive collagen staining in blue. Scale bar = 500 I m. B: Picrosirius red (PSR) staining under brightfield illumination of control myocardium, IHD, HCM, and DCM. Scale bar = 100 I m. C: PSR staining under polarized light of control myocardium, IHD, HCM, and DCM. Scale bars = 100 I m. D: immunofluorescence (IF) images of control myocardium, IHD, HCM, and DCM show the complexity of the tissues. Colors in IF staining: Nuclei (blue), COL I (yellow), and aSMA (red). Scale bar = 100 I m. E: quantification of red collagen and green collagen fibers. F: coherency analysis shows parallel aligned fibers only in IHD. G: quantification of the amount of COL I based on IF images normalized by the whole tissue area. H: quantification of the amount of aSMA based on IF images normalized by the whole tissue area. Statistical analysis: t test, $n = 5$, $P < 0.05$, ns: not significant.

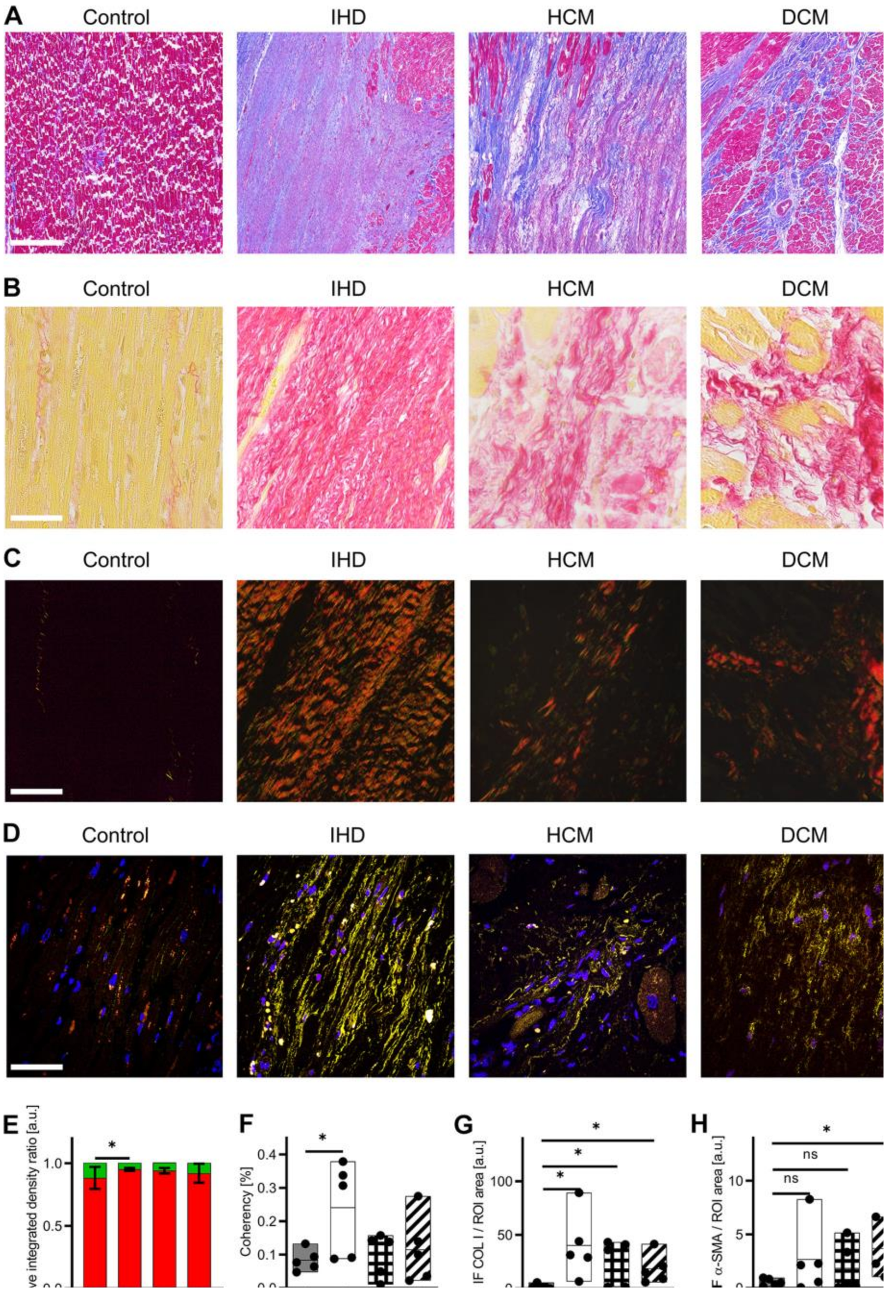
A
Control
IHD
HCM
DCM
B
Control
IHD
HCM
DCM
C
Control
IHD
HCM
DCM
D
Control
IHD
HCM
DCM
E
ve integrated density ratio [a.u.]
1.0
0.5
*
F
Coherency [%]
0.4
0.3
0.2
0.1
*
G
IF COL I / ROI area [a.u.]
100
50
*
*
*
H
F α-SMA / ROI area [a.u.]
10
5
*
ns
ns

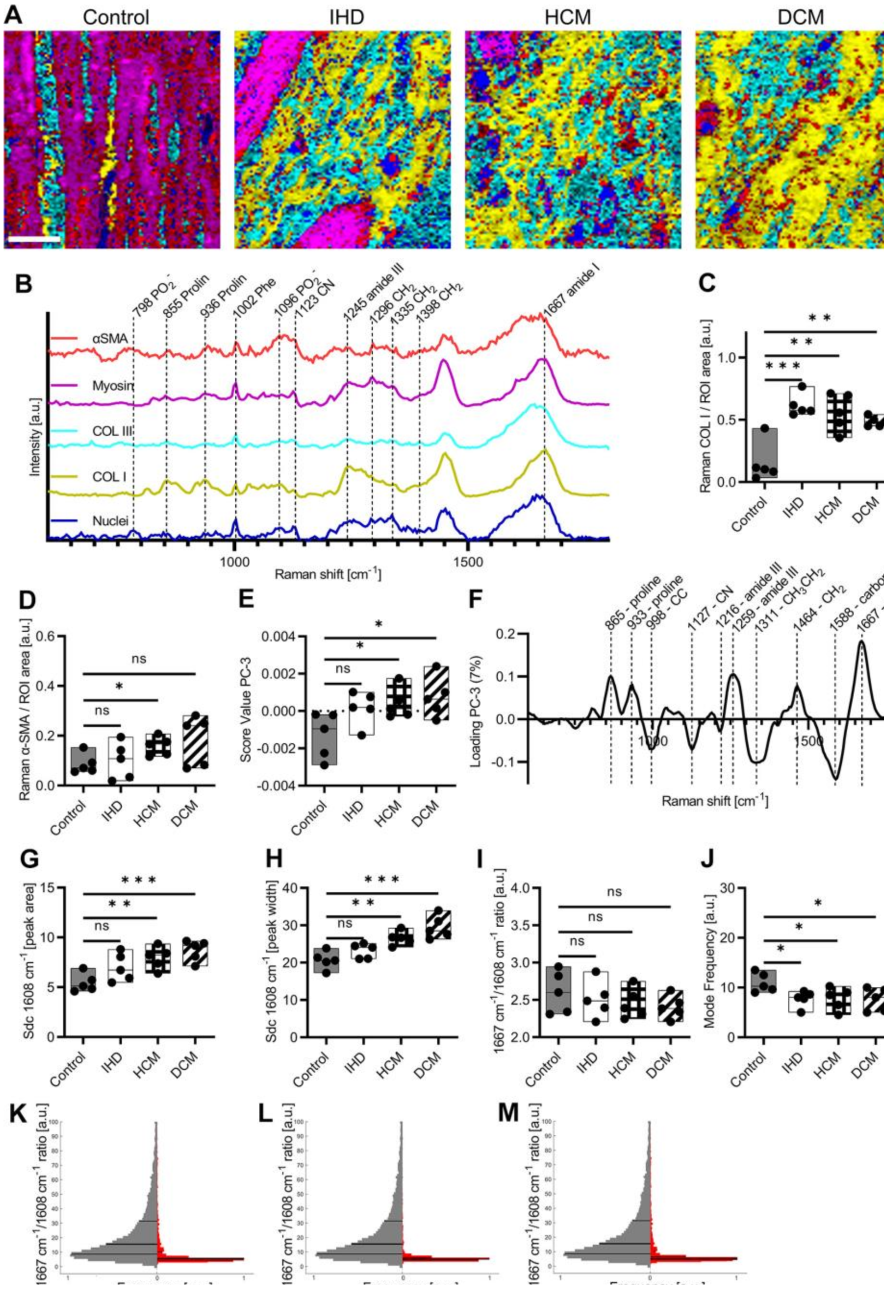
A
Control
IHD
HCM
DCM
B
798 PO2-
855 Prolin
936 Prolin
1002 Phe
1096 PO2-
1123 CN
1245 amide III
1296 CH2
1335 CH2
1398 CH2
1667 amide I
αSMA
Myosin
COL III
COL I
Nuclei
Intensity [a.u.]
1000
1500
Raman shift [cm-1]
C
Raman COL I / ROI area [a.u.]
* *
* *
* * *
1.0
0.5
0.0
Control
IHD
HCM
DCM
D
Raman α-SMA / ROI area [a.u.]
0.6
0.4
0.2
0.0
ns
*
ns
Control
IHD
HCM
DCM
E
Score Value PC-3
0.004
0.002
0.000
-0.002
-0.004
*
*
ns
Control
IHD
HCM
DCM
F
865 - proline
933 - proline
998 - CC
1127 - CN
1216 - amide III
1259 - amide III
1311 - CH3CH2
1464 - CH2
1588 - carbo
1667 -
Loading PC-3 (7%)
0.2
0.1
0.0
-0.1
1000
1500
Raman shift [cm-1]
G
Sdc 1608 cm-1 [peak area]
15
10
5
0
* * *
* *
ns
Control
IHD
HCM
DCM
H
Sdc 1608 cm-1 [peak width]
40
30
20
10
0
* * *
* *
ns
Control
IHD
HCM
DCM
I
1667 cm-1/1608 cm-1 ratio [a.u.]
4.0
3.5
3.0
2.5
2.0
ns
ns
ns
Control
IHD
HCM
DCM
J
Mode Frequency [a.u.]
30
20
10
0
*
*
*
Control
IHD
HCM
DCM
K
1667 cm-1/1608 cm-1 ratio [a.u.]
L
1667 cm-1/1608 cm-1 ratio [a.u.]
M
1667 cm-1/1608 cm-1 ratio [a.u.]

the loadings located at 1,216 and 1,259 cm^{-1}, indicating alterations in the amide III region (39, 40). Shifts located at 1,127, 1,311, and 1,464 cm^{-1} were representatives for C-N vibrations (41), CH_3CH_2 twisting modes of collagen (42), and CH_2 deformation (40). Peaks at 865 and 933 cm^{-1} could be assigned to proline (32, 33).

Furthermore, a PCA excluding the control spectra was performed to identify molecular alterations across the diseases. However, score value analysis was not able to identify statistically significant differences in Col I composition (Supplemental Fig. S1A; https://doi.org/10.6084/m9.figshare.23292443).

Fibrotic COL I Alterations in Cardiomyopathies Are Identified by the Raman Marker at 1,608 cm^{-1}

Spectral deconvolution of the amide I region enabled in detailed analysis of the secondary structure of COL I in control myocardium and different cardiomyopathies. COL I average Raman spectra were cropped to the amide I region (1,508–1,780 cm^{-1}) and normalized to 1 for better comparability. By spectral deconvolution, five substructural peaks located at 1,562, 1,588, 1,608, 1,637, and 1,667 cm^{-1} could be identified based on the shape of the amide I region and literature (22, 27). The subpeaks were assigned to tryptophane, phenylalanine, tyrosine, β-sheets as well β-turns (37, 38). In Supplemental Fig. S1, B–E, the amide I region of averaged COL I spectra and deconvoluted subpeaks in control myocardium, IHD, HCM as well as DCM are displayed. For all deconvolutions, the adjusted R^2 values were above 0.995 indicating a sufficient fitting accuracy. Spectral deconvolution provided information about peak width and the area of substructural peaks. In HCM ($P = 0.0047$) and DCM ($P = 0.0008$), calculated peak areas at 1,608 cm^{-1} were significantly increased compared with control myocardium, whereas for IHD a tendency toward an increased area was detected ($P = 0.0721$) (Fig. 2G). Analysis of the peak width at 1,608 cm^{-1} showed similar results. Significant increases were found in HCM ($P = 0.0025$) and DCM ($P = 0.0009$) compared with control myocardium, whereas trends of increased widths were observed in IHD ($P = 0.1064$) (Fig. 2H). In addition, the peak intensity ratio of 1,608 cm^{-1} to the maximum peak of the amide I peak at 1,667 cm^{-1} was calculated. However, no significant differences were observed when comparing the peak ratio of averaged COL I spectra from control myocardium with IHD ($P = 0.5882$), HCM ($P = 0.3527$), and DCM ($P = 0.2074$) (Fig. 2I). Further to the spectral deconvolution of averaged spectra of COL I, whole COL I Raman maps were analyzed. Based on divided sum filter images created at 1,608 ± 10 cm^{-1} and 1,667 ± 25 cm^{-1}, the peak ratio per pixel in each image was assessed. Figure 2, K–M displays the calculated histograms of peak ratios from control COL I compared with IHD, HCM, and DCM. Lines in the histogram represent the 25, 50, and 75 percentiles while the widest position of the histograms is displaying the mode. Analysis of the mode (Fig. 2J) showed statistically significant decreases in IHD ($P = 0.0207$), HCM ($P = 0.0411$), and DCM ($P = 0.0349$).

RMS Identify Epigentic 5mC Alteration in Cardiomyopathies

In recent years, it has been recognized that epigenetic changes can lead to pathological tissue changes in the heart (43, 44). Therefore, 5mC IF staining was performed on nuclei of control myocardium, IHD, HCM, and DCM. IF staining identified 5mC (turquoise), nuclei (blue), and COL I (yellow), where the COL I stain served to identify the fibrotic ROIs (Fig. 3A). The quantification of 5mC normalized by the nuclei identified significant increases in IHD ($P = 0.0402$) and HCM ($P = 0.0122$), whereas in DCM ($P = 0.6077$) no difference was observed (Fig. 3B). Similar results were identified for the quantification of 5mC fluorescence intensity, where significant differences were displayed in IHD ($P = 0.0078$) and HCM ($P = 0.0071$), but not for DCM ($P = 0.0835$) (Fig. 3C). To further evaluate the potential of RMS in identifying diseased tissue structures, PCA was performed on extracted single spectra of nuclei. A score value analysis of PC-1 identified statistically significant differences in all IHD ($P = 0.0023$), HCM ($P < 0.0001$), and DCM ($P = 0.0002$) compared with controls (Fig. 3D). The corresponding loading plot (Fig. 3E) identified increased spectral signatures in DNA backbone located at 782, 815, and 1,222 cm^{-1} in controls (32, 33, 45). In contrast, cardiomyopathies exhibited increased spectral features located at 1,257, 1,342 cm^{-1} and representatives for cytosine and guanine (31, 46). Alternatively, the peak at 1,257 cm^{-1} could be attributed to methylations as the peaks located at 1,379 and 1,442 cm^{-1} (39, 40, 47). Furthermore, an increased signal in cardiomyopathies was shown in the amide I region at 1,667 cm^{-1}, which in the case of the nuclei could indicate a change in the histone structure. As for COL I Raman spectra, a PCA of nuclei Raman spectra was calculated only for the cardiomyopathies to identify disease-related alterations, however, no statistically significant differences were observed (Supplemental Fig. S1F; https://doi.org/10.6084/m9.figshare.23292443).

DISCUSSION

Myocardial fibrosis is a hallmark of pathological cardiac remodeling leading to heart failure and death. In this study,

Figure 2. Raman imaging and spectral deconvolution (Sdc) allows marker-independent analysis of myocardium and different cardiomyopathies. A: True Component Analysis (TCA) images of control, IHD, HCM, and DCM. Scale bar = 20 μm. B: spectra identified by TCA: nuclei (blue), myosin (pink), COL III (turquoise), COL I (yellow), and αSMA (red). C: quantification of the amount of COL I based on Raman images normalized by the whole tissue area. D: quantification of the amount of αSMA based on Raman images normalized by the whole tissue area. E: score value analysis of PC-3 from COL I Raman spectra from control myocardium and cardiomyopathies. F: corresponding loading plot. G: peak area at 1,608 cm^{-1} calculated based on Sdc of amide I area of averaged COL I spectra from control myocardium and different cardiomyopathies. H: peak width at 1,608 cm^{-1} calculated based on Sdc of amide I area of averaged COL I from control myocardium and different cardiomyopathies. I: peak ratio of averaged COL I spectra at 1,608 cm^{-1} normalized by amide I maximum. J: frequency of modes from filter image ratio at 1,608 cm^{-1} normalized by amide I maximum. K: histogram of filter image ratio at 1,608 cm^{-1} normalized by amide I maximum (1,667 cm^{-1}) of control and IHD. Lines in the histogram represent the 25, 50, and 75 percentiles while the widest position of the histograms is displaying the mode. L: histogram of filter image ratio at 1,608 cm^{-1} normalized by amide I maximum (1,667 cm^{-1}) of control and HCM. M: histogram of filter image ratio at 1,608 cm^{-1} normalized by amide I maximum (1,667 cm^{-1}) of control and DCM. Statistical analysis: t test, $n = 5$, $P < 0.05$, $P < 0.01$, $P < 0.005$, ns: not significant. COL I, collagen type I; COL III, collagen type III; DCM, dilated cardiomyopathy; HCM, hypertrophic cardiomyopathy; IHD, ischemic heart disease.

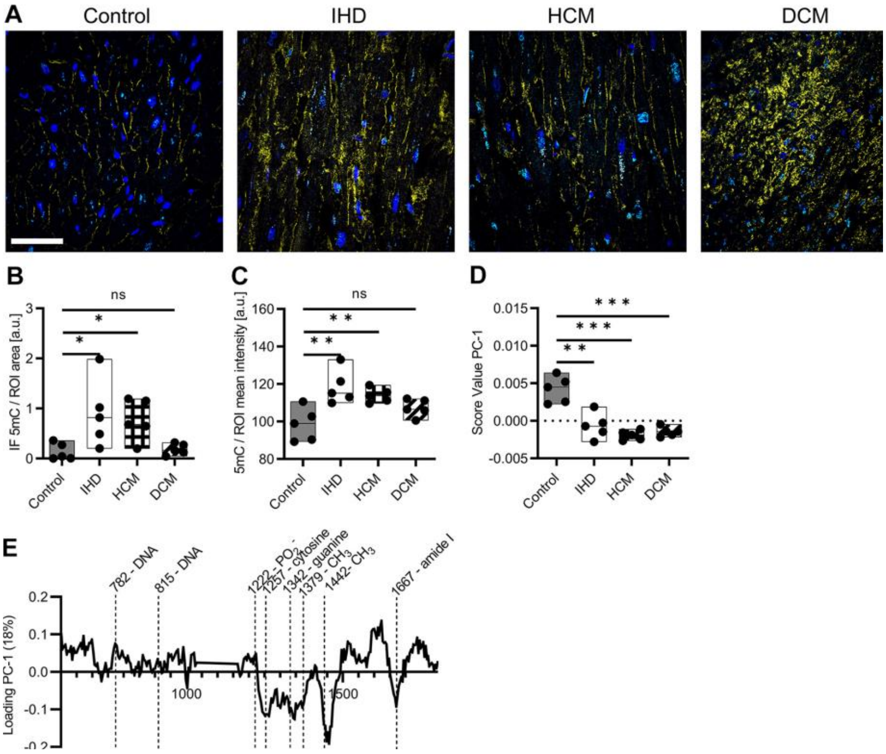

Figure 3. Raman imaging identifies epigenetic alterations in cardiomyopathies. A: IF images of 5mC staining. Colors in IF staining: Nuclei (blue), COL I (yellow), and 5mC (turquoise). Scale bar =100 l m. B: quantification of the amount of 5mC based on IF images normalized by nuclei. C: quantification of the fluorescence intensity of 5mC. D: score value analysis of PC-1 from nuclei Raman spectra from control myocardium and cardiomyopathies. E: corresponding loading plot. Statistical analysis: t test, $n = 5$, $P < 0.05$, $P < 0.01$, $P < 0.005$, ns: not significant. COL I, collagen type I; IF, immunofluorescence.

we demonstrated that noninvasive and marker-independent RMS has the potential to identify fibrotic COL I alterations and epigenetic alterations in different cardiomyopathies such as IHD, HCM, and DCM compared with control myocardium.

Histological analysis of cardiac tissue is currently the most accepted and reliable method for the investigation of pathological fibrosis ex vivo. Collagen staining with Masson's trichrome, Movat's pentachrome, or PSR are established methods for detecting cardiovascular fibrosis (48, 49). These stains provide a distinct contrast to differentiate collagens from their surrounding cells and connective tissues. Although these methods are very useful for the study of collagen density and structure, the staining procedure is tedious and requires large amounts of reagents (50). In addition, histopathological examination by trained pathologists can easily introduce bias and error by selecting nonrepresentative sites from the tissue biopsy, leading to poor reliability of both qualitative and quantitative outcomes. The clinical diagnosis of fibrotic diseases may also occasionally vary based on individual experience and knowledge, leading to divergent diagnostic results (51).

PSR staining is utilized to evaluate information about the condition of collagen fibers by their birefringent characteristics. It is widely reported that thicker more mature collagen fibers polarize light toward a stronger red birefringence while thinner immature fibers to a weaker green birefringence (52). The strong positive birefringence of collagen is due to the superposition of the clockwise collagen superhelix with the counterclockwise helix comprising the three polypeptide chains. In contrast, greenish-yellow collagen fibers were found possibly representing procollagen and intermediate collagen fibers (53). However, greenish collagen fibers may also indicate the presence of procollagen, intermediate, or pathological collagen fibers (54). Differential results were obtained from the quantification of mature and immature fibers in the various cardiomyopathies, indicating the involvement of distinct molecular mechanisms in their pathogenesis. In literature, shifts in birefringence were also linked to the amounts of COL I and COL III (55). The shifts compared with controls could therefore indicate different levels of collagen gene expression. Indeed, varying levels of TGF-b linked to the expression of collagens were found in cardiomyopathies before (56, 57).

In cardiac fibrosis, the differentiation of cardiac fibroblasts into myofibroblasts plays another key role. Upon exposure of the heart to inflammation, hypoxia, ischemia, or other stimulating factors, cardiac fibroblasts proliferate and differentiate into cardiac myofibroblasts expressing aSMA and secreting numerous cytokines and ECM proteins (58–61). Accordingly, aSMA was selected as the second fluorophore in IF stains. The quantification of aSMA revealed increases in the amount in all cardiomyopathies. The result of the statistically increased amount of aSMA in DCM is in line with the results of recent work (62). Although fibroblasts expressing aSMA were observed in large scars after myocardial infarction (63, 64), the absence of aSMA in interstitial fibrosis was found in some cases of pulmonary fibrosis (65, 66) but also in heart muscle (67), which might explain the rather low level of aSMA in some donors.

To overcome the obstacles of histological and IF staining including their high cost and lengthy procedures, RMS was utilized to differentiate between fibrotic and control COL I fibers. TCA-based image generation provided noninvasive and marker-independent determination and localization of major sub- and extracellular structures within the cardiac tissues and respective cardiomyopathies. Heat maps of the intensity distribution of the individual TCA components allowed further exploration of the underlying spectral information. Spectral signatures provided access to changes in molecular composition of COL I and identified fibrosis-specific peak patterns in PCA loadings. Multivariate data analysis tools allowed us to discriminate between control COL I and all different cardiomyopathies mainly by spectral alteration at positions relevant to structural information. In the loadings, peaks representative of amide I and amide III were identified. In addition, peaks attributable to differences in C-C, C-N, CH_2, and CH_2CH_3 vibrations were identified, which together indicate an altered pattern in the amino acid sequence of COL I.

In a recent study, we established a Raman biomarker that allowed us to discriminate fibrotic COL I from controls in various human tissues based on spectral deconvolution of the amide I region at the position at 1,608 cm^{-1} (22). The amide I peak of COL I contains information about the amino acid composition and provides additional information about the secondary structure (27, 68). Performing spectral deconvolution on averaged COL I spectra from control cardiac and different cardiomyopathies revealed statistically significant increased peak areas as well as peak widths at 1,608 cm^{-1} in all fibrotic cases including IHD, HCM, and DCM. In addition, statistically significant differences were found when comparing the modes of peak ratio images where each image contains multiple single spectra of COL I. In fibrotic COL I, the higher peak area and width at the Raman shift of 1,608 cm^{-1} could be attributed to the amino acid tyrosine and its precursor phenylalanine (41, 69). The molecular composition of collagens consists mainly of the repeating amino acid triplet's glycine-Xaa-Yaa, where Xaa and Yaa can constitute any amino acids (70). Most frequently, the amino acids proline and hydroxyproline occupy the positions Xaa and Yaa, but can be replaced by leucine, arginine, phenylalanine, or tyrosine (71, 72). The increase in the Raman signal at 1,608 cm^{-1} accordingly represents an alteration in the amino acid sequence of fibrotic COL I, which has been linked to shifted dissociation constants of heat shock protein 47 (HSP47) (72, 73). The collagen-specific chaperon HSP47 residing in the endoplasmic reticulum is relevant for collagen synthesis in vertebrates and is a promising therapeutic target in fibrosis, which might play an important role in the development of fibrosis (74, 75). It has been demonstrated that hampering HSP47 has the potential to improve the phenotype of different types of fibrosis such as peritoneal fibrosis as well as liver fibrosis (76, 77). Furthermore, the influence of HSP47 in myocardial infarction has been found (78, 79). Our results suggest that RMS may be useful for screening the effects of antifibrotic drugs.

In recent years it was recognized that epigenetic modifications may play another important role in the development of pathological tissue modifications such as fibrosis. The methylation of DNA and modification of the histone structure are regulators for cell proliferation and their behavior (80, 81). The most frequent epigenetic alteration is 5mC, comprising 4% of all cytosines in the human genome, which can be propagated by DNA replication mediated by DNMT1 DNA methyltransferase (82, 83). IF imaging revealed statistically significant increases of 5mC in nuclei located in fibrotic areas. Furthermore, the spectral signatures identified in a PCA of the cell nuclei can be assigned to changes in the DNA and methylation patterns implicating the potential of RMS being utilized to identify epigenetic modifications. When the increased epigenetic signals of the cardiomyopathies were considered together with the results of COL I and aSMA analyses, a consistent correlation emerged. The epigenetic modification of the DNA may cause the myofibroblasts, which normally disappear via apoptosis during normal wound healing, to develop resistance mechanisms such that they continue to secrete COL I even after the healing process has ended (14). The excessive production of COL I could then ultimately lead to pathological tissue modification.

Moreover, the findings from Raman imaging and histological analysis are intriguing, as they demonstrate the potential for distinguishing between various types of cardiomyopathies. It was observed that IHD had a higher collagen content compared with the other types of investigated cardiomyopathies. However, there was no clear correlation between the amount of collagen and molecular markers for fibrosis, suggesting that a higher collagen content does not necessarily correlate with a stronger fibrotic phenotype. This observation is particularly interesting as it may indicate a more complex relationship between collagen deposition and the development of fibrosis, which warrants further investigation in future studies.

The advancement of RMS as a benchtop method for companion diagnostics in pathology or an RMS-based endoscopic device that can be utilized during clinical surgery offers promising alternatives to conventional techniques. Such RMS-based tools enable rapid and precise real-time analysis of tissue samples without the need for prior staining or fixation. RMS provides molecular signatures of cells and tissues, identifies biomarkers and gene expression profiles, and facilitates personalized treatment approaches. In pathology, it allows for faster and more accurate diagnoses while during surgical procedures, it provides real-time diagnostics of tissue structures and margins. Despite certain technical challenges, RMS holds great potential for improved diagnostic procedures and personalized treatments.

The regulatory hurdles associated with the application of RMS as a benchtop method or endoscopic system involve fulfilling regulatory requirements and integrating the technology into clinical practice. These requirements include demonstrating the safety, effectiveness, and reliability of RMS as a diagnostic technique through extensive clinical studies and data that compare its performance to established diagnostic methods and gold standards. In addition, compliance with regulatory standards for the manufacturing, validation, and quality assurance of devices and reagents is necessary. Obtaining regulatory approvals and certification from relevant authorities to officially recognize RMS as a diagnostic procedure can be time-consuming and costly due to varying regulations across different countries or regions (e.g., EMA vs. FDA). Moreover, the integration of RMS into clinical practice requires training medical personnel and pathologists to properly apply the technique and interpret the data, along with the development and implementation of standardized protocols and guidelines for consistent and reliable application. Close collaboration among researchers, manufacturers, regulatory authorities, and medical professionals is necessary to overcome these challenges and fully exploit the potential of this innovative diagnostic technology.

Conclusions

This study highlighted the potential of RMS as a diagnostic tool to evaluate and identify fibrotic COL I and epigenetic DNA modifications in different human cardiomyopathies. RMS allowed discriminating pathological COL I in fibrotic IHD, HCM, and DCM by spectral deconvolution of the amide I band. Moreover, PCA allowed identifying epigenetic 5mC modifications in the DNA of diseased patients. This molecularly sensitive approach enables the monitoring of pathological tissue changes and, at the same time, gives insights into the pathogenesis of the disease. Whereas only a small selection of cardiac fibrotic diseases has been studied, this technique may, in the future, provide pathologists with a nondestructive, marker-independent, and potentially automated method to perform fibrosis and epigenetic studies without the need for conventional time-consuming staining procedures.

DATA AVAILABILITY

The data that support the findings of this study are available from the corresponding author upon reasonable request.

SUPPLEMENTAL DATA

Supplemental Fig S1: https://doi.org/10.6084/m9.figshare.23292443.

GRANTS

This work was conducted in the framework of the Graduate School 2543/1 “Intraoperative Multi-Sensory Tissue-Differentiation in Oncology” funded by the German Research Foundation (DFG - Deutsche Forschungsgemeinschaft). Further funding was received by the Deutsche Forschungsgemeinschaft (INST 2388/64-1, INST 2388/33-1 and Germany’s Excellence Strategy, EXC 2180-390900677), the Ministry of Science, Research, and the Arts of Baden-Wuerttemberg (33-729.55-3/214 and SI-BW 01222-91), and the State Ministry of Baden-Wuerttemberg for Economic Affairs, Labour and Tourism (3-4332.62-NMI/65).

DISCLOSURES

No conflicts of interest, financial or otherwise, are declared by the authors.

AUTHOR CONTRIBUTIONS

A.N. and K.S.-L. conceived and designed research; L.B. performed experiments; L.B. and J.M. analyzed data; L.B., I.A.M.-M., F.F., J.M., and K.S.-L. interpreted results of experiments; L.B. prepared figures; L.B. drafted manuscript; I.A.M.-M., S.L.L., A.N., F.F., J.M., and K.S.-L. edited and revised manuscript; L.B., I.A.M.-M., S.L.L., A.N., F.F., J.M., and K.S.-L. approved final version of manuscript.

REFERENCES

1. Maron BJ, Towbin JA, Thiene G, Antzelevitch C, Corrado D, Arnett D, Moss AJ, Seidman CE, Young JB; Council on Epidemiology and Prevention. Contemporary definitions and classification of the cardiomyopathies. Circulation 113: 1807–1816, 2006. doi:10.1161/circulationaha.106.174287.
2. Lin M-J, Fine M, Lu J-Y, Hofmann SL, Frazier G, Hilgemann DW. Massive palmitoylation-dependent endocytosis during reoxygenation of anoxic cardiac muscle. eLife 2: e01295, 2013. doi:10.7554/elife.01295.
3. Virmani R, Burke AP, Farb A. Sudden cardiac death. Cardiovasc Pathol 10: 211–218, 2001. doi:10.1016/s1054-8807(01)00091-6.
4. Haft JI. Cardiovascular injury induced by sympathetic catecholamines. Prog Cardiovasc Dis 17: 73–86, 1974. doi:10.1016/0033-0620(74)90039-5.
5. Assmann G, Schulte H. The Prospective Cardiovascular Münster (PROCAM) study: prevalence of hyperlipidemia in persons with hypertension and/or diabetes mellitus and the relationship to coronary heart disease. Am Heart J 116: 1713–1724, 1988. doi:10.1016/0002-8703(88)90220-7.
6. Crump C, Sundquist J, Winkleby MA, Sundquist K. Interactive effects of obesity and physical fitness on risk of ischemic heart disease. Int J Obes (Lond) 41: 255–261, 2017. doi:10.1038/ijo.2016.209.
7. Morgado-Pascual JL, Marchant V, Rodrigues-Diez R, Dolade N, Suarez-Alvarez B, Kerr B, Valdivielso JM, Ruiz-Ortega M, Rayego-Mateos S. Epigenetic modification mechanisms involved in inflammation and fibrosis in renal pathology. Mediators Inflamm 2018: 1–14, 2018. doi:10.1155/2018/2931049.
8. Dupont C, Armant D, Brenner C. Epigenetics: definition, mechanisms and clinical perspective. Semin Reprod Med 27: 351–357, 2009. doi:10.1055/s-0029-1237423.
9. Miller JL, Grant PA. The Role of DNA Methylation and Histone Modifications in Transcriptional Regulation in Humans. Netherlands: Springer, 2013, p. 289 317.
10. Nordheim A, Knippers R. Molekulare Genetik (8th ed.). Stuttgart, Germany: Thieme, 2018, vol. 11.
11. Katz AM. The cardiomyopathy of overload: an unnatural growth response in the hypertrophied heart. Ann Intern Med 121: 363–371, 1994. doi:10.7326/0003-4819-121-5-199409010-00009.
12. Hunter JJ, Chien KR. Signaling pathways for cardiac hypertrophy and failure. N Engl J Med 341: 1276–1283, 1999. doi:10.1056/NEJM199910213411706.
13. Weintraub RG, Semsarian C, Macdonald P. Dilated cardiomyopathy. Lancet 390: 400–414, 2017. doi:10.1016/S0140-6736(16)31713-5.
14. Hinz B, Phan SH, Thannickal VJ, Galli A, Bochaton-Piallat M-L, Gabbiani G. The myofibroblast. Am J Pathol 170: 1807–1816, 2007. doi:10.2353/ajpath.2007.070112.
15. Rasotto R, Berlato D, Goldschmidt MH, Zappulli V. Prognostic significance of canine mammary tumor histologic subtypes: an observational cohort study of 229 cases. Vet Pathol 54: 571–578, 2017. doi:10.1177/0300985817698208.

16. Choong CC, Venkatesh SK, Siew EP. Accuracy of routine clinical ultrasound for staging of liver fibrosis. J Clin Imaging Sci 2: 58, 2012. doi:10.4103/2156-7514.101000.
17. Petitclerc L, Gilbert G, Nguyen BN, Tang A. Liver fibrosis quantification by magnetic resonance imaging. Top Magn Reson Imaging 26: 229–241, 2017. doi:10.1097/rmr.0000000000000149.
18. Humphries SM, Swigris JJ, Brown KK, Strand M, Gong Q, Sundy JS, Raghu G, Schwarz MI, Flaherty KR, Sood R, O'Riordan TG, Lynch DA. Quantitative high-resolution computed tomography fibrosis score: performance characteristics in idiopathic pulmonary fibrosis. Eur Respir J 52: 1801384, 2018. doi:10.1183/13993003.01384-2018.
19. Meaburn E, Schulz R. Next generation sequencing in epigenetics: insights and challenges. Semin Cell Dev Biol 23: 192–199, 2012. doi:10.1016/j.semcdb.2011.10.010.
20. Schumacher A, Kapranov P, Kaminsky Z, Flanagan J, Assadzadeh A, Yau P, Virtanen C, Winegarden N, Cheng J, Gingeras T, Petronis A. Microarray-based DNA methylation profiling: technology and applications. Nucleic Acids Res 34: 528–542, 2006. doi:10.1093/nar/gkj461.
21. Brauchle EM, Kasper J, Daum R, Schierbaum N, Falch C, Kirschniak A, Schäffer TE, Schenke-Layland K. Biomechanical and biomolecular characterization of extracellular matrix structures in human colon carcinomas. Matrix Biol 68: 180–193, 2018. doi:10.1016/j.matbio.2018.03.016.
22. Becker L, Lu CE, Montes-Mojarro IA, Layland SL, Khalil S, Nsair A, Duffy GP, Fend F, Marzi J, Schenke-Layland K. Raman microspectroscopy identifies fibrotic tissues in collagen-related disorders via deconvoluted collagen type I spectra. Acta Biomater 162: 278–291, 2023. doi:10.1016/j.actbio.2023.03.016.
23. Becker L, Fischer F, Fleck JL, Harland N, Herkommer A, Stenzl A, Aicher WK, Schenke-Layland K, Marzi J. Data-driven identification of biomarkers for in situ monitoring of drug treatment in bladder cancer organoids. Int J Mol Sci 23: 6956, 2022. doi:10.3390/ijms23136956.
24. Marzi J, Brauchle E, Schenke-Layland K, Rolle MW. Non-invasive functional molecular phenotyping of human smooth muscle cells utilized in cardiovascular tissue engineering. Acta Biomater 89: 193–205, 2019. doi:10.1016/j.actbio.2019.03.026.
25. Daum R, Brauchle EM, Berrio DAC, Jurkowski TP, Schenke-Layland K. Non-invasive detection of DNA methylation states in carcinoma and pluripotent stem cells using Raman microspectroscopy and imaging. Sci Rep 9: 7014, 2019. doi:10.1038/s41598-019-43520-z.
26. Rezakhaniha R, Agianniotis A, Schrauwen JT, Griffa A, Sage D, Bouten CV, van de Vosse FN, Unser M, Stergiopulos N. Experimental investigation of collagen waviness and orientation in the arterial adventitia using confocal laser scanning microscopy. Biomech Model Mechanobiol 11: 461–473, 2012. doi:10.1007/s10237-011-0325-z.
27. Ye H, Rahul, Kruger U, Wang T, Shi S, Norfleet J, De S. Burn-related collagen conformational changes in ex vivo porcine skin using Raman spectroscopy. Sci Rep 9: 19138, 2019. doi:10.1038/s41598-019-55012-1.
28. Li X, Zhang Y, Yu P. Association of bio-energy processing-induced protein molecular structure changes with CNCPS-based protein degradation and digestion of co-products in dairy cows. J Agric Food Chem 64: 4086–4094, 2016. doi:10.1021/acs.jafc.6b00688.
29. Wynn TA. Cellular and molecular mechanisms of fibrosis. J Pathol 214: 199–210, 2008. doi:10.1002/path.2277.
30. Chandler C, Liu T, Buckanovich R, Coffman LG. The double edge sword of fibrosis in cancer. Transl Res 209: 55–67, 2019. doi:10.1016/j.trsl.2019.02.006.
31. Notingher I, Green C, Dyer C, Perkins E, Hopkins N, Lindsay C, Hench LL. Discrimination between ricin and sulphur mustard toxicity in vitro using Raman spectroscopy. J R Soc Interface 1: 79–90, 2004. doi:10.1098/rsif.2004.0008.
32. Huang Z, McWilliams A, Lui H, McLean DI, Lam S, Zeng H. Near-infrared Raman spectroscopy for optical diagnosis of lung cancer. Int J Cancer 107: 1047–1052, 2003. doi:10.1002/ijc.11500.
33. Cheng WT, Liu MT, Liu HN, Lin SY. Micro-Raman spectroscopy used to identify and grade human skin pilomatrixoma. Microsc Res Tech 68: 75–79, 2005. doi:10.1002/jemt.20229.
34. Ó Faoláin E, Hunter MB, Byrne JM, Kelehan P, McNamara M, Byrne HJ, Lyng FM. A study examining the effects of tissue processing on human tissue sections using vibrational spectroscopy. Vibrational Spectroscopy 38: 121–127, 2005. doi:10.1016/j.vibspec.2005.02.013.
35. Cárcamo JJ, Aliaga AE, Clavijo RE, Brañes MR, Campos-Vallette MM. Raman study of the shockwave effect on collagens. Spectrochim Acta A Mol Biomol Spectrosc 86: 360–365, 2012. doi:10.1016/j.saa.2011.10.049.
36. Pascut FC, Goh H, George V, Denning C, Notingher I. Toward label-free Raman-activated cell sorting of cardiomyocytes derived from human embryonic stem cells. J Biomed Opt 16: 045002, 2011. doi:10.1117/1.3570302.
37. Wen ZQ. Raman spectroscopy of protein pharmaceuticals. J Pharm Sci 96: 2861–2878, 2007. doi:10.1002/jps.20895.
38. Belbachir K, Noreen R, Gouspillou G, Petibois C. Collagen types analysis and differentiation by FTIR spectroscopy. Anal Bioanal Chem 395: 829–837, 2009. doi:10.1007/s00216-009-3019-y.
39. Stone N, Kendall C, Smith J, Crow P, Barr H. Raman spectroscopy for identification of epithelial cancers. Faraday Discuss 126: 141–157, 2004. doi:10.1039/B304992B.
40. Frank CJ, McCreery RL, Redd DC. Raman spectroscopy of normal and diseased human breast tissues. Anal Chem 67: 777–783, 1995. doi:10.1021/ac00101a001.
41. Lakshmi RJ, Kartha VB, Murali Krishna C, R. Solomon JG, Ullas G, Uma Devi P. Tissue Raman spectroscopy for the study of radiation damage: brain irradiation of mice. Radiat Res 157: 175–182, 2002. doi:10.1667/0033-7587(2002)157[0175:TRSFTS.
42. Lau DP, Huang Z, Lui H, Man CS, Berean K, Morrison MD, Zeng H. Raman spectroscopy for optical diagnosis in normal and cancerous tissue of the nasopharynx-preliminary findings. Lasers Surg Med 32: 210–214, 2003. doi:10.1002/lsm.10084.
43. Yu J, Zeng C, Wang Y. Epigenetics in dilated cardiomyopathy. Curr Opin Cardiol 34: 260–269, 2019. doi:10.1097/hco.0000000000000616.
44. Pagiatakis C, Di Mauro V. The emerging role of epigenetics in therapeutic targeting of cardiomyopathies. Int J Mol Sci 22: 8721, 2021. doi:10.3390/ijms22168721.
45. Binoy J, Abraham JP, Joe IH, Jayakumar VS, Pettit G, Nielsen OF. NIR-FT Raman and FT-IR spectral studies and ab initio calculations of the anti-cancer drug combretastatin-A4. J Raman Spectrosc 35: 939–946, 2004. doi:10.1002/jrs.1236.
46. Kelly JG, Najand GM, Martin FL. Characterisation of DNA methylation status using spectroscopy (mid-IR versus Raman) with multivariate analysis. J Biophotonics 4: 345–354, 2011. doi:10.1002/jbio.201000085.
47. Dharmalingam P, Venkatakrishnan K, Tan B. Nanoplatform to investigate tumor-initiating cancer stem cells: breaking the diagnostic barrier. ACS Appl Mater Interfaces 14: 6370–6386, 2022. doi:10.1021/acsami.1c21998.
48. Yoon PO, Lee M-A, Cha H, Jeong MH, Kim J, Jang SP, Choi BY, Jeong D, Yang DK, Hajjar RJ, Park WJ. The opposing effects of CCN2 and CCN5 on the development of cardiac hypertrophy and fibrosis. J Mol Cell Cardiol 49: 294–303, 2010. doi:10.1016/j.yjmcc.2010.04.010.
49. Kühn B, Del Monte F, Hajjar RJ, Chang Y-S, Lebeche D, Arab S, Keating MT. Periostin induces proliferation of differentiated cardiomyocytes and promotes cardiac repair. Nat Med 13: 962–969, 2007. doi:10.1038/nm1619.
50. Chen J, Lee SK, Abd-Elgaliel WR, Liang L, Galende E-Y, Hajjar RJ, Tung C-H. Assessment of cardiovascular fibrosis using novel fluorescent probes. PLoS One 6: e19097, 2011. doi:10.1371/journal.pone.0019097.
51. Farhoodi R, Lansdell BJ, Kording KP. Quantifying how staining methods bias measurements of neuron morphologies. Front Neuroinform 13: 36, 2019. doi:10.3389/fninf.2019.00036.
52. Rich L, Whittaker P. Collagen and picrosirius red staining: a polarized light assessment of fibrillar hue and spatial distribution. Braz J Morphol Sci 22: 97–104, 2005.
53. Singh HP, Shetty DC, Wadhwan V, Aggarwal P. A quantitative and qualitative comparative analysis of collagen fibers to determine the role of connective tissue stroma on biological behavior of odontogenic cysts: a histochemical study. Natl J Maxillofac Surg 3: 15–20, 2012. doi:10.4103/0975-5950.102142.
54. Hirshberg A, Sherman S, Buchner A, Dayan D. Collagen fibres in the wall of odontogenic keratocysts: a study with picrosirius red and polarizing microscopy. J Oral Pathol Med 28: 410–412, 1999. doi:10.1111/j.1600-0714.1999.tb02112.x.
55. Arun Gopinathan P, Kokila G, Siddeeqh S, Prakash R, L P. Reexploring picrosirius red: a review. IJPO 7: 196–203, 2020. doi:10.18231/j.ijpo.2020.038.

56. Hanna A, Frangogiannis NG. The role of the TGF-b superfamily in myocardial infarction. Front Cardiovasc Med 6: 140, 2019. doi:10.3389/fcvm.2019.00140.
57. Pauschinger M, Knopf D, Petschauer S, Doerner A, Poller W, Schwimmbeck PL, Kühl, U, Schultheiss, H-P. Dilated cardiomyopathy is associated with significant changes in collagen type I/III ratio. Circulation 99: 2750–2756, 1999. doi:10.1161/01.cir.99.21.2750.
58. Berk BC, Fujiwara K, Lehoux S. ECM remodeling in hypertensive heart disease. J Clin Invest 117: 568–575, 2007. doi:10.1172/jci31044.
59. Díez J. Mechanisms of cardiac fibrosis in hypertension. J Clin Hypertens (Greenwich) 9: 546–550, 2007. doi:10.1111/j.1524-6175.2007.06626.x.
60. Roy S, Khanna S, Rink T, Radtke J, Williams WT, Biswas S, Schnitt R, Strauch AR, Sen CK. $p21^{waf1/cip1/sdi1}$as a central regulator of inducible smooth muscle actin expression and differentiation of cardiac fibroblasts to myofibroblasts. Mol Biol Cell 18: 4837–4846, 2007. doi:10.1091/mbc.e07-03-0270.
61. Driesen R, Nagaraju CK, Abi-Char J, Coenen T, Lijnen PJ, Fagard RH, Sipido KR, Petrov VV. Reversible and irreversible differentiation of cardiac fibroblasts. Cardiovasc Res 101: 411–422, 2014. doi:10.1093/cvr/cvt338.
62. Kern S, Feng H-Z, Wei H, Cala S, Jin JP. Up-regulation of alpha-smooth muscle actin in cardiomyocytes from non-hypertrophic and non-failing transgenic mouse hearts expressing N-terminal truncated cardiac troponin I. FEBS Open Bio 4: 11–17, 2013. doi:10.1016/j.fob.2013.11.002.
63. Vracko R, Thorning D. Contractile cells in rat myocardial scar tissue. Lab Invest 65: 214–227, 1991.
64. Willems IE, Havenith MG, De Mey JG, Daemen MJ. The alpha-smooth muscle actin-positive cells in healing human myocardial scars. Am J Pathol 145: 868–875, 1994.
65. Piquet PF, Van GY, Haas D, Guo J. Heparin attenuates bleomycin but not silica-induced pulmonary fibrosis in mice: possible relationship with involvement of myofibroblasts in bleomycin, and fibroblasts in silica-induced fibrosis. Int J Exp Pathol 77: 155–161, 1996. doi:10.1046/j.1365-2613.1996.d01-214.x.
66. Fireman E, Shahar I, Shoval S, Messer G, Dvash S, Grief J. Morphological and biochemical properties of alveolar fibroblasts in interstitial lung diseases. Lung 179: 105–117, 2001. doi:10.1007/s004080000051.
67. Suurmeijer AJH, Clement S, Francesconi A, Bocchi L, Angelini A, Van Veldhuisen DJ, Spagnoli LG, Gabbiani G, Orlandi A. a-actin isoform distribution in normal and failing human heart: a morphological, morphometric, and biochemical study. J Pathol 199: 387–397, 2003. doi:10.1002/path.1311.
68. Maiti NC, Apetri MM, Zagorski MG, Carey PR, Anderson VE. Raman spectroscopic characterization of secondary structure in natively unfolded proteins: alpha-synuclein. J Am Chem Soc 126: 2399–2408, 2004. doi:10.1021/ja0356176.
69. Gullekson C, Lucas L, Hewitt K, Kreplak L. Surface-sensitive Raman spectroscopy of collagen I fibrils. Biophys J 100: 1837–1845, 2011. doi:10.1016/j.bpj.2011.02.026.
70. Persikov AV, Pillitteri RJ, Amin P, Schwarze U, Byers PH, Brodsky B. Stability related bias in residues replacing glycines within the collagen triple helix (Gly-Xaa-Yaa) in inherited connective tissue disorders. Hum Mutat 24: 330–337, 2004. doi:10.1002/humu.20091.
71. Bella J, Eaton M, Brodsky B, Berman HM. Crystal and molecular structure of a collagen-like peptide at 1.9 A resolution. Science 266: 75–81, 1994. doi:10.1126/science.7695699.
72. Kramer RZ, Bella J, Mayville P, Brodsky B, Berman HM. Sequence dependent conformational variations of collagen triple-helical structure. Nat Struct Biol 6: 454–457, 1999. doi:10.1038/8259.
73. Abraham ET, Oecal S, Mörgelin M, Schmid PWN, Buchner J, Baumann U, Gebauer JM. Collagen’s primary structure determines collagen:HSP47 complex stoichiometry. J Biol Chem 297: 101169, 2021. doi:10.1016/j.jbc.2021.101169.
74. Bellaye PS, Burgy O, Bonniaud P, Kolb M. HSP47: a potential target for fibrotic diseases and implications for therapy. Expert Opin Ther Targets 25: 49–62, 2021. doi:10.1080/14728222.2021.1861249.
75. Ito S, Nagata K. Roles of the endoplasmic reticulum–resident, collagen-specific molecular chaperone Hsp47 in vertebrate cells and human disease. J Biol Chem 294: 2133–2141, 2019. doi:10.1074/jbc.tm118.002812.
76. Brown KE, Broadhurst KA, Mathahs MM, Brunt EM, Schmidt WN. Expression of HSP47, a collagen-specific chaperone, in normal and diseased human liver. Lab Invest 85: 789–797, 2005. doi:10.1038/labinvest.3700271.
77. Nishino T, Miyazaki M, Abe K, Furusu A, Mishima Y, Harada T, Ozono Y, Koji T, Kohno S. Antisense oligonucleotides against collagen-binding stress protein HSP47 suppress peritoneal fibrosis in rats. Kidney Int 64: 887–896, 2003. doi:10.1046/j.1523-1755.2003.00169.x.
78. Sauk JJ, Nikitakis N, Siavash H. Hsp47 a novel collagen binding serpin chaperone, autoantigen and therapeutic target. Front Biosci 10: 107–118, 2005. doi:10.2741/1513.
79. Khalil H, Kanisicak O, Vagnozzi RJ, Johansen AK, Maliken BD, Prasad V, Boyer JG, Brody MJ, Schips T, Kilian KK, Correll RN, Kawasaki K, Nagata K, Molkentin JD. Cell-specific ablation of Hsp47 defines the collagen-producing cells in the injured heart. JCI Insight 4: e128722, 2019. doi:10.1172/jci.insight.128722.
80. Stoll S, Wang C, Qiu H. DNA methylation and histone modification in hypertension. Int J Mol Sci 19: 1174, 2018. doi:10.3390/ijms19041174.
81. Rodenhiser D, Mann M. Epigenetics and human disease: translating basic biology into clinical applications. CMAJ 174: 341–348, 2006. doi:10.1503/cmaj.050774.
82. Breiling A, Lyko F. Epigenetic regulatory functions of DNA modifications: 5-methylcytosine and beyond. Epigenetics Chromatin 8: 24, 2015. doi:10.1186/s13072-015-0016-6.
83. Goll MG, Bestor TH. Eukaryotic cytosine methyltransferases. Annu Rev Biochem 74: 481–514, 2005. doi:10.1146/annurev.biochem.74.010904.153721.

Supplementary information

Identification of Fibrotic and Epigenetic Alterations in Different Cardiomyopathies Using Raman Microspectroscopy

Lucas Becker [a,b], Suzan Khalil [c], Ali Nsair [c], Julia Marzi [a,b,d], Katja Schenke-Layland [a,b,d]

*a - **Institute of Biomedical Engineering, Department for Medical Technologies and Regenerative Medicine**, University of Tübingen, 72076 Tübingen, Germany*
*b - **Cluster of Excellence iFIT (EXC 2180) "Image-Guided and Functionally Instructed Tumor Therapies"**, University of Tübingen, 72076 Tübingen, Germany.*
*c - **Department of Medicine/Cardiology**, Cardiovascular Research Laboratories, David Geffen School of Medicine at UCLA, 675 Charles E. Young Drive South, MRL 3645 Los Angeles, CA, USA*
*d - **Natural and Medical Sciences Institute (NMI) at the University of Tübingen,** 72770 Reutlingen, Germany*

Correspondence: Prof. Dr. Katja Schenke-Layland, Department for Biomedical Engineering, Eberhard-Karls University Tübingen, Silcherstraße 7/1, 72076 Tübingen, DE. katja.schenke-layland@uni-tuebingen.de, https://www.schenke-layland-lab.de

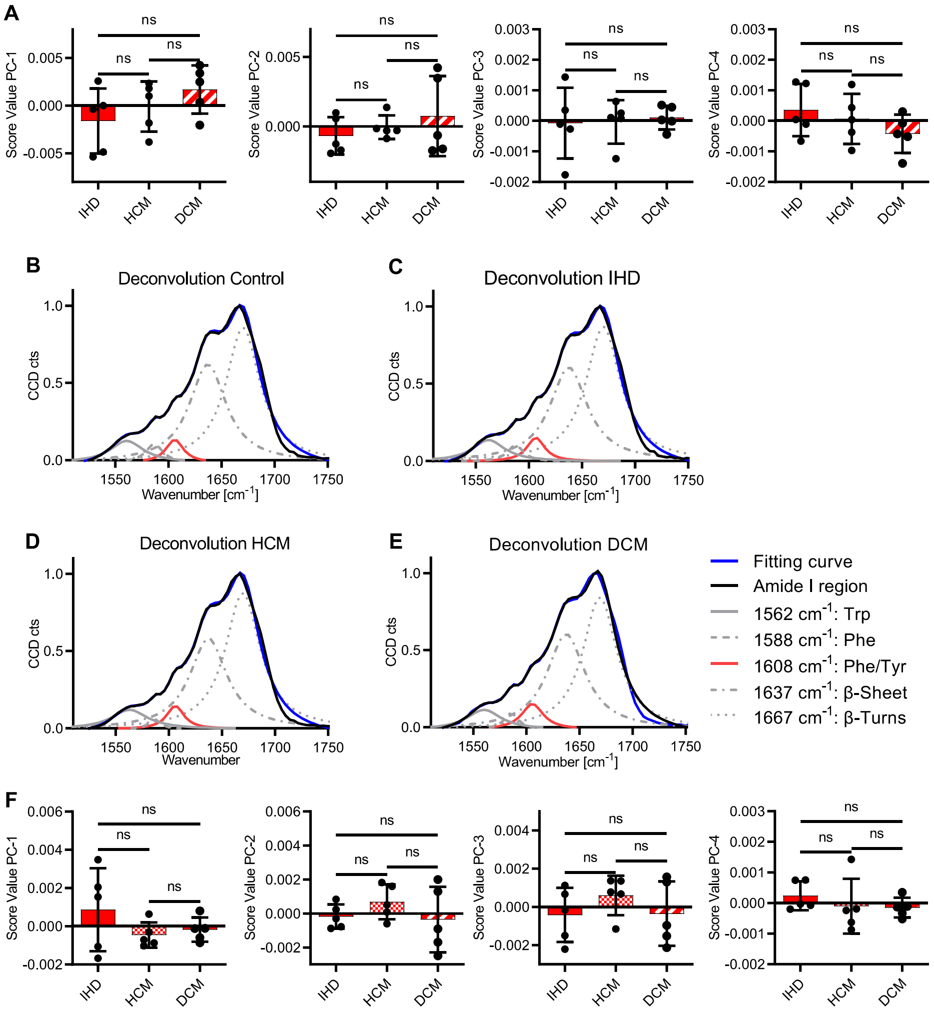

Figure S1: PCA shows no statistically significant differences between different cardiomyopathies. A) Score value analysis of COL I Raman spectra. Spectral deconvolution (Sdc) of averaged COL I Raman spectra of control myocardium (B), IHD (C), HCM (D) and DCM (E). F) Score value analysis of nuclei Raman spectra. Statistical analysis: t-test, *n*=5, ns: not significant.